SHEAR STRENGTHENING OF CONCRETE BEAMS WITH EMBEDDED FRP BARS

by

MANJOLA CARO

A thesis submitted to
the University of Birmingham
for the degree of
DOCTOR OF PHILOSOPHY

School of Engineering
College of Engineering and Physical Sciences
University of Birmingham, UK
July 2018

ABSTRACT

With increasing numbers of strength-deficient concrete infrastructure assets, strengthening and repair of concrete structures is becoming an issue of global importance. This thesis investigates the behaviour of shear-strengthened reinforced concrete (RC) deep beams, which can be found in many concrete infrastructure assets including bridges and high-rise buildings. The thesis examines the bond performance of the deep embedment (DE) technique, also known as the embedded through-section technique (ETS), which utilises fibre reinforced polymer (FRP) bars embedded into concrete using an epoxy adhesive. The bond-slip experimental results were used to develop a nonlinear finite element (NLFE) model for DE-strengthened RC deep beams. After validation, the NLFE model was used to carry out a parametric study, the results of which were used to formulate design models for DE-strengthened RC deep beams.

The literature review revealed that the underpinning understanding of the DE method, particularly with FRP bars, is extensive yet fragmented. The DE technique has clearly been demonstrated to be effective in many respects but to enable further development it is critical that a comprehensive understanding is achieved. In particular, bond behaviour in the DE FRP bar-epoxy-concrete interface is poorly understood and a systematic understanding of the shear behaviour of DE-strengthened RC deep beams is required, to enable robust implementation of the DE technique and effective design. Currently, there are no published FE models and widely accepted design guidelines for predicting the shear strength contribution due to DE FRP bars in RC deep beams.

In this research study, an experimental programme is conducted, which expands the experimental pull-out test results and provides an in-depth understanding of the bond

performance of both CFRP and GFRP bars epoxy-bonded into concrete blocks. For the first time, this study develops a mathematical bond strength model for DE FRP bars. In addition, a thorough examination is provided of the effect of embedment length, FRP bar type and diameter, concrete compressive strength and hole diameter. For both FRP bar types, the pull-out capacity increased whereas the bond strength and initial stiffness of the bond stress-slip curves decreased with the increase in embedded length. The specimens with DE CFRP bars had higher pull-out capacities and better bond performance than the corresponding specimens with DE GFRP bars. For the specimens with DE CFRP bars, the pull-out capacity increased with the increase in concrete strength and bar type, but these two parameters did not affect the behaviour of the specimens with DE GFRP bars. The increase in hole diameter reduced the initial stiffness of the specimens with DE GFRP bars but affected neither the failure mode nor the failure loads.

The shear behaviour of deep beams shear-strengthened with DE FRP bars is poorly understood. Except for shear span-to-effective depth ratio, the effect of the main parameters affecting the shear behaviour has not been investigated. For the first time, in this research study, a three-dimensional FE model is developed and validated using experimental results from large-scale RC T-beams shear-strengthened with DE FRP bars. In addition, a comprehensive parametric study investigates the effect of DE FRP bar diameter, shear span-to-effective depth ratio, DE FRP shear strengthening ratio, FRP bar type and internal steel stirrup-to-DE FRP bar ratio on the shear capacity of FE deep beam models. DE-strengthened FE beam models with carbon-FRP bars achieved higher shear strength capacities than the corresponding FE beam models with DE glass-FRP bars. It was demonstrated that the predicted shear strength gain due to DE FRP bars increased with the increase in FRP bar diameter and DE FRP shear strengthening ratio. The shear span-to-effective depth ratio and internal steel stirrup-to-DE FRP bar ratio affected negatively the shear strength gain, which reduced in both cases.

Most importantly, there are no published design models for estimating the shear strength contribution due to DE FRP bars in deep beams. This research addresses this shortcoming by presenting new shear design formulae for estimating the shear strength gain due to DE FRP bars in deep beams. The design equations are validated against FE modelling results, yielding an acceptable correlation and confirming the potential to be incorporated into the future design guidelines for the DE method.

DEDICATION

I would like to dedicate this thesis to:

My precious mother

My father

My sister and her family

The memory of my grandparents

ACKNOWLEDGEMENTS

Firstly, I would like to express my genuine appreciation and gratitude to my lead supervisor Dr Samir Dirar. I am extremely grateful that I was given the opportunity to be taught and inspired by him throughout both my MEng and PhD degrees in Civil Engineering at the University of Birmingham. I truly admire his philosophy in teaching that the sign of intelligence in research is not seeking simply for knowledge, but awakening within oneself the joy of expressive imagination. He is an exceptional supervisor and cannot thank him enough for helping me accomplish my greatest career goal. I wish him with all my heart that his talent continues to be acknowledged in world-leading civil engineering research.

I would also like to thank you my co-supervisor Dr Andrew Quinn. He inspired and harnessed my talent and ambition for mathematics and engineering by teaching me to never stop questioning the mysteries of science and to follow, not only the deep critical thinking approach, but also the spark that creative imagination brings. He is an inspirational example to engineers, that we should not just strive to be successful but seek to push boundaries and limits.

Appreciation goes to the Engineering and Physical Sciences Research Council (EPSRC) for their financial support through Grant EP/L010364/1.

I would also like to express my deep appreciation to my family and my close friends for their endless support, love, guidance, inspiration and motivation throughout my life. I have been blessed to have amazing parents as role models, who made my dream of being educated abroad a reality and helped me grow into a valuable, strong and compassionate human being. I love you beyond words can express and cannot thank you enough for everything you have done for me.

Finally, I would like this research to act as a proof for the young and talented girls to believe in their extraordinary abilities, and to be brave enough to face and surpass every obstacle even in the most competitive and most challenging world educating systems.

I believed that my greatest achievement through this research would have been my contribution to the field of structural engineering, but inevitably the shear strength enhancement models and bond strength equations that I developed for the Deep Embedment technique were just a true reflection of modelling my inner bond strength in a promising strengthened structure, which is Myself.

Thank you!

Manjola

TABLE OF CONTENTS

LIST OF FIGURES

LIST OF TABLES

ABBREVIATIONS AND NOTATION

Abbreviations

AFRP	Arepree Fibre Reinforced Polymer
BPE	Bertero, Popov and Eligehausen
BRE	Building Research Establishment
CFRP	Carbon Fibre Reinforced Polymer
CMR	Cosenza, Manfredi and Realfonzo
DE	Deep Embedment
EB	Externally Bonded
ETS	Embedded Through Section
FEM	Finite Element Method
FRP	Fibre Reinforced Polymer
GFRP	Glass Fibre Reinforced Polymer
LVDT	Linear Variable Differential Transducer
MCFT	Modified Compression Field Theory
NLFE	Nonlinear Finite Element
NSM	Near Surface Mounted
PVC	Polyvinyl chloride
RC	Reinforced Concrete
TR55	Concrete Society Technical Report TR55
STM	Strut-and-Tie Model

Notation

A_c = Area of the concrete section

A_f = Cross-sectional area of the DE FRP or steel bar

A_l = Cross-sectional area of the longitudinal bars

A_{nz} = Cross-sectional area of the nodal zone

A_{si} = Cross-sectional area of the i-th layer of reinforcement crossing the concrete strut

A_{str} = Effective area of the concrete compressive strut

A_v = Total area of two-leg stirrup

a = Shear span of the RC beam

a/d = Shear span-to-effective depth ratio

a_g = Maximum aggregate size of the concrete mix

b_{si} = Width of concrete strut crossing the i-th layer of shear reinforcement

b_w = Web width of the RC beam

C = Compression force

d = Effective depth of the RC beam

d' = Distance from the outer compressive fibre to the centre of top compression steel

d_b = Bar diameter

d_{fe} = Effective shear depth

d_h = Hole diameter

$\frac{d_w}{d}$ = Factor which considers the positional influence of transverse reinforcement and DE FRP bars

E_c = Modulus of elasticity of concrete

E_f = Modulus of elasticity of FRP reinforcement

E_{fd} = Design elastic modulus of FRP reinforcement

E_p = Modulus of elasticity of adhesive

E_s = Modulus of elasticity of steel reinforcement

F_{nn} = Nominal force in the nodal zone

F_{ns} = Compressive force in the diagonal strut

f_c = Concrete compressive strength at a specific strain ε_c

f'_c = Concrete cylinder compressive strength

f_{ce} = Limiting compressive strength of the diagonal strut

f_{ct} = Uniaxial tensile strength of concrete

f_{cu} = Concrete cube compressive strength

f_{ext} = External force vector

f_{fe} = Effective stress of DE FRP bar

f_{fu} = Ultimate tensile strength of FRP reinforcement

f_{int} = Internal force vector

f_t = Combined tensile strength contribution of the web reinforcement, concrete and DE bars

f_{ta} = Allowable concrete tensile stress

f_u = Ultimate strength of steel reinforcement

f_y = Yield stress of steel reinforcement

f_{yl} = Yield stress of steel longitudinal reinforcement

f_{yh} = Yield stress of steel horizontal reinforcement

f_{yv} = Yield stress of steel vertical reinforcement

$f(S_m)$ = Stress in the FRP bar corresponding to the maximum slip

G_{fs} = Fracture energy of concrete in tension

g = Out-of-balance force vector

g_i = Out-of-balance vector at the start of a specific iteration

g_0 = Force vector of the initial unbalance

h = Total height of the RC beam

K = Transverse stress intensity factor

K_i = Stiffness matrix at a specific iteration

K_h = Horizontal tie index

K_v = Vertical tie index

k = Factor controlling the post-peak branch of the Thorenfeldt compressive stress-strain curve

k_L = Reduction coefficient for the anchorage length of DE FRP bars

κ_r = Factor derived from the classical bending theory for a single RC section

k_s = Reduction coefficient for the presence of steel stirrups

L = Span of the beam

L_{eff} = Minimum anchorage length for DE FRP bars

l_a = Depth of the bottom nodal zone in the STM model

l_b = Embedded length of the DE bar

$l_{b,max}$ = Required anchorage length of FRP bars

l_c = Depth of the top nodal zone in the STM model

l_p = Width of supporting bearing plates

M = Maximum moment applied on the RC beam

M_{CR} = Critical bending moment at shear failure

M_{FL} = Full flexural capacity of the cross section

n = Ratio of steel to concrete elastic moduli

P = Applied load

P_t = Tensile (pull-out) load

p = Curve-fitting parameter of the descending branch of the BPE bond stress-slip model

R = Reaction force

S = Concrete-to-FRP relative slip in the BPE or CMR bond stress-slip model

S_m = Slip corresponding to the peak bond stress in the CMR or BPE bond stress-slip model

s_i = Spacing of the i-th layer of shear reinforcement

s_f = Spacing between DE bars

s_v = Spacing between stirrups

s_r = Curve-fitting parameter of the CMR bond stress-slip model

T = Tensile force

u = Displacement Vector

u^c = Predefined displacement increments

u_x = Displacement in the x-direction

u_y = Displacement in the y-direction

u_z = Displacement in the z-direction

V = Maximum shear force acting on the RC beam

V_a = Aggregate interlock

V_c = Shear resistance provided by concrete

V_{cc} = Shear stress in uncracked concrete

V_d = Dowel action of longitudinal steel bars

V_{Exp} = Experimental shear force capacity

V_{FE} = Finite element predicted shear force capacity

V_f = Shear force contribution due to DE bars

$V_{f,exp}$ = Experimental shear force contribution due to DE bars

V_n = Nominal shear resistance of the beam

V_R = Resultant shear resistance force in the beam-action mechanism

V_{rc} = Residual tensile stresses in concrete after cracking

V_w = Shear force contribution due to steel stirrups

w_{st} = Width of the diagonal concrete compressive strut

W_{eff} = Effective width over which the FRP bars may act

z = Lever arm in the RC beam

α = Curve-fitting parameter of the ascending branch of BPE bond stress-slip model

α_1 = Parameter used in the CSA S806 (2012) STM provisions

α_b = Parameter of the proposed bond strength model of DE FRP bars

α_s = Depth of diagonal concrete strut

β = Curve-fitting parameter of the CMR bond stress-slip model

β_n = Nodal efficiency factor

β_s = Shear retention factor

β_{st} = Strut efficiency factor

$\beta_{\sigma_{cr}}$ = Concrete compressive strength reduction factor due to lateral cracking

γ_A = Partial safety factor for the adhesive

Δ_f = Dimensionless DE reinforcement index

Δ_l = Dimensionless longitudinal reinforcement index

Δ_v = Dimensionless vertical reinforcement index

Δu = Total displacement increment

Δu_0 = Displacement vector of the initial prediction

Δu^c = Constrained displacements increment vector

Δu^u = Unconstrained displacements increment vector

δC = Change in the compression force

δg_i = Change in out-of-balance force vector corresponding to δu_i

δu = Iterative displacement increment

δu_i = Iterative displacement increment at a specific iteration

δT = Change in the tension force

δz = Change in the lever arm

ε = Strain

ε_1 = Average principal tensile strain in concrete

ε_2 = Average principal compressive strain in concrete

ε_c = Concrete compressive strain

ε_c' = Strain corresponding to the cylinder compressive strength, f'_c

ε_{fd} = Design ultimate strain in the FRP reinforcement

ε_{fe} = Effective tensile strain in the FRP reinforcement

ε_{fu} = Ultimate tensile strain of FRP reinforcement

$\varepsilon_{l,1}$ = Tensile damage in the first lateral direction

$\varepsilon_{l,2}$ = Tensile damage in the second lateral direction

ε_{lat} = Average lateral damage

ε_y = Yield strain of the steel reinforcement

θ = Angle between the diagonal compressive concrete strut and the vertical direction

θ_f = Angle of inclination of DE bars to the beam's longitudinal axis

θ_s = Angle of inclination of the diagonal compressive strut to the beam's longitudinal axis

θ_w = Angle of inclination of web reinforcement (stirrups) to the beam's longitudinal axis

λ = Factor to account for low-density concrete

ν = Shear stress

v_c = Shear strength contribution provided by the strut-and-tie mechanism

v_f = Shear strength contribution due to DE FRP bars

v_w = Shear strength contribution due to transverse steel stirrups

v_n = Nominal shear strength

ξ, η, ς = Natural coordinates in elements used in DIANA user's manual, 2016

ζ_c = Concrete softening coefficient

ρ_f = DE shear strengthening ratio

ρ_h = Horizontal reinforcement ratio

ρ_l = Longitudinal reinforcement ratio

ρ_v = Transverse reinforcement ratio

σ = Stress

σ_f = Tensile stress in the DE bar

τ_b = Average bond stress over the anchorage length of DE bars

τ_m = Maximum bond stress of the DE bar

$\tau_{(S)}$ = Bond stress at a specific slip, S

$\tau_{t,p}^{cr}$ = Crack shear strength

Φ_c = Resistance factor of concrete

χ = Non-dimensional interpolating function

ω_h = Dimensionless factor of steel horizontal reinforcement

ω_v = Dimensionless factor of steel vertical reinforcement

CHAPTER 1

INTRODUCTION

1.1 Background

Shear strengthening and repair of deficient reinforced concrete (RC) members, in particular, RC bridges, is an issue of significant economic importance (Dirar et al., 2013b). The strategic and local road networks in the UK are the most highly valued infrastructure assets of Highways England. They comprise 4,400 miles of carriageways and 9,000 bridges at a value of around £344 billion. In 2012/13 approximately £4 billion was spent in maintaining England's strategic road network. The current central government funding allocated to road maintenance for the period of April 2015 to March 2021 is about £10.3 billion (Comptroller and Auditor General of NAO, 2014). In Europe and the United States of America, the estimated investment for replacing structurally deficient bridges reaches significant thresholds of up to €400 billion and $20.5 billion respectively (Holicky et al., 2010; Advisory Council of ASCE, 2013).

Fibre-reinforced polymer (FRP) composites in the form of near surface mounted (NSM) bars or externally bonded (EB) sheets have been widely used to achieve satisfactory rehabilitation and shear strength enhancement of RC infrastructure assets and overcome the costly corrosion maintenance issues associated with steel reinforcement (Rahal and Rumaih, 2011; Qin et al., 2014; Dirar et al., 2013b; Triantafillou, 1998; Bousselham and Chaallal, 2008; Rizzo and De Lorenzis, 2009). FRP composites have a high strength-to-weight ratio, durability and good impact resistance. A recent innovative shear strengthening method is the deep embedment (DE) (Valerio and Ibell, 2003; Valerio et al., 2009), also recognised as embedded through-section (ETS) technique (Chaallal et al., 2011; Mofidi et al., 2012; Breveglieri et al., 2015). In this

technique, vertical or inclined holes are drilled upwards from the soffit in the required positions of the shear spans of existing RC beams. FRP or steel bars are then bonded to the concrete core using high viscosity epoxy resin which is injected into the drilled holes.

Previous experimental and analytical investigations on RC slender beams strengthened with DE FRP bars have proved the shear strengthening pre-eminence of the DE technique compared to the shear strengthening effectiveness of EB FRP sheets and NSM FRP rods (Valerio and Ibell, 2003; Valerio et al., 2009; Chaallal et al., 2011; Mofidi et al., 2012; Breveglieri et al., 2015; Godat et al., 2012; Jemaa et al., 2015; Breveglieri et al., 2016; Qapo et al., 2016b). Different from the EB and NSM techniques, the DE method relies on the concrete core transferring the stresses to the DE bars, hence improving the bond performance and providing higher shear strengthening enhancement. The DE technique prevents the debonding failure mechanism and delamination of concrete cover related to the aforementioned external strengthening methods. The experimental programme conducted by Chaallal et al. (2011) examined the shear strengthening enhancement between DE FRP bars and both NSM FRP rods and EB U-jacket sheet. It was reported that the increase in the shear strength capacity due to DE FRP bars was 61 %, whilst NSM FRP rods and EB U-jacket sheet achieved a shear strength enhancement of about 31% and 23 %, respectively. It was also shown that slender beams strengthened with the EB system experienced FRP sheet debonding. The failure mode of NSM reinforcement was characterised by delamination of the side concrete covers at the location of internal steel stirrups. The failure mode of DE FRP strengthened RC beams occurred only when the FRP potential tensile strength was attained after exhibiting high deformations and before reaching the ultimate flexural failure. In addition, the experimental programme conducted by Breveglieri et al. (2015) on T-beams shear-strengthened with DE carbon-FRP and steel bars showed that the good bond condition between the concrete core of the RC beams and the DE bars enabled yielding for the DE steel

bars, and in particular the inclined CFRP bars, to attain a high maximum tensile strain, resulting in a substantial increase of the shear strength.

The DE method also requires a shorter installation time, less adhesive, reduced surface preparation and offers better resistance against fire, vandalism and environmentally aggressive agents, especially when using FRP bars (Chaallal et al., 2011; Godat et al., 2012). The confinement of bars embedded in the concrete core potentially improves bond performance compared to both EB and NSM methods. However, Valerio et al. (2009) reported that the efficiency of the DE technique is affected by the mechanical properties of epoxy adhesive (e.g. high-viscosity, high-strength) to achieve a good bond in the DE FRP-to-concrete interface and prevent debonding failure. Mofidi et al. (2012) also showed that FRP bars with a plain surface provide a higher shear strengthening efficiency compared to a sand-coated surface because of better shear transfer across the bar-epoxy interface. Despite the above advantages, research has shown that it can be laborious to drill holes in the shear spans of RC members with heavily congested internal steel longitudinal reinforcement and steel stirrups. Furthermore, galvanic corrosion may occur when DE carbon-FRP (CFRP) bars get in direct contact with existing steel reinforcement in RC beams. Caro et al. (2017) suggested using an electrically insulating epoxy to avoid the potential galvanic corrosion.

Valerio et al. (2009) and Godat et al. (2012) highlighted other conditions for FRP DE to be effectively utilised in RC beams, which included adequate concrete strength, sufficient FRP bar embedment length, and an embedded bar spacing between 0.5 to 0.75 of the beam effective depth. This limiting of spacing prevents any shear discontinuity developing between DE bars. It was also recommended that the shear strength gain due to DE FRP bars (V_f) can be evaluated

by restricting their effective strain value (ε_{fe}) to 0.4%. Mofidi et al. (2012) confirmed that a greater shear contribution by the DE bars was achieved by decreasing the FRP bar spacing and using high strength concrete. Increasing FRP bar diameter (d_b) also increased shear contribution (V_f) proportional to $d_b^{3/2}$.

The orientation of DE strengthening is also important. Barros and Dalfre (2013) concluded that both vertical and inclined bars provide significant enhancement in the load-carrying and deflection capacity of the strengthened beams, but inclined DE bars were more effective compared to the vertical ones. In addition, Breveglieri et al. (2015) found that the increase in the load carrying capacity varied between 53% to 136% when using inclined bars, and only between 52% to 68% when vertical DE bars were embedded in the concrete core. This is attributed to the DE shear strengthening ratio (defined as the ratio between the area of the DE bar (A_f) and the product of beam width (b_w), DE bar spacing (s_f) and angle of inclination of DE bar (θ_f)) being higher than that of vertical bars for the same bar spacing and larger available resisting bond length. Furthermore, RC beams strengthened with inclined steel and carbon-FRP DE bars achieved larger deflection capacity. The shear capacity was also found to increase when the spacing between DE bars is decreased, which may alter the brittle shear failure of the beams into a more ductile failure (i.e. flexural).

The contribution of shear strengthening methods to the overall shear capacity is also affected by the existing transverse shear reinforcement. In EB and NSM strengthened RC beams with internal steel stirrups, the contribution of FRP was reported to be significantly reduced compared to beams without existing shear reinforcement. In contrast, the negative effect of the existing transverse shear reinforcement was less significant on RC beams retrofitted with DE bars. The DE technique was able to improve the shear capacity of RC beams with existing steel stirrups by ~35% (Chaallal et al., 2011). However, DE FRP bars were more effective in increasing the shear capacity for RC beams without transverse steel stirrups or with a small

transverse reinforcement ratio (i.e. widely spaced stirrups). In addition, in-depth research by Breveglieri et al. (2015) investigated the impact of internal transverse steel reinforcement ratios in the range of 0 to 0.17 % on the shear strengthening effectiveness of the DE method. They concluded that the reduction in the shear capacity due to internal steel stirrups was more significant in the case of DE strengthened RC beams with the highest ratio of internal steel stirrups ratio (i.e. 0.17 %). The strengthening effectiveness of vertical DE steel bars decreased up to 74% compared to RC beams without stirrups.

Nonetheless, understanding of the effect of concrete strength and shear span-to-effective depth on the shear capacity of slender DE-strengthened beams is yet fragmented.

Research examining the shear behaviour of RC deep beams strengthened in shear with DE FRP bars is very limited. The only experimental study published so far is conducted by Dirar and Theofanous (2017). They tested two series of large-scale RC T-beams, which included an un-strengthened deep beam and a DE shear-strengthened beam. The beams had an a/d ratio of either 1.9 or 3.0, effective depth of about 600 mm and were reinforced with internal steel stirrups. Sand-coated GFRP bars of 12 mm diameter were used for shear strengthening. The study confirmed that the shear strength gain due to the DE GFRP bars varied from 33% to 96% for beams with a/d of 1.9 and 3.0 respectively, proving that the shear strength gain due to the DE GFRP bars is strongly dependent on a/d ratio.

Kani et al. (1964) classified RC beams as deep or slender if their shear span-to-effective depth (a/d) ratio is less or greater than 2.5 respectively. Deep beams are primarily used as transfer girders, bent caps, pile caps and foundation walls. The shear behaviour of RC deep beams differs from that of slender beams due to a different force-transferring mechanism. In cracked RC slender beams (a/d > 2.5), the tension force in the longitudinal reinforcement

varies along the beam length whereas the internal lever arm remains constant. This is defined as beam action. In cracked RC slender beams with internal shear reinforcement, the applied shear force is resisted by an internal truss-like structure. Whereas, in cracked RC deep beams ($a/d < 2.5$), the internal lever arm varies along the beam length, but the tension in the longitudinal reinforcement remains constant. This is defined as arch action, which is the primary force resisting mechanism (Dirar and Theofanous, 2017). Deep beams are characterised by a nonlinear strain distribution in the discontinuity region (refer to Section 2.6.3), and the applied forces are directly transferred to supports through compressive stresses in the concrete struts joining the loading point and support rather than shear stresses (Birrcher et al., 2013; Tuchscherer et al., 2011).

Previous experimental investigation on deep beams reinforced with internal FRP longitudinal reinforcement and without web reinforcement by Andermatt and Lubell (2013) and Farghaly and Benmokrane (2013) documented the development of arch action in FRP-reinforced concrete deep beams utilizing the uniform strain profile of the FRP longitudinal reinforcement. Previous tests in steel-reinforced concrete deep beams (Kong et al., 1972; Tan et al., 1997) revealed that web reinforcement enhanced significantly the shear capacity of deep beams. On the other hand, Mohammed et al. (2017) performed a comprehensive parametric study on deep beams reinforced completely with glass-FRP bars as longitudinal and web reinforcement. It was revealed that vertical FRP web reinforcement had an insignificant impact on the shear strength, but helps in restricting the crack width.

Nonetheless, the shear behaviour of deep beams strengthened with DE FRP bars is very poorly comprehended. As far as can be ascertained, there is only one published experimental study and neither numerical nor analytical studies that investigate the shear strength contribution due to DE FRP bars in deep beams. Moreover, the effects of the main parameters affecting the shear behaviour, e.g. shear span-to-effective depth ratio, FRP bar type and reinforcement ratio, the

interaction between DE bars and steel stirrups, have been very limitedly considered. Further research is required to investigate the development of arch action in DE shear-strengthened deep beams.

It is apparent that the underpinning understanding of DE method, particularly with FRP bars, is extensive yet fragmented. The DE technique has clearly been demonstrated to be effective in many respects but to enable further development it is critical that a comprehensive understanding is achieved. In particular, DE bond behaviour is poorly understood and a systematic understanding of the shear behaviour of DE-strengthened RC deep beams is required, to enable effective design. Currently, there are no published finite element models and widely accepted design guidelines for predicting the shear strength contribution due to DE FRP bars in RC deep beams. Therefore, finite element (FE) modelling of DE-strengthened RC beams can be a powerful method to predict their overall shear behaviour and carry out extensive parametric studies.

1.2 Research Significance

Understanding the shear behaviour of RC slender and deep beams shear-strengthened with deep embedded (DE) FRP bars, as well as the bond behaviour in the DE FRP bar-epoxy-concrete interface is essential to the robust implementation of the DE technique as a promising concrete shear strengthening solution. The literature review revealed that the bond behaviour of the DE technique is partially understood and there is a lack of published analytical models for the bond strength of DE FRP bars. Thus, an experimental programme is conducted, which expands the experimental pull-out test results and provides an in-depth understanding of the bond performance of both CFRP and GFRP bars epoxy-bonded into concrete blocks. For the first time, this study develops a mathematical bond strength model for DE FRP bars. In addition, a

thorough examination is provided of the effect of embedment length, FRP bar type and diameter, concrete compressive strength and hole diameter.

Furthermore, the shear behaviour of deep beams shear-strengthened with DE FRP bars is poorly understood. Except for shear span-to-effective depth ratio, the effect of the main parameters affecting the shear behaviour has not been investigated. For the first time, in this research study, a three-dimensional nonlinear finite element (FE) model using FE package DIANA version 9.4.6 (DIANA user's manual, 2016) is developed and validated using experimental results from large-scale RC T-beams shear-strengthened with DE FRP bars. In addition, a comprehensive parametric study investigates the effect of DE FRP bar diameter, shear span-to-effective depth ratio, DE FRP shear strengthening ratio, FRP bar type and internal steel stirrup-to-DE FRP bar ratio on the shear capacity of FE deep beam models.

Finally, there are no published design models for estimating the shear strength contribution due to DE FRP bars in deep beams. TR55 design guidance (Concrete Society, 2012), Mofidi et al. (2012) and Qapo et al. (2016a) had previously proposed design models applicable only for calculating the contribution of DE FRP bars to the shear capacity in slender beams. Thus, this study addresses this shortcoming by formulating new design models for estimating the shear strength gain due to DE FRP bars in deep beams. The design equations are validated against FE modelling results, yielding an acceptable correlation and confirming the potential to be incorporated into the future design guidelines for the DE method.

1.3 Research Methodology

During the first stage of this research, a comprehensive and critical review of the published literature on the bond performance and shear behaviour of the DE technique was performed. A synthesis has been made of the available bond test results obtained from pull-out tests performed on DE bars epoxy-bonded to concrete blocks. The impact of the main parameters affecting the FRP bar /concrete interface and the adopted analytical bond-slip models have been thoroughly explained. A critical review is also provided for the shear behaviour of deep RC beams. This includes a brief explanation of the key differences between slender and deep concrete beams, the crack development and failure modes in deep beams, as well as the main factors affecting their behaviour. In addition, the key principles of strut-and-tie design provisions provided in CSA S806 (2012) and ACI 318 (2011) for the shear capacity of deep concrete beams have been outlined.

During the second stage of this research, a total of eighteen laboratory pull-out tests on FRP bars epoxy-bonded into 200 × 200 mm concrete cubes were conducted. This experimental programme examined the bond behaviour of both DE GFRP and CFRP bars epoxy-bonded into concrete cubes. The effect of embedment length, FRP bar type and diameter, concrete compressive strength and hole diameter was thoroughly investigated. A new bond strength mathematical model was proposed which yielded accurate predictions.

The third stage involved utilising the FE package DIANA version 9.4.6 (DIANA user's manual, 2016) to develop three-dimensional FE beam models to simulate the shear behaviour of five beams, which were experimentally tested at the University of Birmingham, UK. Appropriate constitutive models and element types were adopted for the geometric and material modelling of concrete, steel and DE FRP reinforcement. The FE model was validated by comparing the experimental results with the predicted results in terms of load-deflection

relationship, shear capacity, deflections, as well as the crack pattern for each FE model. A parametric study was then performed, which extended current knowledge about the impact of key parameters affecting the shear capacity of shear-strengthened RC deep beams with DE FRP bars.

Finally, this research presents new shear design equations for calculating the gain in the shear capacity due to DE FRP in deep RC beams. The design equations were validated against FE modelling results yielding an acceptable correlation.

1.4 Aim and Objectives

The aim of this research is to study the bond behaviour and shear performance of deep embedment (DE) technique in concrete beams with embedded FRP bars.

The key objectives to be fulfilled are:

- To carry out a comprehensive review of the main parameters influencing the bond behaviour of epoxy-bonded DE bars in concrete;
- To carry out a comprehensive review of the key parameters that influence the shear strength of DE-strengthened RC beams;
- To perform pull-out tests that investigate the DE FRP bar-to-concrete bond behaviour and investigate the effect of the main parameters that influence the bond behaviour of epoxy-bonded DE bars in concrete;
- To propose a new bond strength mathematical model and validate it against experimental results;

- To use the FE package DIANA version 9.4.6 in order to develop a three-dimensional FE model and validate it using published experimental results of RC beams strengthened in shear with DE FRP bars;
- To carry out a parametric study using the developed FE model to examine the impact of the main parameters affecting the shear force capacity and the shear strength contribution due to DE FRP bars in deep beams;
- To formulate an innovative design equation for predicting the shear contribution of DE FRP bars for deep beams strengthened using the DE technique.

1.5 Thesis Organisation

This thesis is organised into six chapters as follows:

- Chapter One addresses the research significance, methodology and the key aim and objectives.
- Chapter Two reviews the published literature relating to the DE technique and provides thorough information regarding DE bond behaviour, major findings of experimental and numerical studies and existing design guidelines for the DE FRP shear-strengthening technique.
- Chapter Three provides details of the experimental programme on the bond behaviour of DE FRP bars epoxy-bonded into concrete.
- Chapter Four presents the development and validation of the FE models for FRP shear-strengthened beams with DE bars. This chapter also presents a parametric study, which examines the impact of the main parameters on the shear capacity of DE strengthened deep beams.

- Chapter Five introduces a new design equation for predicting the contribution to the shear capacity due to DE FRP bars in deep RC beams.
- Chapter Six summarises the main findings of the experimental, numerical and analytical work, and presents recommendations for future research.

CHAPTER 2

LITERATURE REVIEW

2.1 Introduction

This chapter provides a comprehensive understanding on the bond behaviour of the deep embedment (DE) technique and its impact on the shear performance of DE-strengthened RC beams with FRP/steel bars. A detailed and comprehensive assessment of the key parameters affecting the bond behaviour of RC shear-strengthened beams is provided by compiling a synthesis of the published experimental findings obtained from pull-out tests performed on epoxy-bonded DE FRP/steel bars. In addition, the adopted bond-slip models, namely the BPE modified model by Eligehausen, Popov, and Bertero (1983) and the CMR model by Cosenza, Manfredi, and Ralfonzo (1997), for representing the bond behaviour of DE FRP bar-to-concrete interface are discussed. The main outcomes of experimental beam tests found in the literature are reviewed to provide a comprehensive assessment of the key parameters that influence the shear capacity of DE shear strengthened beams with FRP or steel bars. In addition, this chapter identifies gaps in the knowledge of the key parameters that have not been investigated sufficiently and suggests recommendations for further research to be carried out with respect to both bond and shear performance of the DE technique.

2.2 Fibre Reinforced Polymer (FRP)

FRP composite materials consist of four main components: fibres, polymer resin matrix, fillers, and additives. The strength of composite materials is governed by the type of fibres. The polymer matrix binds the fibres together, providing the required protection against

environmental factors and allowing the load transfer. Fillers are used for preventing shrinkage cracking and improving the surface roughness. Several additives, such as plasticisers, heat stabilisers, chemical release and foaming agents, ultraviolet stabilisers, antioxidants, pigments or colorants, flame-retardants, thickening and toughening agents, impact modifiers, thermoplastic polymer materials against shrinkage cracking, blowing agents, and silane coupling agents have been used to enhance the overall properties of FRP (Bank, 2006).

FRP composites have been used in various industries, such as the construction, aerospace, automotive, marine, and construction industries since they allow the alignment of the reinforcing fibres such that the strength and resistance to deformation of the polymer can be increased. FRP have been used for shear strengthening of RC members in various forms, such as deep embedded (DE) FRP reinforcing bars (Valerio et al., 2009), near-surface mounted (NSM) FRP rods, externally bonded (EB) U-jacket sheets and closed wraps (complete wraps) (Chaallal et al., 2011).

The three main types of FRP fibres which are currently used for reinforcement purposes are aramid-FRP (AFRP), glass-FRP (GFRP) and carbon-FRP (CFRP). Aramid-FRP are crystalline aromatic polyamide fibres, which have a high strength-to-weight ratio and high resistance to organic solvents, fuels, and lubricants. However, these fibres have low compressive strength and are highly hygroscopic material (GangaRao et al., 2007).

Glass-FRP are the most popular among all reinforcing fibres for polymeric matrix composites. They have been widely used in the form of either reinforcing bars or FRP strengthening fabrics and profiles. Glass fibre is formed when silica-based thin strands are extruded into fibres of small diameters at melting temperatures of about 1400^{o}C. The molten

glass spins from electrically heated platinum-rhodium bushing plates. Following that, individual filaments are manufactured with a surface coating (called sizing), which provides the required protection for filaments prior to them being packed into a bundle, or strand, and reduces the abrasive effects and static friction among filaments (Bank, 2006). The most common types of glass fibres are borosilicate glass known as E-glass (electrical glass), S-glass or R-glass (structural or high strength glass) and C-glass (corrosion resistant). E-glass has been widely used for structural engineering applications because of its high electrical resistivity, low cost and low susceptibility to moisture.

Glass-FRP are low cost and excellent thermal and electrical insulators. They have greater strength resistance when the orientation of polymer fibres is parallel to the direction of applied loads. However, they have a relatively low modulus of elasticity and tensile strength, high sensitivity to abrasion and low fatigue resistance, and a lower strength resistance when fibres are perpendicular to the applied forces. In addition, they are prone to moisture absorption in environments of high alkalinity or salts. Furthermore, such fibres are prone to creep rupture under continuous loading (Bank et al., 1995).

Carbon-FRP have been commonly used as strengthening sheets and fabrics, strips and pre-stressing tendons. They are solid semi-crystalline organic materials consisting of planar two-dimensional arrays of carbon atoms, which comprise 90 % of fibre weight and give the characteristic charcoal-black colour. CFRP are produced at temperatures ranging from 1200^0 to 2400^0C by a controlled pyrolysis of three types of precursor materials, namely synthetic polyacrylonitrile (PAN) textile fibres, natural cellulosic rayon textile fibres and coal-tar pitch fibres (Bank, 2006). During fabrication, the fibres are treated by different processes such as thermosetting, carbonizing and graphitization. As with the other types of FRP, surface

treatment and suitable sizing are required for carbon-FRP to be compatible with vinyl ester epoxy resin systems and improve the bonding strength. The main advantages of CFRP are: (a) high durability, perform well when subjected to fatigue loads; (b) high tensile strength-to-weight ratio and high modulus of elasticity; (c) negative coefficient of linear thermal expansion in the longitudinal direction, which implies exceptional dimensional stability. However, they are thermally and electrically conductive materials; thus, the galvanic reaction may occur when CFRP bars are in contact with other metallic materials, which can lead to the degradation of the polymer resin. In addition, they have low impact resistance and high material cost which limits their widespread application (GangaRao et al., 2007).

2.2.1 Mechanical and Physical Properties

Guadagnini et al. (2003) compared the stress-strain relationship of conventional steel and FRP composites as shown in Figure 2.1. In contrast to steel, FRP bars are characterised by a linear elastic stress-strain behaviour up to failure without exhibiting a yielding plateau. However, the compressive strength of fibres is lower compared to that of steel.

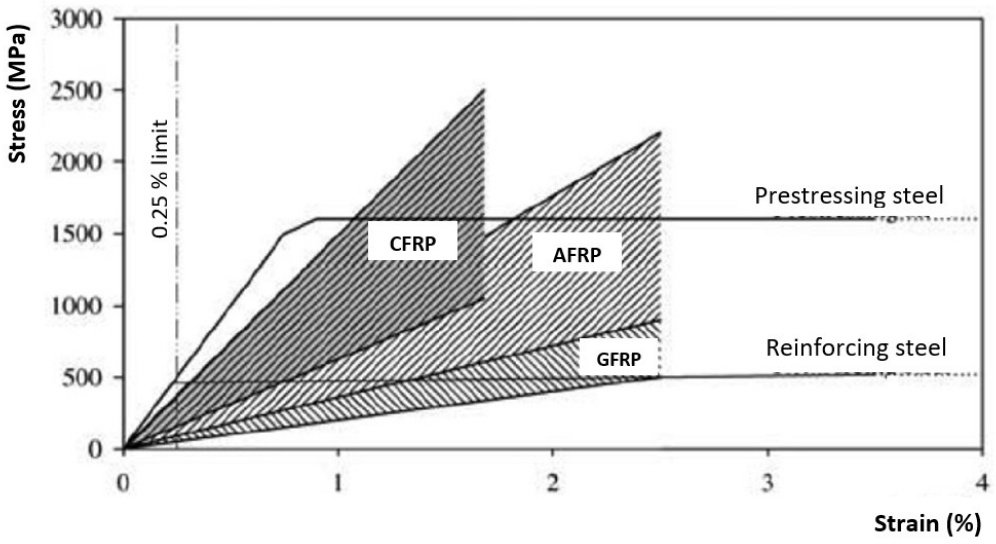

Figure 2.1 Stress-strain relationships for steel and FRP reinforcement (Guadagnini et al., 2003)

The polymeric thermosetting or thermoplastic matrix significantly influence the mechanical properties of FRP. Thermosetting polymers are most commonly used in the industry since their rigid three-dimensional structure is not affected by heat or pressure, as in the case of thermoplastic polymers which are characterised by a linear structural form of molecules joined together using weak secondary bonds. Thermosetting polymers, such as polyesters, vinyl esters and epoxies, enhance chemical resistance, thermal stability, creep resistance and stress relaxation. However, they are prone to fracture during high strains and impact loads, as well as require longer manufacturing time. In order to enhance the mechanical properties of FRP, reduce their cost and improve the processing, inorganic particulate fillers are used such as kaolin clay, calcium carbonate and alumina trihydrate (Bank, 2006). Polyester and vinyl-ester protruded FRP bars and profiles contain between 10 to 30 % by weight of filler. Fillers can be used to improve the transfer of stresses in the transverse direction of fibres, reduce shrinkage and increase corrosion resistance (Meyer, 1985). On the other hand, additives can affect resin chemistry, influencing both the mechanical and physical properties of FRP bars. Table 2.1 provides a comparison of the mechanical properties of steel and FRP bars.

Table 2.1 Comparison of mechanical properties between steel and FRP (fib, 2007)

Properties	Steel	AFRP	GFRP	CFRP
Elastic modulus (GPa)	200 to 210	42 to 126	35 to 51	120 to 580
Tensile strength (MPa)	483 to 690	1723 to 2544	484 to 1600	600 to 3690
Yield strength (MPa)	277 to 518	N/A	N/A	N/A
Yield strain (%)	0.14 to 0.25	N/A	N/A	N/A
Rupture strain (%)	6 to 12	1.9 to 4.4	1.2 to 3.1	0.5 to 1.7

2.3 Mechanics of Stress Transfer from Concrete to FRP bars

Previous research studies on the bond behaviour between concrete and FRP reinforcement directly embedded into concrete without epoxy, have reported that the key mechanisms of stress transfer by the bond between FRP reinforcement and concrete are chemical bond adhesion, friction due to micro surface roughness and mechanical interlock due to bar ribs or another type of shaping. Such ribs induce bearing stresses in the surrounding concrete (ACI 440.1R, 2006). The bond strength of straight bars (including smooth, sand-grain-covered, sandblasted and strand-shaped bars) is dominated by friction, whilst in deformed bars (e.g. ribbed, indented, twisted, braided) the dominant mechanism appears to be interlocking (Kanakubo et al., 1993; Nanni et al., 1995). Chemical bond strength between the FRP bars and concrete was found to be weak, breaking first during the initial pull-out. These bond mechanisms are influenced by the anisotropic nature of FRP bars (i.e. resin governs the shear and transverse properties while the fibres dictate the longitudinal properties) leading to different mechanical and physical properties in each direction. In addition, the bond performance is influenced by other parameters such as the bar's surface finish, diameter, embedment length, concrete strength, and reinforcement stiffness.

Confinement pressure, variations of temperature and environmental conditions during the entire lifetime also affect the bond performance. Nanni et al. (1995) also concluded that the bond behaviour of FRP bars to concrete without epoxy is different compared to that of conventional steel bars. Lower FRP modulus of elasticity (i.e. lower stiffness), lower surface undulations, lower shear strength and stiffness in the transverse direction and higher normal strains at failure affect the bond behaviour. When using steel bars, the primary cracks in the concrete substrate will extend with additional inclined secondary cracks along the bar length if

the tensile stress of the concrete is exceeded. However, the concrete matrix will prevent them from propagating further. In contrast, the FRP bar's resin dependent strength can be lower than the compressive strength. As a consequence, failure may occur due to damage of the FRP bars' ribs and partial failure in the concrete rather than concrete crushing (bearing causing side-splitting or shearing of concrete) which occurs in the case of steel bars' bond failure (fib, 2007). Therefore, the FRP to concrete bond behaviour is influenced by such failure stresses and strains due to the lower Young's modulus in the longitudinal and transverse direction.

On the other hand, in the deep embedment (DE) technique with either FRP or steel bars, high viscosity epoxy resin is injected into the drilled holes to bond the bars to the concrete core. Godat et al. (2012) reported that bond behaviour between FRP bars and concrete is strongly dependent on the chemical bond within the FRP-epoxy-concrete interface rather than mechanical bond. In particular, plain-surface CFRP rods exhibited a superior bond performance due to a better shear transfer and significant chemical bond within the FRP-epoxy-concrete interface compared to sand-coated surface FRP bars. This observation was attributed to the similar polar molecular groups between the epoxy and FRP bars, which are mutually attractive and chemically compatible. In addition, it was suggested that the sand coating of FRP rods may hinder the full compatibility between the epoxy and FRP bars; thus, the chemical bond is reduced. Of note is that, Cosenza et al. (1997) showed that it is the mechanical bond rather than chemical bond which controls the interfacial bond behaviour, if the FRP rods are directly embedded in concrete without epoxy. In this case, the rough-surfaced FRP rods achieved a better bond performance compared to plain-surface FRP bars.

Pull-out testing is a practical procedure for investigating the bond behaviour for both steel and FRP bars embedded in concrete blocks. The results of such tests are expressed in terms of the average bond-slip relationships at the loaded and free ends of the tested bars.

Figure 2.2 shows the typical setup arrangement of the pull-out bond test for assessing the bond behaviour of the DE technique. Even though the stresses developed in the concrete and the obtained bond values during such tests differ significantly from those happening in practice, these tests are widely adopted due to their applicability, simplicity and economic advantage in examining the bond performance (Achillides and Pilakoutas, 2004).

Tighiouart et al. (1998) also suggested using flexural bond tests, such as beam tests, which can offer a more realistic presentation of the bond behaviour by solving the stress field discrepancies present in pull-out tests, but such tests are not currently widely adopted.

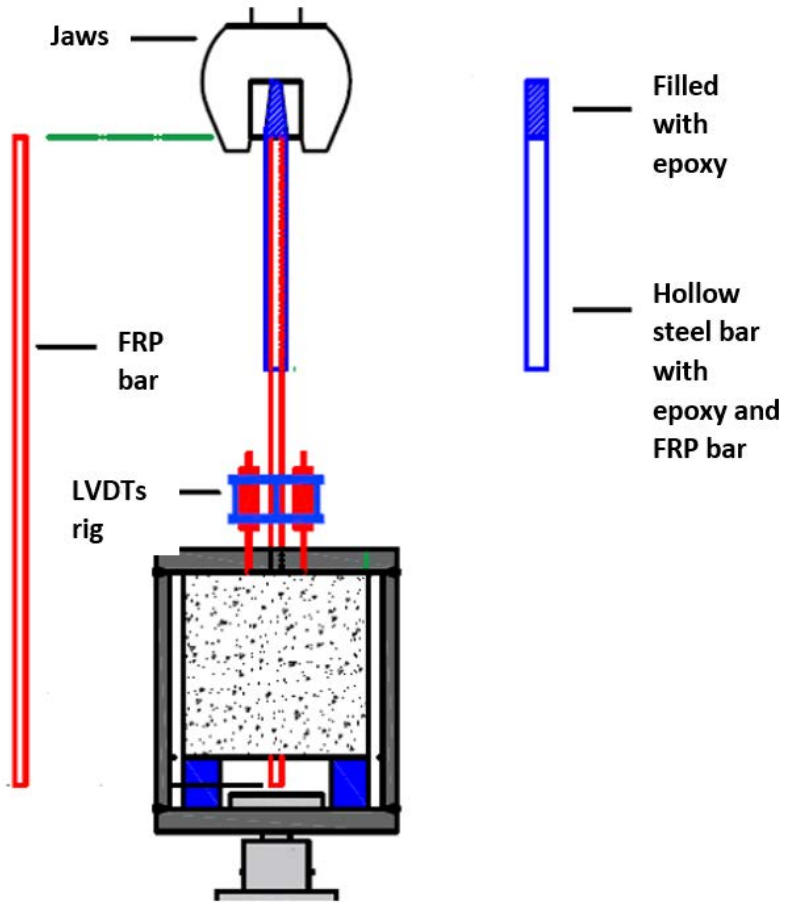

(a)

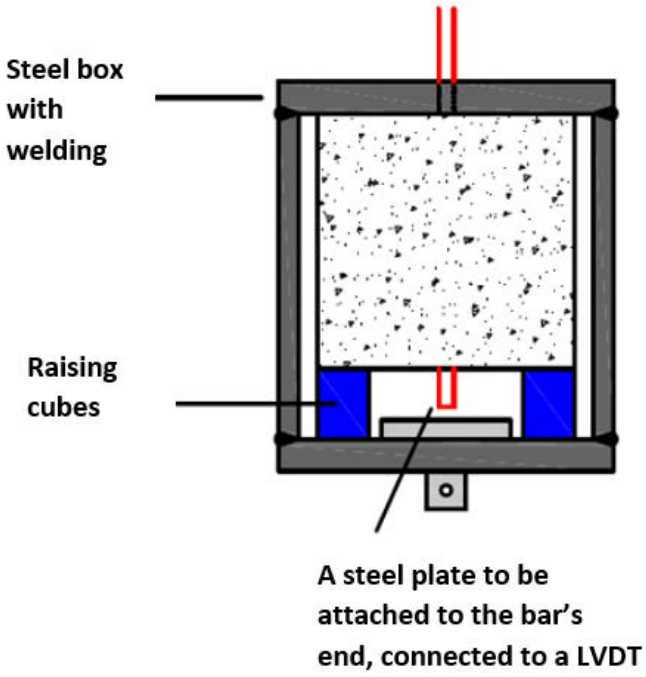

(b)

Figure 2.2 Setup arrangement of the pull-out test: (a) frame and (b) concrete specimen

The most comprehensive pull-out bond test studies are published by Valerio et al. (2009) and Godat et al. (2012). Table 2.2 provides a summary of the bond tests performed and the key parameters in these studies. Detailed data on the test specimens including specimen configuration, concrete properties, properties of DE bars and epoxy used can be found in Table 2.3.

Valerio et al. (2009) performed sixty-five pull-out tests using bars of four materials: aramid-FRP, glass-FRP, carbon-FRP and steel as shown in Figure 2.3. These bars were epoxy bonded into 150 x 150 mm concrete cubes (compressive strength = 60 MPa**)** at five embedment lengths of 15, 30, 45, 60 and 75 mm with hole diameter between 1.2 and 1.3 bar diameter.

Three commercially available adhesives were used: low-viscosity epoxy (Araldite), non-sag, high-strength epoxy (Hilti 500) and a medium strength paste (Hilti 150).

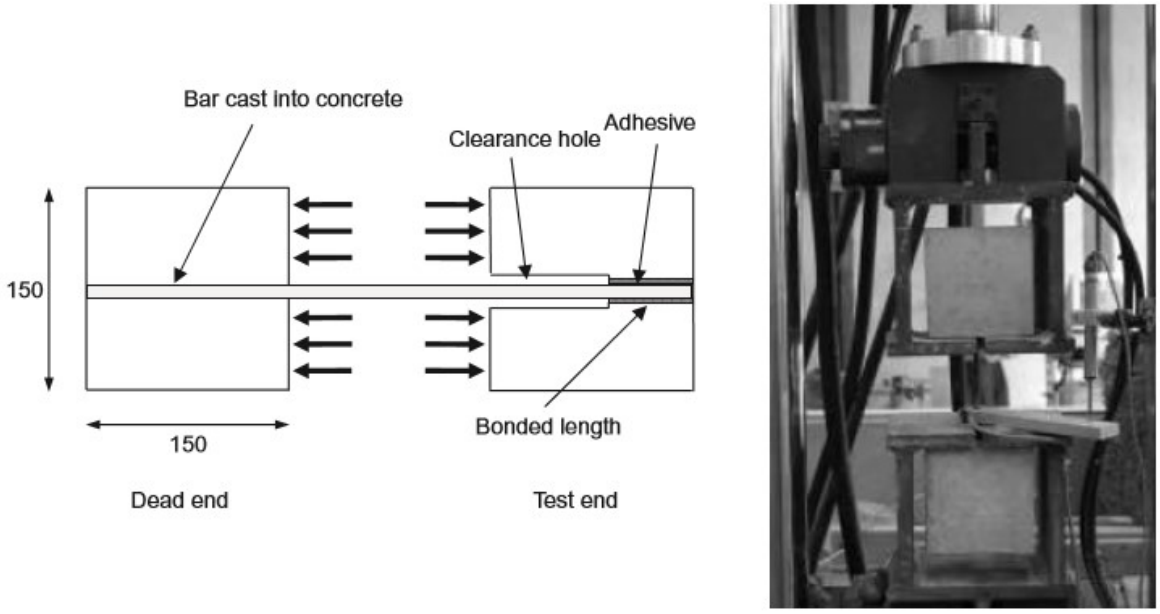

Figure 2.3 Pull-out test setup arrangement by Valerio et al. (2009)

Godat et al. (2012) performed thirteen direct shear tests on DE carbon-FRP bars only. These bars were epoxy bonded into 190 x 190 mm concrete prisms as shown in Figure 2.4. Two values of concrete compressive strength were considered, 20.7 MPa and 42.7 MPa, and the hole diameters of 1.25, 1.5 and 2 times that of the FRP bars' diameter. Nine embedment lengths were considered ranging from 48 to 285 mm. A commercially available epoxy paste was used (Sikadur AnchorFix-4), which was capable of providing a good contact bond with a tensile strength of 29.7 MPa (refer to Tables 2.2 and 2.3).

(a)

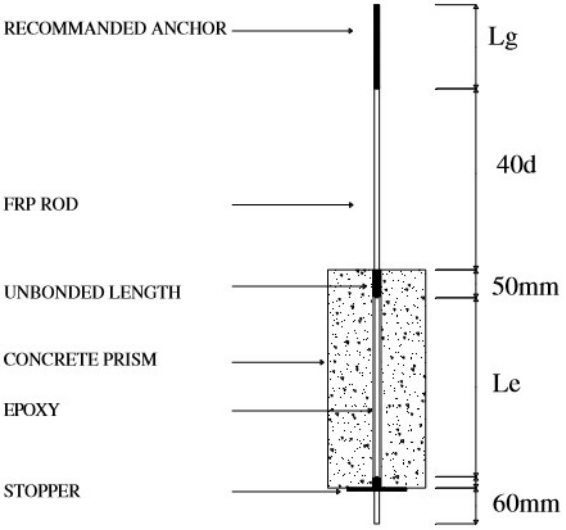

(b)

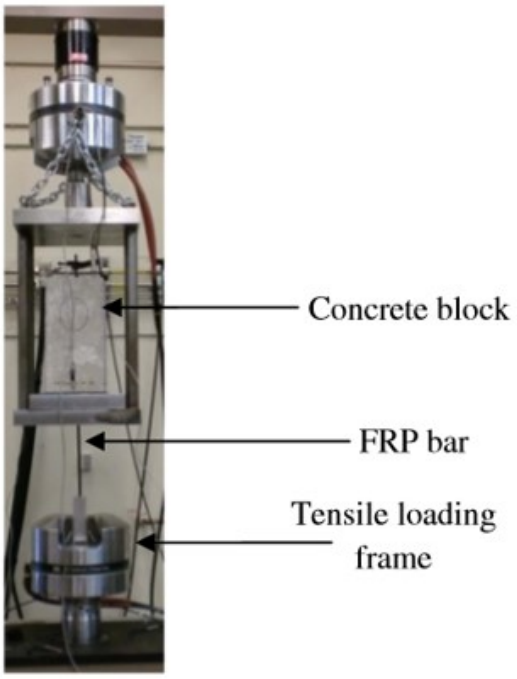

(c)

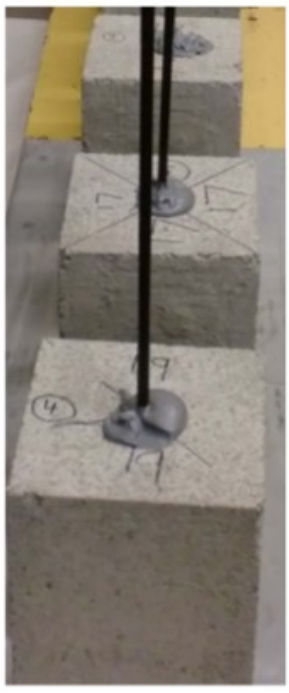

(d)

Figure 2.4 Pull-out test setup by Godat et al. (2012): (a) concrete block, (b) specimen details, (c) test setup and (d) test specimen

Table 2.2 Summary of research on the bond behaviour of the DE strengthening method

Research study		DE bar properties					Adhesive properties		
	Concrete strength (MPa)	Type	Diameter (mm)	Same material tested for bar diameter	Bonded length (mm)	Surface treatment	Type	Thickness (mm)	Tensile strength (MPa)
Valerio et al. (2009)	60	Steel, CFRP, GFRP, AFRP	6, 7.5, 8, 9	6 and 7.5 mm CFRP	15 to 75 or ($1.7d_b$-$12.5\ d_b$)	Sand coated	Hilti 150 and Hilti 500[a], Araldite[b]	8 to 11 or ($1.2\ d_b$ - $1.3\ d_b$)	15.9, 43.5, 60
Godat et al. (2012)	20.7, 42.7	CFRP	9.5, 12.7	9.5 and 12.7 mm CFRP	48 to 285 or ($5d_b$-$30d_b$)	Pultrall sand coated, Sika smooth	Sikadur Anchor-Fix-4[c]	12-22 or ($1.25d_b$-$2\ d_b$)	29.7

Note: Bonded length and adhesive thickness are also expressed as a function of DE bar diameter (d_b) and the hole diameter (d_h), respectively;

[a] Medium strength paste Hilti 150 and non-sag, high strength epoxy Hilti 500 with a tensile strength of 15.9 MPa and 43.5 MPa, respectively;

[b] Low viscosity epoxy Araldite with a tensile strength of 60 MPa;

[c] Commercially available epoxy.

Table 2.3 Detailed data of test specimens, concrete properties and epoxy

Specimen	Concrete strength	Bar type	FRP bar surface type	Bar diameter	Tensile strength for FRP or Yield strength for steel	Elastic Modulus	Ultimate strain	Embedded length	Hole diameter	Epoxy type	Average bond stress	Failure mode
	(MPa)			(mm)	(MPa)	(GPa)	(%)	(mm)	(mm)		(MPa)	
[a]Specimens 1 to 5	60	Steel	Sand coated spirally wound with a fibre tow	8	500	200	2.5	15/30/45/60/ 75 or 1.9/ 3.75/ 5.6/ 9.4 db	10 (1.25 db)	Non-sag epoxy (Hilti 500)	37 /36/27/20/ 16	SR/ BY/BY/BY/ BY
[a]Specimens 6 to 10	60	CFRP (Carbo-pree)	Sand coated	7.5	2300	130	1.8	15/30/45/60/ 75 or 2/4/ 6 /8/10 db	9.5 (1.27 db)	Non-sag epoxy (Hilti 500)	36/32/28/ 24/25	All interlaminar shear
[a]Specimens 11 to 15	60	Aslan CFRP	Sand coated external helical wrap along with a sand coating	6	2060	124	1.7	15/30/45/60/ 75 or 2.5/6/7.5/10/ 12.5 db	8 (1.3 db)	Non-sag epoxy (Hilti 500)	33/30/27/ 23/21	All interlaminar shear
[a]Specimens 16 to 20	60	Aslan GFRP	Sand coated	9	760	40.8	1.6	15/30/45/60/ 75 or 1.7/ 3.3/ 5/ 6.7/ 8.3 db	11 (1.2 db)	Non-sag epoxy (Hilti 500)	25/27/24/ 20/16	IS/IS/IS/IS/ BR
[a]Specimens 21 to 25	60	AFRP (Arapree)	Quartz sand coated	7.5	1400	60	2.4	15/30/45/60/ 75 or 2/4/ 6 / 8/10 db	9.5 (1.27 db)	Non-sag epoxy (Hilti 500)	17/14/10/ 7/7	All interlaminar shear
[a]Specimens 26 to 30	60	Steel	Sand coated spirally wound with a fibre tow	8	500	200	2.5	15/30/45/60/ 75 or 1.9/ 3.75/ 5.6/ 9.4 db	10 (1.2 db)	Low viscosity epoxy (Araldite)	37 /27/26/21/ 16	SR/ SR/BY/BY/ BY

Specimen	Concrete strength	Bar type	FRP bar surface type	Bar diameter	Tensile strength for FRP or Yield strength for steel	Elastic Modulus	Ultimate strain	Embedded length	Hole diameter	Epoxy type	Average bond stress	Failure mode
	(MPa)			(mm)	(MPa)	(GPa)	(%)	(mm)	(mm)		(MPa)	
[a]Specimens 31 to 35	60	CFRP (Carbo-pree)	Sand coated	7.5	2300	130	1.8	15/30/45/60/ 75 or 2/4/6/ 8/10 db	9.5 (1.27 db)	Low viscosity epoxy (Araldite)	33/22/28/ 30/31	All interlaminar shear
[a]Specimens 36 to 40	60	Aslan GFRP	Sand coated	9	760	40.8	1.6	15/30/45/60/ 75 or 1.7/ 3.3/ 5/ 6.7/ 8.3 db	11 (1.2 db)	Low viscosity epoxy (Araldite)	36/24/27/ 22/25	IS/IS/IS/IS/ BR
[a]Specimens 41 to 45	60	AFRP (Arapree)	Quartz sand coated	7.5	1400	60	2.4	15/30/45/60/ 75 or 2/4/ 6 / 8/10 db	9.5 (1.27 db)	Low viscosity epoxy (Araldite)	26/20/18/ 17/13	All interlaminar shear
[a]Specimens 46 to 50	60	Steel	Sand coated spirally wound with a fibre tow	8	500	200	2.5	15/30/45/60/ 75 or 1.9/ 3.75/ 5.6/ 9.4 db	10 (1.2 db)	Medium strength paste (Hilti 150)	10 /17/26/21/ 16	SR/ SR/BY/BY/ BY
[a]Specimens 51 to 55	60	CFRP (Carbo-pree)	Sand coated	7.5	2300	130	1.8	15/30/45/60/ 75 or 2/4/ 6 / 8/10 db	9.5 (1.27 db)	Medium strength paste (Hilti 150)	17/17/16/ 19/19	All interlaminar shear
[a]Specimens 56 to 60	60	Aslan GFRP	Sand coated	9	760	40.8	1.6	15/30/45/60/ 75 or 1.7/ 3.3/ 5/ 6.7/ 8.3 db	11 (1.2 db)	Medium strength paste (Hilti 150)	16/16/17/ 17/17	All interlaminar shear
[a]Specimens 61 to 65	60	AFRP (Arapree)	Quartz sand coated	7.5	1400	60	2.4	15/30/45/60/ 75 or 2/4/ 6 / 8/10 db	9.5 (1.27 db)	Medium strength paste (Hilti 150)	7/6/8/ 8/5	All interlaminar shear

Specimen	Concrete strength	Bar type	FRP bar surface type	Bar diameter	Tensile strength for FRP or Yield strength for steel	Elastic Modulus	Ultimate strain	Embedded length	Hole diameter	Epoxy Type	Average bond stress	Failure mode
	(MPa)			(mm)	(MPa)	(GPa)	(%)	(mm)	(mm)		(MPa)	
[b]C1-1.5 d-9.5B-15 d	20.7	CFRP	Pultrall sand coated	9.52	1596	120	1.33	143 (15 db)	15 (1.5 db)	Sikadur AnchorFix-4	8.4	Concrete splitting
[b]C1-1.5 d-12.7 B-15 d	20.7	CFRP	Pultrall sand coated	12.7	1899	144	1.32	144 (15 db)	15 (1.5 db)	Sikadur AnchorFix-4	7.5	Concrete splitting
[b]C2-1.25 d-9.5S-15 d	42.7	CFRP	Sika smooth	9.52	2800	155	1.8	145 (15 db)	12 (1.25 db)	Sikadur AnchorFix-4	18.8	Bar pullout
[b]C2-1.5 d-9.5 S-15 d	42.7	CFRP	Sika smooth	9.52	2800	155	1.8	146 (15 db)	15 (1.5 db)	Sikadur AnchorFix-4	22.3	Bar pullout
[b]C2-2.0 d-9.5 S-15 d	42.7	CFRP	Sika smooth	9.52	2800	155	1.8	147 (15 db)	19 (2.0 db)	Sikadur AnchorFix-4	18.4	Bar pullout
[b]C2-1.5 d-9.5S-5 d	42.7	CFRP	Sika smooth	9.52	2800	155	1.8	48 (5 db)	15 (1.5 db)	Sikadur AnchorFix-4	29.9	Bar pullout
[b]C2-1.5 d-9.5S-7.5 d	42.7	CFRP	Sika smooth	9.52	2800	155	1.8	71 (7.5 db)	16 (1.5 db)	Sikadur AnchorFix-4	26.9	Bar pullout
[b]C2-1.5 d-9.5S-10.0 d	42.7	CFRP	Sika smooth	9.52	2800	155	1.8	95 (10 db)	17 (1.5 db)	Sikadur AnchorFix-4	22.3	Bar pullout
[b]C2-1.5 d-9.5S-12.5 d	42.7	CFRP	Sika smooth	9.52	2800	155	1.8	119 (12.5 db)	18 (1.5 db)	Sikadur AnchorFix-4	20.1	Bar pullout
[b]C2-1.5 d-9.5S-17.5d	42.7	CFRP	Sika smooth	9.52	2800	155	1.8	166 (17.5 db)	19 (1.5 db)	Sikadur AnchorFix-4	20.3	Bar pullout

Specimen	Concrete strength	Bar type	FRP bar surface type	Bar diameter	Tensile strength for FRP or Yield strength for steel	Elastic Modulus	Ultimate strain	Embedded length	Hole diameter	Epoxy type	Average bond stress	Failure mode
	(MPa)			(mm)	(MPa)	(GPa)	(%)	(mm)	(mm)		(MPa)	
[b]C2-1.5 d-9.5S-20 d	42.7	CFRP	Sika smooth	9.52	2800	155	1.8	190 (20 db)	20 (1.5 db)	Sikadur AnchorFix-4	18.1	Bar pullout
[b]C2-1.5 d-9.5S-25 d	42.7	CFRP	Sika smooth	9.52	2800	155	1.8	238 (25 db)	21 (1.5 db)	Sikadur AnchorFix-4	16.1	Bar rupture
[b]C2-1.5 d-9.5S-30 d	42.7	CFRP	Sika smooth	9.52	2800	155	1.8	285 (30 db)	22 (1.5 db)	Sikadur AnchorFix-4	15.1	Bar rupture

Note: [a] Test specimens by Valerio et al. (2009), [b] Test specimens by Godat et al. (2012),

IS=Interlaminar shear in FRP, SR=Shearing in resin, BY=Bar yielding, BR=Bar rupture.

2.4 Impact of Parameters on the Bond Behaviour of Deep Embedment Technique

This section provides a comprehensive review of the main parameters that affect the bond behaviour of epoxy-bonded DE bars in concrete. The key studied parameters are concrete compressive strength, embedded length, bar diameter and quantity of epoxy used. Figures 2.5 to 2.8 present the impact of these parameters on the average bond stress-slip relationships, bond force and stress. The correlation between the average bond stress and tensile load (pull-out bond force) was expressed by ACI 440.1R (2006) in Equation (2-1):

$$\tau_b = \frac{P_t}{\pi\, d_b\, l_b} \qquad (2\text{-}1)$$

The tensile load (P_t) = $\sigma_f A_f$ where A_f = DE bar area, σ_f = tensile stress in the DE bar, l_b = embedded length of the bar, d_b = bar diameter.

Equation (2-1) assumes the bond stress (τ_b) to be constant along the embedded length and does not consider the impact of concrete strength. This assumption allows comparison of the average bond stress-slip curves and the bond force-slip curves (Godat et al., 2012). This assumption is used here for a simple analysis of the factors above on the experimental bond stress/force-slip relationships. However, Tepfers and De Lorenzis (2003) and Baena et al. (2009) stated that this average bond stress (τ_b) varies along the embedded length and decreases due to non-uniform distribution of the bond stresses. Further studies should be conducted to examine the distribution of the bond shear stress and the interfacial slip along the embedded length for the DE technique.

2.4.1 Effect of Concrete Strength

Figure 2.5 illustrates the representative bond stress-slip curves showing the impact of concrete strength on the bond behaviour. These specimens all used carbon-FRP bars embedded into the centre of concrete cubes/prisms using high-viscosity adhesives that ensured a good contact bond along the embedded bar length, thus exhibiting an effective and comparable bond performance. The selected specimens of Godat et al. (2012) had a diameter of 9.5 mm and embedded length of 15 d_b, whereas Valerio et al. (2009) had a bar diameter of 7.5 mm with an embedded length of 10 d_b.

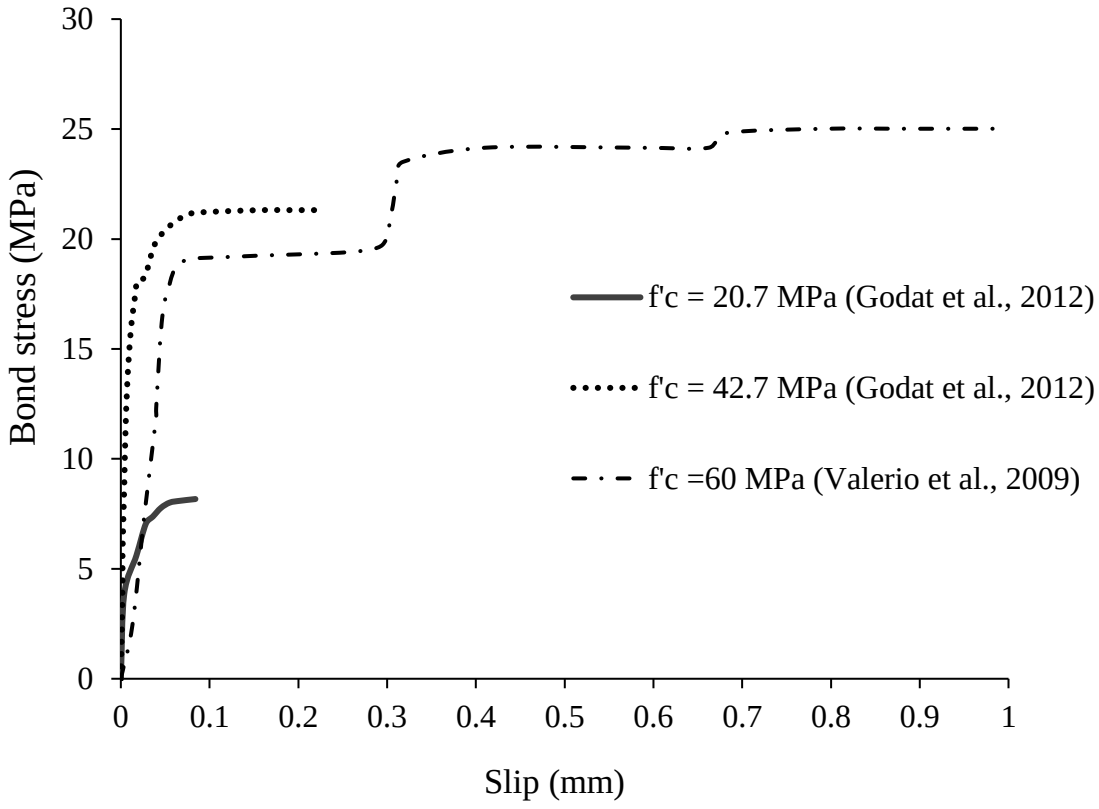

Figure 2.5 Effect of concrete strength on the bond stress-slip relationship

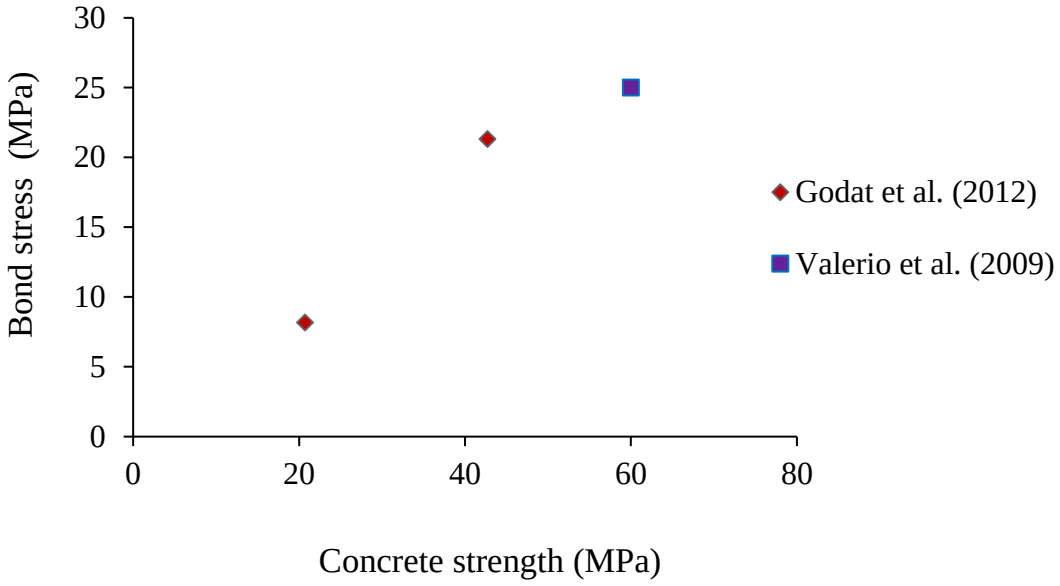

Figure 2.6 Effect of concrete strength on the bond stress

Figure 2.5 shows that the overall bond stress-slip behaviour of all three specimens is characterised by an initial nonlinear increase in the bond stress, followed by a constant plateau once the maximum bond stress has been achieved up to the failure point of the specimens. However, the lowest strength specimen differs because it fails by concrete splitting as the maximum stress is reached. For both specimens of higher concrete strength, the bond stress remained high even with further increase in slip values until pull-out failure, with the 'plateau phase' of the specimen of f'_c = 60 MPa longer than that with f'_c = 42.7 MPa. It can be observed in both Figures 2.5 and 2.6 that as the concrete strength increases, the maximum bond stress also increases. The increase in the compressive strength for the two specimens tested by Godat et al. (2012) was about 2.1 times, while the corresponding increase in the bond stress was about 2.6 times. Since the bond stress is directly proportional to the bond force (Equation 2-1), that means that as the concrete strength increases, the bond force should

also increase. A better bond between concrete and DE bars allows the stresses to be transferred more efficiently; thus, making the average stress contribution of concrete higher.

The concrete compressive strength also affected the failure mode of the tested specimens. The mode of failure for the low strength concrete (f'_c = 20.7 MPa) was concrete splitting (i.e. the bond failure happened at the concrete matrix since that was the weakest part of the section), while the mode of failure for both specimens of higher concrete strength was pull-out at the bar/adhesive interface without cracks evolving on the concrete block surface. The long flat plateau of the bond-stress curves (after the peak stress is reached) is an indication of this failure mode.

2.4.2 Effect of Embedded Length

Figure 2.7a illustrates the effect of embedded lengths varying between 15 mm to 75 mm on the bond stress for the concrete specimens tested by Valerio et al. (2009). For this analysis, only those concrete specimens where non-sag epoxy was used to bond bars of four materials: steel, carbon-FRP, glass-FRP and aramid-FRP bars were selected since the bond performance of this adhesive was more effective leading to bond strength values higher than 20 MPa for most bars.

Tepfers and De Lorenzis (2003) and Baena et al. (2009) reported that the bond stress is dependent on the embedded length. The stress distribution along the bar is nonlinear due to stress transfer during pull-out testing, where the maximum bond stress migrates gradually from the loaded end toward the unloaded end of the bar. It can be observed in Figure 2.7a that for all bar types as the embedded length increased, the bond stress decreased. This observation is in agreement with the Equation (2-1) where the bond stress is inversely proportional to the embedded length.

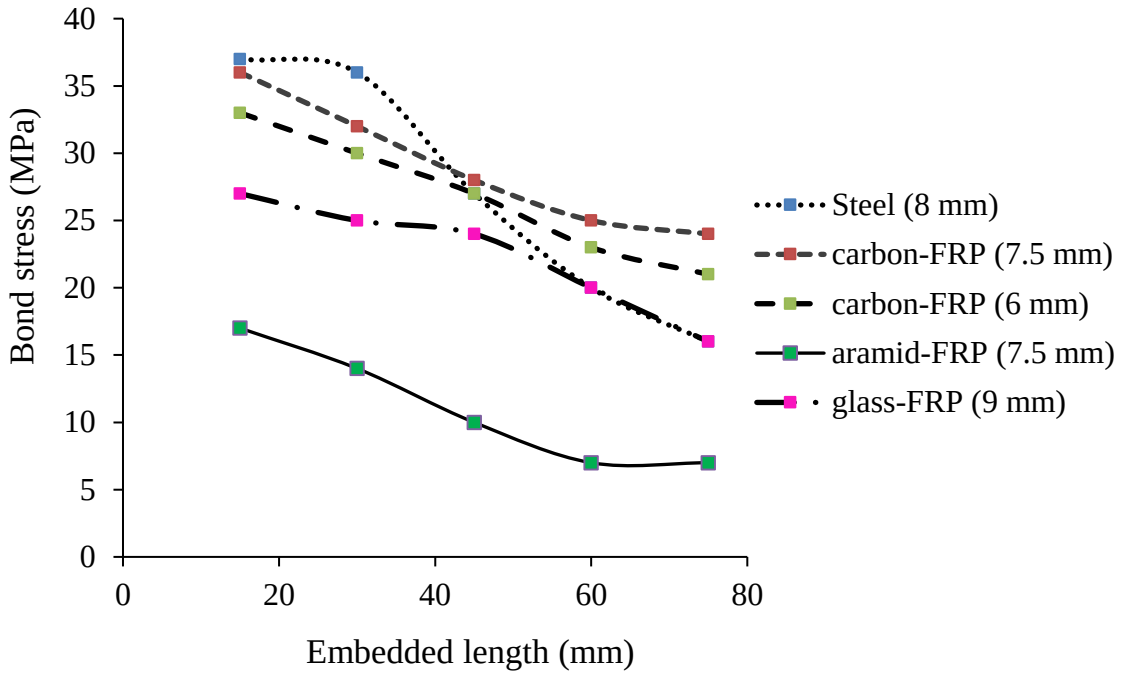

(a)

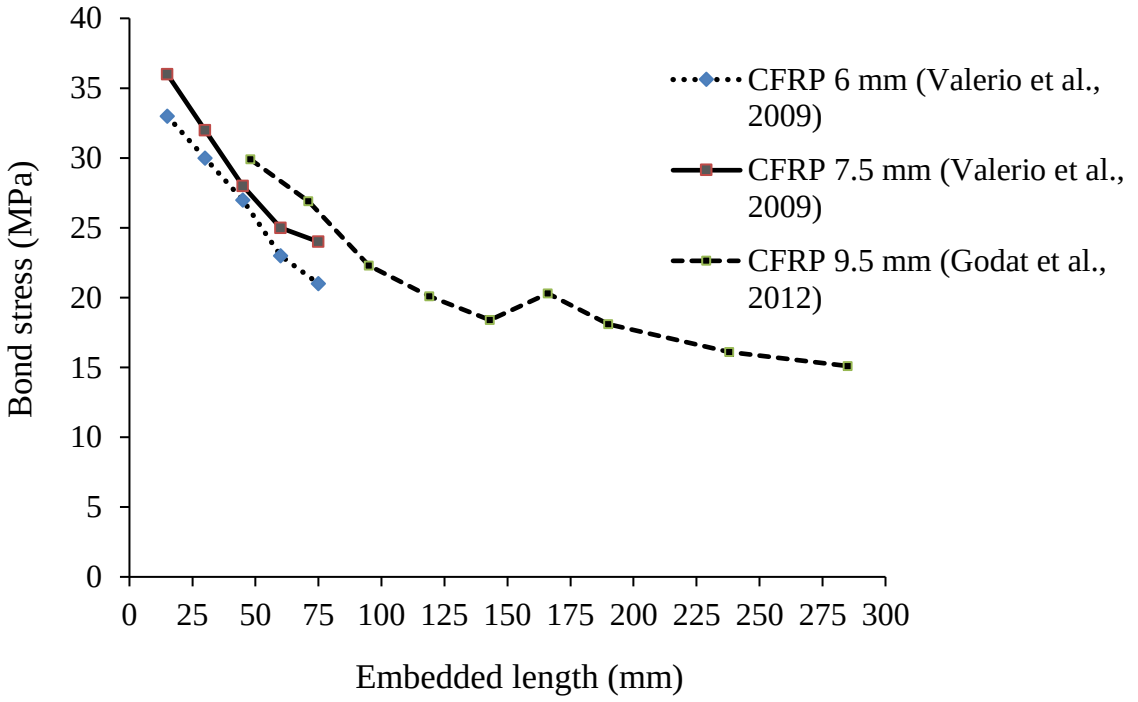

(b)

Figure 2.7 Effect of embedded length on the bond stress: (a) specimens of Valerio et al. (2009), (b) specimens of Valerio et al. (2009) and Godat et al. (2012)

It can be also noted that the bond stress values for the DE strengthening combination of non-sag epoxy with the steel and carbon-FRP bars are higher than those achieved by the glass-FRP and aramid-FRP bars. This observation can be attributed to a better bond performance and a more ductile bond stress-slip response achieved by these two strengthening combinations utilising bars that have an elastic modulus significantly higher than that of glass and aramid bars. A 500 % increase in the embedded length from 15 to 75 mm for carbon-FRP bars of 7.5 mm and 6 mm diameter led to a corresponding decrease in the bond stress of about one third. Higher bond stress values were obtained for each embedded length by the bar of larger diameter. The steel bar exhibited a greater proportional decrease in the bond stress over the same range of embedded lengths and the stress decreased more rapidly for embedded lengths between 45 and 60 mm compared to the other materials. The bond stress values and capacities for the aramid-FRP bars were considerably lower compared to the other types of bars due to low modulus of elasticity and a poor sand coating which caused premature failure of the outer bar layer (i.e. interlaminar shear failure) and the excessive opening of shear cracks. Therefore, aramid-FRP bars are not recommended to be used for DE strengthening purposes.

Figure 2.7b extends this comparison of embedded lengths to 285 mm for carbon-FRP bars, of 6, 7.5 and 9.5 mm diameter, embedded using high-viscosity epoxies that ensured a good contact bond along the embedded length of the bars. This shows that the bond stress continues to decrease as the embedded length increased, with some suggestion of an asymptotic limit. It can be also observed that for the same embedded length increased bond stress values were attained by specimens with a larger diameter.

The embedded length also influenced the failure modes of these tested specimens. For both research studies, pull-out at the bar/adhesive interface along the embedded length was the main failure mode for the tested specimens with short embedded lengths (5 d_b to 10 d_b).

Godat et al. (2012) observed that pull-out failure was the governing failure mode for embedded lengths ranging between 5 d_b to 20 d_b, while for greater embedded lengths (25d_b to 30 d_b), bar tensile failure occurred with the FRP bar remaining fully attached to the concrete core. Considering the correlation expressed by Equation (2-1) between the bond stress and bond force, as the embedded length increases, the bond force must also increase. This observation agrees with the test results reported by Nanni et al. (1995) for FRP RC members.

2.4.3 Effect of Quantity of Adhesive and Bar Diameter

The effect of the adhesive quantity on the bond behaviour was only studied by Godat et al. (2012). He considered three different hole diameters (1.25 d_b, 1.5 d_b and 2 d_b) concluding that as the hole's diameter increased from 1.25 d_b to 1.5 d_b, the bond performance was improved leading to a greater bond force. On the other hand, for larger hole sizes ranging from 1.5d_b to 2.0 d_b, the effect of confinement was reduced due to possible larger shrinkage occurring in larger holes compared to smaller ones. Thus, it leads to the conclusion that the optimum hole diameter for the DE method is around 1.5d_b.

Figure 2.8 illustrates the impact of bar diameter on the bond force by comparing two specimens tested by Godat et al. (2012), with carbon-FRP bar diameters of 9.5 mm and 12.7mm, and two specimens by Valerio et al. (2009), with carbon-FRP bars of 6 mm and 7.5 mm. It is shown that the bond force increased as the bar diameter increased for both sets of CFRP bars. The bond capacity is higher for FRP bars of greater diameter due to a larger contact area leading to a higher bond force and bond stress. In contrast, Baena et al. (2009) reported that for FRP RC members, bond strength is lower for larger bar diameters due to a greater amount of elastic energy released.

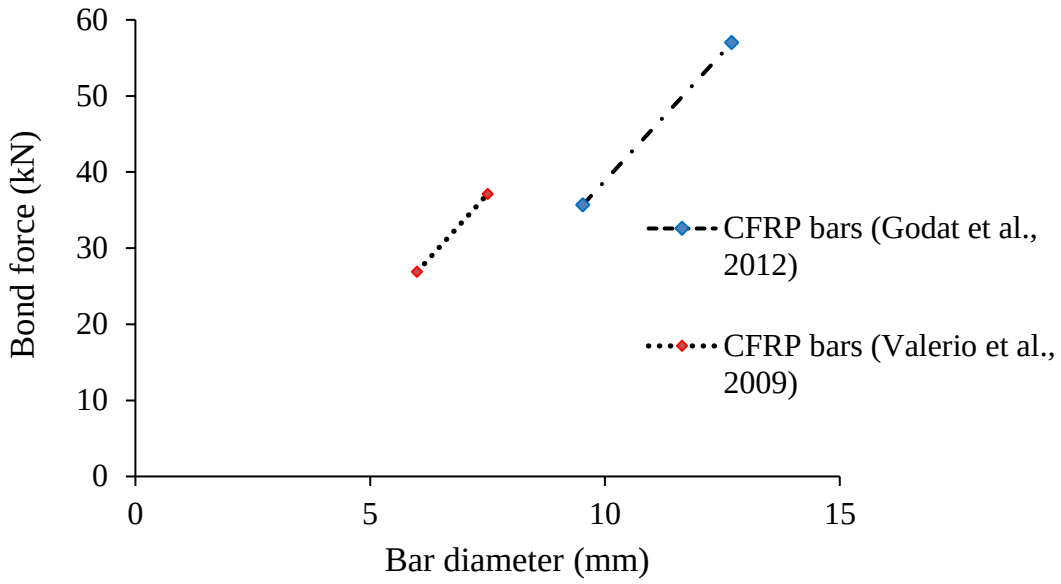

Figure 2.8 Effect of bar diameter on the bond force

2.5 Analytical Modelling of the Bond Stress-Slip Relationship

This section provides a brief review of two theoretical bond stress-slip models that have been suggested by the International Federation for Structural Concrete (fib, 2007) for analysing the FRP bar-to-concrete interfacial behaviour. The behaviour of the bond stress-slip relationships for the FRP-reinforced concrete models was observed to be similar to that of DE technique (Godat et al., 2012). However, these constitutive bond stress-slip relations need to be modified and calibrated with suitable curve-fitting parameters so that they can simulate correctly the experimental DE FRP bar/concrete interfacial bond behaviour. The role of an analytical model is crucial for performing correctly finite-element analysis of the behaviour of the DE-strengthened RC beams as well as predicting realistically the DE FRP bar's strain and the overall stiffness.

The key theoretical bond stress-slip models that have been recommended to describe the FRP-to-concrete interfacial behaviour, are the modified BPE model and the CMR model.

Firstly, Cosenza et al. (1997) proposed a double-branch model (see Figure 2.9) as a modification of the Eligehausen, Popov, and Bertero (BPE) model with equations to characterise the ascending (Equation 2-2) and descending (Equation 2-3) branches:

$$\tau_{(S)} = \tau_m \left({}^{S}/_{S_m}\right)^{\alpha} \tag{2-2}$$

$$\tau_{(S)} = \tau_m \left(1 + p - p\ {}^{S}/_{S_m}\right) \tag{2-3}$$

where τ_m is the peak bond stress and S_m is the corresponding slip, and α and p = curve-fitting parameters related to slopes of the ascending and descending branches, respectively.

Secondly, in the Cosenza, Manfredi, and Realfonzo (CMR) model proposed by Cosenza et al. (1997), the ascending branch of the BPE model is modified and a single equation is used to illustrate the correlation between the local bond stress ($\tau_{(S)}$) and the relative slip (S) for the entire behaviour of FRP bar-to-concrete interface:

$$\tau_{(S)} = \tau_m \left(1 - e^{-S/s_r}\right)^{\beta} \tag{2-4}$$

where s_r and β = curve-fitting parameters.

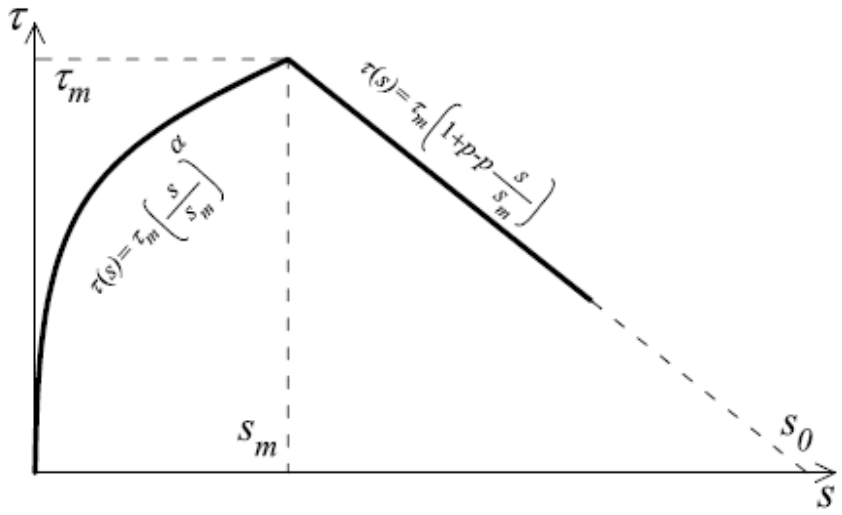

Figure 2.9 BPE modified bond stress-slip model (Cosenza et al., 1997)

The only research study that has attempted to define these curve-fitting parameters for the DE technique has been that by Godat et al. (2012). For the BPE model, it was proposed using α =0.125 and p=0.01 for smooth-surfaced DE FRP bars and values of α = 0.09 and p =0.07 for sand-coated DE FRP bars. Lower values were suggested for the sand-coated bar since they exhibited a less stiff initial bond behaviour. Whereas in case of CMR model, it was suggested using s_r and β parameters equal to 0.035 and 0.2 for smooth-surfaced CFRP bars and 0.028 and 0.33 for sand-coated CFRP bars, respectively. However, further investigation and additional calibrations need to be conducted not only for the carbon-FRP bars but also for the glass-FRP bars.

2.6 Shear Resistance Mechanisms

Kani (1964) revealed that under increased loading after the cracks initiate, a reinforced concrete beam will behave as a comb-like structure, as shown in Figure 2.10.

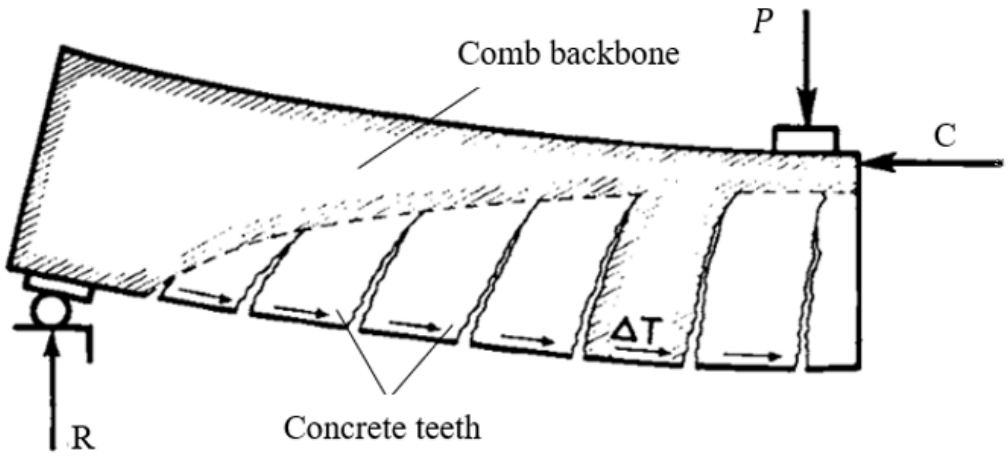

Figure 2.10 Illustration of the comb-like structure (Kani, 1964)

Concrete teeth are developed in the tensile zone due to flexural cracks and act as short cantilevers carrying horizontal tensile ΔT forces. The concrete backbone represents the compressive zone.

In addition, Kani (1964) concluded that there are two distinct load-carrying mechanisms which govern the behaviour of RC beams after cracking, namely the beam-action and arch-action mechanism. Beam-action will govern the shear behaviour when the concrete teeth capacity is not exceeded, whilst a tied arch-action will characterise the behaviour after the resistance of the concrete teeth has been exceeded. Figure 2.11 relates the ratio of M_{CR} to M_{FL} (i.e. ratio of the critical bending moment at shear failure to that at flexural failure respectively) of the concrete teeth and remaining arch to three different zones of shear span-to-effective depth (a/d) ratio as follows:

a) (1<a/d <2.5): The capacity of the arch-action is higher than that of the concrete teeth. In this region, the transformation from arch-action to beam-action occurs under gradually increased loading till failure happens when the arch capacity is exceeded. Beams having a/d ratios in this range are classified as deep beams (refer to Section 2.6.3).
b) (2.5<a/d<5.6): The capacity of the arch is lower than that of the concrete teeth; thus, a sudden collapse occurs which is characterized by a brittle tensile failure of the concrete teeth. Beams having a/d ratios in this range are classified as slender beams (refer to Section 2.6.3).
c) (a/d>5.6): The full capacity of the RC beam is reached; thus, only flexural failure may occur.

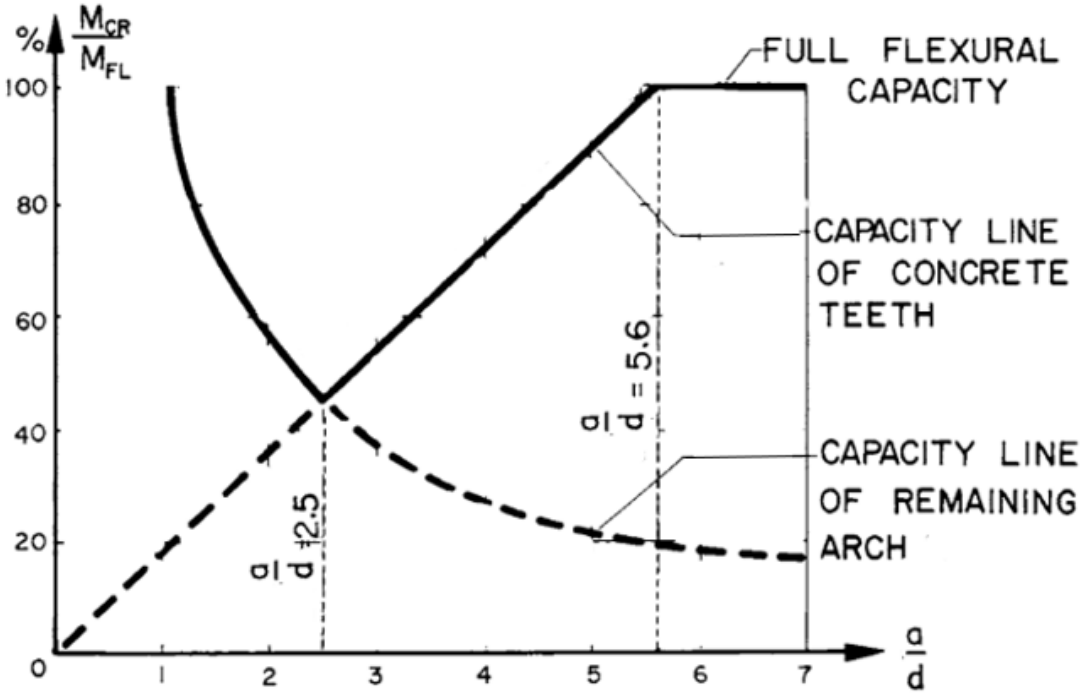

Figure 2.11 Kani's graph with distinct regions of a/d ratio (Kani, 1964)

2.6.1 Beam Action

According to the ASCE-ACI Committee 445 (1998), the main components of shear transfer in cracked RC members having a/d ratios between 2.5 to 5.6 (i.e. beam-action dominates the behaviour) without web reinforcement can be illustrated as shown in Figure 2.12.

a) Aggregate interlock, V_a: This component represents the ability of concrete to redistribute internal shear forces after cracking by the resistance of a tangential slippage which occurs between the rough interfaces formed on the crack's faces. This component provides about 33 % to 50 % of the total shear resistance and increases with the increase in aggregate size in the concrete mix. On the other hand, an increase in the crack width reduces the contribution of the aggregate interlock (Taylor, 1974). Razaqpur et al. (2001) explained that aggregate interlock in FRP-reinforced members

is similar to frictional resistance and results from the resistance to relative slip between two rough interlocking surfaces of the crack. This mechanism can be significant if the crack is not too wide.

b) Shear transfer in uncracked concrete, V_{cc}: This component represents the contribution of the concrete in the compression zone and is dependent on the zone's depth. The magnitude of this component is about 20 % to 40 % (Taylor, 1974). Previous research studies on FRP-reinforced beams have confirmed that such members develop wider and deeper cracks, attributable to the low modulus of elasticity of FRP composite material compared to steel. In addition, El Sayed et al. (2006) reported that the shear strength contribution from the un-cracked concrete in FRP-reinforced beams with deeper cracks is reduced due to the lower depth of concrete in compression.

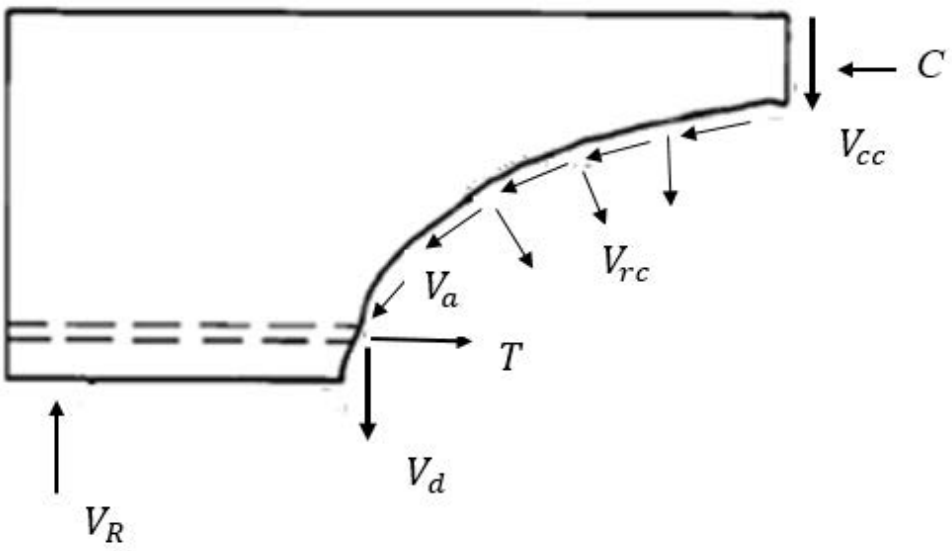

Figure 2.12 Shear resistance components in the beam-action mechanism (ASCE-ACI Committee 445, 1998)

c) Residual tensile stress in concrete after cracking, V_{rc}: ACI-ASCE Committee 445 (1998) states that concrete softening does not occur abruptly, but even after cracking,

small pieces of concrete will transmit tensile forces up to crack widths in the range between 0.05 to 0.15 mm. In the case of FRP-reinforced beams, the wider cracks will reduce the contribution due to residual tensile stresses.

d) Dowel action of longitudinal reinforcing bars, V_d: Dowel action occurs when the steel or FRP longitudinal bars intersect a diagonal shear crack. This component represents the resistance to shearing displacements and splitting tensile forces beneath the longitudinal bars and is dependent on the stiffness and distribution of the longitudinal reinforcement and tensile strength of the surrounding concrete. Dowel action has a magnitude of about 15 % to 25 % of the applied shear force (Taylor, 1974). The contribution due to dowel action of FRP flexural bars is relatively small, due to the small transverse strength of FRP bars compared to that of steel bars and wider cracks in FRP-reinforced members (El Sayed et al., 2006).

In the case of RC members reinforced with either steel or FRP shear reinforcement, the applied shear forces will be resisted by an internal truss-like mechanism. Studies have shown that transverse reinforcement allows transferring of tensile forces across inclined shear cracks and prevents them from propagating further into the shear spans of RC beams. The design guidelines recommended by ACI 440.1R (2006) estimate the shear capacity of RC beams reinforced with steel shear links based on the sum of shear contribution provided by concrete (V_c) and the transverse shear links (V_w). It is worth noting that DE FRP bars in the DE technique are embedded into the concrete core, thus acting as internal transverse reinforcement. In addition, since shear strengthening is internal in the DE technique, the shear contribution provided by DE FRP bars in RC slender beams is based on the truss analogy and is evaluated by limiting the effective strain value of DE FRP bars to ε_{fe} = 0.4 %, as suggested by fib (2007), Godat et al. (2012) and Qapo et al. (2016a).

2.6.2 Arch Action

RC beams having a shear span-to-effective depth ratio (a/d) less than 2.5 are classified as deep beams (Kani, 1964). Deep beams have been primarily used as transfer girders, pile caps and foundation walls (Andermatt and Lubell, 2013). The shear behaviour of RC deep beams differs from that of slender beams due to a different force-transferring mechanism, known as the arch-action, which is the main load resisting mechanism in deep beams. This mechanism allows applied forces to be directly transferred to supports through compressive stresses in the inclined compression struts joining the loading point and support (Smith and Vantsiotis, 1982; Mau and Hsu, 1987; Tuchscherer et al., 2011), whilst, the longitudinal reinforcement will act as a tie, ensuring the base of the arch is held together, and provide resistance to the horizontal component of the shear force (Andermatt and Lubell, 2013). In contrast to slender members, deep members develop significant reserve capacity after diagonal cracking (Farghaly and Benmokrane, 2013). Section 2.6.3 provides further details of the arch-action in deep beams.

2.6.3 Differences in the Shear Behaviour between Slender and Deep Beams

As previously mentioned, deep beams (i.e. a/d<2.5) allow compression struts to be developed between loads and support (Kani, 1964). Previous research by Birrcher et al. (2009), Wight and Macgregor (2009) showed that the transition from deep members to slender members happens gradually at a shear span-to-effective depth ratio between 2.0 and 2.5, rather than at a fixed a/d ratio. Zsutty (1968) and Kani et al. (1979) demonstrated as the a/d ratio approaches 2.5, the arch action is the dominant load transferring mechanism in deep beams following diagonal cracking, with nonlinear shearing strains governing the shear behaviour.

This shear behaviour changes from that of slender beams since the plane sections do not remain plane in bending. Therefore, the principles of stress analysis, Bernoulli's hypothesis or conventional beam theory, are both nonacceptable for evaluating the internal state of stress.

In slender beams (i.e. a/d > 2.5) the strain distribution is linear with the load being transferred through a uniform compression field. In contrast to slender beams, deep beams are identified as disturbed (discontinuity) regions or also known as D-regions (Schlaich et al., 1987), where the strain distribution is nonlinear due to either abrupt changes in geometry or in loading (St. Venant's Principle). This is displayed in Figure 2.13, where section A-A refers to a Bernoulli beam-region (i.e. stresses can be evaluated based on sectional analysis) and section B-B is a deep beam region (i.e. nonlinear shear stresses dominate the behaviour). According to the ACI 318 (2008) code of practice for steel RC beams, the D-region extends longitudinally from the discontinuity region to a distance equal to the beam's effective depth.

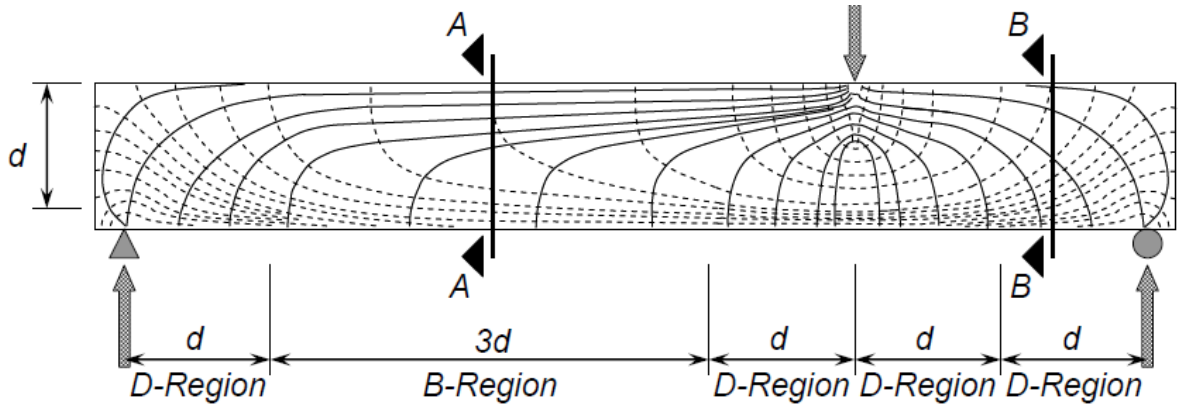

Figure 2.13 D-regions and B-regions in a simply supported beam (Wight and MacGregor, 2009)

Research by Kani et al. (1979) and Wight and MacGregor (2009) concluded that a/d ratio has a significant effect on the shear behaviour of RC members and their mode of failure (see

Figure 2.14). In addition, the shear stress at failure is also influenced by the a/d ratio. Figure 2.15 demonstrates that for a/d ratios smaller than 2.0, the shear stress is significantly greater.

In cracked RC slender beams (a/d > 2.5), the tensile force in the longitudinal reinforcement varies along the beam length, whereas the internal lever arm remains constant. This is known as beam action (see Figure 2.16a). On the other hand, in cracked RC deep beams (a/d < 2.5), the internal lever arm varies along the beam length whereas the tension in the longitudinal reinforcement remains constant. This is known as arch action of the diagonal strut (Figure 2.16b), which is the main force resisting system in RC deep beams following diagonal cracking (Dirar and Theofanous, 2017).

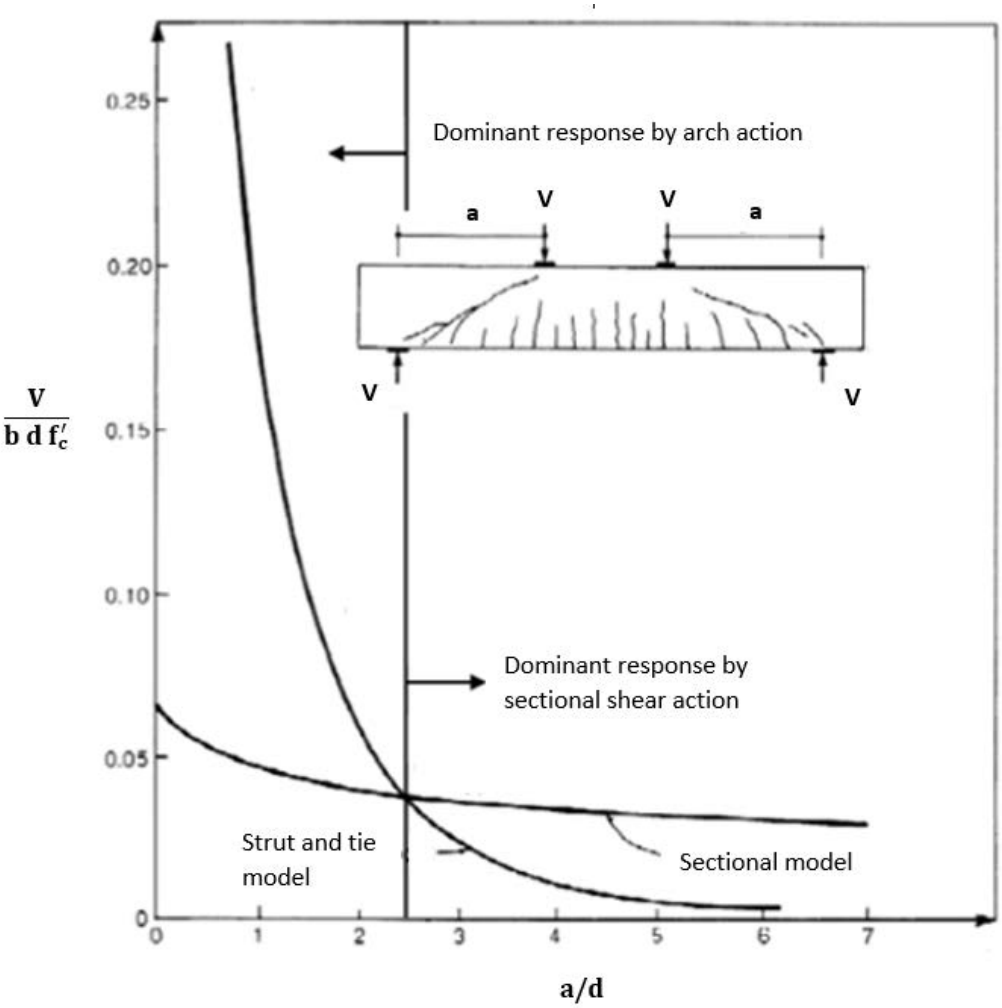

Figure 2.14 Effect of a/d ratio on the normalised shear strength of steel RC beams (Kani et al., 1979)

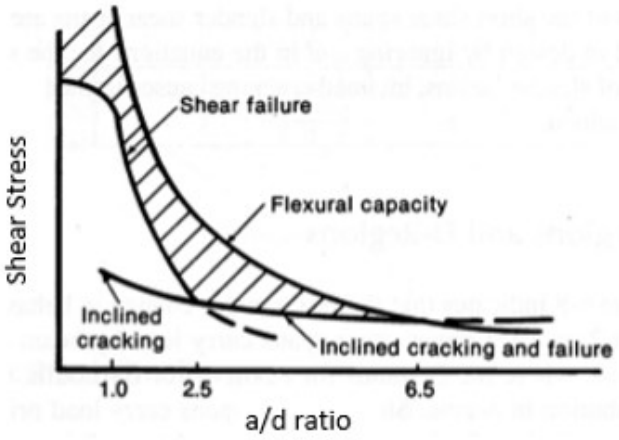

Figure 2.15 Effect of a/d ratio on the shear stress at cracking and failure in a simply supported beam (Wight and MacGregor, 2009)

De Paiva and Siess (1965) also explained that the change in the bending moment in the case of deep beams is primarily dependent on the change in the lever arm between the developed horizontal forces rather than on their magnitude. This is because the tension carried by the tension reinforcement at ultimate limit states remains constant along the beam span. Therefore, such beams cannot depend on the beam action to carry the shear forces, but on a tied arch action as shown in Figure 2.16b.

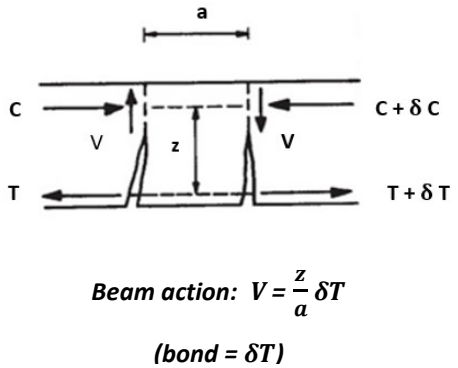

(a)

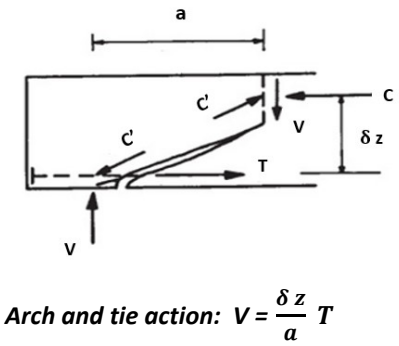

(b)

Figure 2.16 Mechanisms: (a) beam action, (b) arch and tie action in concrete beams (De Paiva and Siess, 1965)

Previous experimental investigations by Andermatt and Lubell (2013) and Farghaly and Benmokrane (2013) on FRP-reinforced concrete deep beams without shear reinforcement, confirmed the development of arch action using the uniform strain profile of the FRP longitudinal reinforcement. It was concluded that the redistribution of internal stresses in deep beams due to arch action enhances the stiffness of specimens by reserve capacity. Figure 2.15 also shows that deep beams have considerable reserve capacity after diagonal cracking, unlike slender beams. In addition, shear failure exceeds flexural failure for beams having a/d ratios less than about 6.5 (Wight and MacGregor, 2009). Arch action in beams with internal FRP reinforcement is also dependent on the member's deformation capacity (e.g. due to flexural and shear cracks) for distributing the applied forces, and on the conservation of the internal equilibrium, with applied stresses in all strut-and-tie elements not exceeding their capacities. Mohammed et al. (2017) tested ten GFRP-reinforced deep beams with different web reinforcement ratios. The uniform strain profile of the longitudinal reinforcement in the tested specimens confirmed the arch action. In addition, the tested beams exhibited the required deformability level to satisfy the internal equilibrium of applied stresses and prevent violation of failure criteria for any strut-and-tie elements.

Different analysis approaches have been currently used in various codes for slender and deep members. Sectional flexural and shear models which assume uniform shear stress distribution are commonly adopted for slender beams with a/d > 2.5 (ASCE-ACI 445, 1998). In deep beams, non-linear strain distribution dominates the shear behaviour and plane sections do not remain plane. Thus, the adoption of sectional shear design approaches can lead to underestimation of the true shear capacity. Therefore, other approaches are used for deep beams, such as strut-and-tie models (STM), empirically derived formulae or finite element (FE) analysis. STM has been widely adopted for deep RC beams with internal steel or FRP-

reinforcement. STM approach is based on the lower bound theorem. Even though FRP exhibit a linear-elastic stress-stain behaviour, this theorem can be consistent for estimating the shear capacity, as long as the stress field satisfies the requirement of internal equilibrium and the applied stresses do not exceed the tensile strength of the FRP bar and the plastic capacity of concrete (i.e. failure of any strut-and-tie elements does not occur) (Tuchscherer et al., 2011; Mohamed et al., 2017). The size of the boundary conditions (i.e. loading and support areas) should be taken into consideration whilst applying the STM method (Collins and Mitchell, 1997).

2.7 Impact of Parameters on the Shear Capacity of DE Shear-Strengthened Beams

This section provides detailed information on the experimental tests on the DE shear-strengthening technique. Table 2.4 summarises the key details of the published studies on this subject. Table 2.5 includes information about the tested DE-strengthened beams that failed in shear only and compiles the relevant data of the experimental tests available in the form of a database. Table 2.5 also specifies the contribution to the shear resistance offered by the DE bars for each tested beam. This database is then used to analyse the effects of these key parameters: concrete strength, shear span-to-effective depth ratio, beam depth, internal steel transverse reinforcement ratio, DE shear strengthening ratio, internal steel longitudinal ratio and DE surface coating on the shear resistance. Each parameter is analysed in terms of its impact on the shear strength contribution due to DE FRP bar shear reinforcement (i.e. $\frac{V_f}{V_n - V_f}$). The advantage of analysing the gain in shear strength due to DE strengthening bars depends on the fact that this value is experimentally measured and has not been derived by using shear design guidelines/provisions or truss analogy models, such as the effective strain. From Tables 2.4 and 2.5, the following observations can be made: a)

most of the tested beams are T-beams, the width varies between 110-450 mm, effective depth varies between 150-600 mm and shear span-to effective depth ratio between 1.9 to 4; b) the main studied parameters are related to the properties of DE bars; c) there is limited data about the impact of parameters such as concrete strength, shear span-to-effective depth ratio, scale effect, internal longitudinal and transverse steel reinforcement; d) there is no valid experimental data on the behaviour of preloaded (pre-cracked) members.

Table 2.4 Summary of research on the tested RC beams shear-strengthened with DE bars

	Geometry			Type of the beam		Studied parameters of concrete and reinforcement				Type of DE bars	DE strength. scheme
Research study	Shape	Width (mm)	Depth (mm)	a/d	Pre-stressed or pre-cracked	Concrete strength (MPa)	Long. Reinf. Ratio (ρ_l) (%)	Trans. Reinf. Ratio (ρ_v) (%)	DE Streng. Ratio (ρ_f) (%)	Material	Angle θ_f (degrees)
Valerio and Ibell (2003)	Rect.	110	189	2.65	-	59	1.09	-	0.16 to 0.71	AFRP Steel	60, 90
Valerio et al. (2009)	Rect.	110, 450	150, 260	3, 4	Pre-stressed	55 to 60	0.93	0, 0.13	0.04 to 0.49	CFRP Steel	90
Mofidi et al. (2012)	T-shape	152	350	3	-	25, 35	3.76	0.25, 0.38	0.18 to 0.64	CFRP	90
Barros and Dalfre (2013)	Rect.	150, 300	261.5	3,4	-	28.8, 30.8	1.88, 2.51	0.03 to 0.17	0.06, 0.11	Steel	45, 90
Breveglieri et al. (2015)	T-shape	180	360	2.5	-	24.7, 27.6	2.79	0 to 0.17	0.15 to 0.34	Steel, CFRP	45, 90
Dirar and Theofanous (2017)	T-shape	150	600	2.5, 1.9	-	40	2.22	0.11, 0.15	0.17, 0.38	CFRP, GFRP	90

Table 2.5 Details of beams strengthened in shear with DE bars (shear failure mode)

Beam ID	a/d	f'_c / f_{cu} (MPa)	Type of DE bars	Angle (θ_f)	DE Reinf. Ratio (ρ_f) (%)	Trans. Reinf. Ratio (ρ_v) (%)	Gain due to DE bars (kN)	Gain due to DE bars (%)	Ref.
Beam 7	2.65	59	AFRP	90	0.28	0	19	42	Valerio and Ibell (2003)
Beam 8	2.65	59	AFRP	90	0.16	0	19	42	
SSB R3d-C6@0.7d	3	55-60	CFRP	90	0.24	0	22.9	97	Valerio et al. (2009)
SSB R3d-C6@0.5d	3	55-60	CFRP	90	0.34	0	27	114	
SLB-P4d-C7.5@d	4	55-60	CFRP	90	0.04	0	19.1	6.5	
SLB -P4d-2C7.5@d	4	55-60	CFRP	90	0.08	0	43.2	14.6	
SLB -P4d-2S8@d	4	55-60	Steel	90	0.09	0	53.2	18	
S0-12d-130s	3	25	CFRP	90	0.64	0	99.5	122	Mofidi et al. (2012)
S1-9d-260s	3	25	CFRP	90	0.18	0.38	14	6	
S1-12d-260s	3	25	CFRP	90	0.32	0.38	20.3	8	
S1-9d-260p	3	25	CFRP	90	0.18	0.38	34.4	14	
S3-12d-130s	3	35	CFRP	90	0.64	0.25	87.1	45	
A.3 E300.90	3.4	30.8	Steel	90	0.17	0	31.2	47.7	Barros Dalfre (2013)
A.4 E300.45	3.4	28.8	Steel	45	0.25	0	57.1	87.4	
A.5	3.4	30.8	Steel	90	0.17	0.13	40.3	40.8	
S300.90/E300.90	3.4	30.8	Steel	90	0.11	0	21.3	17.5	
B.3 E300.90	3.4	28.8	Steel	45	0.16	0	98.5	65.3	
B.4 E300.45	3.4	30.8	Steel	90	0.11	0.06	94.7	67.9	
B5. S300.90/E300.90	2.5	24.7	Steel	90	0.15	0	37	39.5	Breve-glieri et al. (2015)
0S-S300-90	2.5	24.7	Steel	45	0.21	0	115.5	123.4	
0S-S300-45	2.5	24.7	Steel	90	0.24	0	6 0.5	64.6	
0S-S180-90	2.5	24.7	Steel	45	0.34	0	127.7	136.3	
0S-S180-45	2.5	24.7	Steel	90	0.15	0.1	44.2	30.4	
2S-S300-90	2.5	24.7	Steel	45	0.21	0.1	99.0	68.2	
2S-300-45	2.5	24.7	Steel	90	0.24	0.1	98.8	68.1	
2S-180-90	2.5	24.7	Steel	45	0.34	0.1	157.6	108.5	
2S-S180-45	2.5	24.7	CFRP	90	0.16	0.1	77.1	53.1	
2S-C180-90	2.5	24.7	CFRP	45	0.22	0.1	175.6	120.9	
2S-C180-45	2.5	27.6	Steel	90	0.15	0.17	10.3	4.8	
4S-S300-90	2.5	27.6	Steel	45	0.21	0.17	119.2	56.1	
4S-S300-45	2.5	27.6	Steel	90	0.24	0.17	35.6	16.8	
4S-S180-90	2.5	27.6	Steel	45	0.34	0.17	127.6	60.1	
4S-S180-45	2.5	27.6	CFRP	90	0.16	0.17	13.9	6.5	
4S-C180-90	2.5	27.6	CFRP	45	0.22	0.17	157.8	74.4	
4S-C180-45									
C/1.9	1.9	40	CFRP	90	0.19	0.15	177.6	57.6	Dirar and Theofa-nous (2017)
G/1.9	1.9	40	GFRP	90	0.19	0.15	102.3	33.2	
G/3.0	3.0	40	GFRP	90	0.38	0.11	143.5	96.0	

2.7.1 Effect of Concrete Strength

Figure 2.17 illustrates the impact of the $\frac{E_f\ \rho_f}{{f_c}'^{2/3}}$ ratio (i.e. ratio between the elastic modulus of DE bars (E_f) multiplied by DE shear strengthening ratio (ρ_f) to ${f_c}'^{2/3}$) on the shear force gain due to DE FRP bars. It can be observed that the shear gain increases up to a ratio value of approximately 0.05. This observation was previously confirmed for RC beams externally bonded with FRP systems indicating that 0.05 is a threshold for the shear rigidity of the FRP, as well as a criterion for establishing a cost-effective design (Triantafillou, 1998). Godat et al. (2012) concluded that as the concrete compressive strength increases, the shear gain due to DE bars increases because the bond force/strength resistance of DE bar-to-concrete interface increases leading to a greater shear strength contribution by DE bars. The concrete strength also affects the failure mode of the RC beams (Godat et al., 2012). However, more experimental tests need to be conducted to examine the influence of concrete strength considering a wider range of values from 25 MPa up to 60 MPa and keeping constant other factors to avoid coupling effects.

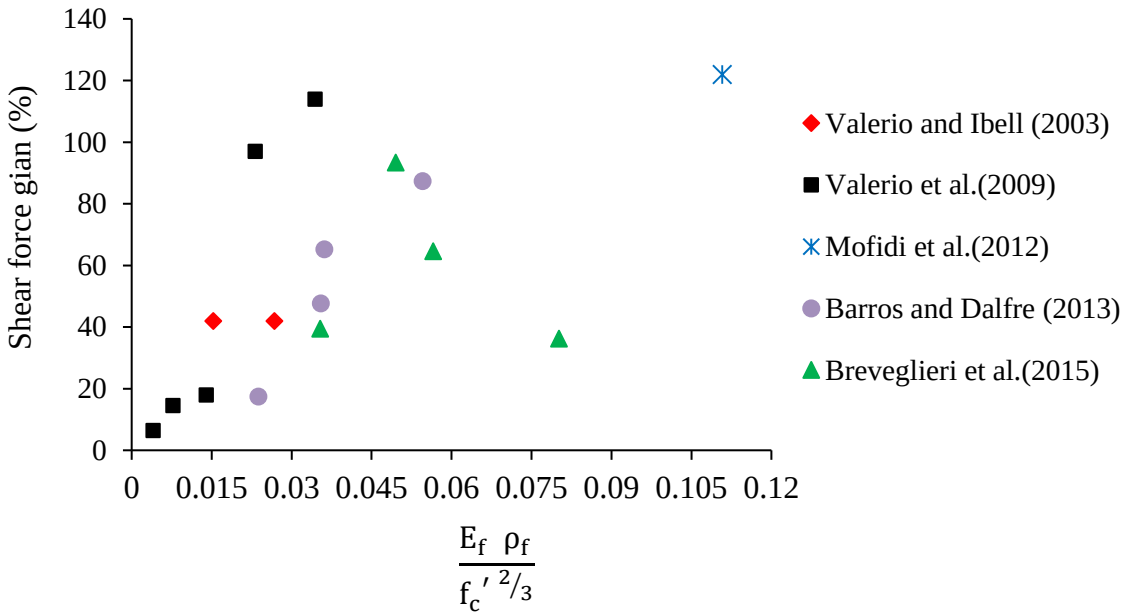

Figure 2.17 Effect of the $\frac{E_f\ \rho_f}{{f_c}'^{2/3}}$ ratio on the shear force gain (beams without steel stirrups)

2.7.2 Effect of the Shear Span-to-Effective Depth Ratio

Shear span-to-effective depth ratio (a/d) is another key factor which influences the shear strength. Experimental test results by Nagasaka et al. (1993) and Zhao et al. (1995) on FRP RC members with internal FRP web reinforcement, showed that increasing the a/d ratio led to a proportional linear decrease in the shear strength. This observation agrees with the test results by Valerio et al. (2009), who tested small-scale rectangular RC beams shear-strengthened with DE CFRP bars. It was concluded that as the a/d ratio reduced from 4d to 3d, the shear strength increased for both pre-stressed and non-prestressed RC beams altering even their mode of failure.

Figure 2.18 illustrates the impact of the a/d ratio on the shear force gain for the shear-strengthened RC beams with DE bars, as listed in Table 2.5. It can be observed, that the shear force gain decreases with the increase in the a/d ratio, in particular for a/d ratios greater than 2.5 (i.e. shear behaviour is governed by the beam action). In the case of deep beams (i.e. a/d <2.5), the concrete will transfer the shear forces through the arch action directly to the supports, leading to a greater contribution to the shear strength. Dirar and Theofanous (2017) tested two series of large-scale RC T-beams, which included an unstrengthened deep beam and a DE shear-strengthened beam. The beams had a/d ratio of either 1.9 or 3.0, effective depth of about 600 mm and were reinforced with internal steel shear reinforcement. Sand-coated GFRP bars of 12 mm diameter were used for the DE shear-strengthening. The test results confirmed that the shear strength enhancement due to the DE GFRP bars varied from 33% to 96% for beams with a/d of 1.9 and 3.0 respectively, proving that the shear strength enhancement attributable to the DE GFRP bars is strongly dependent on the a/d ratio. Additional experiments need to be conducted, examining the effect of a/d ratios less than 2.5, on the shear strength gain due to DE bars.

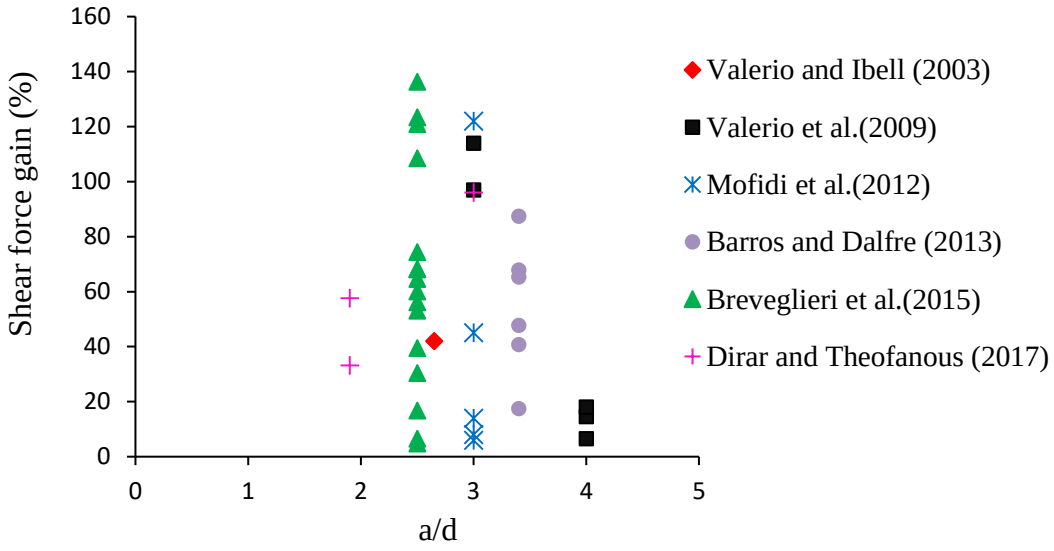

Figure 2.18 Effect of a/d on the shear force gain

2.7.3 Effect of Beam Effective Depth

Limited studies have examined the impact of effective depth for large-scale DE FRP shear-strengthened beams. Valerio et al. (2009) tested large-scale rectangular beams strengthened in shear with DE bars. They observed that, as the beam effective depth increased, the percentage increase in the shear capacity reduced for the large-scale DE shear-strengthened beams without stirrups compared to the small-scale beams. Previous studies on FRP strengthened RC beams have explained the decrease in the shear strength contribution by concrete with the increase in the member depth. This was attributed to the fact that diagonal cracks of larger widths are developed in beams with larger effective depths (Lubell et al., 2004). However, more experiments taking into consideration a wider range of effective depth values are required in order to evaluate realistically the impact of the scale effect on DE shear strengthened beams.

2.7.4 Effect of Internal Transverse Steel Reinforcement Ratio

Figure 2.19 illustrates the impact of the internal transverse steel reinforcement ratio on the shear gain offered by the DE bars for the strengthened RC beams (refer to Table 2.5). It can be observed that the shear gain due to DE bars decreases as the $\frac{E_s \rho_v}{E_f \rho_f}$ ratio increases, confirming the adverse effect of the presence of internal transverse steel links on the shear contribution due to DE bars. The ratio $E_s \rho_v / E_f \rho_f$ is defined as the ratio between the elastic modulus of steel stirrups (E_s) multiplied by the steel stirrups reinforcement ratio (ρ_v) to the elastic modulus of DE FRP bars (E_f) multiplied by the DE shear strengthening ratio (ρ_f).
This interaction between FRP reinforcement and internal steel stirrups has been previously demonstrated in the case of externally bonded (EB) FRP shear-strengthened beams (Bousselham and Chaallal, 2008).

The results of experimental tests performed by Chaallal et al. (2011) and Mofidi et al. (2012) revealed that the presence of closely spaced steel stirrups reduced the contribution by the DE FRP bars to shear capacity. The RC beam with a DE shear strengthening ratio (i.e. $\rho_f = \frac{A_f}{b_w s_f}$, where ($A_f$) is the area of the DE bar, (b_w) is the beam width and (s_f) is DE bar spacing) of 0.64 % experienced a 122 % increase in the shear capacity compared to the unstrengthened beam. Strengthened beams with the same DE reinforcement ratio, but also reinforced with steel stirrups with a transverse reinforcement ratio (i.e. $\rho_v = \frac{A_v}{b_w s_v}$, where ($A_v$) is the area of the steel stirrups, (b_w) is the beam width and (s_v) is the spacing between steel stirrups) of 0.38 % and 0.25 % respectively, exhibited a corresponding increase in the shear capacity of only 13% and 45% respectively. In addition, the failure mode of the DE strengthened beams was affected by the presence of steel stirrups.

The experimental tests performed by Barros and Dalfre (2013) on DE-strengthened beams, reinforced also with steel shear links, confirmed that the shear gain by the DE steel bars was 40.8 % for the beams with steel stirrups spaced at 300 mm (i.e. ρ_v =0.13 %), and reduced to 35.4 % when the steel stirrups were spaced at 225 mm (i.e. ρ_v= 0.17 %).

Finally, Breveglieri et al. (2015) assessed the impact of the internal steel reinforcement ratio on the shear strengthening enhancement for three series of RC T-beams, namely 0S, 2S and 4S. These series had different percentages of internal steel transverse reinforcement ranging from 0 to 0.17 %. It was observed that the shear strengthening effectiveness of the DE bars reduced by 74% when the internal transverse steel reinforcement ratio increased from 0 % (0S beam series) to 0.17 % (4S beam series).

However, there is lack of experimental data examining the impact of existing steel reinforcement on the contribution of DE bars for RC deep beams with a/d ratios less than 2.5. This shortcoming was addressed in Chapter 4.

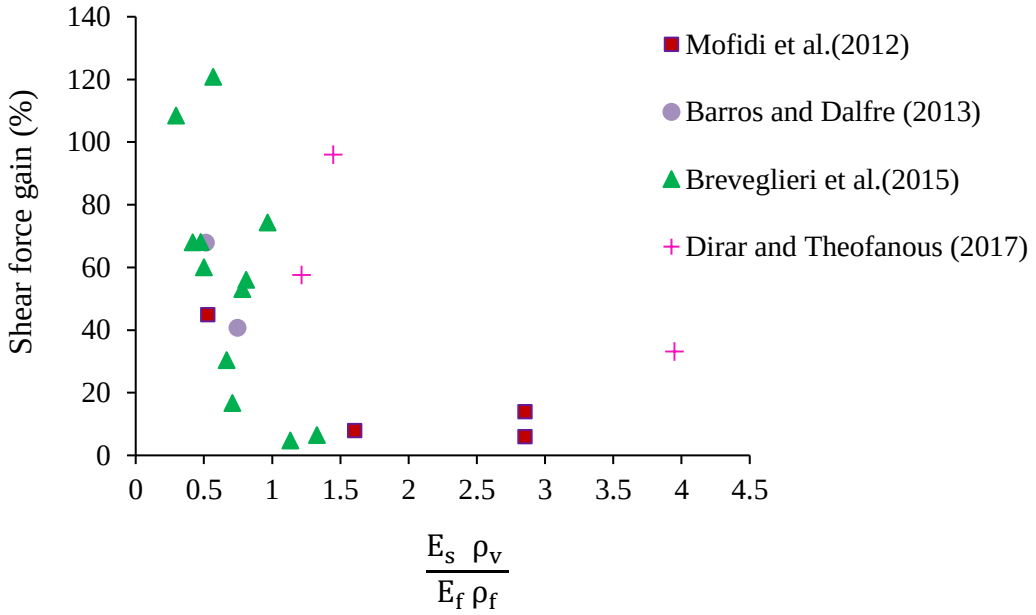

Figure 2.19 Effect of the $\frac{E_s\ \rho_v}{E_f\ \rho_f}$ ratio on the shear force gain

2.7.5 Effect of DE Shear Strengthening Ratio

Figure 2.20 illustrates the effect of DE shear strengthening ratio on the shear strength gain due to DE bars. Full details of tested RC beams shear-strengthened with DE bars can be found in Table 2.5. It can be observed that the gain in shear strength increases with the increase in the DE shear strengthening ratio. This agrees with the shear design guidelines proposed by Mofidi et al. (2012), who found the shear contribution due to DE bars to be directly proportional to the DE shear reinforcement ratio.

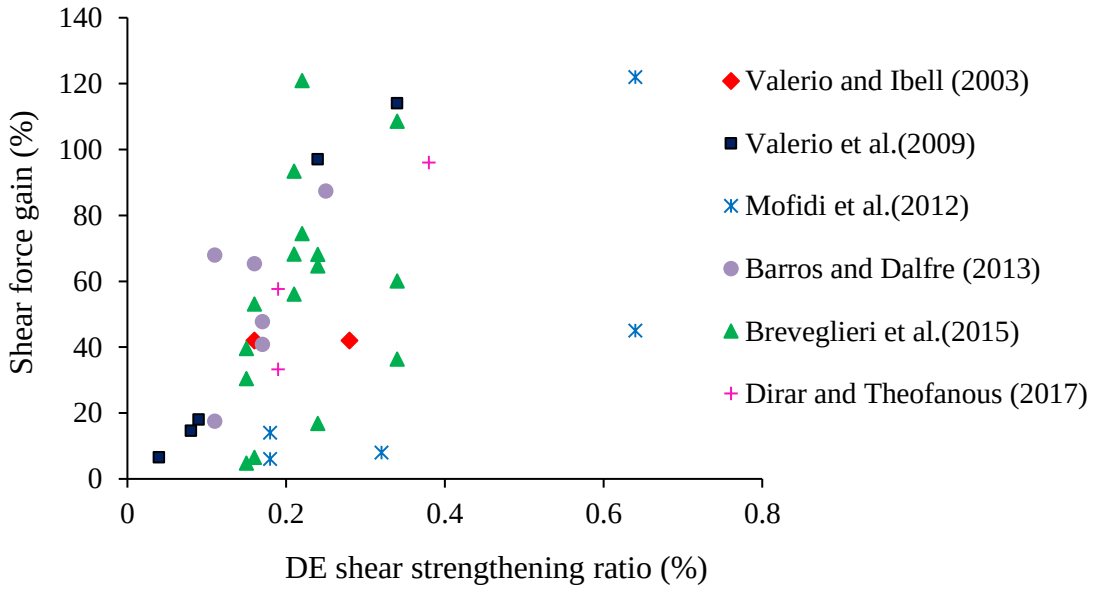

Figure 2.20 Effect of ρ_f ratio on the shear force gain

The same correlation was confirmed for FRP RC reinforced beams, where the shear contribution due to the FRP transverse reinforcement increased almost linearly with the FRP reinforcement ratio, which agrees with the CSA S806 (2006).

The experimental tests conducted by Chaallal et al. (2011) and Mofidi et al. (2012) proved that decreasing the spacing of the DE FRP bars (i.e. increasing the DE shear strengthening ratio) led to higher shear resistance. Hence, for RC T-beams strengthened in shear with 12.7-

mm CFRP bars, decreasing their spacing by 50 % led to an almost 55 % increase in the shear resistance. Thus, a proportional increase in the shear contribution due to DE FRP bars can be suggested to occur with the reduction in the FRP bar spacing due to a better confinement and crack control. Design guidelines limit the strain value for DE FRP bars to 0.004. This is to prevent potential shear failure of the concrete cross-section, due to concrete softening because of aggregate interlock loss (fib, 2012).

In addition, Valerio and Ibell (2003) tested RC beams strengthened with DE FRP bars with a FRP reinforcement ratio of 0.24 %, 0.48 % and 0.64 % respectively. The recorded increase in the load-carrying capacity due to DE FRP bars was 33 %, 42 % and 84 % respectively. This observation also agrees with the test results of Valerio et al. (2009). They tested small-scale rectangular RC beams strengthened with DE bars. Decreasing the spacing of the DE CFRP bars from 0.7d to 0.5d, led to an increase in the DE FRP reinforcement ratio from 0.25 % to 0.34 %, which resulted in an increase of 27 % in the shear capacity.

Barros and Dalfre (2013) tested RC beams strengthened with DE steel bars at different angles of inclination. They concluded that as the DE steel reinforcement ratio increased from 0.17 % to 0.25 %, by reducing the angle of inclination of the DE steel bars from 90^0 to 45^0, the load-carrying capacity increased from 47.8 % to 87.4 %. Breveglieri et al. (2015) tested RC beams with DE steel bar strengthening ratios varying between 0.15 % to 0.34 % and DE CFRP bar strengthening ratios ranging from 0.16 % to 0.22 %. The highest DE shear strengthening ratios corresponded to inclined steel and CFRP bars at 45^0. As the ratio increased from 0.15 % to 0.34 %, the shear strength gain due to steel DE bars increased from 39.5 % to 136.3 % for beam series 0S, from 30.4 % to 108.5 % for beams series 2S and from 4.8 % to 60.1% for beam series 4S. When CFRP bars were used, as the DE strengthening ratio

increased from 0.16 % to 0.22 %, the gain in shear resistance increased from 53.1 % to 120.9 % for series 2S and from 6.5 % to 74.4 % for series 4S respectively. DE steel and CFRP inclined bars achieved higher strengthening effectiveness due to their orientation almost orthogonal to the diagonal cracks. This can be attributed to a larger ultimate force in the case of inclined bars at 45^{o}. It was also observed that for similar DE shear strengthening ratios, CFRP bars led to higher shear strengthening effectiveness compared to steel bars.

2.7.6 Effect of the Longitudinal Steel Reinforcement

Figure 2.21 presents the variation in the shear gain due to DE bars as a function of $\frac{E_s \rho_l}{E_f \rho_f}$ ratio (i.e. the ratio between the elastic modulus of steel longitudinal reinforcement (E_s) multiplied by the steel longitudinal reinforcement ratio (ρ_l) to the elastic modulus of DE FRP bars (E_f) multiplied by the DE shear strengthening ratio (ρ_f). The longitudinal reinforcement ratio of DE-strengthened beams varied between 0.93 % to 3.76 % with an average of 1.97%. Figure 2.21 shows that as this ratio increases, the shear gain decreases, which may suggest an interaction between the DE bars and longitudinal steel reinforcement. However, more experimental tests need to be conducted to examine the influence of this ratio for both slender and deep beams.

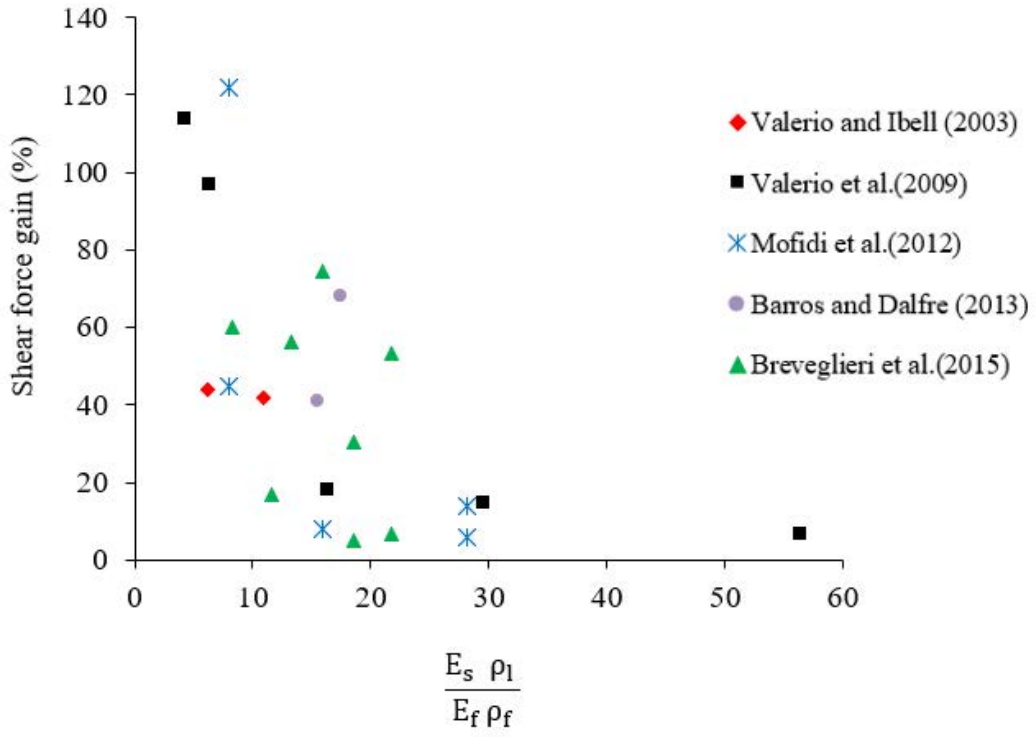

Figure 2.21 Effect of $\frac{E_s\ \rho_l}{E_f\ \rho_f}$ ratio on the shear force gain (beams without steel stirrups)

2.7.7 Effect of the FRP Bar Surface Coating

Mofidi et al. (2012) examined the effect of the DE CFRP bar surface coating on the shear strength gain. The tested T-beams were strengthened with DE FRP bars of same diameter and spacing (i.e. same DE strengthening ratio ρ_f), but had a different surface coating (i.e. sand-coated and plain surface). It was concluded that the shear strength gain due to FRP bars was higher when using DE CFRP bars with a plain surface rather than a sand-coated surface. The compatible chemical bond which develops at the interface between similar polar molecular groups of the epoxy and FRP bars with plain-surface finish provides a better shear performance, whilst, the chemical bond is less compatible when FRP bars with a sand coating are used; thus, the shear performance is deteriorated.

2.8 Modes of Shear Failure in RC beams

This section describes the typical stages of crack development (see Figure 2.22) and the typical modes of shear failure encountered in simply supported RC beams (see Figures 2.23-2.25). Flexural cracks (1) will initiate first due to concrete reaching its tensile strength. They usually develop in the centre of the beams and extend vertically / straight towards the upper part of the RC beam. The next type of cracks (2) is commonly defined as shear cracks and occur due to beam action (i.e. because of biaxial compression and tension stresses). These cracks will propagate vertically up to the point of reaching the main reinforcement and then tend to incline to an angle between 30 to 45 degrees. In deep beams, diagonal tensile splitting cracks (3) will also develop from the bottom face of the RC beam near the support and extend towards the top face of the beam near the loading point. These deep inclined cracks occur because of the arch-action, when the developed stresses reach the ultimate compressive strength of concrete under biaxial tension-compression and will eventually lead to failure of the compression zone of the shear span. These inclined cracks penetrate deeper in the compression zone of the cross section compared to other types of flexural cracks. The role of transverse reinforcement is crucial in delaying the process of propagation of such cracks and allowing the beam to sustain the design load. The concrete section will reach its minimum volume level at the compressive area of the cross-section coinciding with the tip of the inclined crack. Further increase in applied load after that will lead to volume dilation of the concrete by inducing transverse tensile stresses in the surroundings. Failure of concrete in these regions will occur due to the combined action of compressive and tensile stress. Therefore, the collapse of the beam will occur at load levels smaller than the ultimate flexural capacity (4).

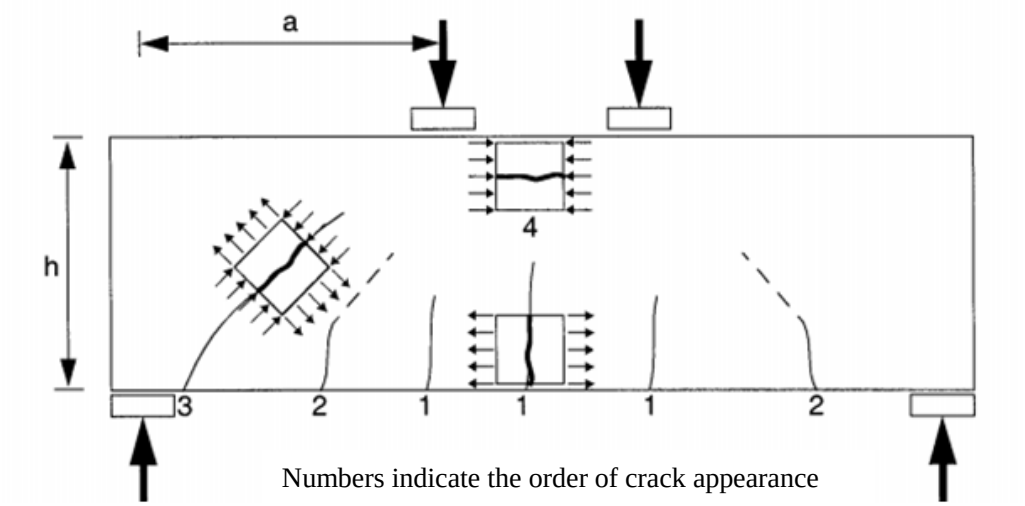

Figure 2.22 Stages of crack development in RC beams (ACI 318R, 2005)

The main modes of shear failure that have been observed in experimental tests can be categorised as follows:

a) Strut crushing and splitting failure: Wight and MacGregor (2009) revealed that crushing of the compression strut (see Figure 2.23) is common in FRP or steel-reinforced deep beams with a/d <1.0. It occurs because of inclined cracks which are developed along the line connecting the loading and reaction supports. Splitting failure occurs due to either anchorage/bearing failure at the ends of the RC beam or due to fracture of longitudinal reinforcement at the locations of developed inclined cracks.

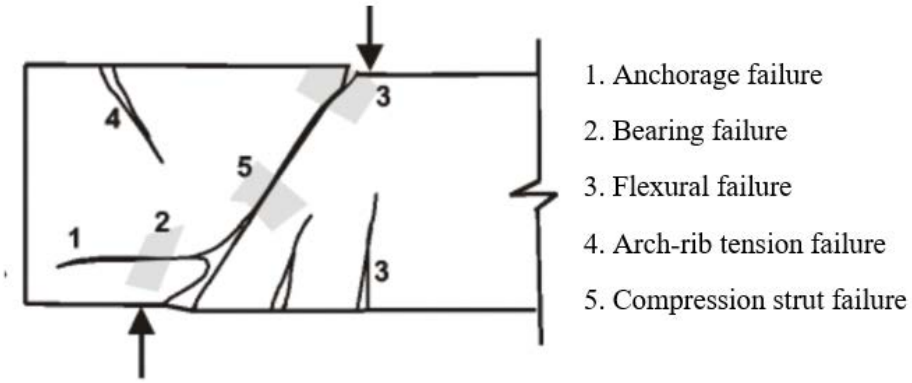

Figure 2.23 Failure mode of deep beams with 0 < a/d < 1.0 (Wight and MacGregor, 2009)

b) Shear-tension and shear-compression: These modes of failure are typical for deep beams having a/d ratios between 1.0 and 2.5. Shear-tension failure (see Figure 2.24a) occurs when the developed cracks extend towards the tension reinforcement, causing splitting of the surrounding concrete along the tension reinforcement. Shear-compression failure (see Figure 2.24b) is characterised by concrete crushing in the compression zone of the RC beam at the tip of the diagonal shear cracks. The CSA S806 (2012) code specifies a crack-width limit of 0.5 mm for the minimum amount of web reinforcement to be used in FRP-reinforced deep beams. This requirement is essential for unforeseen actions during the design process of RC deep beams.

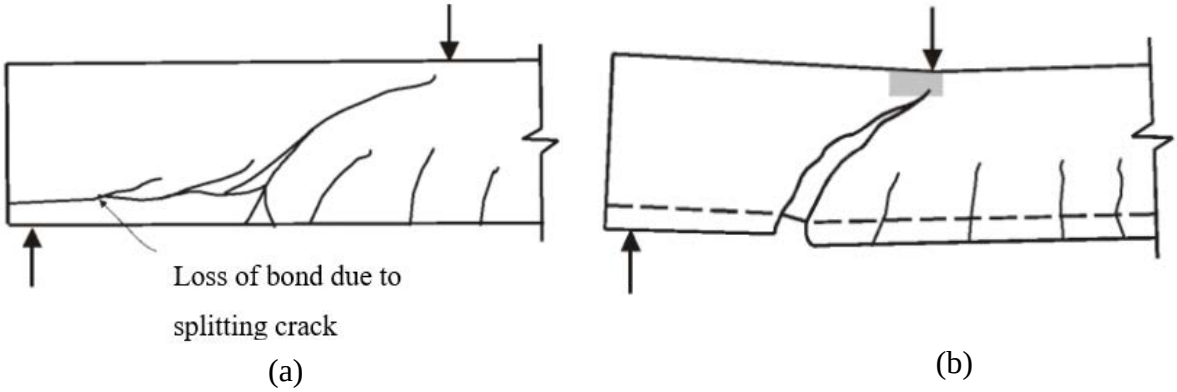

Figure 2.24 Failure mode of deep beams with $1.0 < a/d < 2.5$: (a) shear-tension failure and (b) shear-compression failure (Wight and MacGregor, 2009)

c) Diagonal tension failure: Experimental tests have observed this type of failure (see Figure 2.25) in slender beams with a/d ratios greater than 2.5 and smaller than 5.6. The failure initiates with the formation of a flexural crack which propagates upon further loading and converts into an inclined crack. Splitting of the RC beam into two portions, resulting in complete collapse, occurs when the crack width increases substantially, and the crack propagates rapidly towards the loading point.

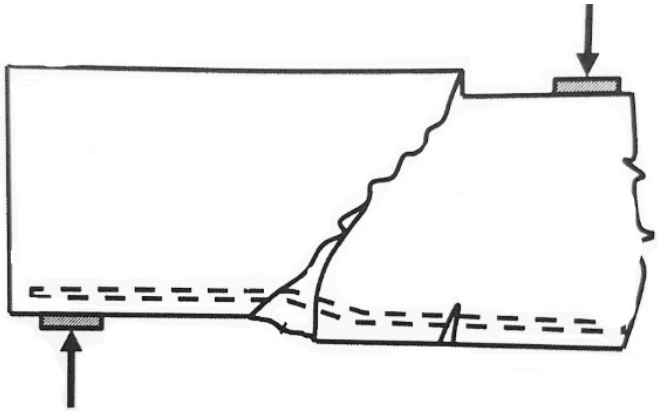

Figure 2.25 Diagonal tension failure in slender beams

2.9 FE Studies on RC Beams Strengthened in Shear with DE bars

To date, there are only three numerical studies that address the finite element (FE) modelling procedure of RC beams strengthened in shear with deep embedment (DE) bars. The studies were conducted by Godat et al. (2013), Qapo et al. (2016b) and Breveglieri et al. (2016).

Godat et al. (2013) developed a two-dimensional FE model to represent the CFRP bar-to-concrete interfacial behaviour of the DE CFRP bar during pull-out testing. Discrete truss elements were used to connect the DE CFRP bars to the two sides of the concrete. The bond behaviour was represented by adopting the Cosenza-Manfredi-Realfonzo (CMR) bond stress-slip model. In addition, a three-dimensional FE model was developed to predict the experimental results of three slender RC beams strengthened in shear with DE CFRP bars, and three control unstrengthened beams tested by Mofidi et al. (2012). The fixed crack model with a linearly variable shear retention factor was adopted to simulate the nonlinear behaviour of concrete. Concrete was modelled using three-dimensional solid brick elements. The steel reinforcement and DE FRP bars were modelled using truss-elements which were directly connected to the concrete solid brick elements. A full-contact bond was assumed between the

CFRP bars and concrete since debonding was not the governing failure mode of the tested beams. The FE model was developed using FE package ADINA 8.5.4 (ADINA R&D Incorporation, 2009). The displacement control method was used for simulating the applied load. The FE results confirmed the accuracy of the adopted FE model in predicting the load-carrying capacity, load-deflection relationship, axial strains in the reinforcing bars and the crack patterns of beams.

Qapo et al. (2016b) developed a three-dimensional FE model for RC beams strengthened in shear with DE FRP bars using published experimental test results by Valerio et al. (2003), Mofidi et al. (2012) and Qin et al. (2014). Several constitutive models and element types available in DIANA 9.4.4 software package (DIANA user's manual, 2012) were used to represent the concrete, steel plates, steel reinforcement and DE FRP bars. Concrete and steel plates were modelled using eight-node isoparametric solid brick elements and six-node isoparametric solid wedge elements respectively. The steel reinforcement was represented by embedded truss-like elements with no degrees of freedom. DE FRP bars were modelled using three-dimensional two-node truss elements. A linear elastic stress-strain model was used to characterise the behaviour of DE FRP bars. The FRP bar-to-concrete interface was modelled with four-node three-dimensional interface elements. The overall FRP bar-to-concrete interface behaviour was represented using the bond-slip model of Mofidi et al. (2012). A total strain rotating crack model was adopted for simulating the behaviour of concrete. Steel reinforcement, support and reaction plates were modelled as elastic-perfectly plastic materials. The comparison of FE predictions with experimental results demonstrated the capability of the FE model in predicting correctly the shear force capacity, load-deflection behaviour and failure mode. In addition, Qapo et al. (2016b) carried out a comprehensive FE parametric study on DE strengthened RC slender beams. This study examined the effect of DE FRP bar orientation, a/d ratio, concrete compressive strength, effective beam depth, and

interaction between DE FRP bars and internal steel stirrups. The FE results revealed that the shear strength was enhanced when using inclined DE bars and with the increase in the concrete compressive strength. On the other hand, increasing the steel stirrup-to-DE FRP bar and the a/d ratio reduced the predicted shear strength. Finally, the FE results revealed that the effective beam depth didn't have a significant effect on the shear strength gain due to DE FRP bars.

Breveglieri et al. (2016) performed a nonlinear FE modelling study on the shear behaviour of slender RC beams strengthened in shear with steel DE bars, using a multi-directional fixed smeared crack model FE software (FEMIX). In this study, a new shear softening law was developed as another option to the shear retention function. This approach simulated correctly both the shear stiffness degradation of concrete and stress transfer during the crack opening in concrete RC beams. The results of the experimental programme by Breveglieri et al. (2015) were used to calibrate the parameters which characterised the crack shear stress-strain softening diagram for each tested beam. The numerical simulations were performed by assuming a perfect bond between the concrete and the DE bars. The FE results confirmed the ability of the proposed shear softening law to simulate the deformational and cracking behaviour of RC elements, the crack patterns and the strain in both steel stirrups and DE bars. A linear regression analysis was performed to determine the parameters that defined the crack shear softening diagram, namely the shear retention function, β_s, the concrete shear fracture energy, G_{fs} , and the crack shear strength, $\tau_{t,p}^{cr}$. It was revealed that G_{fs} increases with the increase in transverse reinforcement whilst β_s decreases. The load-deflection response and the crack pattern at failure were highly influenced by these parameters, unlike the maximum load carrying capacity.

2.10 Strut-and-Tie Models for Shear Modelling in RC Deep Beams

Strut-and-tie models (STM) are used to analyse the discontinuity regions (D-regions) of nonlinear strain distribution in RC deep members (Schlaich et al., 1987; Marti, 1985; Wight and Macgregor, 2009).

The STM approach assumes that the complex flow of forces in deep beams after diagonal cracking can be idealised using pin-jointed trusses comprised of struts and ties, as shown in Figure 2.26. Secondly, the STM applies the principles of the lower-bound theory of plasticity. This states that the stress field must satisfy the requirement of internal equilibrium, with the applied stresses on STM elements not exceeding the tensile strength of FRP reinforcement/ yield strength of steel reinforcement or the plastic capacity of concrete. Sufficient deformation capacity and strength must be attained by the STM elements to ensure full redistribution of the applied forces (Schlaich et al., 1987). The STM of a deep beam comprises struts subjected to compressive forces and ties which represent the longitudinal tension reinforcement and are subjected to tensile stresses. The tie location corresponds to the centroid of the longitudinal reinforcement. In STM, the ties must be properly anchored either by a bearing plate or by a bond with compressive stresses acting on the edges of the node (Wight and MacGregor, 2009).

The points where the struts and ties connect are called nodes. ACI 318 (2008) identifies three major node types: CCC nodes (bounded by struts only), CCT nodes (bounded by one tie and two or more struts), and CTT nodes (bounded by one strut and two or more ties) (see Figure 2.28).

Figure 2.27 illustrates two types of struts, namely the prismatic and bottle-shaped. The prismatic struts have a constant width and are located in the compression zone of the beam's

flexural region, as well as between the two loading plates. On the other hand, the width of a bottle-shaped strut varies along its length. Distribution of compressive stresses in a bottle-shaped strut induces transverse tensile stresses, which in turn cause parallel cracks to be developed with respect to the strut axis. For simplification in calculations, in the STM model, the bottle-shaped struts are idealised to have a prismatic shape, as shown in Figure 2.27. The dimensions of a strut are governed by the size of the nodal zone at each end of the strut.

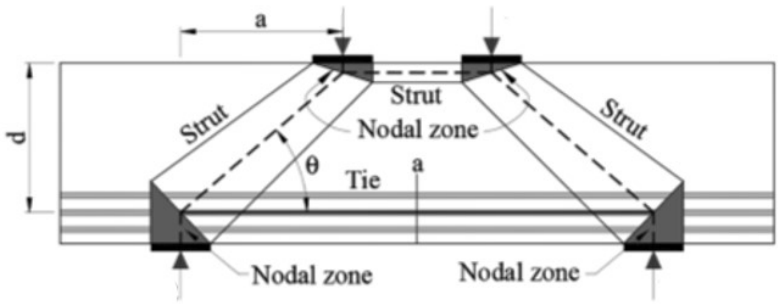

Figure 2.26 Strut-and-tie model for a simply supported deep beam (Andermatt and Lubell, 2013)

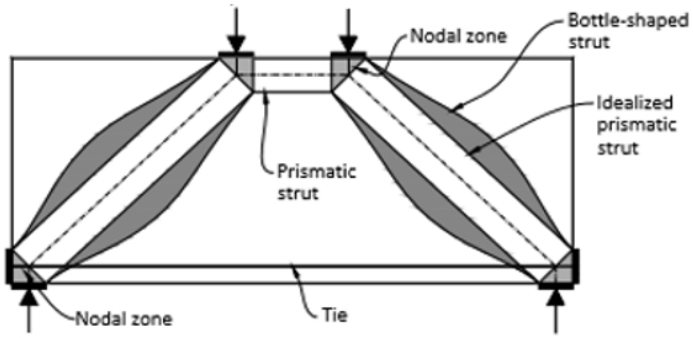

Figure 2.27 Prismatic and bottle-shaped struts (Andermatt and Lubell, 2013)

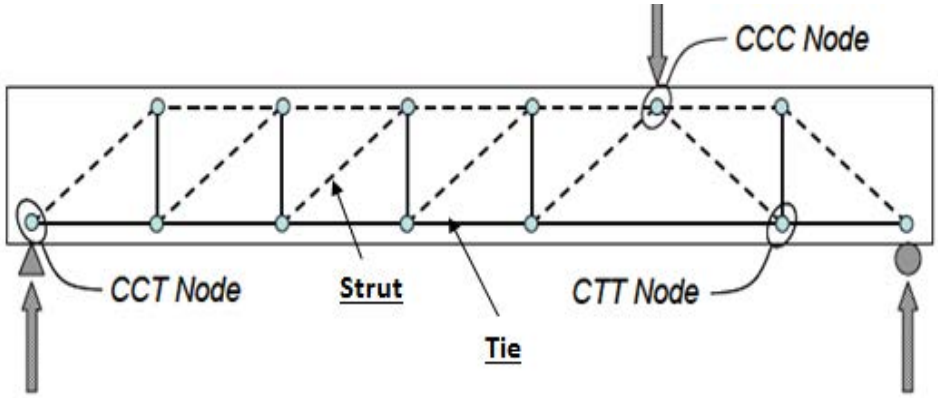

Figure 2.28 Type of nodes: CCC, CCT and CTT (ACI 318, 2008)

The one-panel STM (see Figure 2.29) has been used as the preferred mechanism for steel RC deep beams (Brown and Bayrak, 2007), and has been also applied for FRP-reinforced deep beams (Mohamed et al., 2016). In this model, the shear force is resisted primarily by the compressive strut between the load point and the support.

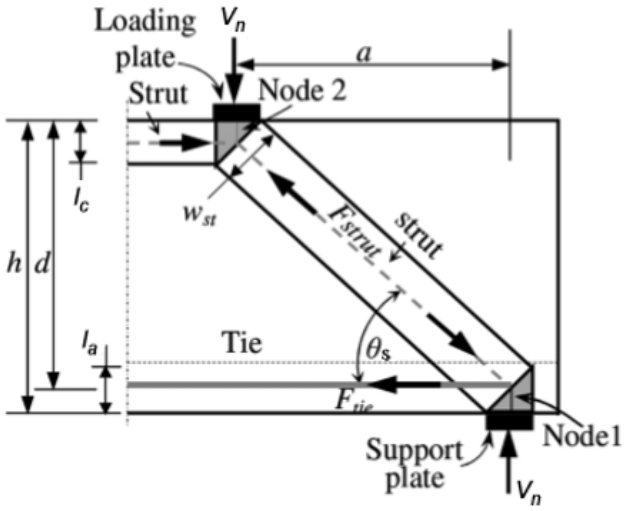

Figure 2.29 One-panel STM geometry (Mohamed et al., 2016)

The strut width is assumed to be uniform (see Figure 2.29) and is determined by the geometry of the node at the support as follows:

$$w_{st} = (l_p \sin\theta_s + l_a \cos\theta_s) \quad (2\text{-}5)$$

This assumption is based on a model adopted by Collins and Mitchell (1997), where l_p is the base-plate width and l_a is twice the distance between the centroid of the main reinforcement and the beam bottom.

The angle θ_s is estimated as:

$$tan\ \theta_s = \frac{d - l_c/2}{a} \quad (2\text{-}6)$$

where l_c is the width of the horizontal strut and *a* is the shear span of the beam.

This section introduces two STM shear design provisions, namely CSA S806 (2012) and ACI 318 (2011). Several studies have examined the applicability of these strut-and-tie models in estimating the shear capacity of FRP-reinforced deep beams (Andermatt and Lubell et al., 2013; Farghaly and Benmokrane, 2013; Mohamed et al., 2016).

2.10.1 CSA S806 (2012) Provisions

CSA S806 (2012) proposes a strut-and-tie model which adopts the same principles for disturbed regions in deep beams as the CSA A23.3 (2004) for steel-reinforced members.

In all these models the compressive force (F_{ns}) in the strut shall comply with the following criterion:

$$F_{ns} < \Phi_c\ f_{ce}\ A_{str} \quad (2\text{-}7)$$

where Φ_c = 0.65 is the resistance factor of concrete, A_{str} (= $w_{st}\ x\ b_w$; b_w is the beam width and w_{st} is the strut width) is the effective cross-section area of the strut and f_{ce} is the limiting compressive strength in the strut.

STM provisions do not specify a limit on the angle (θ_s) between adjoining struts and ties. This model utilises a MCFT-based approach in estimating the maximum compressive stresses permitted in concrete struts, taking into account the influence of cracking caused by coexisting transverse tensile strain (Vecchio and Collins, 1993).

The limiting compressive stress (f_{ce}), in a concrete strut crossed by a tension tie, can be estimated as follows:

$$f_{ce} = \frac{f_c'}{0.8+170\ \varepsilon_1} \leq \alpha_1\ f_c' \text{ or } 0.85\ f_c' \tag{2-8}$$

where ε_1 is the tensile strain in concrete given by:

$$\varepsilon_1 = \varepsilon_{fe} + (\varepsilon_{fe} + 0.002)\ cot^2\ \theta_s \tag{2-9}$$

CSA S806 (2012) code provisions state that parameter θ_s is the angle between the compressive strut and the adjoining tension ties (see Figure 2.29) and ε_{fe} is the tensile strain in the tie bar positioned closest to the tension face of the RC deep beam (Mohamed et al., 2016).

Parameter α_1 in Equation (2-8) is given as follows:

$$\alpha_1 = 0.85\text{-}0.0015\ f_c' \geq 0.67 \tag{2-10}$$

CSA S806 (2012) provisions impose a limit on the calculated concrete compressive stress, f_{ce} , for different node regions. The stress limit shall not exceed 0.85 Φ_c f_c' (or 0.55 f_c') in CCC nodes, 0.75 Φ_c f_c' (or 0.49 f_c') in CCT nodes, and 0.65 Φ_c f_c' (or 0.42 f_c') in CTT nodes.

The code also states that for new RC members, an orthogonal grid of crack control reinforcement shall be provided near each face of the RC member. The minimum required web reinforcement ratio should be at least 0.003 in each direction and the maximum bar spacing should not be greater than 200 mm for crack control.

From Equations (2-8) and (2-9), it can be suggested that the compressive strength of the strut reduces with the increase in the strut angle or increase in the tensile reinforcement strain. Thus, the shear strength capacity of the RC deep beam which is influenced by the strength of the strut will reduce with an increase in the a/d ratio (Andermatt and Lubell, 2013). In addition, the axial stiffness of the reinforcement influences the member capacity.

Mohamed et al. (2016) examined the accuracy of CSA S806 (2012) provisions in predicting the shear capacity of FRP-reinforced deep beams using a database of 28 deep beams reinforced longitudinally with FRP bars and without web reinforcement. The data were collected from the experimental studies published by Farghaly and Benmokrane (2013), Andermatt and Lubell (2013) and Mohamed et al. (2016). The shear capacity predictions using the STM in CSA S806 (2012) were underestimated since the adopted STM exaggerates the negative impact of concrete softening in the diagonal strut due to ε_1 (Equation 2-9). It is worth noting that the maximum strain in longitudinal reinforcement in the case of FRP-reinforced deep beams can reach values as high as 0.01, which increases ε_1; thus, the efficiency of the strut is underestimated.

2.10.2 ACI 318 (2011) Provisions

In 2002, the American Concrete Institute (ACI) Committee 318 introduced a STM model in its Building Code for structural concrete, and further revisions were made in 2005, 2008 and 2011.

In Appendix-A of ACI 318 (2011), the evaluation of the compressive strength of a strut (F_{ns}) is based on the product of the effective concrete strength (f_{ce}) (i.e. crushing strength of concrete in the strut) and the smaller cross-sectional area at each end of the strut (A_{str}).

$$F_{ns} = f_{ce}\, A_{str} \tag{2-11}$$

The ACI 318 (2011) code provisions restrict the minimum angle θ_s between the axis of any strut and tie to 25 degrees, to prevent incompatibilities caused by shortening of the strut and lengthening of the ties.

ACI 318-08 (2011) also proposes a strength reduction factor to take into account the cracking conditions in the struts. The proposed values vary from 0.3 for heavily cracked struts to 0.85 for diagonal struts subjected to either uniaxial or biaxial compression (Yun and Ramirez, 1996).

The effective compressive strength of the concrete, f_{ce}, in a concrete strut without longitudinal reinforcement is given by:

$$f_{ce} = 0.85\, \beta_{st}\, f_c' \tag{2-12}$$

The strut efficiency factor β_{st} is dependent on the strut geometry and stress conditions of the RC member, as well as the reinforcement provided. This factor is taken as β_{st}=1.0 for struts of uniform cross-sectional area across their length, 0.6 for bottle-shaped struts without distributed reinforcement, and 0.75 for bottle-shaped struts with distributed web reinforcement.

ACI 318 (2011), clause A3.3 specifies the minimum amount of web reinforcement as given in Equation (2-13):

$$\sum \frac{A_{si}}{b_{si}\, s_i}\, sin\, \theta_i \geq 0.003 \tag{2-13}$$

where b_{si} is the strut width perpendicular to the plane of the reinforcing bars, A_{si} is the reinforcement cross-sectional area crossing the strut in the i-th layer of reinforcement at spacing s_i and angle θ_i to the strut axis.

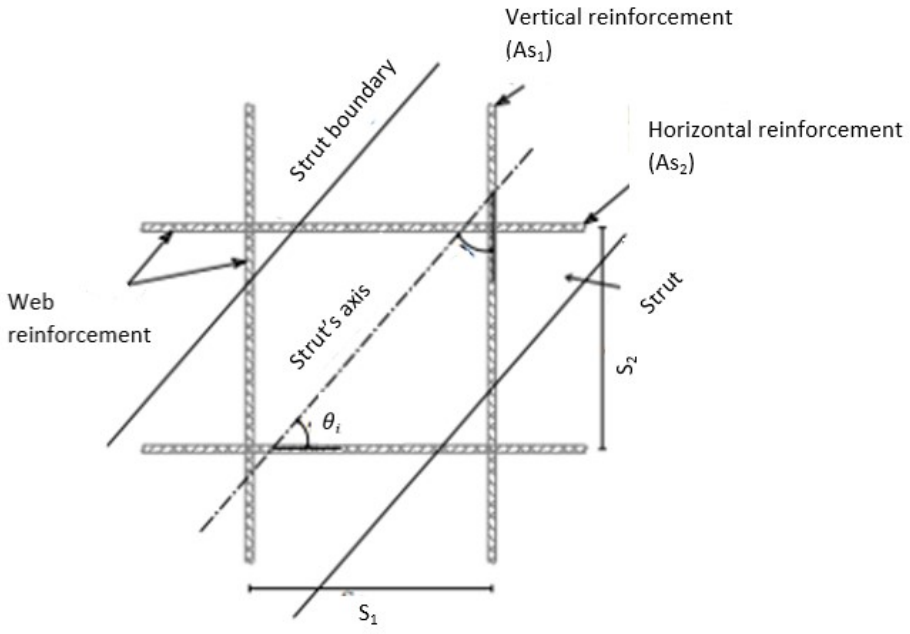

Figure 2.30 Web reinforcement crossing the compressive strut (ACI 318, 2011)

In addition, ACI 318 (2011) specifies a limit on the allowable compressive stress at the nodal zones. The design provisions stated that the nominal force in the nodal zone can be estimated as $F_{nn} = f_{ce}\, A_{nz}$; where A_{nz} is the area of the nodal face.

The effective compressive stress, f_{ce}, on a face of a nodal zone due to the strut-and-tie forces can be expressed as:

$$f_{ce} = 0.85\, \beta_n\, f_c' \qquad (2\text{-}14)$$

The code specifies the values of the nodal efficiency factor β_n to be taken as 1.0 for CCC nodes and 0.8 for CCT nodes.

If deep beams contain no web reinforcement to resist the transverse tensile force caused by the spreading of the compression force in the strut, then the strut efficiency factor β_{st} shall be taken as 0.6 λ, where λ is taken equal to 1.0 for normal-weight concrete.

Mohamed et al. (2016) examined the accuracy of ACI 318 (ACI 2011) provisions in predicting the shear capacity of FRP-reinforced deep beams using a database of 28 deep beams reinforced longitudinally with FRP bars and without web reinforcement. The data was collected from the experimental studies published by Farghaly and Benmokrane (2013), Andermatt and Lubell (2013) and Mohamed et al. (2016). The shear capacity predictions using the STM in ACI 318 (2011) were overestimated since the STM neglects the effect of concrete softening in the diagonal strut due to high strains in the FRP longitudinal reinforcement.

2.11 Concluding Remarks

The analysis of the published research studies on the bond behaviour of the DE technique revealed various gaps that need to be addressed in future studies as follows:

- The impact of DE FRP bar diameter, surface coating and embedded length was investigated in particular for carbon-FRP bars, but not sufficiently for glass-FRP bars.
- The impact of surface treatment on the bond properties was investigated only for smooth and sand-coated FRP bars, but not for ribbed FRP bars.
- In order to control the bonded length during casting, plastic tubes can be used as an alternative for the post-drilling procedure.

- The effect of the concrete strength was not examined adequately, and additional bond tests need to be performed with concrete strength varying between 25 to 60 MPa. These bond test results can be used to provide a more accurate bond-slip model that can address sufficiently the bond behaviour at the DE FRP bar-to-concrete interface.

The published experimental studies on the shear behaviour of RC beams strengthened in shear with DE bars documented the influence of DE bar type, DE bar diameter and strengthening ratio and presence of existing steel stirrups on the shear contribution by DE FRP bars. However, various gaps that need to be addressed in future studies are listed as follows:

- There is limited experimental data available which addresses the influence of the concrete strength, the shear span-to-effective depth, the longitudinal steel reinforcement ratio, scale effect, effective depth and existing level of pre-cracking of RC beams on the shear capacity and the strain experienced by the transverse shear and DE reinforcement.
- Most of the tested DE-strengthened RC beams had a shear span to effective depth (a/d) ratio greater than 2.5, thus there is lack of a rationale behind the shear behaviour and impact of the mentioned parameters for RC deep beams with a/d <2.5.
- The analysis performed in this study identified the impact of the a/d ratio, the effective depth of the beam and the potential interaction between the DE bars and the internal longitudinal reinforcement on the shear gain of DE bars. However, further experimental and parametric studies need to be performed to confirm such correlation for both deep and slender RC beams since the variables often varied simultaneously. The results should aim to explain the distinct load-deformation behaviour of slender and deep RC beams, their modes of failure and experienced strain.

- Neither finite element (FE) models nor design models have been developed for predicting the shear strength contribution due to embedded FRP bars in concrete deep beams. As far as can be ascertained, previous FE studies and existing design guidelines for predicting the shear strength contribution due to DE FRP bars in slender RC beams are not fully developed. To date, there are only three design procedures available for shear strengthening of RC slender beams with DE technique.
- Additional numerical and analytical studies must be conducted to improve the current STMs in the shear design provisions of ACI 318 (2011) and CSA S806 (2012) for deep beams and develop a new expression for the contribution to the shear resistance by DE FRP bars.

CHAPTER 3

BOND PERFORMANCE OF DEEP EMBEDMENT FRP BARS EPOXY-BONDED INTO CONCRETE

This chapter has been published as a peer-reviewed article in:

Caro, M., Yemaa, Y., Dirar, S. and Quinn, A. (2017) Bond Performance of Deep Embedment FRP Bars Epoxy-Bonded into Concrete. **Engineering Structures**, 147: 448-457.

3.1 Introduction

With increasing numbers of strength-deficient concrete infrastructure assets, strengthening and repair of concrete structures is becoming an issue of international importance. Understanding the FRP-to-concrete bond behaviour is crucial to the safe implementation of the DE shear strengthening technique. This chapter examines the bond behaviour of deep embedment (DE) glass fibre reinforced polymer (GFRP) and carbon FRP (CFRP) bars embedded into concrete prisms using an epoxy adhesive.

Pull-out testing has been commonly adopted as a practical approach to assessing the bond performance for both steel and FRP bars embedded in concrete. The bond behaviour of DE FRP bars is not fully understood. This is reflected in the lack of mathematical models for the bond strength of DE FRP bars. Moreover, except for embedment length, the effect of the main parameters influencing the bond behaviour has so far been limitedly considered. This study examines the effect of embedment length, bar type and diameter, concrete compressive strength and hole diameter on the bond behaviour of DE FRP bars. For the first time, this

study presents a mathematical model for predicting the bond strength of DE FRP bars. The mathematical model was validated against experimental results and demonstrated to produce accurate predictions. It is envisaged that both the mathematical model and the experimental results will contribute to the development of future design guidelines for DE concrete shear strengthening.

3.2 Experimental Programme

The experimental programme is based on the recommendations of CSA S806 (2007) as well as the experimental pull-out test studies performed by Valerio et al. (2009) and Godat et al. (2012). A total of eighteen concrete cube specimens with embedded GFRP or CFRP bars were tested as reported in Table 3.2. The effect of embedment length, bar type and diameter, concrete strength and adhesive quantity on the bond behaviour of the bars was examined. The following sections provide details of the material properties, test specimens, installation of FRP bars and pull-out test setup.

3.2.1 Materials

Two concrete mixes were used. The concrete mixes were designed according to the BRE (1997) guidelines (Teychenné et al., 1997) (refer to Appendix A). Portland cement (Class 32.5) and aggregates with a maximum size of 10 mm were used in both concrete mixes. Two batches were used to cast the pull-out specimens with lower concrete strength whereas one batch was used to cast the pull-out specimens with higher concrete strength. Each batch was used to cast six concrete cubes (200 mm × 200 mm × 200 mm) and seven ancillary control specimens (four cubes (100 mm × 100 mm × 100 mm) and three cylinders (100 mm diameter × 200 mm height)). The control specimens were used to characterise the concrete compressive strength (refer to Appendix A). The average cylinder compressive strength for each batch on the day of pull-out

testing was 26.1 MPa (referred to as C26), 24.8 MPa (referred to as C25) and 45.6 MPa (referred to as C46).

Two types of sand-coated FRP bars (CFRP and GFRP) were used in this study. The sand-coated FRP bars had diameters of either 10 mm or 12 mm. The GFRP bars had an elastic modulus, tensile strength and ultimate strain of 40 GPa, 973 MPa and 2.43 %, respectively, as declared by the manufacturer. The CFRP bars had an elastic modulus, tensile strength and ultimate strain of 130 GPa, 2300 MPa and 1.76 %, respectively, as declared by the manufacturer and reported in Table 3.1.

A commercially available high viscosity epoxy resin (Hilti 500) was used to bond the DE FRP bars to the concrete. This epoxy resin had a compressive strength, compressive modulus, tensile strength, bond strength and ultimate strain at failure of 82.7 MPa, 1493 MPa, 43.5 MPa, 12.4 MPa and 2%, respectively, as certified by the manufacturer and reported in Table 3.1.

Table 3.1 Mechanical properties of concrete, FRP bars and epoxy resin

Material	Elastic modulus (MPa)	Compressive strength (MPa)	Tensile strength (MPa)	Ultimate strain (%)	Bond strength (MPa)
Concrete (C26)	-	26.1	-	-	-
Concrete (C25)	-	24.8	-	-	-
Concrete (C46)	-	45.6			
Ø10 and Ø12 mm CFRP bars	130,000	-	2300	1.76	-
Ø10 and Ø12 mm GFRP bars	40,000	-	973	2.43	-
Hilti 500 Epoxy	1493	-	43.5	2	12.4

3.2.2 Test Specimens

Table 3.2 provides a summary of the pull-out test specimens. Each specimen had a four-part designation. The first part (C25, C26 or C46) specifies the concrete cylinder compressive strength. The second part identifies the embedded length of the FRP bar ($5d_b$, $10d_b$ or $15d_b$ where d_b is the nominal bar diameter). The third part denotes the FRP bar type and diameter (CFRP 10/12 or GFRP 10/12). The last part represents the hole diameter (either $1.5d_b$ or $1.8d_b$). Hence C26-$15d_b$-CFRP12-$1.5d_b$ refers to a specimen with a concrete cylinder compressive strength of 26.1 MPa, embedment length of $15d_b$ (180 mm), 12 mm diameter CFRP bar and a central hole with a diameter of $1.5d_b$ (18 mm).

Table 3.2 Bond test specimens

Specimen	Concrete compressive strength (MPa)	Bar type	Bar diameter (mm)	Embedded length (mm)	Hole diameter (mm)
C26-$15d_b$-CFRP12-$1.5d_b$	26.1	CFRP	12	180 ($15d_b$)	18 ($1.5d_b$)
C26-$15d_b$-GFRP12-$1.5d_b$ [1]	26.1	GFRP	12	180 ($15d_b$)	18 ($1.5d_b$)
C26-$15d_b$-GFRP12-$1.5d_b$ [1]	26.1	GFRP	12	180 ($15d_b$)	18 ($1.5d_b$)
C26-$15d_b$-GFRP10-$1.5d_b$	26.1	GFRP	10	150 ($15d_b$)	15 ($1.5d_b$)
C26-$15d_b$-GFRP10-$1.8d_b$	26.1	GFRP	10	150 ($15d_b$)	18 ($1.8d_b$)
C26-$15d_b$-CFRP10-$1.5d_b$	26.1	CFRP	10	150 ($15d_b$)	15 ($1.5d_b$)
C25-$10d_b$-GFRP12-$1.5d_b$	24.8	GFRP	12	120 ($10d_b$)	18 ($1.5d_b$)
C25-$10d_b$-CFRP12-$1.5d_b$	24.8	CFRP	12	120 ($10d_b$)	18 ($1.5d_b$)
C25-$5d_b$-GFRP12-$1.5d_b$ [2]	24.8	GFRP	12	60 ($5d_b$)	18 ($1.5d_b$)
C25-$5d_b$-GFRP12-$1.5d_b$ [2]	24.8	GFRP	12	60 ($5d_b$)	18 ($1.5d_b$)
C25-$5d_b$-CFRP12-$1.5d_b$ [3]	24.8	CFRP	12	60 ($5d_b$)	18 ($1.5d_b$)
C25-$5d_b$-CFRP12-$1.5d_b$ [3]	24.8	CFRP	12	60 ($5d_b$)	18 ($1.5d_b$)
C46-$15d_b$-GFRP10-$1.5d_b$	45.6	GFRP	10	150 ($15d_b$)	15 ($1.5d_b$)
C46-$15d_b$-CFRP10-$1.5d_b$	45.6	CFRP	10	150 ($15d_b$)	15 ($1.5d_b$)
C46-$10d_b$-GFRP10-$1.5d_b$	45.6	GFRP	10	100 ($10d_b$)	15 ($1.5d_b$)
C46-$10d_b$-CFRP10-$1.5d_b$	45.6	CFRP	10	100 ($10d_b$)	15 ($1.5d_b$)
C46-$5d_b$-GFRP10-$1.5d_b$	45.6	GFRP	10	50 ($5d_b$)	15 ($1.5d_b$)
C46-$5d_b$-CFRP10-$1.5d_b$	45.6	CFRP	10	50 ($5d_b$)	15 ($1.5d_b$)

[1,2,3] Repeated specimens

3.2.3 Installation of FRP Bars

In order to install the CFRP and GFRP bars, vertical holes were cast along the centrelines of the 200 mm concrete cubes using polyvinyl chloride (PVC) rods with diameters of either 15 mm or 18 mm (diameter = epoxy thickness + d_b). The PVC rods were positioned vertically at the centres of the moulds prior to concrete casting. To control the embedded length of the FRP bar in a given pull-out specimen, a square (40 mm × 40 mm) polystyrene block with a central hole equal to the PVC rod diameter acted as a cast-in-concrete bond breaker (see Figure 3.1a). The polystyrene block was glued with waterproof silicon around the PVC rod. The lengths of the polystyrene blocks varied from 10 to 130 mm depending on the required value of the embedded length. This approach was selected for simplicity and also to prevent any cracking or local damage that may occur if a drilling machine was used. It should be noted that drilling would probably provide a rougher hole surface and consequently improve the bond between the FRP bars and the concrete. Two wood pieces (length=280 mm, width=40 mm, thickness=20 mm) were glued and drilled in the middle with a hole diameter same as that of PVC rod and bolted at the edges of the moulds by M20 bolts (see Figure 3.1b). These wood pieces were used to ensure that the PVC rods were rigidly kept in a vertical position during the vibrating process of the moulds filled with concrete. Before every stage of casting, a thin film of oil was applied inside the edges of the plastic moulds to ensure sufficient water tightness. Grease was applied as well around the PVC rod and mould to make easier the removal of the PVC rods and de-moulding of concrete cubes with pressurised air applied with a high-pressure air gun.

During each stage of casting, six concrete cubes of 200 x 200 mm (see Figure 3.2a), four control concrete cubes (100 x 100 mm) and three control concrete cylinders (diameter = 100 mm and height =200 mm) were produced (see Figure 3.2b). These control specimens were

produced from the same concrete batch to estimate the average concrete compressive strengths. Steel moulds were used for casting these control specimens as displayed in Figure 3.2b. A thin layer of oil was applied to all sides of the steel moulds before casting to ensure water tightness and easy de-moulding.

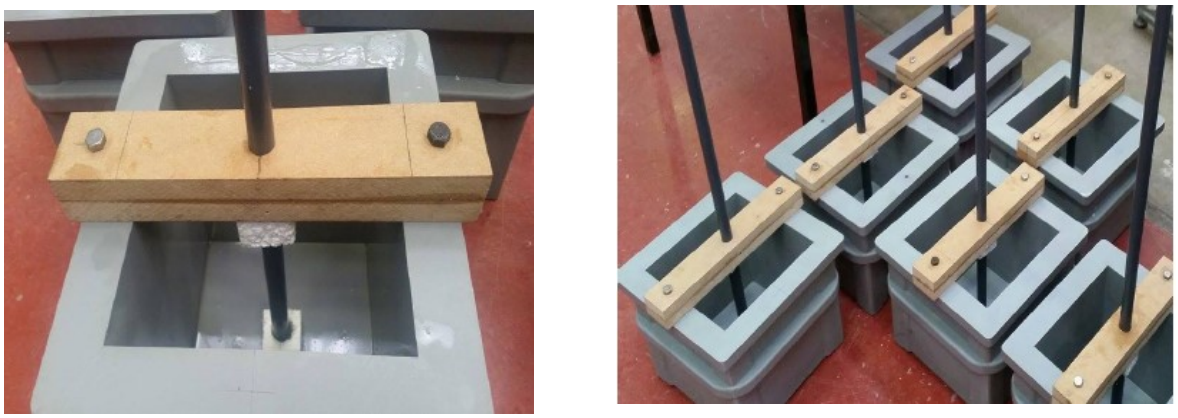

(a) (b)

Figure 3.1 Installation of PVC rods in the plastic moulds prior to concrete casting: (a) cast-in-concrete bond breaker and (b) vertical positioning of PVC rods

(a) (b)

Figure 3.2 Casting of concrete: (a) pull-out concrete cubes and (b) control specimens (cubes and cylinders)

Two up to three layers of fresh concrete with equal thickness were placed inside the plastic moulds and steel cubic and cylindrical moulds. Each layer was then vibrated for a few seconds on the vibrating table as shown in Figure 3.3.

Figure 3.3 Pull-out concrete cubes and control specimens on the vibrating table

Meanwhile, a slump test as shown in Figure 3.4 was also performed to check the workability of the fresh concrete and to ensure that a true slump was achieved between 60-180 mm.

Figure 3.4 Slump test

A careful precaution was given during the vibrating process of the plastic moulds to ensure that the wood frame on their top was holding the PVC rod vertically with no disturbance. The surface of each specimen was levelled and trowel finish to prevent any voids, cracks or geometric irregularities and create a smooth surface. All specimens in the moulds were then covered with nylon sheet and were left overnight. De-moulding of all the concrete specimens and the removal of the PVC rods were carried out 24 hours after casting. Following de-moulding, the concrete specimens were marked and cured at room temperature (about 20^0 C) for at least 28 days (see Figure 3.5).

(a) (b)

Figure 3.5 Pull-out concrete cubes and control specimens: (a) after de-moulding and (b) after 28-day air curing

Before installing the FRP bars, a wire brush was used to roughen the internal surfaces of the holes. This was followed by using compressed air to clean the holes from any cement and aggregate residues. The bottom ends of the holes were blocked to prevent leakage and high viscosity epoxy resin (Hilti 500) was used to fill two-thirds of the holes. A thin layer of epoxy

was also applied along the embedded lengths of the FRP bars and then the bars were twisted as they were being inserted vertically into the holes. This step was deemed necessary in order to ensure that no air pockets were formed or left inside the holes. The excess epoxy was removed from the top surfaces of the holes. The specimens were then cured for a week at room temperature (about 20^0 C) before testing. Of note is that, this installation technique was used by Jemaa et al. (2015) to strengthen large-scale deficient RC beams using GFRP bars and epoxy adhesive similar to those reported in this study. The technique resulted in 96 % shear strength enhancement and GFRP strain of up to 0.91%.

3.2.4 Test Setup

Figure 3.6 illustrates the pull-out test setup. The FRP bars were cut into 700 mm lengths to meet the recommendations of Godat et al. (2012) and to ensure that the test specimens fitted properly within the testing machine. The concrete cube, together with the DE FRP bar, was placed inside a steel box as shown in Figure 3.6. To ensure that the FRP bar remained undamaged during testing, a 310 mm long hollow steel tube with 42 mm external diameter and 4.8 mm wall thickness was bonded to the upper end of the FRP bar using Hilti 500 epoxy resin. The steel tube surrounding the FRP bar was then gripped by the testing machine.

Linear variable differential transducers (LVDTs) were mounted on a PVC rig to measure the slip between the FRP bar and the concrete cube at the loaded end. A displacement-controlled testing machine was used to apply the pull-out force at a rate of 0.03 mm/s. This arrangement is similar to that used by Godat et al. (2012).

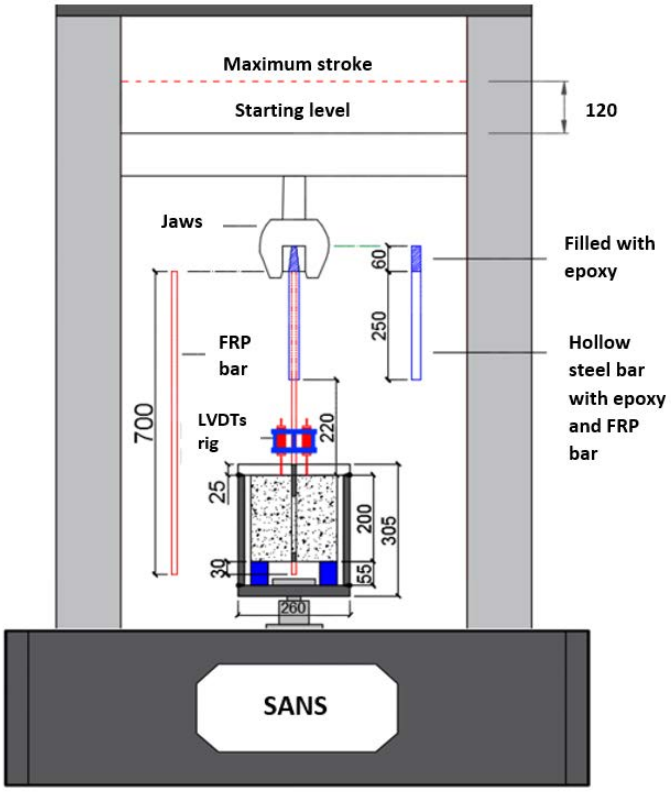

(a)

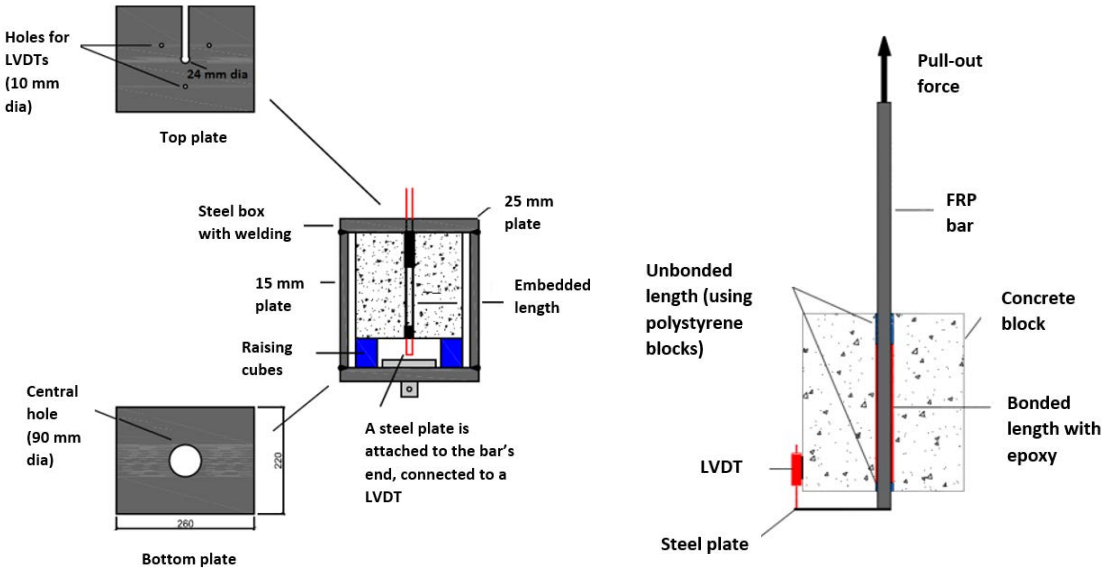

(b) (c)

Figure 3.6 Test details (all dimensions in mm): (a) test setup, (b) steel box and (c) test Specimen

3.3 Experimental Results

Table 3.3 gives the peak pull-out force (i.e. pull-out capacity), maximum average bond stress, slip at peak pull-out force and failure mode for each tested specimen. Based on ACI 440.1R (2006), the average bond stress (τ) is given by:

$$\tau_b = \frac{P_t}{\pi\, d_b\, l_b} \tag{3-1}$$

where P_t is the pull-out force, d_b is the bar diameter and l_b is the embedded length of the bar. Equation (3-1) assumes the average bond stress to be constant along the embedded length. Although this assumption is not fully accurate due to the non-uniform variation of bond stresses along the embedded length (Godat et al., 2012; Tepfers and De Lorenzis, 2003; Baena et al., 2009), the concept of average bond stress is used in this study as it facilitates comparison of results.

Table 3.3 Pull-out test results

Specimen	Peak pull-out force (kN)	Maximum average bond stress (MPa)	Slip at peak pull-out force (mm)	Failure mode
C26-15d_b-CFRP12-1.5 d_b	73.3	10.8	3.2	Concrete splitting
C26-15d_b-GFRP12-1.5d_b [1]	61.9	9.1	3.2	Bar rupture
C26-15d_b-GFRP12-1.5d_b [1]	48.8	7.2	2.3	Bar rupture
C26-15d_b-GFRP10-1.5d_b	58.2	12.4	3.7	Bar rupture
C26-15d_b-GFRP10-1.8d_b	54.7	11.6	5.5	Bar rupture
C26-15d_b-CFRP10-1.5d_b	56.2	11.9	1.6	Bar pull-out
C25-10d_b-GFRP12-1.5d_b	36.3	8.0	1.9	Bar pull-out
C25-10d_b-CFRP12-1.5d_b	49.6	11.0	1.5	Bar pull-out
C25-5d_b-GFRP12-1.5d_b [2]	22.8	10.1	1.4	Bar pull-out
C25-5d_b-GFRP12-1.5d_b [2]	27.1	12.0	2.1	Bar pull-out
C25-5d_b-CFRP12-1.5d_b [3]	31.6	14.0	1.0	Bar pull-out
C25-5d_b-CFRP12-1.5d_b [3]	30.1	13.3	1.2	Bar pull-out
C46-15d_b-GFRP10-1.5d_b	61.2	13.0	4.7	Bar rupture
C46-15d_b-CFRP10-1.5d_b	74.8	15.9	2.2	Bar pull-out
C46-10d_b-GFRP10-1.5d_b	40.4	12.9	2.8	Bar pull-out
C46-10d_b-CFRP10-1.5d_b	43.5	13.8	1.2	Bar pull-out
C46-5d_b-GFRP10-1.5d_b	21.6	13.8	1.7	Bar pull-out
C46-5d_b-CFRP10-1.5d_b	21.1	13.4	1.1	Bar pull-out

[1,2,3] Repeated specimens	Peak pull-out force (kN)	Maximum average bond stress (MPa)		
Average (AVG)	37.05	10.95		
Coeffiecient of variation (COV)	0.407	0.291		

3.3.1 Failure Modes

One specimen, C26-15d_b-CFRP12-1.5d_b, failed due to concrete splitting. This failure mode involved a crack plane that crossed the central hole and split the concrete cube into two parts (see Figure 3.7a). This failure mode was sudden and brittle due to the tensile failure of the concrete. Except for C26-15d_b-CFRP10-1.5d_b and C46-15d_b-CFRP10-1.5d_b, the mode of failure for the remaining specimens with an embedded length of 15d_b was bar rupture (see Figure 3.7b). The FRP bars remained well attached to the concrete cubes, with no visible cracks, until the end of testing. C26-15d_b-CFRP10-1.5d_b, C46-15d_b-CFRP10-1.5d_b and the specimens with shorter embedded lengths (5d_b and 10d_b) experienced pull-out at the adhesive/concrete interface (see Figure 3.7c).

(a)

(b) (c)

Figure 3.7 Failure modes: (a) concrete splitting, (b) bar rupture and (c) bar pull-out

A thin adhesive layer was attached to the FRP bars at failure. These results confirm previous findings (Valerio et al., 2009; Godat et al., 2012) suggesting that the increase in embedment length eventually leads to tensile failure of the bar.

Three sets of specimens were tested twice to examine repeatability of the results. The first set of specimens, C26-15d_b-GFRP12-1.5d_b, failed due to rupture of the GFRP bar (see Figure 3.7b). The difference in pull-out force at failure was 13.1 kN (21.2%) and might be attributable to unintended bending effects. The second set of duplicate specimens, C25-5d_b-GFRP12-1.5d_b, failed due to bar pull-out (slip) at the adhesive/concrete interface. The difference in peak pull-out force and maximum average bond stress were 4.3 kN (15.9%) and 1.9 MPa (15.9%), respectively. The third set of duplicate specimens, C25-5d_b-CFRP12-1.5d_b, experienced bar pull-out without developing cracks in the concrete (see Figure 3.7c). The difference in peak pull-out force and maximum average bond stress were 1.5 kN (4.8%) and

0.7 MPa (4.8%), respectively. Of note is that, each set of duplicate specimens had comparable initial stiffness values.

Specimen C46-15d_b-CFRP10-1.5d_b is comparable to specimen C2-1.5d-9.5S-15d tested by Godat et al. (2012). The former specimen, which had cast-in-concrete holes, failed due to bar pull-out at a force of 74.8 kN whereas the latter specimen, which had drilled holes, failed due to bar pull-out at a force of 91.2 kN. This result suggests that the bond strength of the specimens with cast-in-concrete holes is about 82% of that of the specimens with drilled holes.

3.3.2 Stiffness of the Bond-Slip Curves

Figures 3.8a and 3.8b illustrate the pull-out force-slip and average bond stress-slip curves for the specimens with 12 mm FRP bars, respectively. The corresponding curves for the specimens with 10 mm FRP bars are presented in Figures 3.9a and 3.9b, respectively. It should be noted that both Figures 3.8 and 3.9 give the global bond behaviour which is characterised by the pull-out force (or average bond stress) and the slip at the loaded end. On the other hand, the local bond behaviour defines the FRP/concrete interaction at a sectional level and is characterised by the interfacial bond stress at a given section and the corresponding interfacial slip at the same section. The global behaviour can, therefore, be thought of as summing up the local response along the bonded length. Two types of behaviour can be seen in Figures 3.8 and 3.9. The majority of specimens that experienced pull-out failure had a behaviour that is characterised by an initial, almost linear, increase in the pull-out force or average bond stress with slip (ascending branch), followed by a gradually descending branch once the maximum pull-out force or average bond stress is achieved. On the other hand, the specimens that failed due to bar rupture had a similar initial

response to those specimens which failed due to pull-out. However, there was a sudden drop at the peak load caused by the brittle failure of the FRP bars.

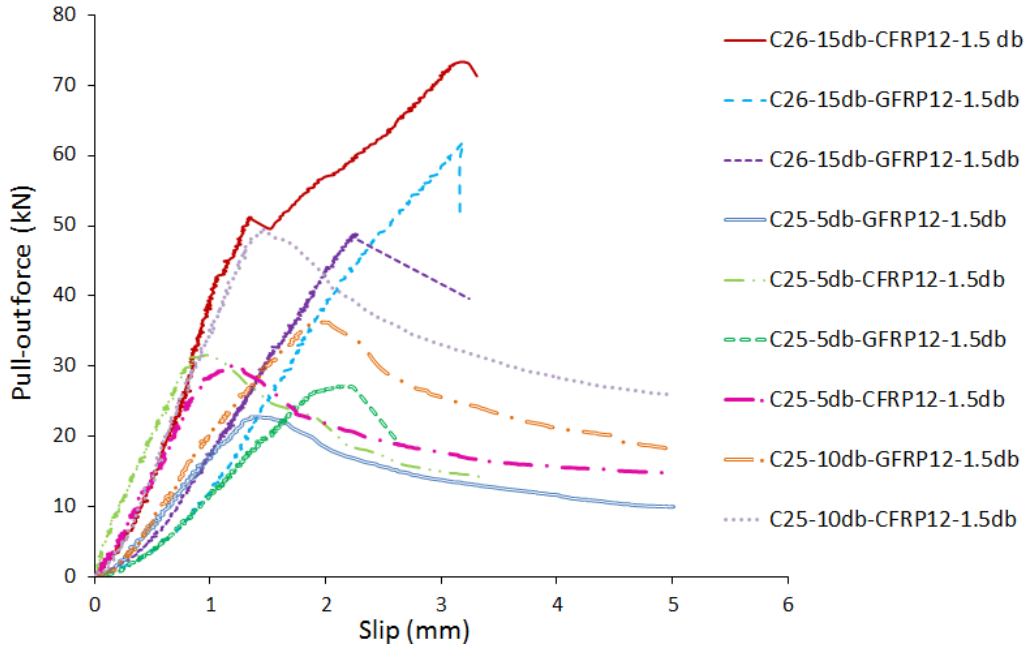

(a)

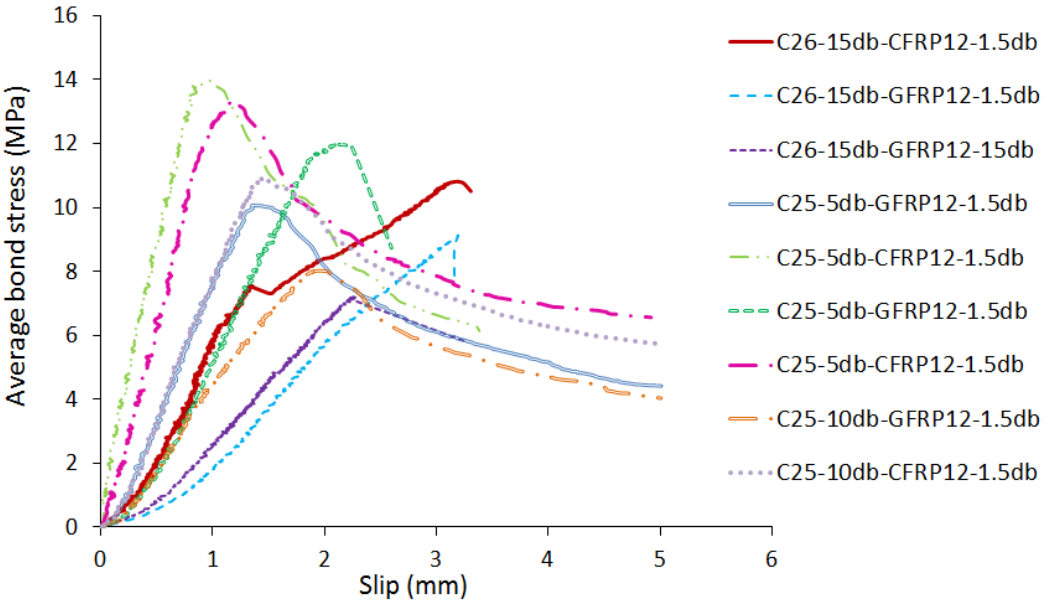

(b)

Figure 3.8 Bond-slip curves for the specimens with 12 mm FRP bars: (a) pull-out force-slip curves and (b) average bond stress-slip curves

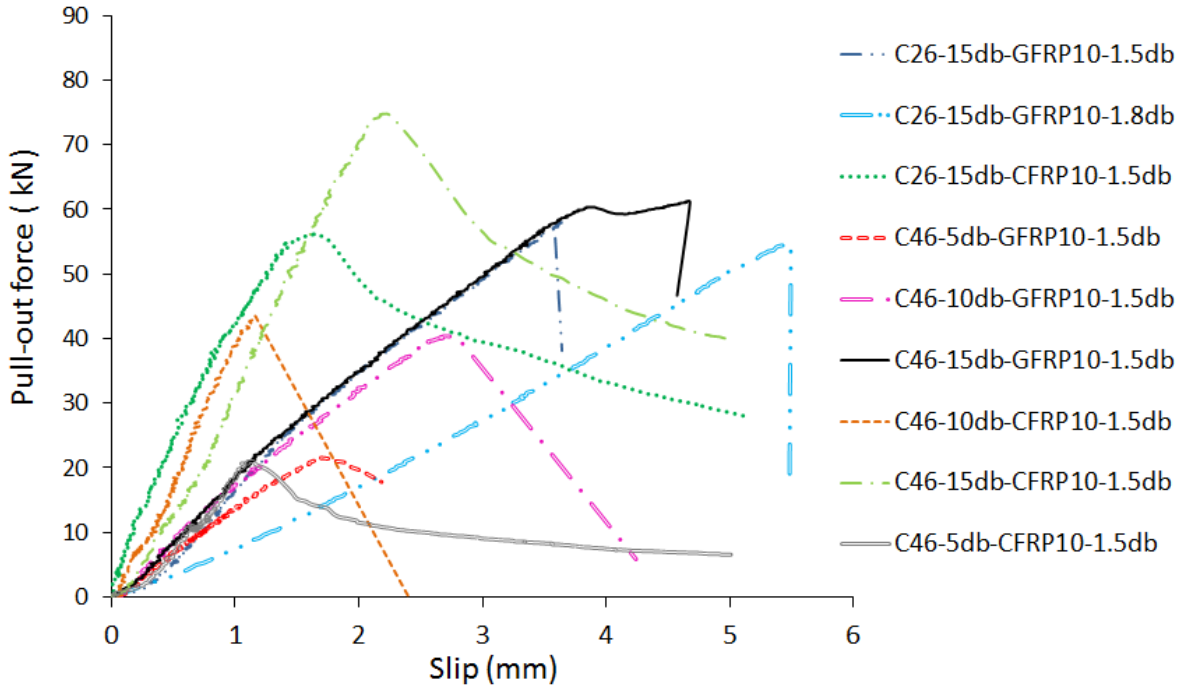

(a)

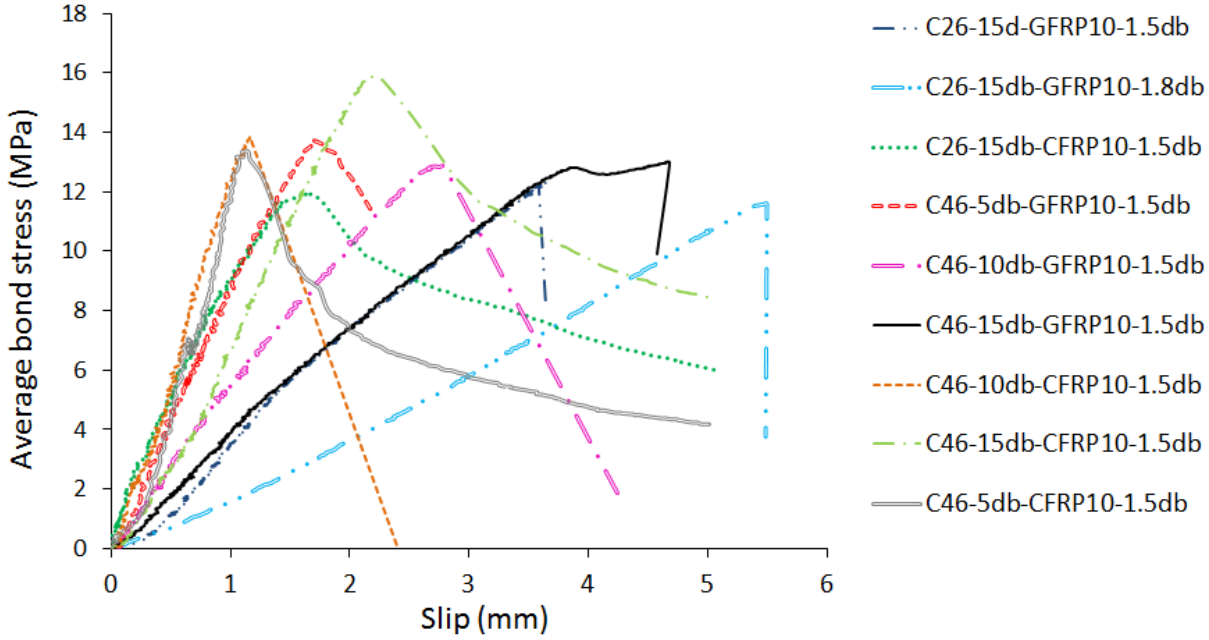

(b)

Figure 3.9 Bond-slip curves for the specimens with 10 mm FRP bars: (a) pull-out force-slip curves and (b) average bond stress-slip curves

The effect of embedded length on the initial stiffness (i.e. the stiffness of the ascending branch) of the pull-out force-slip curves is unclear. However, Figures 3.8b and 3.9b clearly show that as the embedment length increased from $5d_b$ to $15d_b$, the initial stiffness of the average bond stress-slip curves was reduced. As a result, the slip values corresponding to the maximum average bond stresses increased with increasing the embedded length for both bar types. The highest slip values corresponding to the maximum average bond stresses were obtained by the FRP bars with an embedment length of $15d_b$.

As can be observed in Figures 3.8 and 3.9, the specimens with CFRP bars had higher initial stiffness than the corresponding specimens with GFRP bars. The higher stiffness for the specimens with CFRP bars was to be expected as the elastic modulus of the CFRP bars is higher than that of the GFRP bars. As a result, the slip values corresponding to the peak pull-out forces (see Figures 3.8a and 3.9a) and maximum average bond stresses (see Figures 3.8b and 3.9b) were lower for the specimens with CFRP bars; while the maximum bond stresses were higher for these specimens confirming a better bond performance.

The concrete compressive strength did not have a significant impact on the initial stiffness of the specimens with GFRP bars. As can be seen in Figures 3.8a and 3.8b, C26-$15d_b$-GFRP10-$1.5d_b$ and C46-$15d_b$-GFRP10-$1.5d_b$, which differed in concrete strength only, had approximately equal initial stiffness. C26-$15d_b$-CFRP10-$1.5d_b$ had higher initial stiffness than that of C46-$15d_b$-CFRP10-$1.5d_b$ although the latter specimen had higher concrete compressive strength. Premature cracking (e.g. due to shrinkage) could have resulted in the lower stiffness of C46-$15d_b$-CFRP10-$1.5d_b$. Further testing is required to confirm this result.

The increase in hole diameter from $1.5d_b$ to $1.8d_b$ resulted in a reduction in the initial stiffness of C26-$15d_b$-GFRP10-$1.8d_b$ compared to that of C26-$15d_b$-GFRP10-$1.5d_b$ (see Figures 3.9a and 3.9b). C26-$15d_b$-GFRP10-$1.8d_b$ had the lowest initial stiffness suggesting

that the combination of GFRP bars and a higher quantity of adhesive (i.e. larger hole diameter) has a detrimental effect on stiffness. Yet, the mode of failure was not affected by the increase in the quantity of adhesive as both specimens experienced rupture of the GFRP bars.

3.3.3 Effect of Embedment Length

Table 3.2 shows that the pull-out capacity increased with the increase in embedded length. An increase of two times (from $5d_b$ to $10d_b$) in the embedded length led to increases of 46% and 61% in the pull-out capacity of the 12 mm GFRP and CFRP specimens with a concrete compressive strength of 24.8 MPa, respectively. The corresponding increases for the specimens with a concrete compressive strength of 45.6 MPa and 10 mm GFRP or CFRP bars were 87% and 106%, respectively.

Figure 3.10 combines the results of this study with the results of Valerio et al. (2009) and Godat et al. (2012). Except for the few pull-out specimens with a concrete compressive strength of 45.6 MPa, Figure 3.10 shows that the maximum average bond stress generally decreased with the increase in embedded length, which is in agreement with Equation (3-1). An increase of two times (from $5d_b$ to $10d_b$) in the embedded length led to decreases of about 28% and 20% in the maximum average bond stresses of the 12 mm GFRP and CFRP specimens with a concrete compressive strength of 24.8 MPa, respectively. This trend is further highlighted by the results of Valerio et al. (2009) and Godat et al. (2012) which show that increases of five and six times, respectively, in the embedded length led to decreases of almost 1.5 and 2 times, respectively, in the maximum average bond stress.

The results of this study combined with those of Valerio et al. (2009) show that, at given embedded length and concrete strength values, the specimens with CFRP bars had generally

higher bond strength values than the corresponding specimens with GFRP bars (see Figure 3.10). This result may be explained by the better bond performance of the CFRP bars which have higher elastic modulus than that of the GFRP bars. Of note is that, Godat et al. (2012) did not test GFRP pull-out specimens.

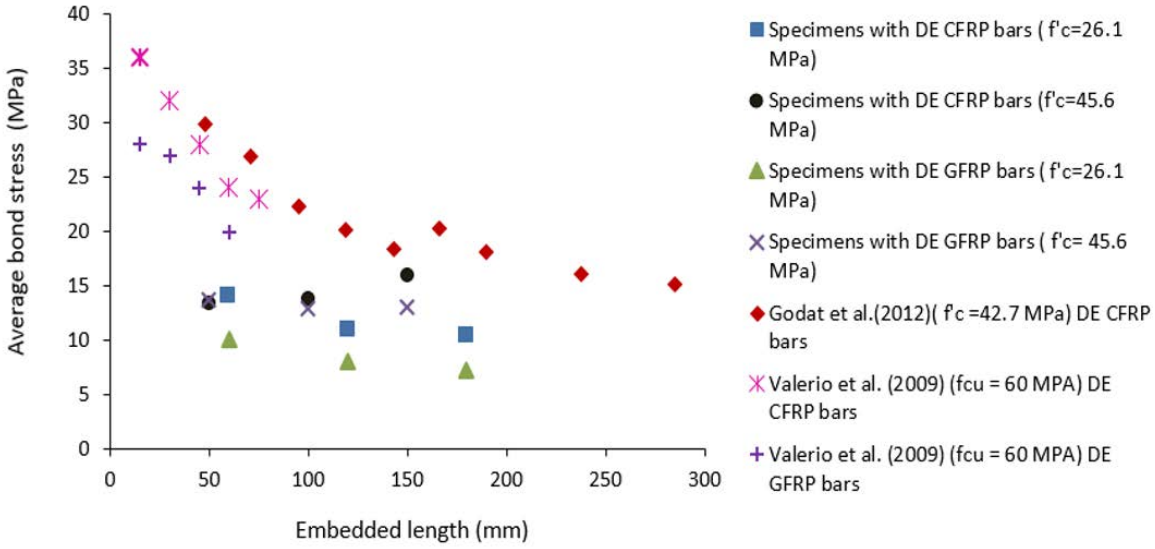

Figure 3.10 Effect of embedment length on maximum average bond stress

3.3.4 Effect of Bar Diameter

The impact of bar diameter on pull-out and bond strengths can be inferred from specimens C26-15d_b-CFRP12-1.5d_b and C26-15d_b-CFRP10-1.5d_b (see Table 3.3). The corresponding specimens with GFRP bars failed due to bar rupture; so both their failure mode and failure loads were not affected by the change in bar diameter. The increase in bar diameter from 10 to 12 mm resulted in a 17.1 kN (30.4%) increase in the pull-out capacity for the tested specimens with DE CFRP bars. For a larger bar diameter, the greater bond area results in a higher pull-out capacity (Godat et al., 2012). In contrast, the maximum average bond stress decreased by 1.1 MPa (9.2%). This decrease may be explained by the higher amount of

elastic energy available when using large diameter bars (Godat et al., 2012; Baena et al., 2009).

3.3.5 Effect of Concrete Compressive Strength

The effect of concrete compressive strength on pull-out capacity and maximum average bond stress can be inferred from specimens C26-15d_b-CFRP10-1.5d_b and C46-15d_b-CFRP10-1.5d_b (see Table 3.3). The corresponding specimens with GFRP bars failed due to bar rupture; so both their failure mode and failure loads were not affected by the change in concrete compressive strength. As the concrete strength increased from 26.1 to 45.6 MPa, the pull-out capacity increased by 18.6 kN (33%). C26-15d_b-CFRP10-1.5d_b and C46-15d_b-CFRP10-1.5d_b had the same bar diameter and embedment length and thus the maximum average bond stress increased by 4 MPa (33%) due to the increase in concrete strength. The pull-out force induces shear stresses along the DE FRP bar. Pull-out (bond) failure occurs when the applied interfacial stresses exceed the resistance of the FRP-to-concrete interface (Tepfers and De Lorenzis, 2003). Increasing the concrete compressive strength increases the resistance of the FRP-to-concrete interface. This, in turn, enhances the bond strength.

3.3.6 Effect of Hole Diameter

The two specimens with different hole diameters (C26-15d_b-GFRP10-1.5d_b and C26-15d_b-GFRP10-1.8d_b) failed due to bar rupture at 58.2 kN and 54.7 kN, respectively. Hence it can only be inferred that the increase in hole diameter from 15 mm to 18 mm affected neither the failure mode nor the tensile capacity of the GFRP bars. Godat et al. (2012) investigated the effect of three different hole diameters (1.25d_b (12 mm), 1.5d_b (15 mm) and 2.0d_b (19 mm)). The three tested specimens failed due to bar pull-out. They reported that increasing the hole diameter from 1.25d_b to 1.5d_b increased the pull-out capacity by 10.8 kN (13.4%) whereas the further increase in hole diameter to 2.0d_b decreased the pull-out capacity by 12.5 kN (13.9%).

They argued that the increase in hole diameter to $1.5d_b$ improved bonding while maintaining a greater confinement whereas the further increase to $2.0d_b$ reduced the effect of confinement. However, this latter effect was not observed for the specimens with DE GFRP bars tested in this study as explained above.

3.4 Mathematical Modelling

Currently, there are no published mathematical models for predicting the bond strength of DE FRP bars. The Concrete Society Technical Report 55 (TR55) (2012) suggests that the bond strength of DE FRP bars may be taken as 15 MPa in the absence of test data. Mofidi et al. (2012) proposed the bond strength values of 21.3 MPa and 8.4 MPa for plain and sand-coated FRP bars, respectively. However, the experimental results clearly demonstrate that the bond behaviour of DE FRP bars is so complex that the bond strength cannot be represented by a single fixed value.

This study proposes a new model for the bond strength of DE FRP bars. The form of the mathematical model chosen is given by:

$$\tau_b = \alpha_b \, f'^{j}_c \, l_b^{\,q} \, d_b^{\,l} \, E_f^{\,r} \, E_p^{\,t} \tag{3-2}$$

where τ_b is the average bond strength; f'_c is the concrete cylinder compressive strength; l_b, d_b and E_f are the embedded length, bar diameter and elastic modulus of the DE FRP bar, respectively; and E_p is the elastic modulus of the adhesive.

The key advantage of the proposed model is that it explicitly takes into account the constituent parameters influencing the bond behaviour, thus permitting variations during the design

process. The role of such a mathematical model is crucial for developing shear strengthening design guidelines.

In the calibration process, data were restricted to experiments where bar pull-out failure occurred. The model was calibrated using a multiple linear regression (refer to Appendix B) on two sets of data (11 experimental tests from this research study and 9 tests by Godat et al. (2012) which suggest parameter values of: $j = 0.31 \pm 0.18$, $q = -0.32 \pm 0.05$, $l = -0.59 \pm 0.59$, $r = 0.23 \pm 0.05$ and $t = 0.52 \pm 0.1$. The suggested value of α_b is exp (–0.52) = 0.59 but the uncertainty of this is large (–0.52 ± 2.4 in the exponent), possibly because of factors (e.g. roughness of the adhesive-to-concrete interface) which have not been included in the model. The large uncertainty of the *l* value is probably related to the small range of diameters and thus contact surface areas considered. Additional tests need to be conducted considering a larger range of bar diameters and other parameters. The proposed model may be written as:

$$\tau_b = 0.59\, f'_c{}^{0.31} l_b{}^{-0.32} d_b{}^{-0.59} E_f{}^{0.23}\, E_p{}^{0.52} \qquad (3\text{-}3)$$

In terms of statistical probability, elastic modulus of the epoxy adhesive, elastic modulus of the bar and embedded length are all highly significant (p-value < 0.001) whereas concrete compressive strength and bar diameter are less significant. The justification for including these parameters in the model is therefore theoretical rather than statistical and further work is required to improve the values associated with these parameters. In addition, as the selected data were restricted only to bar pull-out failure mode, the impact of concrete strength is not significant (or does not play a significant role) as long as the compressive strength of concrete is sufficient to achieve the bond strength between the concrete and DE FRP bar. In comparison between predicted and measured values (see Figure 3.11), the typical error of the proposed model is ± 2% and the standard error is ± 9%.

The proposed model was validated against the results of nineteen pull-out specimens tested by Valerio et al. (2009). These specimens were selected from a larger database of 65 specimens on the basis of bar material, epoxy adhesive and failure mode. Only the specimens with AFRP, GFRP or CFRP bars bonded into concrete using a high viscosity adhesive were deemed adequate for validation purposes. The remaining specimens with steel bars and/or low viscosity adhesive are beyond the scope of the proposed model. It should be noted that a low viscosity adhesive is unsuitable for DE strengthening applications and will negatively impact the bond performance (Godat et al., 2012). The nineteen specimens chosen for validation purposes had embedment lengths ranging from 15 to 75 mm and hole diameters of 1.2 or 1.3 times the bar diameter. All the selected specimens experienced bar pull-out failure mode only.

Figure 3.12 displays the comparison between the predicted and experimental bond strength values for fourteen specimens with CFRP/GFRP bars and five specimens with AFRP bars. It must be noted that for the same bar diameter and embedded length, the experimental bond strength values achieved by CFRP bars were almost twice as those achieved by AFRP bars. This different bond performance of AFRP bars suggests a smaller alpha coefficient (α_b = 0.5 × 0.59 = 0.295) be adopted for the proposed bond strength model (Equation 3-2) which led to more accurate predictions.

It can be seen in Figure 3.12 that the proposed model predicted well the results of Valerio et al. (2009) tests. In comparison between predicted and measured values, the typical error of the proposed model for this data set is ± 2% and the standard error is ± 18%. The predictions were more accurate for CFRP/GFRP bars compared to AFRP bars, but this can be addressed through a change to the alpha value used in the model. Additional tests need to be conducted using AFRP bars to assess the consistency of results and their bond performance.

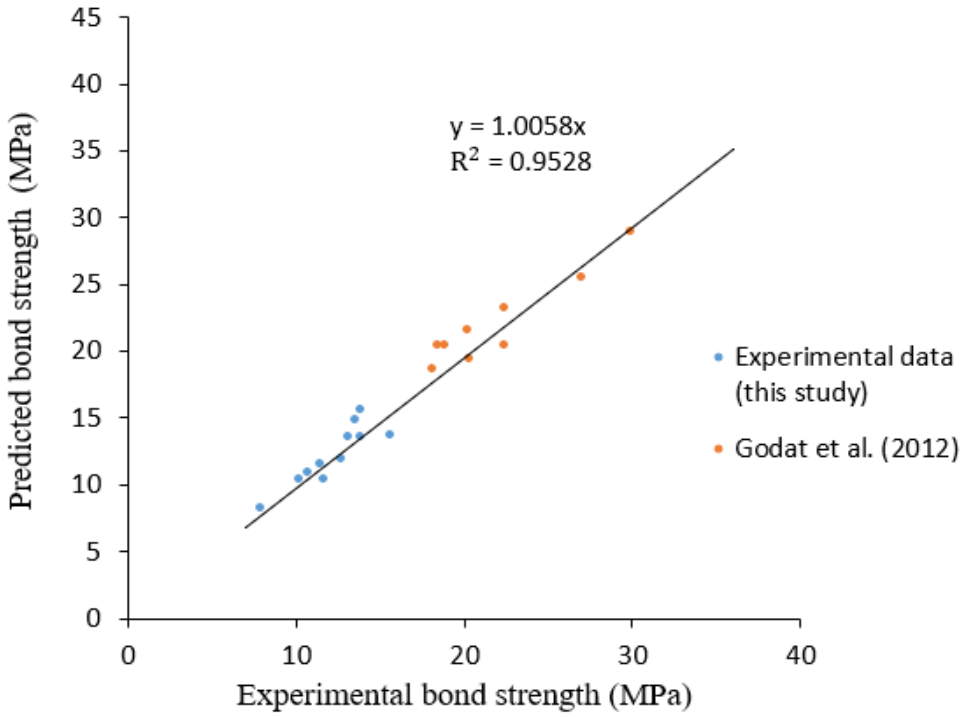

Figure 3.11 Model calibration – comparison between predicted and measured values

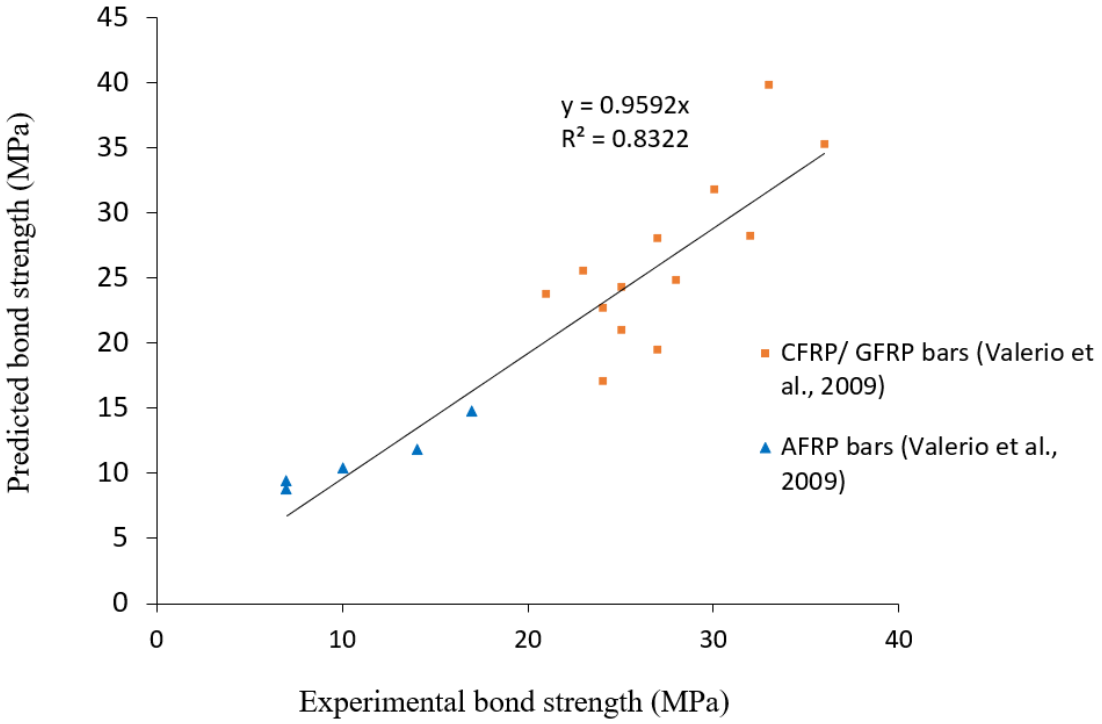

Figure 3.12 Model calibration – comparison between predicted and measured values

3.5 Concluding Remarks

This research study has expanded the experimental results and has provided further insight into the bond performance of DE FRP bars by conducting pull-out tests on both CFRP and GFRP bars epoxy-bonded into 200 mm × 200 mm × 200 mm concrete cubes. The impact of embedment length, bar type and diameter, concrete strength and hole diameter on the bond behaviour was examined. Based on the results of this study, the following conclusions can be made:

- The increase in embedded length enhanced the pull-out capacity but reduced both the maximum average bond stress and the initial stiffness of the bond stress-slip curves. The GFRP bars with embedded lengths of $15d_b$ failed by rupture whereas the GFRP bars with shorter embedded lengths ($5d_b$ and $10d_b$) failed due to bar pull-out. Except for one specimen which failed due to concrete splitting, the CFRP bars failed due to bar pull-out.
- The specimens with CFRP bars had higher pull-out and bond strengths as well as higher initial bond-slip stiffness than the corresponding specimens with GFRP bars. The slip values corresponding to both the peak pull-out forces and the maximum average bond stresses were lower while the average bond stresses were higher for the specimens with CFRP bars, confirming a better bond performance.
- The increase in bar diameter from 10 to 12 mm led to a 30.4% increase in the pull-out capacity and 9.2% decrease in the maximum average bond stress for the specimens with DE CFRP bars. The behaviour of the corresponding specimens with DE GFRP bars was not affected by the change in bar diameter and these specimens failed due to bar rupture.

- The increase in concrete compressive strength from 26.1 to 45.6 MPa increased both the pull-out capacity and the maximum average bond stress for the specimens with DE CFRP bars by about 33%. The concrete compressive strength did not have a significant impact on the initial stiffness, pull-out capacity or failure mode of the specimens with DE GFRP bars.
- The increase in hole diameter from $1.5d_b$ to $1.8d_b$ reduced the initial stiffness of the specimens with DE GFRP bars but affected neither the failure mode (bar rupture) nor the failure loads.
- A new mathematical model was proposed to predict the bond strength of DE FRP bars epoxy-bonded into concrete. The model was validated against experimental results and was demonstrated to produce accurate predictions.

CHAPTER 4

NUMERICAL INVESTIGATION OF REINFORCED CONCRETE BEAMS SHEAR-STRENGTHENED WITH DEEP EMBEDDED BARS

4.1 Introduction

To date, there is only one published experimental study that examines the shear behaviour of RC deep beams shear-strengthened with DE FRP bars. This experimental study was performed by Dirar and Theofanous (2017) and involved testing two series of large-scale reinforced concrete (RC) T-beams which included an un-strengthened (control) deep beam and a DE shear-strengthened beam. As far as can be ascertained, there are no published numerical studies that investigate the shear strength contribution due to DE FRP bars in deep beams. Therefore, the shear behaviour of RC deep beams retrofitted with DE FRP bars is very poorly understood.

This chapter introduces the development and validation of a three-dimensional finite element (FE) model using published experimental results from two series of large-scale RC T-beams shear-strengthened with DE FRP bars. These beams were tested at the University of Birmingham, UK (Dirar and Theofanous, 2017). FE package DIANA version 9.4.6 (DIANA user's manual, 2016) was used for developing the FE models. This software provides extensive constitutive models, element types and advanced nonlinear phased analysis. A comparison was made between the FE predictions and the published experimental results in terms of load-deflection relationships, crack patterns and failure modes. The carefully developed FE model for deep beams was then used to carry out a parametric study. This

chapter provides a thorough analysis of the main parameters that influence shear capacity and govern the shear behaviour of deep beams shear-strengthened with DE FRP bars. A set of FE models was used to numerically examine the impact of shear span-to-effective depth ratio, DE FRP bar type, DE FRP strengthening ratio and interaction between DE FRP bars and steel stirrups on the shear capacity of FE deep beam models. It is envisioned that the FE results of the parametric study will contribute to the reliable application of the DE technique.

4.2 Summary of Experimental Work

Three-dimensional nonlinear models were developed for two sets of large-scale DE-shear strengthened beams tested at the University of Birmingham, UK. The experimental work (Dirar and Theofanous, 2017) was carried out as part of a research programme funded by the Engineering and Physical Sciences Research Council (EPSRC). Four beams failed in shear and one in flexure. Table 4.1 shows the concrete, steel and FRP reinforcement material properties of experimentally tested T-beams.

Table 4.1 Material properties of the tested RC beams

Beam ID	f'_c (MPa)	a/d	Longitudinal reinforcement *Ø25mm steel bars*		Web steel Reinforcement *Ø 8 mm stirrups*			DE FRP Reinforcement *Ø 12 mm DE FRP bar*		
			E_s (GPa)	f_y (MPa)	E_s (GPa)	f_y (MPa)	ρ_v (%)	E_f (GPa)	f_{fu} (MPa)	ρ_f (%)
Set 1- Slender beams										
U/3.0	40	3.0	200	580	200	540	0.112	-	-	-
C/3.0								130	2300	0.377
Set 2 - Deep beams										
U/1.9	40	1.9	200	580	200	540	0.149	-	-	-
C/1.9								130	2300	0.168
G/1.9								40	973	0.168

4.2.1 Details of Test Specimens

The first set consists of two RC T-shaped slender beams U/3.0 and C/3.0.
U/3.0 was the un-strengthened (control) beam reinforced only with steel stirrups whereas C/3.0 was strengthened in shear with DE carbon-FRP bars (see Figure 4.1). The beams had a total length of 4700 mm, a total height of 650 mm, a flange width of 400 mm, a web width of 150 mm and a flange thickness of 125 mm (see Figure 4.3). They had a shear span-to-effective depth (a/d) ratio of 3.0 and were tested in four-point bending with a constant moment region of 500 mm as illustrated in Figure 4.1.

The steel longitudinal reinforcement consisted of four Ø25 (4T25) tension steel bars (A_l =500 mm^2) and four Ø12 (4T12) compression steel bars (A_l =113 mm^2). Each beam had internal steel shear links of 10 mm diameter, spaced at 100 mm above the supports and at 250 mm in the constant moment region (9 shear links in total). Two steel shear links of 8 mm diameter, spaced at 600 mm centre-to-centre (c/c), were used in both shear spans (see Figure 4.1). The strengthened beam, C/3.0, had six 12 mm CFRP rods inserted in each shear span at equal spacing (200 mm) between the steel shear links (see Figure 4.1).

The second set included the three RC deep concrete beams, U/1.9, C/1.9 and G/1.9. The control (U/1.9) and DE shear-strengthened T-shaped deep beams (C/1.9 and G/1.9) had the same cross-section dimensions as the slender beams (see Figure 4.3).

The beams were 2900 mm long and had a shear span-to-effective depth ratio (a/d) of 1.9. They were tested under three-point bending, as illustrated in Figure 4.2. Each beam was reinforced in the longitudinal direction with four Ø25 steel tension bars and four Ø12 compression steel bars. Steel shear links of 10 mm diameter were used above the supports, and under and between the loading point (7 shear links in total). Two steel shear links of 8 mm diameter were located in each shear span at 450 mm spacing (see Figure 4.2). The two

DE shear-strengthened beams were strengthened with 12 mm CFRP or GFRP bars. There were two FRP rods in each shear span inserted in between the steel shear links at an equal spacing of 450 mm (c/c).

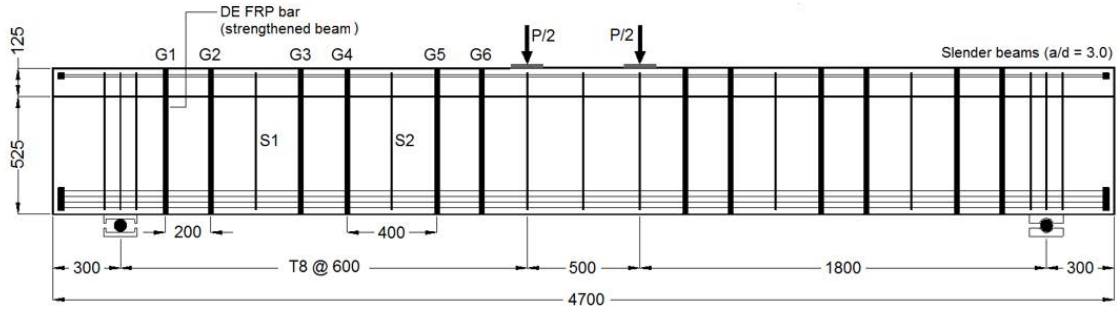

Figure 4.1 Details of the tested CFRP-strengthened slender RC beam C/3.0 (Dirar and Theofanous, 2017)

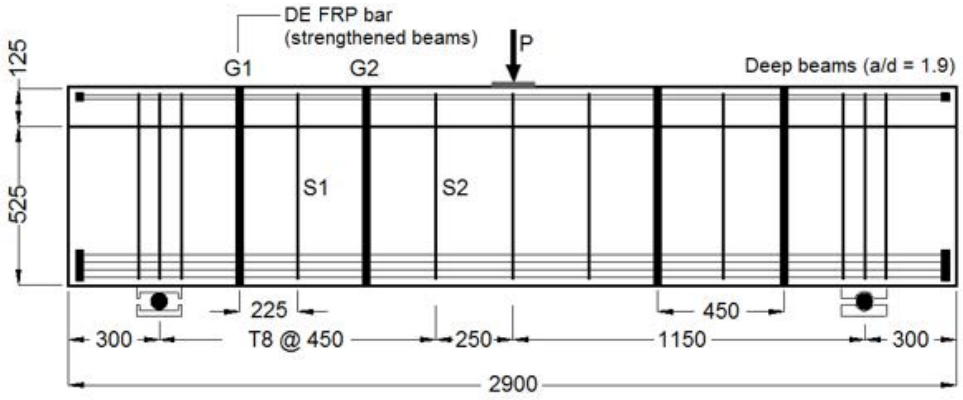

Figure 4.2 Details of the tested CFRP and GFRP-strengthened RC deep beams C/1.9 and G/1.9 (Dirar and Theofanous, 2017)

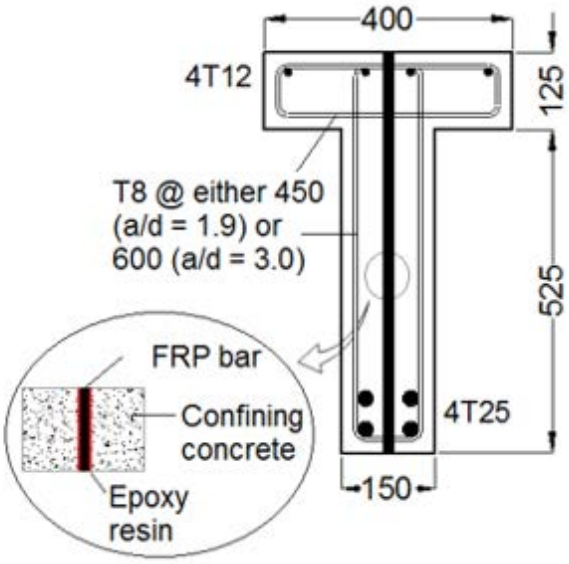

Figure 4.3 Cross-section details of the slender and deep beams shear-strengthened with DE FRP bars (Dirar and Theofanous, 2017)

4.3 Finite Element Model

A three-dimensional nonlinear FE model was adopted using DIANA 9.4.6 structural software package (DIANA user's manual, 2016). This model was developed along the lines of FE models for shear-strengthened concrete beams from the published literature (Qapo et al., 2016b; Dirar et al., 2013; Qapo et al., 2015). The following subsections illustrate the details of the modelling procedures that have been adopted in this study. DIANA FE package user's manual (2016) provides additional information about the adopted element types and material models.

4.3.1 Geometric Modelling

4.3.1.1 Concrete and steel plates

Three-dimensional eight-node isoparametric solid brick elements (HX24L) were used for modelling the concrete, as shown in Figure 4.4 (DIANA user's manual, 2016).

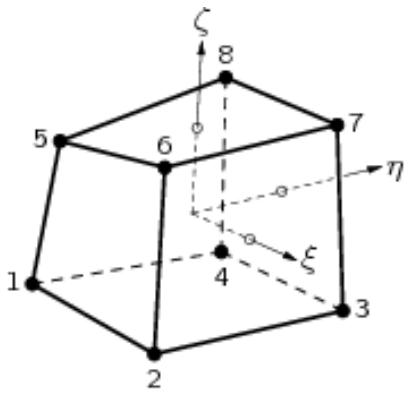

Figure 4.4 Eight-node isoparametric brick element (DIANA user's manual, 2016)

Three-dimensional six-node isoparametric solid wedge elements (TP18L) were adopted for representing the loading and support steel plates, as illustrated in Figure 4.5 (DIANA user's manual, 2016).

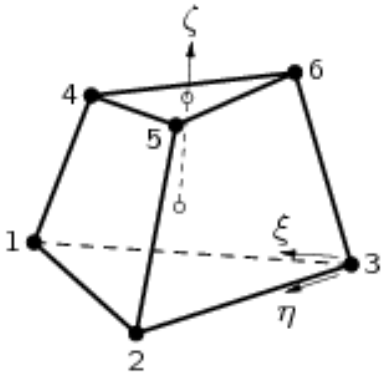

Figure 4.5 Six-node isoparametric solid wedge element (DIANA user's manual, 2016)

These elements have three degrees of freedom at each node (i.e. allowing translations in the x, y, z directions). The stress field is three-dimensional and the applied loading on the structural FE beam can be provided in any of these three directions as well. Various mesh densities were considered for representing the concrete. Bažant and Oh (1983) have previously recommended using a mesh size of 3 a_g (where a_g is the maximum aggregate size of the concrete mix of 10 mm) in each direction. A finer mesh with element sizes ranging from 12.5 mm to 20 mm was considered in this numerical study. From the comparison of the FE results, it was observed that adopting a finer mesh size by decreasing the element size from 20 mm to 12.5 mm caused an insignificant difference in the shear strength and deflection results. Therefore, 20 mm (i.e. 2 a_g) concrete element size was adopted for all the FE models in this study (see Figure 4.6). To enhance the nonlinear analysis speed and reduce the computational time, only half the beam span was modelled by restraining the horizontal movement and allowing the vertical deflection at the midspan nodes. This strategy yielded accurate results while reducing efficiently the computational time for the non-linear finite element analysis.

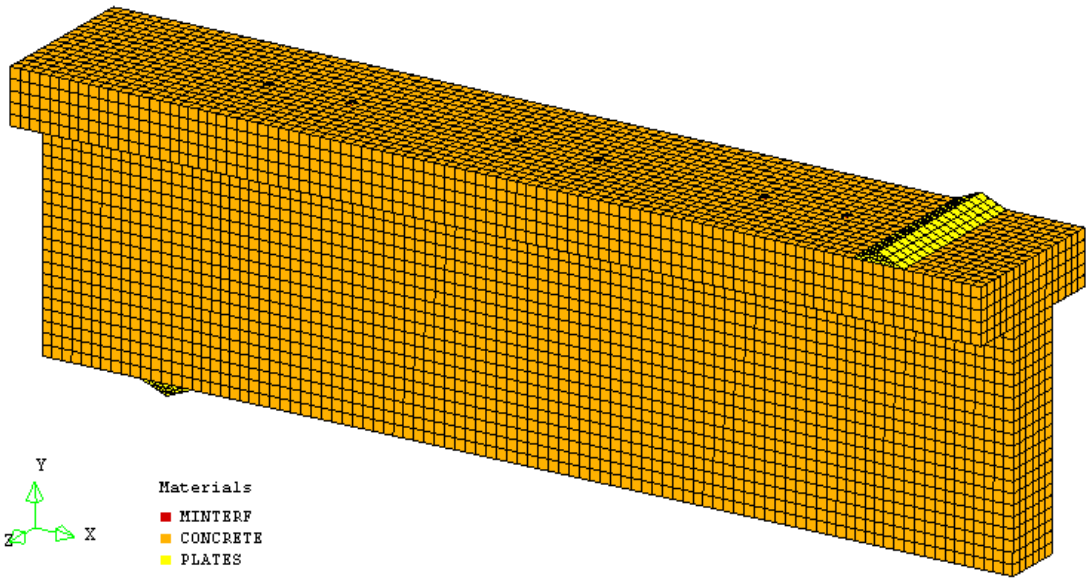

(a)

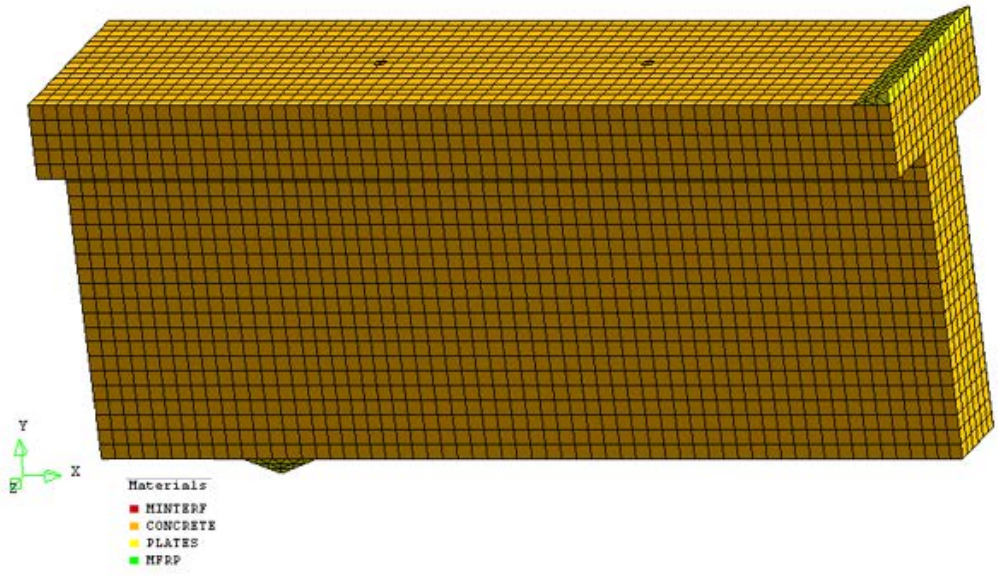

(b)

Figure 4.6 3-D Finite element model: (a) slender beams and (b) deep beams

4.3.1.2 Steel reinforcement

The longitudinal steel reinforcement and steel shear stirrups were modelled as embedded bar (truss-like) elements, as illustrated in Figures 4.7 and Figure 4.10.

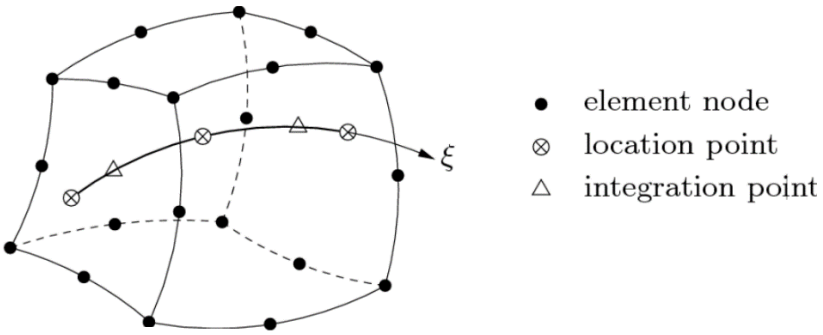

Figure 4.7 Embedded bar in solid brick element (DIANA user's manual, 2016)

These reinforcement elements do not have independent degrees of freedom, and their strains can be calculated from the displacement fields of the surrounding concrete elements. Studies conducted previously by Dirar et al. (2013) and Qapo et al. (2015) proved that the shear

behaviour of FRP shear-strengthened concrete beams can be accurately predicted adopting the perfect bond assumption if the bond failure between the steel reinforcement and the concrete is not the dominant failure mode. Therefore, in this numerical study, perfect bond was adopted between the internal steel reinforcement and surrounding concrete because bond failure was not detected for any of the experimentally tested beams, as further explained in Section 4.4.

4.3.1.3 DE FRP bars

The DE FRP bars were modelled using three-dimensional two-node truss elements (DIANA user's manual, 2016) (see Figures 4.8 and 4.10). Previous studies (Dirar et al., 2013; Qapo et al., 2015) have successfully used these elements for modelling FRP bars in FRP-strengthened structures. These elements allow axial deformation whilst preventing bending and shear deformations.

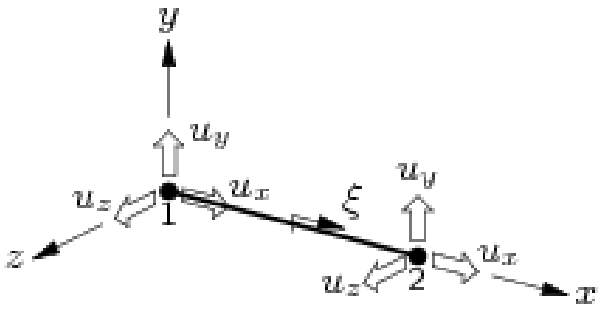

Figure 4.8 Three-dimensional two-node truss element (DIANA user's manual, 2016)

4.3.1.4 FRP bar-to-concrete interface

Four-node three-dimensional interface elements (DIANA user's manual, 2016) were used for representing the interfacial bond area between the DE FRP bars and the surrounding concrete (see Figure 4.9). These elements can successfully link the edges of the isoparametric solid brick elements, which represented the concrete, to the two-node truss elements which were

employed to represent the DE FRP bars. The main advantage of these elements is that they allow the modelling of the slip in the DE FRP bar-to-concrete interface.

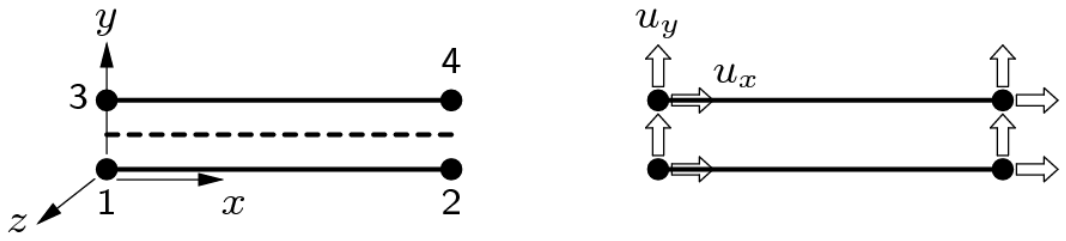

Topology Displacements

Figure 4.9 Four-node three-dimensional interface element (DIANA user's manual, 2016)

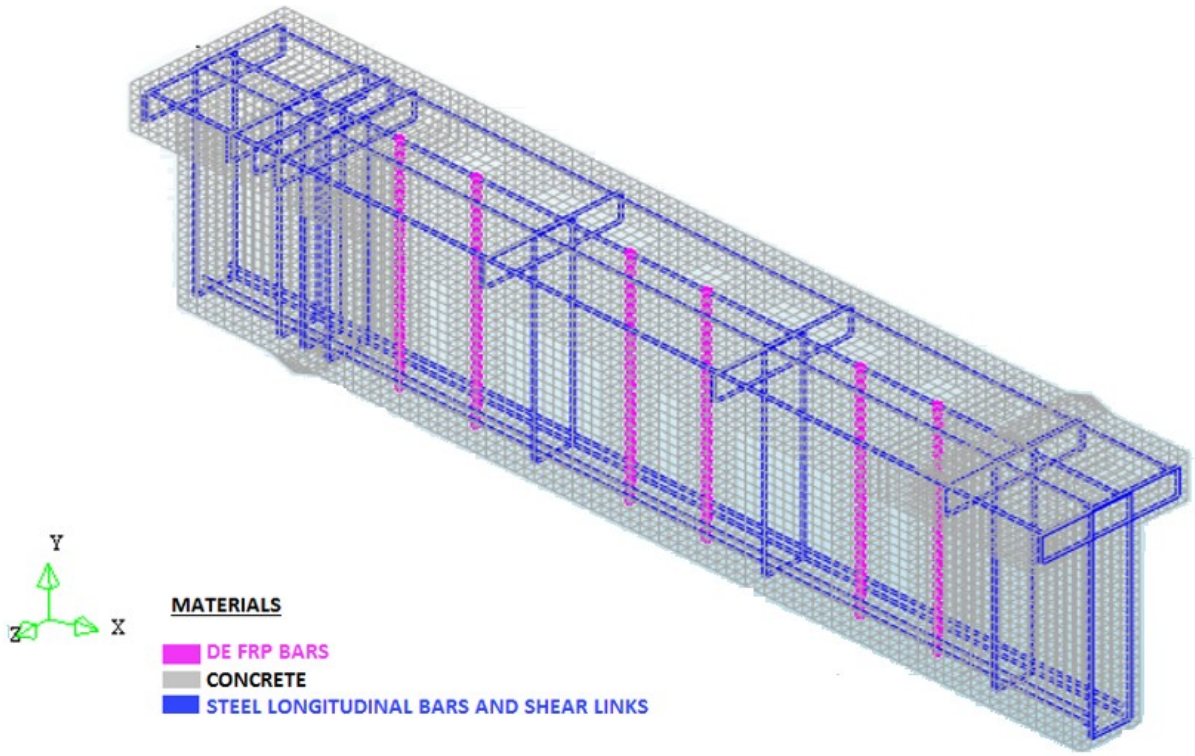

Figure 4.10 Steel reinforcement and DE FRP bars

4.3.2 Material Modelling

4.3.2.1 Concrete

Two different crack modelling approaches defined as the fixed angle crack model and total strain rotating crack model, have been previously adopted for representing the post-cracking behaviour of concrete. In the fixed angle crack modelling approach, the crack initiates in a perpendicular direction to that of the principle tensile stress. After that, the orientation of the crack remains unaltered/ fixed with respect to change in principal tensile stress directions. With changes in the direction of the principal tensile stresses, shear stresses develop parallel to the existing crack, but they can't be fully transferred through the concrete because of the existence of the weakened plane (Dirar et al., 2013a). Consequently, there will be a reduction in the shear stiffness parallel to the crack. In FE modelling using DIANA 9.4.6 (DIANA user's manual, 2016), a shear retention factor ($0<\beta_s<1$) is used to consider this reduction (Dirar et al., 2013a).

On the other hand, in the rotating crack modelling approach, the direction of the crack is not fixed, but changes with the change in the principal tensile stress direction. Thus, this approach does not require an explicit model to simulate the post-cracking shear behaviour of the concrete. Any crack plane in the rotating crack model will be a principal plane, and subsequently, there are no shear stresses acting on this plane (Dirar et al., 2013a; Qapo et al, 2015).

In this research study, both models were taken into consideration. The rotating crack model predicted more reasonably the shear behaviour of concrete as well as the crack patterns of the tested RC beams. Thus, only the results obtained from this model are presented.

The stress-strain curve of Thorenfeldt et al. (1987) was adopted to represent the behaviour of concrete in compression and is given by:

$$\frac{f_c}{f'_c} = \frac{m\,(\frac{\varepsilon_c}{\varepsilon'_c})}{m-(1-(\frac{\varepsilon_c}{\varepsilon'_c})^{mk})} \tag{4-1}$$

where m is a parameter equal to 0.18 + (f'_c /17), f_c is the concrete compressive stress at a specific strain ε_c, f'_c is the concrete cylinder compressive strength, ε'_c is the strain corresponding to the concrete compressive strength (f'_c) in the stress-strain curve (a parameter which is automatically calculated in DIANA 9.4.6) based on several predefined curves (e.g. constant and brittle curves).

The parameter k, governs the post-peak of the stress-strain curve (i.e. descending branch) of Equation (4-1) and is equal to:

$$k = \begin{cases} 1 & (\varepsilon'_c > \varepsilon_c > 0) \\ 0.67 + \left(\frac{f'_c}{62}\right) & (\varepsilon'_c \leq \varepsilon_c) \end{cases} \tag{4-2}$$

The following model, developed by Vecchio and Collins (1993), was adopted to represent the softening of concrete in compression due to lateral cracking, as given by:

$$\beta_{\sigma_{cr}} = \frac{1}{1+0.27\,(-\frac{\varepsilon_{lat}}{\varepsilon'_c}-0.37)} \leq 1 \tag{4-3}$$

where $\beta_{\sigma_{cr}}$ is the concrete compressive strength reduction factor and ε_{lat} is the average lateral damage variable, which is a function of the internal variables governing the tensile damage in the first lateral and second lateral directions, $\varepsilon_{l,1}$ and $\varepsilon_{l,2}$, respectively, as given below:

$$\varepsilon_{lat} = \sqrt{{\varepsilon_{l,1}}^2 + {\varepsilon_{l,2}}^2} \quad (4\text{-}4)$$

A linear stress-strain relationship up to concrete cracking was adopted for the tensile behaviour of concrete. Qapo et al. (2015) successfully adopted Remmel's model (1994), which is a linear tension softening model that calculates the fracture energy, G_{fs} , as given by Equation (4-5). This model was capable of simulating successfully the gradual decrease in tensile stress after concrete cracking.

$$G_{fs} = 0.065\ ln(1 + \frac{f'_c}{10}) \quad (4\text{-}5)$$

In this study, the Poisson's ratio of concrete was chosen as 0.15, in accordance with the recommendations of CEB-FIP Model Code 2010 (fib, 2012).

The elastic modulus of concrete was calculated according to CSA-A23.3 (2004), as given in Equation (4-6):

$$E_c = 3300\sqrt{f'_c} + 6900 \qquad \text{(in MPa)} \quad (4\text{-}6)$$

The uniaxial tensile strength of concrete was estimated based on Concrete Society TR55 (2012), as shown in Equation (4-7):

$$f_{ct} = 0.18\ (f_{cu})^{2/3} \quad (4\text{-}7)$$

Table 4.2 shows the parameters used for the material modelling of concrete in the FE models.

Table 4.2 Parameters used for material modelling of concrete

Parameter	f'_c	*m*	*k*	G_{fs}	E_c	f_{ct}	Poisson's ratio
	(MPa)	(MPa)	(MPa)	(MPa)	(MPa)	(MPa)	
	40	2.533	1.315	0.1046	27771	2.105	0.15

4.3.2.2 Steel reinforcement and steel plates

The internal steel longitudinal bars and steel shear stirrups were modelled using an elastic-perfectly plastic strain model in DIANA 9.4.6. Table 4.1 provides the experimental yield strength and modulus of elasticity values of the steel reinforcement as reported by Dirar and Theofanous (2017). The loading and supporting steel plates were also modelled as elastic-perfectly plastic material combined with von-Misses criterion (DIANA user's manual, 2016). The assumed values of elastic modulus, Poisson's ratio and yield stress were taken as 200 GPa, 0.15 and 1000 MPa, respectively.

4.3.2.3 DE FRP bars

As previously mentioned in Chapter 2, Section 2.2, FRP bars are linear-elastic materials. Therefore, the DE FRP bars were modelled using a linear-brittle stress-strain model. This model was based on the experimental ultimate tensile strength values as reported in Table 4.1 and shown in Figure 4.11 (Dirar and Theofanous, 2017).

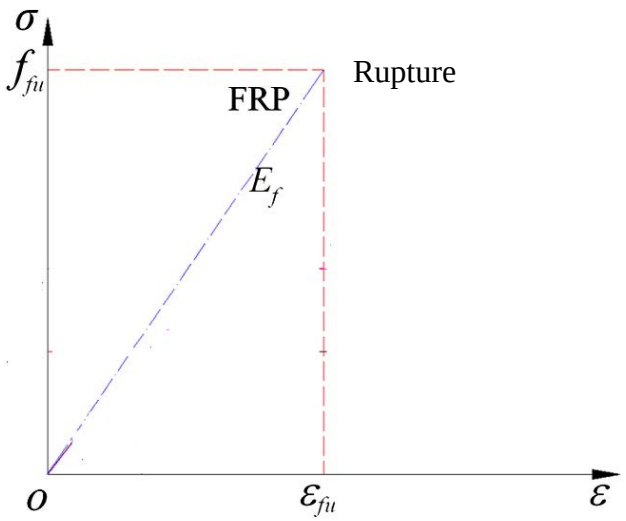

Figure 4.11 Stress-strain curve for DE FRP bars

4.3.2.4 DE FRP bar-to-concrete interface

An experimental pull-out test study was conducted previously by Caro et al. (2017) as described in Chapter 3. This study investigated the bond behaviour of deep embedment (DE) glass-FRP and carbon-FRP bars epoxy-bonded into 200 mm x 200 mm x 200 mm concrete cubes (refer to Chapter 3). The experimental programme comprised of eighteen concrete cube specimens with embedded GFRP or CFRP bars, as reported in Chapter 3. The method of installation of FRP bars, physical and material properties of FRP bars, concrete and epoxy resin replicated the properties of the DE shear-strengthening system for the large-scale shear-strengthened beams tested by Dirar and Theofanous (2017). Therefore, the average bond stress-slip curves for the pull-out specimens with 12 mm carbon-FRP and glass-FRP bars of this experimental study were adopted to represent the interface behaviour between the DE FRP bars and concrete in the FE model (see Figure 4.12).

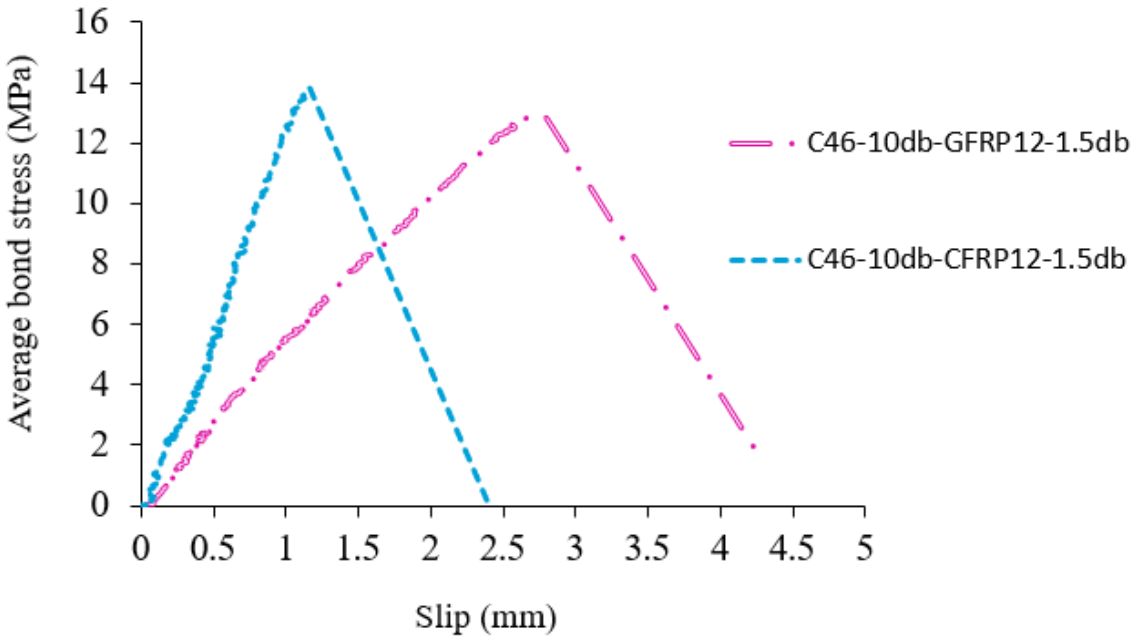

Figure 4.12 Average bond stress-slip curves for the specimens with 12 mm FRP bars (refer to Chapter 3)

4.3.3 Solution Algorithm and Analysis Procedure

A suitable incremental-iterative analysis procedure was used to perform the nonlinear analysis and obtain a convergence as shown in Figure 4.13. The total displacement increment (Δu) was adapted by iterative increments (δu) until reaching equilibrium. In this analysis procedure, the displacement increment at a specific iteration (δu_i) is calculated as the product between the stiffness matrix (K_i) and the out-of-balance vector at the start of that iteration (g_i), as given by (DIANA user's manual, 2016):

$$\delta u_i = {K_i}^{-1} g_i \tag{4-8}$$

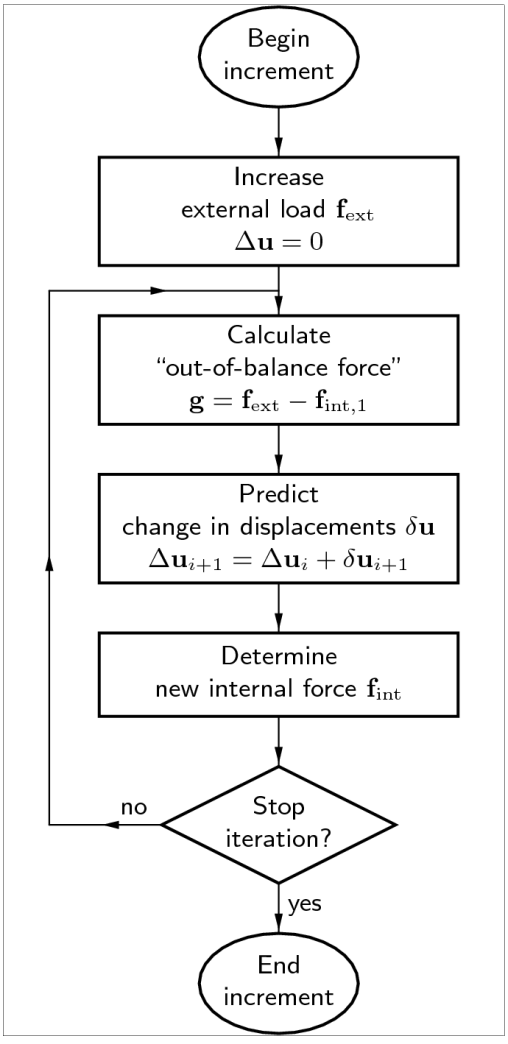

Figure 4.13 Iteration procedure (DIANA user's manual, 2016)

To simulate the non-linear load-deformation behaviour of the tested RC beams, the vertical loads were applied as displacement increments of 0.1 mm. In the displacement control method, the load increment will be indirectly applied by predefining specific displacement increments (u^c) in the external force vector, as illustrated in Figure 4.14.

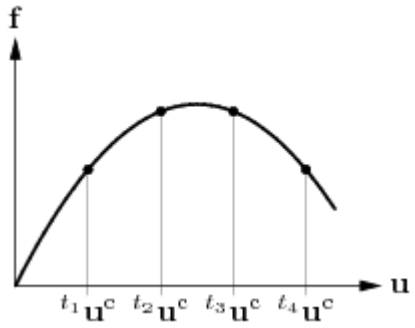

Figure 4.14 Displacement control (DIANA user's manual, 2016)

The Quasi-Newton iterative method (also known as the Secant method) was employed, where a secant formulation (BFGS) is used for calculating the stiffness matrix and an implicit line search technique is built into the iterative algorithm, as illustrated in Figure 4.15 (DIANA user's manual, 2016). This method can achieve convergence and result in computational efficiency by achieving less expensive equilibrium iterations.

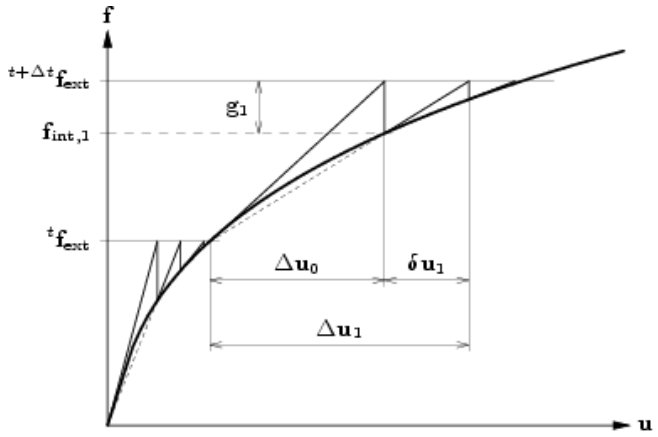

Figure 4.15 Quasi-Newton iterative method (DIANA user's manual, 2016)

Alongside this method, a displacement based convergence criterion of 0.1% was chosen in accordance with the recommendations by Hee and Jefferson (2008).

DIANA user's manual (2016) states that the convergence in the displacement criterion is checked by comparing the displacement increment after the current iteration against the displacement increment of the first prediction (Δu_0) as given in Equation (4-9):

$$\text{Displacement criterion ratio} = \sqrt{\frac{\delta u_i^T \, \delta u_i}{\Delta u_0^T \, \Delta u_0}} \tag{4-9}$$

A total of 400 iterations were specified for the non-linear analysis procedure. A similar solution algorithm was successfully adopted by Dirar et al. (2013a) and Qapo et al. (2016b) and yielded accurate FE predictions.

4.4 Model Validation

4.4.1 Load-Deflection Response

The FE predictions were compared with the experimental results in terms of shear force capacity, load-deflection response and crack patterns at failure. Table 4.3 gives the FE-predicted and experimental shear strength for each beam. It can be observed that the deep beams had higher shear strength values compared to slender beams. This is due to the arch action which offers higher shear resistance than the beam action. The overall mean FE-predicted/experimental shear force capacity ratio is 0.963 with a standard deviation of 0.036. The FE predictions were more accurate for the set of deep beams with a mean predicted/experimental shear force capacity ratio of 0.962 and a standard deviation of 0.006. The FE results correctly demonstrated that the shear strength gain attributable to DE FRP bars was higher in the strengthened slender beam compared to the corresponding deep beam. The

shear effectiveness of the FRP reinforcement in the deep beams was limited since the concrete arch resists most of the applied shear force and truss action is less effective.

Table 4.3 Experimental and FE predicted shear force capacities

Beam ID	Shear force capacity, (kN)		Ratio V_{FE}/V_{Exp}	Gain attributable to DE FRP bars, V_f (kN)	
	Experimental	FE analysis		Experimental analysis	FE
FE1 (U/3.0)	149.5	151.7	1.015	-	-
FE2 (C/3.0)	318.1	290.6	0.914	168.6	139.0
FE3 (U/1.9)	308.4	297.6	0.965	-	-
FE4 (C/1.9)	426	412.2	0.968	117.6	114.6
FE5 (G/1.9)	410.7	392.6	0.956	102.3	95.0
		Average	**0.963**		
		Standard Deviation	**0.036**		

Figure 4.16 compares the FE-predicted and experimental shear force versus mid-span deflection curves for the control slender beam (U/3.0) tested by Dirar and Theofanous (2017). It can be observed that the curves are quite comparable, demonstrating a very good match starting from initial loading up to the shear failure of the beam. Figure 4.16 also shows that both curves are characterized by an almost linear initial increase in the shear force with deflection up to the flexural crack formation. Following crack formation, the curves exhibited a nonlinear behaviour because of stiffness deterioration and propagation of flexural cracks into the shear spans until the peak load. Subsequently, there was an immediate drop at the peak load, which distinguishes the shear failure, confirming the accuracy of the FE model.

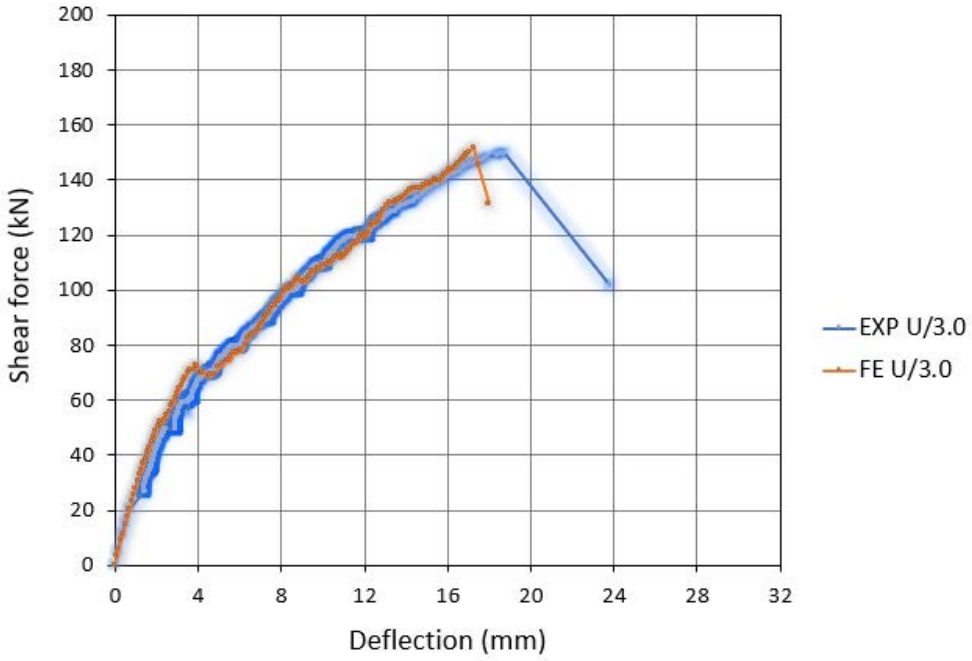

Figure 4.16 Experimental (Dirar and Theofanous, 2017) and FE predicted shear force-deflection curves for control slender beam U/3.0

Figure 4.17 illustrates the experimental and FE predicted shear force versus mid-span deflection curves for the strengthened slender beam (C/3.0). This beam was strengthened with 12 mm DE CFRP bars. The FE model has successfully simulated the initial phase of loading (before cracks start to form) characterized by a linear shear force-deflection relationship, showing a very good correlation with the experimental curve. Following cracking, a slightly stiffer behaviour characterizes the response of the FE model up to failure. The FE model accurately predicted the flexural failure mode of the strengthened beam after reaching the flexural capacity, exhibiting a ductile behaviour, as shown in Figure 4.17.

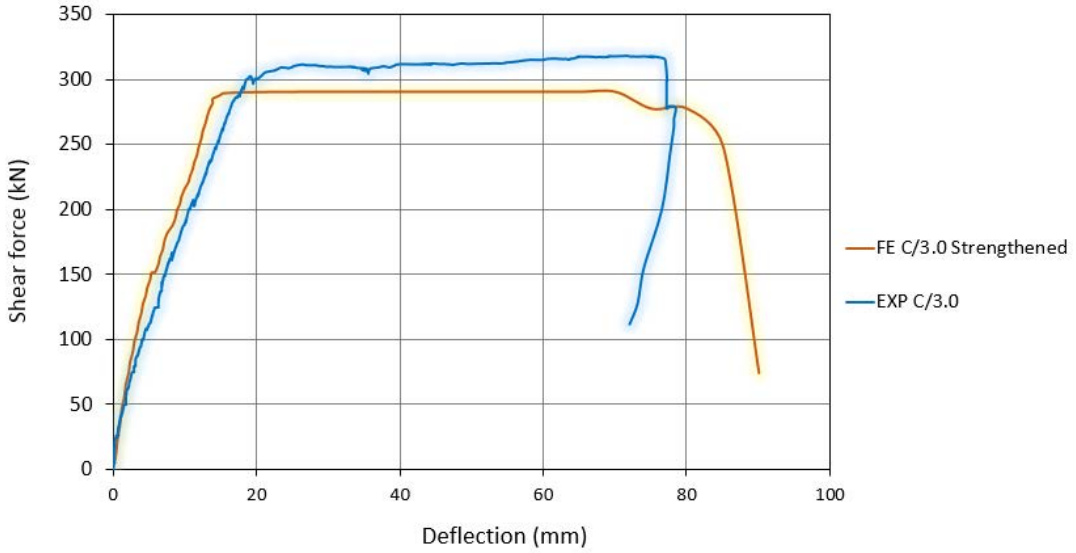

Figure 4.17 Experimental (Dirar and Theofanous, 2017) and FE predicted shear force–deflection curves for strengthened slender beam C/3.0

Figure 4.18 compares the FE predicted and experimental shear force versus mid-span deflection relationships for the set of deep beams. It illustrates that the curves for each FE model are approximately linear up to crack formation. The initial stiffness of the deep beams predicted by the FE model is in a very good correlation with the experimental results up to the formation of the flexural cracks. As the loading increased, the FE curves showed that the stiffness of the beam decreased until the formation of the diagonal crack. Figure 4.18b and 4.18c show that a less stiff behaviour is exhibited by the FE model compared to the experimental results. However, all FE models predicted a sudden drop at the peak load, which characterizes the shear failure in accordance with the experimental results. The presented results confirmed that the developed FE models were able to capture successfully the shear behaviour of both the control and strengthened RC deep beams.

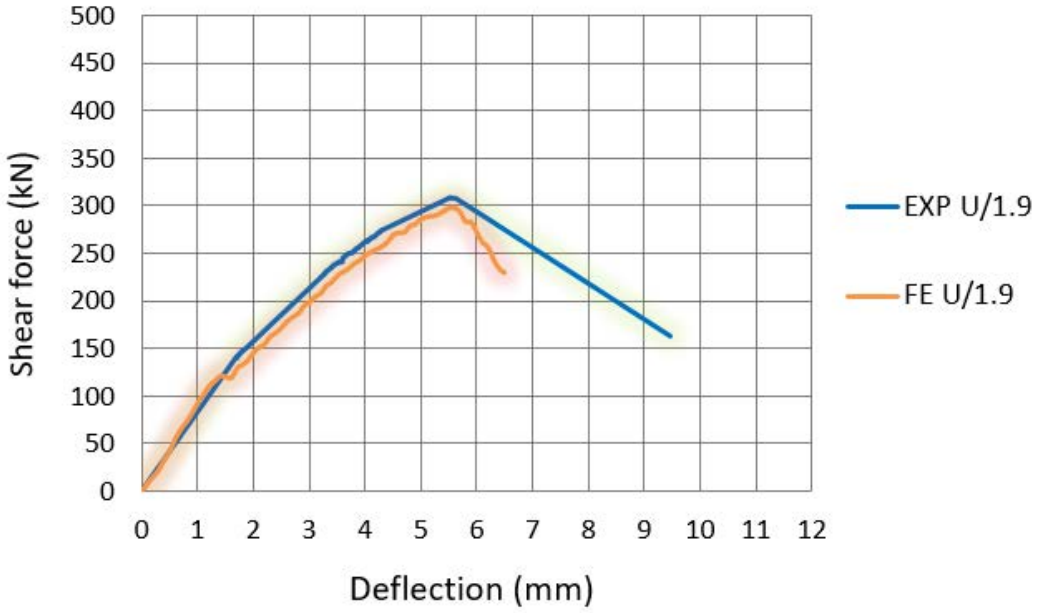
Shear force (kN)
500
450
400
350
300
250
200
150
100
50
0
0 1 2 3 4 5 6 7 8 9 10 11 12
Deflection (mm)
EXP U/1.9
FE U/1.9

(a)

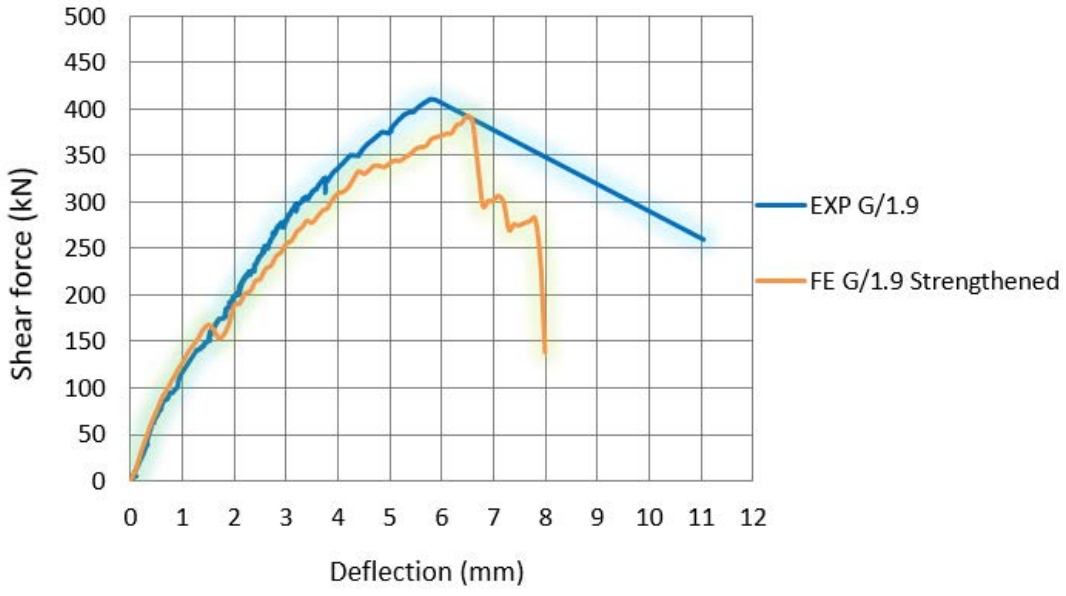
Shear force (kN)
500
450
400
350
300
250
200
150
100
50
0
0 1 2 3 4 5 6 7 8 9 10 11 12
Deflection (mm)
EXP G/1.9
FE G/1.9 Strengthened

(b)

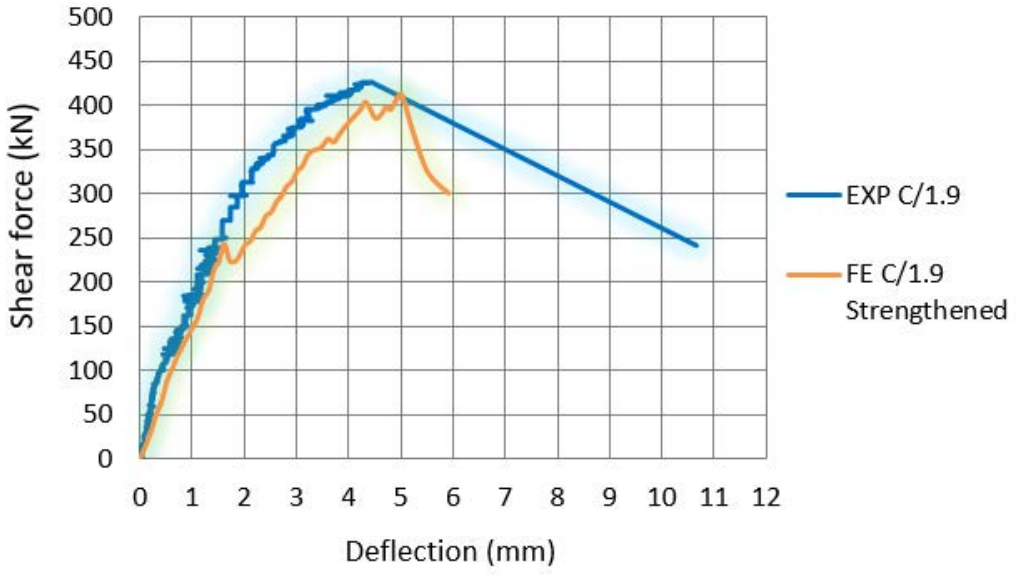

(c)

Figure 4.18 Experimental (Dirar and Theofanous, 2017) and FE predicted shear force-deflection curves: (a) control deep beam U/1.9, (b) GFRP-strengthened deep beam G/1.9 and (c) CFRP-strengthened deep beam C/1.9

4.4.2 Crack Patterns and Failure Modes

All RC deep beams failed in shear, as shown in Figures 4.19 - 4.21. Experimental tests and FE modelling results revealed that cracking in the unstrengthened slender beam (U/1.9) and the DE FRP-strengthened beams (C/1.9 and G/1.9) initiated with a set of mid-span flexural cracks at a shear force of approximately 55 kN. Flexural cracks started to propagate to the shear spans of the RC deep beams with increased loading. A set of shear cracks appeared near the centre of the shear spans at a shear force of approximately 90 kN, as successfully simulated by the FE model.

The FE model also predicted a series of parallel inclined cracks which formed in the shear spans of the DE FRP-shear strengthened beams. Upon further loading, the inclined cracks extended towards the support and steel plates, and penetrated into the concrete compression zone (i.e. flange), and eventually led to a shear-compression failure as depicted in Figures 4.19 to 4.21. Such observation can be attributed to the arch action where the applied shear force is mainly transferred by direct compression to the supports.

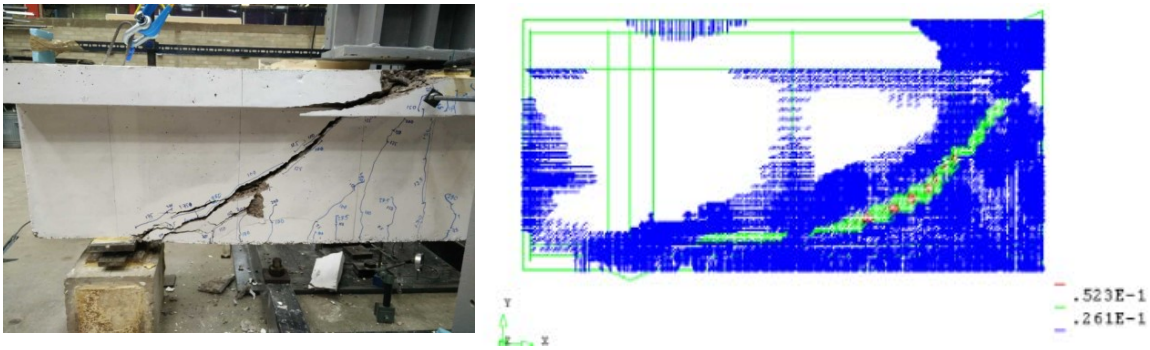

(a)

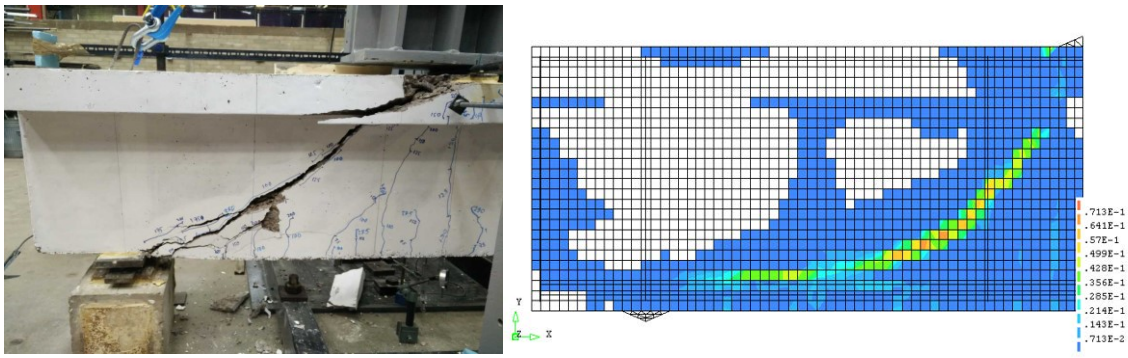

(b)

Figure 4.19 Experimental crack pattern (Dirar and Theofanous, 2017) (left) and FE crack patterns (right) for control deep beam U/1.9: (a) FE crack strain-based pattern, (b) FE principal tensile strain-based crack pattern

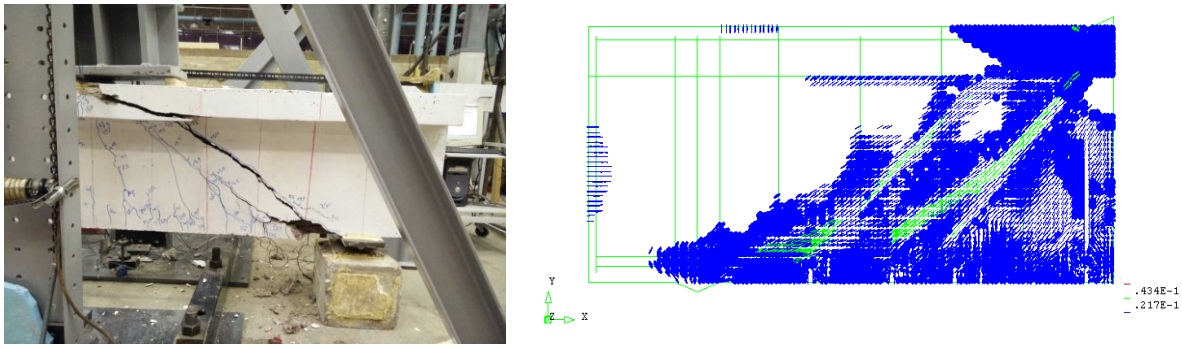

(a)

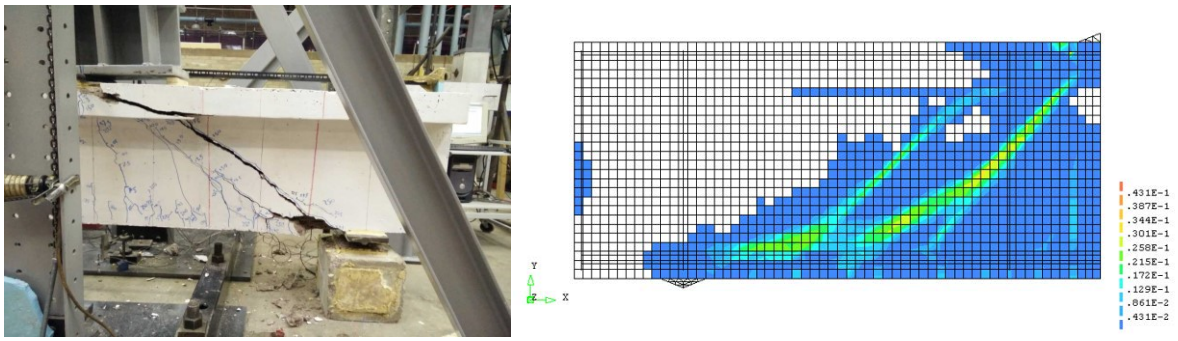

(b)

Figure 4.20 Experimental crack pattern (Dirar and Theofanous, 2017) (left) and FE crack patterns (right) for GFRP-strengthened deep beam G/1.9: (a) FE crack strain-based pattern, (b) FE principal tensile strain-based crack

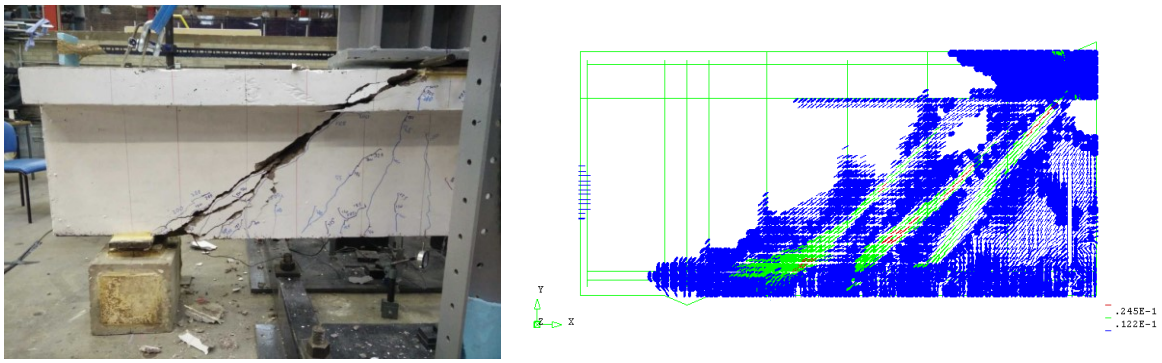

(a)

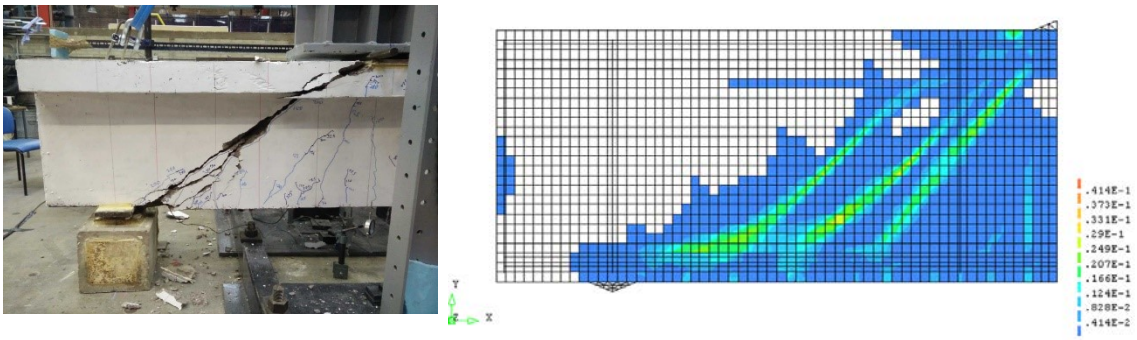

(b)

Figure 4.21 Experimental crack pattern (Dirar and Theofanous, 2017) (left) and FE crack patterns (right) for CFRP-strengthened deep beam G/1.9: (a) FE crack strain-based pattern, (b) FE principal tensile strain-based crack

In both slender beams (U/3.0 and C/3.0), FE modelling results confirmed that the mid-span flexural cracks initiated at a shear force of approximately 34 kN, similar to the experimental test results. The FE model successfully captured the propagation of the flexural cracks to the shear spans of the RC slender beams with increased loading. The flexural cracks in the control beam converted into inclined shear cracks at a shear force of about 76 kN. More inclined cracks developed in the shear spans and continued to extend from support to loading plates, causing a diagonal tension failure (see Figure 4.22). The DE-strengthened beam with CFRP bars experienced a ductile response and failed in flexure (see Figure 4.23).

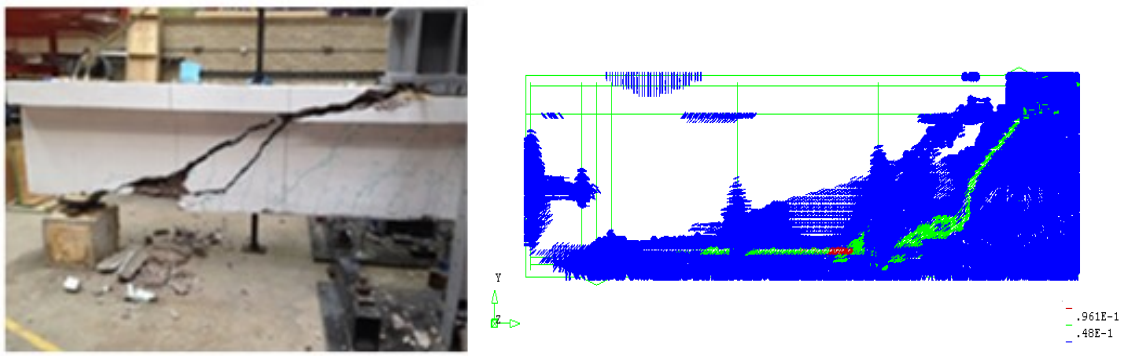

(a)

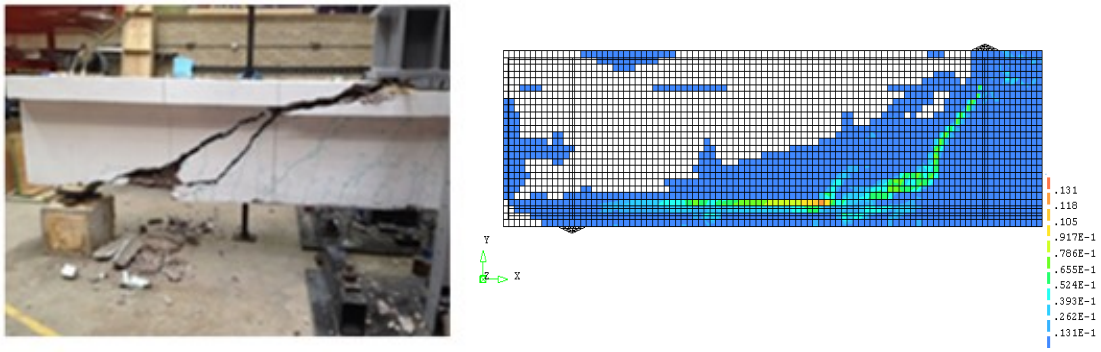

(b)

Figure 4.22 Experimental crack pattern (Dirar and Theofanous, 2017) (left) and FE crack patterns (right) for control beam slender U/3.0: (a) FE crack strain-based pattern, (b) FE principal tensile strain-based crack pattern

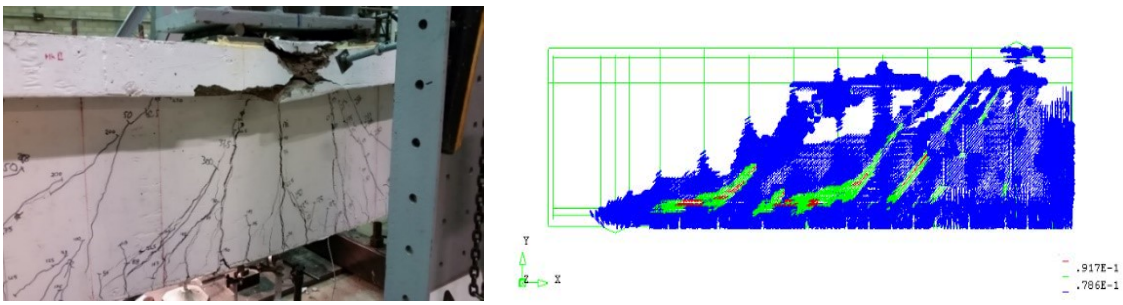

(a)

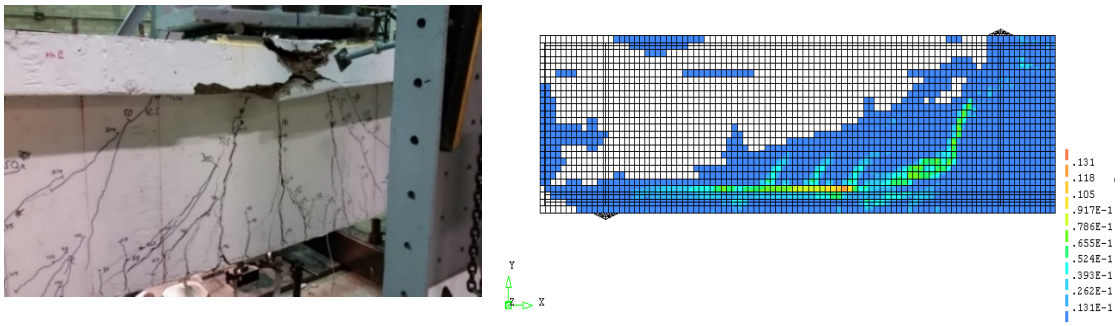

(b)

Figure 4.23 Experimental crack pattern (Dirar and Theofanous, 2017) (left) and FE crack patterns (right) for CFRP-strengthened slender beam G/3.0: (a) FE crack strain-based pattern, (b) FE principal tensile strain-based crack

4.5 Parametric Study

Qapo et al. (2016b) carried out a comprehensive FE parametric study on DE FRP-strengthened RC slender beams. However, research studies on DE FRP-strengthened RC deep beams have been very limited. Moreover, the effect of the main parameters governing the strengthened behaviour of RC deep beams has been so far limitedly considered. Following the proven accuracy of the FE model presented in Section 4.4, a numerical parametric study was conducted based on the deep beams tested by Dirar and Theofanous (2017) as described in Section 4.4. The investigated parameters were the DE FRP bar diameter, FRP bar material, DE strengthening ratio, shear span-to-effective depth (a/d) ratio, and interaction between steel stirrups and DE FRP bars. The effects of these parameters on the shear strength of FE modelled deep beams using the DE technique are presented and analysed in the following sub-sections. Based on the findings, a new shear design model is then proposed for calculating the shear contribution of DE FRP bars (refer to Chapter 5). Table 4.4 provides a

summary of the numerical FE models. Of note is that the material properties of the concrete, steel reinforcement, and DE FRP bars are the same as those displayed in Table 4.1 (refer to Section 4.3).

Table 4.4 Parametric study details

Beam	f'_c	a	d	a/d	b_w	Stirrup diameter	Stirrup spacing	DE FRP diameter	DE FRP spacing
	MPa	mm	mm		mm	mm	mm	mm	mm
FE1 (U/3.0)	40	1800	600	3	150	8	600		
FE2 (C/3.0)	40	1800	600	3	150	8	600	12	200
FE3 (U/1.9)	40	1150	600	1.9	150	8	450		
FE4 (C/1.9)	40	1150	600	1.9	150	8	450	12	450
FE5 (G/1.9)	40	1150	600	1.9	150	8	450	12	450
FE6	40	1150	600	1.9	150	7	450		
FE7-GFRP	40	1150	600	1.9	150	7	450	14.7	450
FE8-CFRP	40	1150	600	1.9	150	7	450	14.7	450
FE9 (U/2.2)	40	1320	600	2.2	150	8	440		
FE10 (C/2.2)	40	1320	600	2.2	150	8	440	12	440
FE11 (G/2.2)	40	1320	600	2.2	150	8	440	12	440
FE12 (U/2.5)	40	1500	600	2.5	150	8.5	500		
FE13 (C/2.5)	40	1500	600	2.5	150	8.5	500	12	500
FE14 (G/2.5)	40	1500	600	2.5	150	8.5	500	12	500
FE15	40	1150	600	1.9	150	6	450		
FE16-GFRP	40	1150	600	1.9	150	6	450	12	450
FE17-CFRP	40	1150	600	1.9	150	6	450	12	450
FE18	40	1150	600	1.9	150	10	450		
FE19-GFRP	40	1150	600	1.9	150	10	450	12	450
FE20-CFRP	40	1150	600	1.9	150	10	450	12	450
FE21	40	1150	600	1.9	150	6	450		
FE22-GFRP	40	1150	600	1.9	150	6	450	10	450
FE23-CFRP	40	1150	600	1.9	150	6	450	10	450
FE24	40	1150	600	1.9	150	8	450		
FE25-GFRP	40	1150 1150	600	1.9	150	8	450	10	450

FE26-CFRP	40		600	1.9	150	8	450	10	450
		1150							
FE27	40	1150	600	1.9	150	10	450		
FE28-GFRP	40	1150	600	1.9	150	10	450	10	450
FE29-CFRP	40		600	1.9	150	10	450	10	450

4.5.1 DE FRP Bar Diameter

The impact of the DE FRP bar diameter on the shear force can be inferred from two sets of FE beam models strengthened with CFRP and GFRP bars. FE4 (C/1.9) and FE26-CFRP were strengthened with 12 mm and 10 mm CFRP bars spaced at 450 mm, respectively. The corresponding FE models with 12 mm and 10 mm GFRP bars were FE5 (G/1.9) and FE25-GFRP, respectively. Table 4.5 and Figure 4.24 present the FE-predicted results. All FE models predicted shear failure, so the failure mode was not affected by the change in diameter.

The shear force gain due to CFRP bars in FE4 (C/1.9) model was 114.6 kN, compared with 94.9 kN for the FE26-CFRP model. Hence, increasing the CFRP bar diameter from 10 to 12 mm led to an increase of 19.7 kN (20.8%) in the shear force gain due to DE CFRP bars. The increase in the shear force enhancement was smaller for the corresponding set of GFRP strengthened FE beam models due to a lower modulus of elasticity of GFRP bars compared to CFRP bars. Increasing the GFRP bar diameter from 10 to 12 mm resulted in an increase of 13.2 kN (16.1%) in the shear force gain. The higher strength gain offered by the DE bars with larger bar diameter may be attributable to two reasons. Firstly, Caro et al. (2017) recently assessed the influence of bar diameter on the bond behaviour of DE FRP bars epoxy-embedded into concrete prisms. The increase in CFRP bar diameter from 10 to 12 mm led to a 17.1 kN (30.4%) increase in the pull-out capacity. It was concluded that for a larger bar diameter, the greater bond area resulted in a higher pull-out capacity. Secondly, for the same

values of b_w (web width) and DE bar spacing (s_f), the shear strengthening ratio of DE FRP bars (A_f / b_w s_f), is higher for bars with larger diameters. Thus, DE bars with larger diameter offer higher resistance to crack propagation and opening, compared to bars with a smaller diameter. Therefore, the FE model predictions proved that increasing the bar diameter of DE FRP bars enhances both the shear force resistance and shear force gain in RC deep beams.

Table 4.5 Effect of DE FRP bar diameter

Beam ID	Bar diameter (mm)	DE strengthening Ratio, $\boldsymbol{\rho_f}$ (%)	Shear force capacity, $\boldsymbol{V_{FE}}$ (kN)	Shear force gain, $\boldsymbol{V_f}$ (kN)	Shear force gain (%)
FE4 (C/1.9)	12	0.17	412.2	114.6	20.8
FE26-CFRP	10	0.12	392.5	94.9	-
FE5 (G/1.9)	12	0.17	392.6	95.0	16.1
FE25-GFRP	10	0.12	379.4	81.8	-

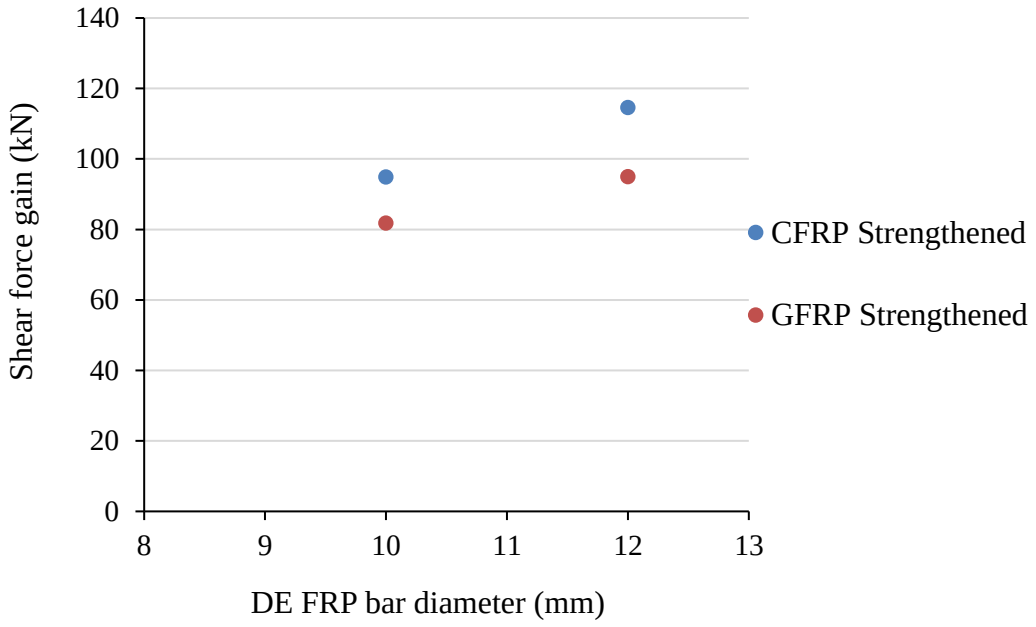

Figure 4.24 Effect of DE FRP bar diameter on the shear force gain

4.5.2 Shear Span-to-Effective Depth Ratio (a/d)

The shear-span-to-effective depth (a/d) ratio has a significant impact on the shear behaviour of RC beams as it governs the shear-resisting mechanism. The behaviour of beams with a/d ratios less than 2.5 (i.e. deep beams) is dominated by a nonlinear distribution of strains (disturbed region) and the plane section assumption of the flexural theory is not applicable. A tied arch becomes the primary force transfer mechanism after diagonal crack formation.

The impact of a/d ratio on the shear strength enhancement due to DE FRP bars in deep beams has been limitedly examined. This study examines the effect of a/d ratio by developing three sets of FE models. The first set consists of control FE models, namely FE3 (U/1.9), FE9 (U/2.2) and FE12 (U/2.5), reinforced only with steel stirrups. The second set comprises three FE models, FE4 (C/1.9), FE10 (C/2.2) and FE13 (C/2.5), strengthened with DE carbon-FRP bars also. Finally, the third set comprises three deep beam FE models strengthened with DE glass-FRP bars, namely FE5 (G/1.9), FE11 (G/2.2) and FE14 (G/2.5). For each set of modelled beams, three different a/d ratios of 1.9, 2.2 and 2.5 were considered. Table 4.6 provides details of the FE models. Of particular note was that the range of ratios was considered in such a way that allows all FE models to fail in shear, which was the case.

The influence of a/d ratio on the predicted shear force at failure for each FE model is shown in Table 4.6 and illustrated in Figure 4.25. The maximum reduction in the shear force capacity for the set of control deep beams in this parametric study was about 27.1%. The predicted shear force at failure for the strengthened beams reduced by 33 % as the a/d ratio increased from 1.9 to 2.5. This is in broad agreement with the results presented previously for DE FRP-shear strengthened beams tested by Dirar and Theofanous (2017). Tests were carried out on DE GFRP shear-strengthened large-scale RC T beams with two a/d ratios. The shear

force capacity of the strengthened deep beams with a/d of 1.9 was 410.7 kN and dropped to 293.0 kN for the strengthened slender beams with a/d of 3.0.

Figure 4.25b also shows that increasing the a/d had a detrimental influence on the shear contribution due to DE CFRP bars. Increasing the a/d ratio from 1.9 to 2.5 led to a decrease in the predicted shear force gain by approximately 46.9%. Finally, for the set of DE shear-strengthened FE models with glass-FRP bars, the predicted shear force gain decreased by 55.2 % with the increase in the a/d ratio from 1.9 to 2.5. These results confirm that the shear strength gain attributable to the DE FRP bars is strongly influenced by the a/d ratio. Nonetheless, this is not picked up by current design models. The reduction in shear strengthening effectiveness may be attributed to the concrete arch which becomes less effective with the increase in the a/d ratio. Furthermore, for large a/d ratios, the angle between the FRP reinforcement and the main inclined crack is small. Tan et al. (2003) suggested that the tensile force contribution of the web reinforcement [$A_v\ f_y \sin(\theta_s + \theta_W)$] in deep beams is dependent on the a/d ratio and the angle between the longitudinal tension reinforcement and the diagonal strut (θ_s). For large a/d ratios, θ_s reduces. Hence, the tensile force contribution by the web reinforcement reduces and ultimately decreases the ultimate shear resistance. In addition, CSA S806 (2012) strut-and-tie model (refer to Section 2.10.1) suggests that the compressive strength of the strut reduces with the increase in the strut angle or increase in the tensile reinforcement strain. Thus, the shear strength capacity of the deep RC beam which is influenced by the strength of the strut will reduce with increase in the a/d ratio (Andermatt and Lubell, 2013).

Currently, there are no shear design guidelines for RC deep beams shear-strengthened with DE FRP bars. This shortcoming is addressed in Chapter 5, where a new design model is proposed based on the FE parametric study results.

Table 4.6 Effect of the a/d ratio

Beam ID	a/d	Shear force capacity, V_{FE}, (kN)	Shear force gain by DE FRP bars V_f, (kN)	Decrease in shear gain due to increasing a/d (%)
FE3 (U/1.9)	1.9	297.6	Control beam	
FE9 (U/2.2)	2.2	248.7	Control beam	
FE12 (U/2.5)	2.5	217.0	Control beam	
FE4 (C/1.9)	1.9	412.2	114.6	
FE10 (C/2.2)	2.2	322.0	73.2	36.1
FE13 (C/2.5)	2.5	277.7	60.8	46.9
FE5 (G/1.9)	1.9	392.6	95.0	
FE11 (G/2.2)	2.2	300.4	51.7	45.6
FE14 (G/2.5)	2.5	259.5	42.5	55.2

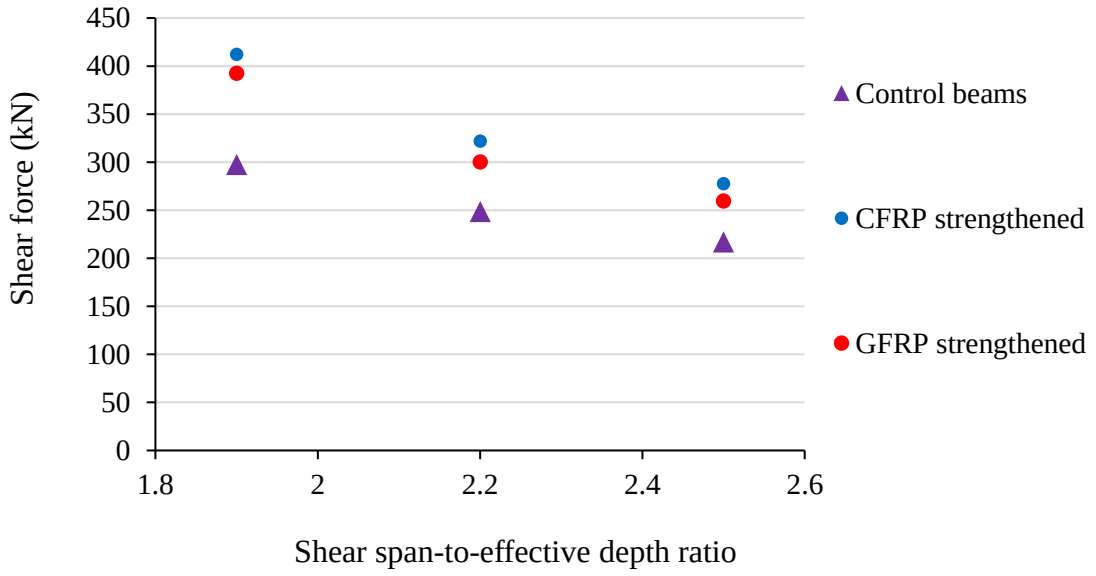

(a)

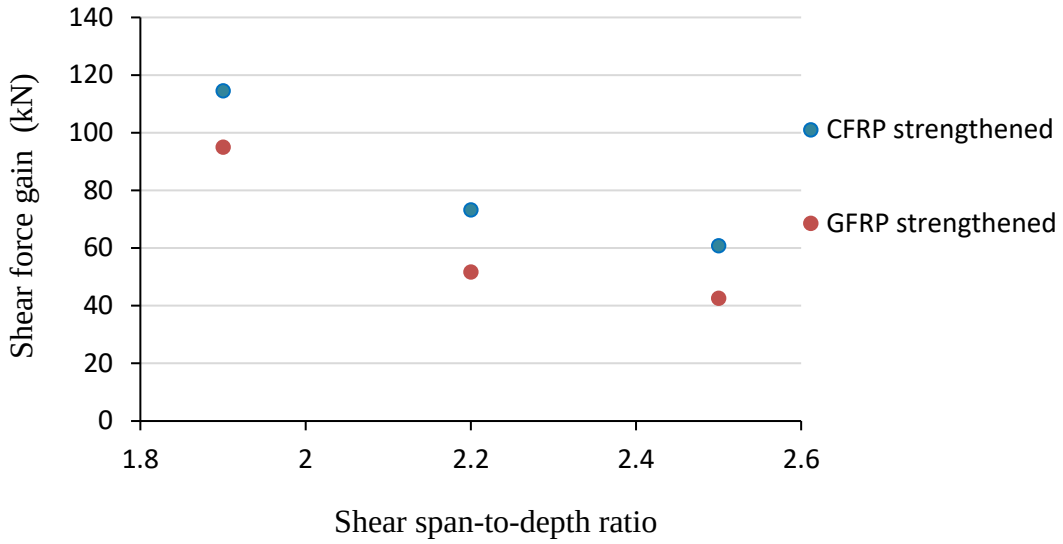

(a)

Figure 4.25 Effect of a/d ratio on (a) shear force and (b) shear force gain

4.5.3 Interaction Between Steel Stirrups and DE FRP Bars

The contribution of shear strengthening methods to shear capacity is also affected by the existing transverse shear reinforcement. It has been found (Chaallal et al., 2012) that DE FRP bars were more effective in increasing the shear capacity for RC beams without transverse steel stirrups or with a small transverse reinforcement ratio (i.e. widely spaced stirrups). In addition, Qapo et al. (2016b), who modelled DE shear-strengthened slender concrete beams, reported that the predicted shear enhancement due to DE FRP bars is inversely proportional to $E_s \rho_v / E_f \rho_f$.

The ratio $E_s \rho_v / E_f \rho_f$ is defined as the ratio between the elastic modulus of steel stirrups (E_s) multiplied by the steel stirrups transverse reinforcement ratio (ρ_v) to the elastic modulus of DE FRP bars (E_f) multiplied by the DE FRP shear strengthening ratio (ρ_f).

The effect of the steel stirrup-to-DE FRP bar ratio on the shear behaviour of DE shear-strengthened deep beams with DE FRP bars has not so far been considered. The effect of this ratio was examined in this study by modelling two sets of FE deep beam models strengthened with CFRP and GFRP bars. The FE models had different steel stirrup-to-DE FRP bar ratios varying from 0.698 to 10.0 and (a/d) = 1.9.

Table 4.7 and Figure 4.26 present the relationship between the predicted shear force gain due to DE FRP bars and $E_s \rho_v / E_f \rho_f$ ratio. The FE results given in Table 4.7 show that as the $E_s \rho_v / E_f \rho_f$ ratio increased from 0.698 to 3.077, the predicted shear gain due to DE CFRP bars decreased by 19.4 %. In the case of FE models strengthened with glass-FRP bars, increasing the ratio $E_s \rho_v / E_f \rho_f$ from 2.268 to 10 caused a decrease of about 27.9 % in the shear force gain. However, it is noticeable in Figure 4.26 that the rate of decrease is not as significant as previously investigated in the case of slender beams strengthened with DE carbon-FRP bars or EB FRP sheets (Qapo et al., 2016b). This may be attributed to the tied arch action after diagonal cracking of the beams. Further experimental tests should be conducted to confirm this correlation.

Currently, there are no mathematical models available which consider the interaction between DE FRP bars and existing steel stirrups, in the case of deep beams, to compare the FE results. Consequently, the proposed shear design equations in Chapter 5 take into account the $E_s \rho_v / E_f \rho_f$ ratio as one of the key parameters influencing the shear force gain. These equations will contribute to a more reliable application of the DE technique for deep beams with high steel stirrup ratios.

Table 4.7 Effect of $E_s \rho_v / E_f \rho_f$ ratio

Beam ID	$\mathbf{E_s \rho_v / E_f \rho_f}$	Shear force capacity, V_{FE} (kN)	Shear force gain by DE FRP bars, V_f (kN)
FE8-CFRP	0.698	419.6	137.9
FE17-CFRP	0.769	390.9	114.5
FE23-CFRP	1.108	377.1	100.6
FE4-CFRP	1.367	412.2	114.6
FE26-CFRP	1.969	392.5	94.9
FE20-CFRP	2.137	440.0	123.8
FE29-CFRP	3.077	427.3	111.1
FE7-GFRP	2.268	407.6	125.8
FE5 (G/1.9)	4.444	392.6	95.0
FE16-GFRP	2.500	369.8	93.3
FE22-GFRP	3.600	360.8	84.3
FE25-GFRP	6.400	379.4	81.8
FE19-GFRP	6.944	413.9	97.7
FE28-GFRP	10.000	406.9	90.7

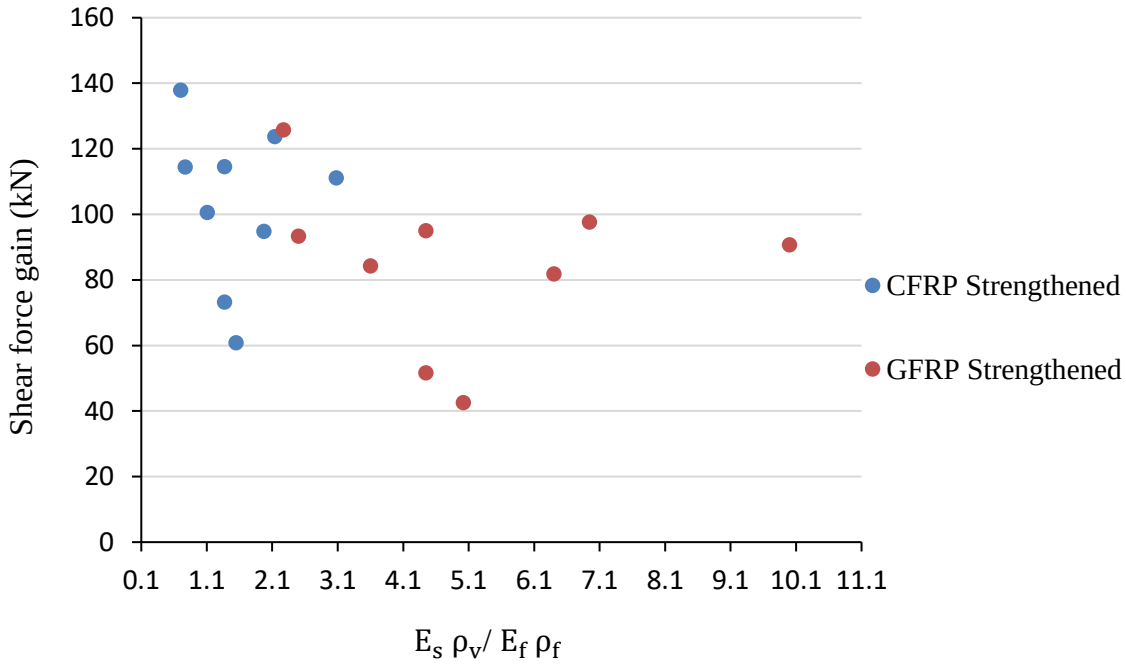

Figure 4.26 Effect of $E_s \rho_v / E_f \rho_f$ ratio on the shear force gain

4.5.4 Effect of FRP Bar Type and DE Shear Strengthening Ratio

The impact of DE FRP bar type on the shear force capacity and shear force gain can be inferred from two sets of FE beam models strengthened with carbon-FRP and glass-FRP bars, respectively. Table 4.8 and Figure 4.27 present the FE predicted results. The results show that at a given DE shear strengthening ratio, FE models with carbon-FRP bars have generally higher shear capacity values than the corresponding models with glass-FRP bars. Furthermore, the shear force gain due to carbon-FRP bars is higher than that from glass-FRP bars due to a higher elastic modulus; thus, better bond performance. This observation is compatible with the results reported previously in the experimental pull-out study (refer to Chapter 3), where it was concluded that CFRP bars achieve higher pull-out bond strengths as well as better bond performance than the GFRP bars.

Secondly, the shear strengthening ratio of DE FRP bars is another parameter affecting the shear capacity of deep beams. It is expressed as (A_f / b_w s_f $\sin\theta_f$) where A_f is the cross-section area of the DE bar, b_w is the web width, s_f is the DE bar spacing and θ_f is the angle of inclination of the DE FRP bar. Table 4.8 presents the predicted results for the selected FE models. Figure 4.18 illustrates the effect of the shear strengthening ratio of DE FRP bars for three sets of deep beam FE models with steel stirrup reinforcement ratios of 0.149, 0.233 and 0.084 %. The shear span-to-effective depth ratio for all FE models was 1.9. Increasing the DE FRP bar ratio from 0.116 to 0.168 led to an increase in the shear force gain of 19.7 kN (20.8%), 12.7 % (11.4%) and 3.4 kN (3.4%) for CFRP-strengthened FE models with transverse steel reinforcement ratios of 0.149, 0.233 and 0.084 %, respectively. For the corresponding deep beam FE models with DE GFRP bars, increasing the DE FRP bar ratio from 0.116 to 0.168 led to an increase in the shear force gain of 13.2 kN (16.1%), 7 % (7.7%) and 9 kN (10.7%).

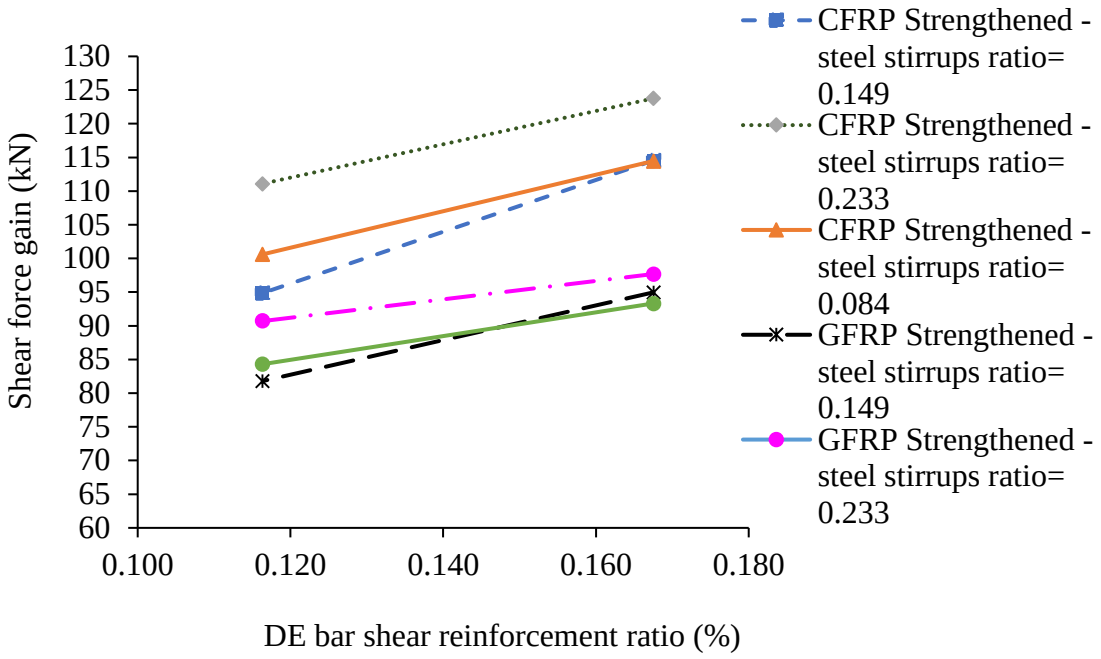

Figure 4.27 Effect of DE shear strengthening ratio on the shear force gain

Since the selected deep beam FE models had the same values of b_w (web width) and bar spacing (s_f) but different bar diameters, the shear strengthening ratio of DE FRP bars (A_f / b_w s_f) was higher for bars with larger diameters. In addition, bars with a larger diameter (i.e. greater bond area) achieve a higher pull-out capacity (Chapter 3). Thus, DE bars with a larger shear strengthening ratio restrict the crack opening and propagation compared to bars with smaller shear reinforcement ratio. Therefore, it can be concluded that increasing the shear strengthening ratio of DE FRP bars enhances both the shear force resistance and shear force gain in RC deep beams.

Table 4.8 Effect of FRP bar type (i.e. Young Modulus) and DE shear strengthening ratio

Beam ID	$\mathbf{E_f}$ (MPa)	$\boldsymbol{\rho_f}$ (%)	$\boldsymbol{\rho_v}$ (%)	Shear force capacity, $\boldsymbol{V_{FE}}$ (kN)	Shear force gain by DE FRP bars, $\boldsymbol{V_f}$ (kN)
FE4 (C/1.9)	130000	0.168	0.149	412.2	114.6
FE5 (G/1.9)	40000	0.168	0.149	392.6	95.0
FE7-GFRP	40000	0.251	0.114	407.6	125.8
FE8-CFRP	130000	0.251	0.114	419.6	137.9
FE10 (C/2.2)	130000	0.171	0.152	322.0	73.2
FE11 (G/2.2)	40000	0.171	0.152	300.4	51.7
FE13 (C/2.5)	130000	0.151	0.151	277.7	60.8
FE14 (G/2.5)	40000	0.151	0.151	259.5	42.5
FE16-GFRP	40000	0.168	0.084	369.8	93.3
FE17-CFRP	130000	0.168	0.084	390.9	114.5
FE19-GFRP	40000	0.168	0.233	413.9	97.7
FE20-CFRP	130000	0.168	0.233	440.0	123.8
FE22-GFRP	40000	0.116	0.084	360.8	84.3
FE23-CFRP	130000	0.116	0.084	377.1	100.6
FE25-GFRP	40000	0.116	0.149	379.4	81.8
FE26-CFRP	130000	0.116	0.149	392.5	94.9
FE28-GFRP	40000	0.116	0.233	406.9	90.7
FE29-CFRP	130000	0.116	0.233	427.3	111.1

4.6 Concluding Remarks

In this research study, a three-dimensional nonlinear finite element (FE) model successfully replicated the experimental results of five large-scale T-beams shear-strengthened with DE FRP bars.

- The FE results provided accurate predictions of the shear force capacity of the control and DE strengthened beams. The FE predicted versus experimental shear strength gain ratio was 0.963 with a standard deviation of 0.036.
- A comprehensive numerical parametric study investigated the effect of DE FRP bar diameter, shear span-to-effective depth ratio, DE FRP strengthening ratio, FRP bar

type and internal steel stirrup-to-DE FRP bar ratio on the shear strength of deep beams strengthened with DE FRP bars. The FE predictions revealed that the predicted shear strength gain depends on most of the investigated parameters.

- The DE shear-strengthened FE beam models with carbon-FRP bars achieved higher shear strength capacities than the corresponding FE beam models with DE glass-FRP bars.
- It was demonstrated that the predicted shear strength gain attributed to DE FRP bars increased with the increase in FRP bar diameter and DE FRP bar shear reinforcement ratio.
- The shear span-to-effective depth ratio and internal steel stirrup-to-DE FRP bar ratio negatively affected the shear strength gain, which reduced in both cases.

CHAPTER 5

ANALYTICAL INVESTIGATION OF REINFORCED CONCRETE DEEP BEAMS SHEAR-STRENGTHENED WITH DEEP EMBEDDED BARS

5.1 Introduction

Currently, there are no published design models for predicting the shear strength contribution due to embedded FRP bars in concrete deep beams. The aim of this chapter is to derive an explicit equation that takes into consideration the main shear resistance components in RC deep beams: the first component due to longitudinal main reinforcement and diagonal concrete strut (i.e. strut-and-tie mechanism), the second component due to steel stirrups, and the third component due to vertical DE FRP bars. The proposed coefficients for each of the above components are calibrated using a subset of the results presented in the parametric study for a total of 27 deep beam FE models (refer to Chapter 4).

Various design models have been previously developed for determining the shear capacity of RC deep beams reinforced only with horizontal or vertical steel shear reinforcement. These models can be categorised into semi-empirical methods (Mau and Thomas, 1989; Mihaylov et al., 2013; Russo et al., 2005; Siao, 1994), non-linear finite element models (Mohammed and Goma, 1993) or by using compatibility-aided truss models (Mau and Hsu, 1987; Hwang et al., 2000), including strut-and-tie models (Russo et al., 2005).

ACI-ASCE Committee 445 (1998) provides design guidance on the application of the strut-and tie-model (STM) for estimating the shear capacity of RC deep beams. This model applies the

principles of the lower bound theorem of plasticity. However, it is possible to apply several STMs, which implies that there is no unique shear design solution. Therefore, inadequate and over-conservative predictions may arise (Kassem, 2015). Furthermore, empirical models for steel-reinforced deep beams give biased predictions of the shear capacity; thus, their estimates have yielded significant scatter.

Various analytical studies have proposed shear strength equations for calculating the shear capacity of RC deep beams which employ the fundamental principles of the stress equilibrium condition, the strain compatibility condition and the constitutive laws of concrete and steel. These proposed design formulae have been previously validated using published experimental results of RC deep beams. Studies have proved that their predictions yield more consistent results and their closed-forms are less tedious and time-consuming when compared to finite element (FE) analysis and STM procedures. These shear strength formulae are summarised in Section 5.2 and have become the basis for formulating a new shear design model applicable for the DE shear strengthening technique.

5.2 Existing Shear Design Models

5.2.1 Mau and Hsu (1987)

Mau and Hsu (1987) proposed a Rotating Angle Softened Truss Model (RA-STM) (see Figure 5.1). This model assumes a perpendicular orientation of the developed cracks to the principal tensile stress in the concrete. However, this assumption implies that shear strength is due entirely to the steel, i.e. concrete makes no contribution, which in turn underestimates the shear strength of RC deep beams.

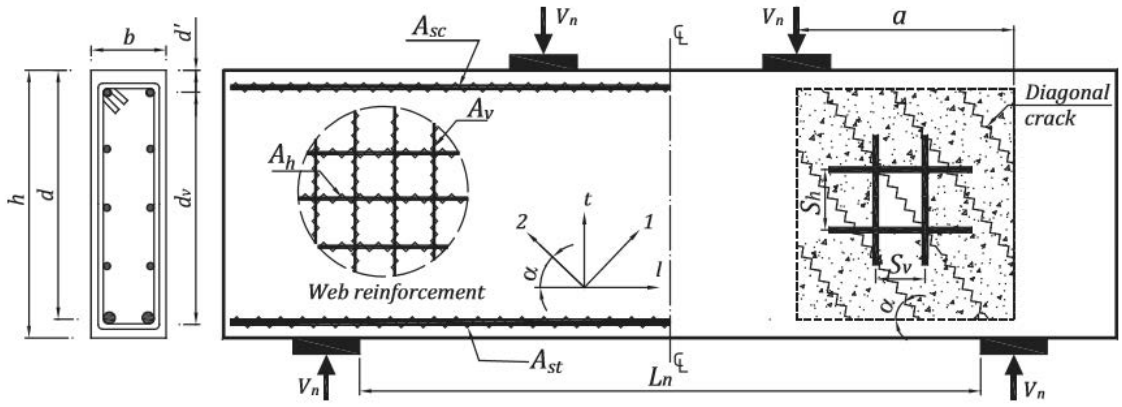

Figure 5.1 Strut-and-tie model for deep beams (Mau and Hsu, 1987)

The RC deep beam is envisioned as an assembly of three different elements: the concrete in compression region, top compression steel, and bottom tension steel, resisting the longitudinal compressive and tensile stresses respectively, and the web concrete and web steel reinforcement subjected to in-plane normal and shear stresses (Mau and Hsu, 1987).

The flexural capacity of the deep beam is assumed to be sufficiently greater than its shear capacity. The nominal shear strength is expressed as $v_n = \frac{V_n}{b_w\, d}$, where b_w is the beam width and d is the beam effective depth.

The ultimate shear strength (v_n) in this model is given by:

$$v_n = \frac{1}{2} f_c' \left[K\,(\omega_h + 0.003) + \sqrt{K^2(\omega_h + 0.03)^2 + 4\,(\,\omega_h + 0.03)(\omega_v + 0.03)} \right] \leq 0.3\, f_c' \qquad (5\text{-}1)$$

with the limitations $\omega_h = \rho_h\, f_y / f_c' \leq 0.26$ and $\omega_v = \rho_v\, f_y / f_c' \leq 0.12$.

where ρ_h and ρ_v are the steel horizontal reinforcement ratio and vertical reinforcement ratio, respectively.

This model introduces a transverse stress factor coefficient, (K), which accounts for the shear span effect as follows:

$$\begin{cases} K = \frac{2\,d_{fe}}{h} & \text{for } 0 \leq \frac{a}{h} \leq 0.5 \\ K = \frac{d_{fe}}{h}\left[\frac{h}{a}\left(\frac{4}{3} - \frac{2}{3}\,\frac{a}{h}\right)\right] & \text{for } 0.5 \leq \frac{a}{h} \leq 2.0 \\ K = 0 & \text{for } a/h \geq 2.0 \end{cases} \quad (5\text{-}2)$$

where $d_{fe} = d - d'$ is the effective shear depth, with d' the distance between the outer compressive fibre and the centre of top compression steel reinforcement (refer to Figure 5.1).

5.2.2 Kassem (2015)

The following Equation (5-3) is a modified form of the design model adopted by Mau and Hsu (1987). However, the analysis approach utilizes a fixed-angle softened truss model (FA-STM), which assumes that the orientation of cracks in the concrete is at a fixed angle; consequently, it allows the contribution due to concrete to be considered. This model proposes a new modified equation for the transverse stress intensity factor (K), which was formulated to calculate the theoretical shear strength of RC deep beams.

The ultimate shear strength (v_n) is given by:

$$v_n = 0.93\, f_c' \left[K\,(0.024 + \Delta_l) + \sqrt{K^2\,(0.024 + \Delta_l)^2 + 4\,(0.024 + \Delta_l)(0.049 + \Delta_v)} \right] \quad (5\text{-}3)$$

The dimensionless reinforcement index Δ can be determined as follows:

$$\Delta_l = \rho_l \, f_{yl} / f_c' \tag{5-4}$$

$$\Delta_v = \rho_v \, f_{yv} / f_c' \tag{5-5}$$

where ρ_l and ρ_v are the steel longitudinal reinforcement ratio and transverse reinforcement ratio, respectively; f_{yl} and f_{yv} are the steel yield stress of the longitudinal and transverse reinforcement, respectively. Of note is that, the longitudinal steel ratio of the shear element (ρ_l) includes both the tension and compression steel reinforcement (Kassem, 2015).

The transverse stress intensity factor, K, is estimated as follows:

$$\begin{cases} K = -98.02 - 0.18\,\rho_l\,f_{yl} - 580\;\rho_v + 130.30\,\frac{d_{fe}}{h} - 224.445\,\rho_h - 0.006\,a & \text{for } 0 \le \frac{a}{h} \le 0.5 \\ K = 1.29 - 0.62\,\frac{a}{d} - 0.045\,\rho_v\,f_{yv} - 0.012\,\rho_l\,f_{yl} + 0.003\,f_c' - 0.001\,h & \text{for } 0.5 \le \frac{a}{h} \le 2.0 \\ K = 0 & \text{for } a/h \ge 2.0 \end{cases} \tag{5-6}$$

5.2.3 Siao (1994)

The ultimate shear strength in this model (v_n) is given by:

$$v_n = 1.8\, f_{ta} \tag{5-7}$$

where f_{ta} is the allowable concrete tensile stress.

Two different expressions were formulated for f_{ta} as follows:

a) In the case of un-cracked concrete, f_{ta} can be estimated by:

$$f_{ta} = 0.58\sqrt{f_c'}\;[\,1 + n\,(\,\rho_h\,sin^2\,(\theta_s) + \rho_v\,cos^2\,(\theta_s))] \tag{5-8}$$

where n is the ratio of steel to concrete elastic moduli ($n = E_s / E_c$), ρ_h and ρ_v are the steel reinforcement ratios in the horizontal and vertical directions respectively, and θ_s is the angle between the inclined concrete strut and the beam's longitudinal axis.

b) In the case of cracked concrete, f_{ta} can be estimated by:

$$f_{ta} = f_y \left[\rho_h \sin^2(\theta_s) + \rho_v \cos^2(\theta_s) \right] \quad (5\text{-}9)$$

where f_y is the steel yield strength of the transverse steel reinforcement.

The greater value of Equations (5-8) and (5-9) is used to estimate the shear strength using Equation (5-7).

$$f_{ta} = max. \begin{cases} 0.58 \sqrt{f_c'} \left[1 + n \left(\rho_h \sin^2(\theta_s) + \rho_v \cos^2(\theta_s) \right) \right] \\ f_y \left(\rho_h \sin^2(\theta_s) + \rho_v \cos^2(\theta_s) \right) \end{cases} \quad (5\text{-}10)$$

5.2.4 Hwang et al. (2000)

Hwang et al. (2000) proposed an iterative procedure that is based on the strut-and-tie approach and the fundamental principles of equilibrium, compatibility, and constitutive laws of concrete and steel.

The ultimate shear strength (v_n) is given by:

$$v_n = \left(K_h + K_v - 1 \right) \zeta_c \, f_c' \, A_{str} \cos(\theta_s) \quad (5\text{-}11)$$

where ζ_c is the concrete softening coefficient and is based on the laws of softened concrete given by Zhang and Hsu (1998) as follows:

$$\zeta_c = \frac{5.8}{\sqrt{f_c'}} \frac{1}{\sqrt{1+400\,\varepsilon_1}} \leq \frac{0.9}{\sqrt{1+400\,\varepsilon_1}} \tag{5-12}$$

Hwang et al. (2000) proposed the value of principal tensile strain (ε_1) to be taken as 0.005. The concrete softening coefficient was given by:

$$\zeta_c \approx 3.35/\sqrt{f_c'} \leq 0.52 \tag{5-13}$$

The effective area of the diagonal concrete strut A_{str} which bears the diagonal pressure is defined as:

$$A_{str} = \alpha_s\, w_{st} \tag{5-14}$$

where α_s is the depth of the diagonal strut and w_{st} is the width of the diagonal strut.

K_h and K_v are the horizontal and vertical tie indices respectively. They are a function of the transverse steel reinforcement and are used to represent the flow of forces and the strut-and-tie idealization for the disturbed stress region (refer to Figure 5.2).

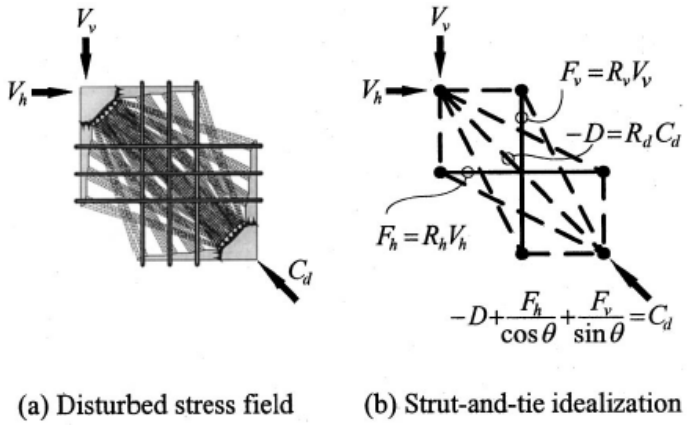

Figure 5.2 Complete mechanisms (Hwang et al., 2000)

5.2.5 Russo et al. (2005)

Russo et al. (2005) developed a parametric expression for estimating the nominal shear strength of RC deep beams reinforced with horizontal and vertical reinforcement using Equation (5-15) as follows:

$$v_n = 0.76\,(\kappa_r\,\chi\,f_c'\,\cos\theta + 0.25\,\rho_h\,f_{yh}\cot\theta + 0.35\,\frac{a}{d}\,\rho_v\,f_{yv}) \tag{5-15}$$

where $\kappa_r = \sqrt{(n\rho_l)^2 + 2\,n\,\rho_l}$ - $n\,\rho_l$; with n the ratio of steel to concrete elastic moduli ($n = E_s/E_c$) and ρ_l the longitudinal reinforcement ratio ($\rho_l = \frac{A_l}{b_w\,d}$).

The angle (θ) between the compression concrete strut and the vertical direction can be estimated using any of the following expressions for deep beams with web reinforcement:

$$\begin{cases} \theta_1 = \arctan\left(\frac{a}{jd}\right)\ \ where\ jd = d - \frac{\kappa_r d}{3}\ \ ;\ \ \textbf{\textit{Hwang et al.}}\,(\mathbf{2000}) \\ \theta_2 = \arctan\left(\frac{a}{0.9\ d}\right)\ where\ 0.9d\ is\ the\ lever\ arm\ \ ;\ \ \textbf{\textit{Siao}}\ (\mathbf{1994}) \end{cases} \tag{5-16}$$

The non-dimensional interpolating function (χ) can be obtained using:

$$\chi = 0.74\,(\frac{f_c'}{105})^3 - 1.28\,(\frac{f_c'}{105})^2 + 0.22\,\frac{f_c'}{105} + 0.87 \tag{5-17}$$

where a is the shear span, ρ_h and ρ_v are the steel horizontal and vertical web reinforcement ratios respectively, f_{yh} and f_{yv} are the yield strengths of the horizontal and vertical web reinforcement respectively, and d is the effective depth of the beam.

5.3 Proposed Design Formulae

Kassem (2015) predicted the shear capacity of 445 steel-reinforced deep beams using Mau and Hsu (1987), Siao (1994), Hwang et al. (2000), Russo et al. (2005) and Kassem (2015) formulae. He concluded that Mau and Hsu (1987), Siao (1994) and Hwang et al. (2000) formulae were unable to yield accurate shear strength predictions of the investigated RC deep beams. On the other hand, the proposed formulae by Kassem (2015) and Russo et al. (2005) yielded reliable and safe predictions, with the smallest coefficient of variations among the other models.

Therefore, this study presents new shear design equations for the DE technique which are modified forms of the shear strength equations formulated by Russo et al. (2005), Kassem (2015) and an additional shear strength formula proposed by Tan et al. (2003), which was not previously investigated in the study by Kassem (2015).

The predictions of the modified equations are comparable to those of the FE model. The proposed coefficients for each of the modified equations are calibrated using the shear strength results presented in the parametric study for a total of 27 deep beam FE models (refer to chapter 4). An additional term is added in each of the modified models to consider the contribution of the DE FRP web reinforcement. The proposed expressions are as follows.

5.3.1 Design Formula 1: Modified Form of Tan et al. (2003) Formula

Tan et al. (2003) developed an expression (refer to Equation 5-18) for the ultimate shear strength (V_n) of steel-reinforced deep beams. The adopted strut-and-tie model is shown in Figure 5.3.

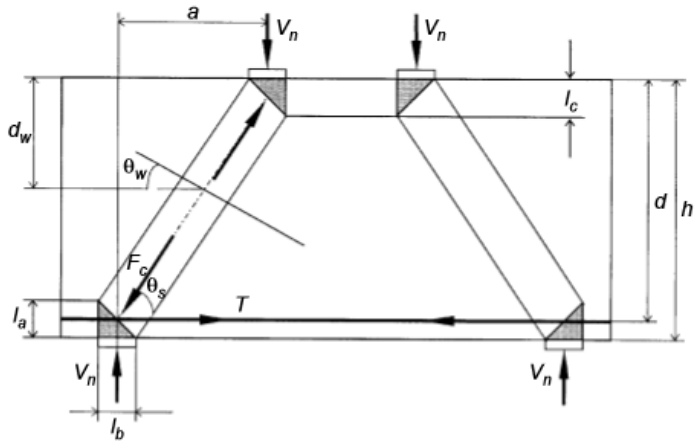

Figure 5.3 Strut-and-tie model for RC deep beams (Tan et al., 2003)

$$V_n = \frac{1}{\frac{sin\,2\,\theta_s}{f_t\,A_c} + \frac{1}{f_c'\;A_{str}\,sin\,\theta_s}} \tag{5-18}$$

In Equation (5-18), the angle of the inclined diagonal strut θ_s, is estimated as:

$$tan\,\theta_s = \frac{h - \frac{l_a}{2} - \frac{l_c}{2}}{a} \tag{5-19}$$

The angle of the inclined diagonal strut was estimated by assuming a value of $l_c = l_a$, where l_a = 2(h-d) and l_c is the depth of the top nodal zone, and its value is derived from the equilibrium of the top nodal zone as follows:

$$l_c = \frac{V_n/_{tan\,\theta_s}}{f_c'\;b_w} \tag{5-20}$$

The term A_{str} is the cross-sectional area of the diagonal strut estimated as:

$$A_{str} = b_w\,(l_a\;cos\,\theta_s + \;l_p\,sin\,\theta_s) \tag{5-21}$$

where b_w is the web width, l_a is the depth of the bottom nodal zone and l_p is the width of the support bearing plates (see Figure 5.3).

Equation (5-22) provides the combined tensile strength contribution of the concrete and web reinforcement, given by:

$$f_t = \frac{2\,A_l\,f_{yl}\sin\theta_s}{A_c/\sin\theta_s} + \frac{2\,A_v\,f_{yv}\,\sin(\theta_s+\theta_w)}{A_c/\sin\theta_s}\,\frac{d_w}{d} + f_{ct} \qquad (5\text{-}22)$$

where A_l and A_v are the total areas of steel longitudinal and web reinforcement respectively, f_{yl} and f_{yv} are the yield strengths of steel longitudinal and web steel reinforcement respectively, f_{ct} is the tensile strength of concrete $f_{ct} = 0.5\sqrt{f_c'}$ and A_c is the area of concrete section.

The first term in Equation (5-22) represents the tensile force contribution of longitudinal steel reinforcement. The second term denotes the tensile force contribution from the inclined web reinforcement at an angle θ_w to the beam's longitudinal axis, as shown in Figure 5.3. For vertical web reinforcement, $\theta_w = 90^0$. The factor $\frac{d_w}{d}$ takes into account the positional influence of web reinforcement. It should be noted that the further the web reinforcement is from the support or beam tensile fibre, the less efficient it is to resist the splitting of the diagonal strut, as the corresponding lever arm is smaller (Tan et al., 2003). The third term denotes the tensile capacity of concrete.

In the case of DE shear-strengthened deep beams, Equation (5-22) can be modified by introducing a fourth term to represent the contribution of the DE FRP bars to f_t in the form $A_f\,\varepsilon_{fe}\,E_f\,\sin(\theta_s+\theta_f)$. For vertical DE FRP bars, $\theta_f = 90^0$. The factor $\frac{d_w}{d}$ is again introduced to consider the positional influence of this type of reinforcement along the shear span, similar to the case of steel transverse reinforcement. Therefore, the combined tensile

strength contribution of longitudinal steel reinforcement, transverse steel reinforcement, concrete and vertical DE FRP bars can be determined as in Equation (5-23):

$$f_t = \frac{2\,A_l\,f_{yl}\,\sin\theta_s}{A_c/\sin\theta_s} + \frac{2\,A_v\,f_{yv}\,\sin(\theta_s+\theta_w)}{A_c/\sin\theta_s} * \left(\frac{d_w}{d}\right) + \frac{A_f\,\varepsilon_{fe}\,E_f\,\sin(\theta_s+\theta_f)}{A_c/\sin\theta_s} * \left(\frac{d_w}{d}\right) + f_{ct} \quad (5\text{-}23)$$

where the effective stress of DE FRP bar (f_{fe}) = $E_f\ \varepsilon_{fe}$ is estimated by limiting the effective strain (ε_{fe}) of DE FRP bars to 0.004, as suggested by fib (2007). Of note is that, the DE FRP bar strain at failure due to debonding and bar fracture is usually higher than 0.004 (as confirmed by the pull-out test results of Chapter 3 and the mechanical properties of the DE FRP bars). The strain limit of 0.004 is therefore presented as it represents the critical (i.e. lowest) strain value that causes failure.

The value obtained for the combined tensile strength contribution (f_t) using Equation (5-23) for each FE model was then substituted into Equation (5-18) and the ultimate shear strength was estimated for each FE model, as presented in Table 5.1. The shear strength results obtained from the proposed formula (Equation 5-18) are compared with the predictions provided by the nonlinear FE analysis using DIANA 9.4.6 (DIANA user's manual, 2016), as already explained in Chapter 4. The proposed formula gives an average ratio $V_{Caro\ 1}/V_{FE}$ equal to 0.806 and a standard deviation of 0.127. However, the results show that Equation (5-23) and Equation (5-18) predicted successfully only the total shear capacity of FE beam models but failed to yield accurate predictions for the shear force contribution due to DE FRP bars. Therefore, this study suggests that design formula 1: modified form of Tan et al. (2003) is not applicable for DE strengthened deep beams. Other formulae are therefore presented in the following sections.

Table 5.1 Design formula 1: - predictions of shear strength capacity and shear force gain due to FRP bars

	Shear force capacity, V_n (kN)			**Shear force gain due to DE FRP bars V_f (kN)**		
Beam ID	*FE analysis*	*Caro's formula No.1*	*Ratio* $V_{Caro\ 1}/V_{FE}$	*FE analysis*	*Caro's Formula No.1*	*Ratio* $V_{f,Caro\ 1}/V_{f,FE}$
FE3 (U/1.9)	297.6	277.8	0.93			
FE4 (C/1.9)	412.1	280.1	0.68	114.6	5.2	0.046
FE5 (G/1.9)	392.6	278.6	0.71	95.0	1.7	0.017
FE6	281.8	277.5	0.99			
FE7-GFRP	407.6	278.6	0.68	125.8	2.5	0.02
FE8-CFRP	419.6	280.9	0.67	137.9	7.8	0.057
FE9 (U/2.2)	248.7	248.8	1.00			
FE10 (C/2.2)	322.0	250.8	0.78	73.2	4.2	0.026
FE11 (G/2.2)	300.4	249.4	0.83	51.7	1.3	
FE12 (U/2.5)	216.9	223.9	1.03			
FE13 (C/2.5)	277.7	225.5	0.81	60.8	3.2	0.053
FE14 (G/2.5)	259.5	224.4	0.87	42.5	1.0	0.024
FE15	276.5	277.3	1.00			
FE16-GFRP	369.8	278.0	0.75	93.3	1.7	0.018
FE17-CFRP	390.9	279.6	0.72	114.5	5.4	0.047
FE18	316.2	278.6	0.88			
FE19-GFRP	413.9	279.3	0.68	97.7	1.6	0.016
FE20-CFRP	439.98	280.8	0.64	123.8	5.0	0.04
FE21	276.5	277.3	1.00			
FE22-GFRP	360.8	277.8	0.77	84.3	1.2	0.014
FE23-CFRP	377.1	278.9	0.74	100.6	3.8	0.038
FE24	297.6	277.8	0.93			

FE25-GFRP	379.4	278.3	0.73	81.8	1.2	0.014
FE26-CFRP	392.5	279.4	0.71	94.9	3.7	0.039
FE27	316.2	278.6	0.88			
FE28-GFRP	406.9	279.3	0.69	90.7	20.6	0.227
FE29-CFRP	427.3	280.9	0.66	111.1	22.2	0.201
Average			**0.806**			**0.053**
Standard Deviation			**0.127**			**0.060**

5.3.2 Design Formula 2: Modified Form of Russo et al. (2005) Formula

A single parametric expression is proposed for evaluating the nominal shear strength ($v_n = \frac{V_n}{b_w\, d}$) of deep beams with vertical steel reinforcement and strengthened in shear with deep embedded FRP bars as follows:

$$v_n = \frac{V_n}{b_w\, d} = c_1\, \kappa_r\, \chi\, f_c'\, cos\,\theta + c_2\, \frac{a}{d}\, \rho_f\, f_{fe} + c_3 \frac{a}{d}\, \rho_v\, f_{yv} \qquad (5\text{-}24)$$

where *a* is the shear span, *d* is the beam's effective depth, ρ_f ($= \frac{A_f}{b_w\, s_f}$) is the vertical DE shear strengthening reinforcement ratio, ρ_v ($= \frac{A_v}{b_w\, s_v}$) is the steel shear reinforcement ratio, f_{yv} is the yield stress of steel stirrups, and f_{fe} ($=E_f\, \varepsilon_{fe}$) is the effective stress of the DE FRP bar, with the effective strain (ε_{fe}) of the DE FRP bar limited to 0.004, as suggested by fib (2007).

Equation (5-24) is a function of the three unknown parameters, c_1, c_2, and c_3, which are defined based on the FE results (refer to Chapter 4) by minimizing the coefficient of variation

(COV), which is calculated as the ratio of the standard deviation (STD) to the average (AVG) of the ratios between the FE model and the proposed formula shear strength predictions.

The proposed model assumes that the nominal shear strength of deep beams (v_n) is given by the sum of three independent components:

$$v_n = v_c + v_w + v_f \tag{5-25}$$

where v_c is the shear strength contribution due to the diagonal compression strut and the longitudinal tension steel, v_w is the shear strength contribution from the transverse steel stirrups and v_f is the shear strength contribution given by the DE FRP bars.

The shear strength contribution (v_c) is determined based on the model by Hwang et al. (2000):

$$v_c = c_1 \kappa_r \chi f_c' \cos\theta \tag{5-26}$$

where $\kappa_r = \sqrt{(n\rho_l)^2 + 2n\rho_l} - n\rho_l$, with n the ratio of steel to concrete elastic moduli ($n = E_s / E_c$) and ρ_l the longitudinal reinforcement ratio ($\rho_l = \frac{A_l}{b_w d}$).

C_1 (<1.0) is a factor determined based on the FE modelling results using half of FE control deep beam models (i.e. with steel stirrups only and without DE FRP bars) by solving a series of systems of equations with two known independent variables, namely $\frac{v_c}{C_1}$ (i.e. $\kappa_r \chi f_c' \cos\theta$) and $\frac{v_w}{C_3}$ (i.e. $\frac{a}{d} \frac{A_v}{b_w s_v} f_{yv}$), and two unknown parameters c_1 and c_3. Then the proposed factor c_1 was validated against the results of the remaining five FE control beam models (refer to Chapter 4). In this study, the proposed value for c_1 is 0.43.

The angle (θ) between the concrete compression strut and the vertical direction can be estimated using the expression developed by Siao (1994):

$$\theta = tan^{-1}(\frac{a}{0.9\,d}) \quad (5\text{-}27)$$

where 0.9 d is the lever arm, and d is the effective depth.

The non-dimensional interpolating function (χ) is given by:

$$\chi = 0.74\,(\frac{f'_c}{105})^3 - 1.28\,(\frac{f'_c}{105})^2 + 0.22\,\frac{f'_c}{105} + 0.87 \quad (5\text{-}28)$$

The contribution of the DE FRP bars (v_f) is given by:

$$v_f = c_2\,\frac{a}{d}\,\frac{A_f}{b_w\,s_f}f_{fe} \quad (5\text{-}29)$$

Equation (5-29) shows that v_f is influenced by the main parameters governing the behaviour of shear-strengthened RC deep beams (i.e. a/d, DE FRP shear strengthening ratio and effective stress of DE FRP bars).

FE shear strength predictions for deep embedded shear strengthened beams (refer to Chapter 4) show that different FRP bars with different elastic moduli have comparable contributions. As a result, the coefficient c_2 is dependent upon the FRP bar material. Carbon-FRP bars with high elastic modulus values will have low c_2 values and glass-FRP bars with low elastic modulus values will have high c_2 values.

C_2 was determined based on the FE modelling results using half of FE beam models strengthened with CFRP and GFRP bars by solving a series of systems of equations with three known variables, $\frac{v_c}{c_1}$ $(\text{i.e. } \kappa_r\,\chi\,f'_c\cos\theta)$, $\frac{v_f}{c_2}$ $(\text{i.e. } \frac{a}{d}\,\frac{A_f}{b_w\,s_f}f_{fe})$, $\frac{v_w}{c_3}$ $\left(\text{i.e. } \frac{a}{d}\,\frac{A_v}{b_w\,s_v}\,f_{yv}\right)$, and three unknown parameters, c_1, c_2 and c_3. Then the proposed parameters were validated against the

results of the remaining FE models (refer to chapter 4). In this study, the proposed c_2 values for carbon-FRP bars and glass-FRP bars are 0.76 and 1.76 respectively. However, an extensive number of experimental tests and FE models need to be conducted to establish the accuracy of the proposed model.

The contribution of the transverse steel stirrups (v_w) is given by:

$$v_w = c_3 \frac{a}{d} \frac{A_v}{b_w s_v} f_{yv} \tag{5-30}$$

The value of factor c_3 is determined using the same procedure as in the case of factor c_1. In this study, the proposed value for the coefficient c_3 is 0.47.

Substituting the values of c_1, c_2, and c_3, Equation (5-24) becomes:

- Case 1: using DE carbon-FRP bars

$$v_n = \frac{V_n}{b_w d} = 0.43\, \kappa_r\, \chi\, f_c'\, cos\, \theta + 0.76 \frac{a}{d} \frac{A_f}{b_w s_f} f_{fe} + 0.47 \frac{a}{d} \frac{A_v}{b_w s_v} f_{yv} \tag{5-31}$$

- Case 2: using DE glass-FRP bars

$$v_n = \frac{V_n}{b_w d} = 0.43\, \kappa_r\, \chi\, f_c'\, cos\, \theta + 1.76 \frac{a}{d} \frac{A_f}{b_w s_f} f_{fe} + 0.47 \frac{a}{d} \frac{A_v}{b_w s_v} f_{yv} \tag{5-32}$$

Table 5.2 compares the predictions of Equation (5-31) and Equation (5-32) with the corresponding FE shear strength results. The average (AVG) of the ratios $V_{\text{Caro 2}}/V_{FE}$ (i.e. the ratio of the predicted shear strength using the proposed formulae to the non-linear FE predictions) is equal to 1.023 with a standard deviation of 0.148. The results show that Equations (5-31) and (5-32) successfully predicted the shear capacity, not only for the FE control beam models but also for the DE FRP shear-strengthened models. The average (AVG) of the ratios $V_{\text{f,Caro 2}}/ V_{\text{f,FE}}$ between the predicted shear gain, due to DE FRP bars using the proposed formulae and the non-linear FE predictions, is equal to 1.119 with a standard

deviation of 0.531. Therefore, this study suggests that design formula 2 has the potential to provide good estimates of both the total shear force capacity and the shear strength contribution of the DE FRP bars. Additional experimental tests and FE simulations are required to further confirm the accuracy of the proposed formulae.

Table 5.2 Design formula 2: - predictions of shear strength capacity and shear force gain due to FRP bars

	Shear force capacity, V_n (kN)			**Shear force gain due to DE FRP bars V_f (kN)**		
Beam ID	*FE analysis*	*Caro's formula No.2*	*Ratio* $V_{Caro\ 2}/V_{FE}$	*FE analysis*	*Caro's formula No.2*	*Ratio* $V_{f,Caro\ 2}/V_{f,FE}$
FE3 (U/1.9)	297.6	285.9	0.93			
FE4 (C/1.9)	412.1	400.1	0.95	114.6	114.2	0.997
FE5 (G/1.9)	392.6	367.3	0.92	95.0	81.4	0.857
FE6	281.8	270.6	0.84			
FE7-GFRP	407.6	392.7	0.88	125.8	122.1	0.971
FE8-CFRP	419.6	442.0	0.98	137.9	171.4	1.243
FE9 (U/2.2)	248.7	273.1	1.25			
FE10 (C/2.2)	322.0	407.2	1.33	73.2	134.1	1.831
FE11 (G/2.2)	300.4	368.7	1.31	51.7	95.5	1.848
FE12 (U/2.5)	216.9	262.3	1.58			
FE13 (C/2.5)	277.7	396.3	1.61	60.8	134.1	2.206
FE14 (G/2.5)	259.5	357.8	1.60	42.5	95.5	2.246
FE15	276.5	257.3	0.74			
FE16-GFRP	369.8	338.7	0.77	93.3	81.4	0.872
FE17-CFRP	390.9	371.6	0.81	114.5	114.2	0.998
FE18	316.2	322.5	1.18			
FE19-GFRP	413.9	403.9	1.09	97.7	81.4	0.833
FE20-CFRP	439.98	436.8	1.11	123.8	114.2	0.923

FE21	276.5	257.3	0.74			
FE22-GFRP	360.8	313.9	0.72	84.3	56.5	0.671
FE23-CFRP	377.1	336.7	0.75	100.6	79.3	0.789
FE24	297.6	285.9	0.93			
FE25-GFRP	379.4	342.4	0.88	81.8	56.5	0.691
FE26-CFRP	392.5	365.2	0.91	94.9	79.3	0.836
FE27	316.2	322.5	1.17			
FE28-GFRP	406.9	379.1	1.05	90.7	56.5	0.623
FE29-CFRP	427.3	401.9	1.06	111.1	79.3	0.714
Average			**1.023**			**1.119**
Standard Deviation			**0.148**			**0.531**

5.3.3 Design Formula 3: Modified Form of Kassem (2015) Formula

The following proposed equation is a modified form of the equation developed previously by Kassem (2015) (refer to section 5.2.2). This model proposes a new expression for predicting the shear capacity of deep beams shear-strengthened with DE FRP bars. A stepwise multiple linear regression analysis was previously carried out by Kassem (2015) to define the set of independent variables that significantly influence the dependent variable K in the case of steel-reinforced deep beams (Equation 5-33).

The analytical study by Kassem (2015) revealed that for steel-reinforced deep beams and shear span to depth ratio varying between $1.9 \leq$ a/d ≤ 3.0, the transverse stress factor (K) is dependent on the concrete compressive strength f_c', shear span-to-effective depth ratio (a/d),

steel longitudinal reinforcement ratio ($\rho_l = \frac{A_l}{b_w\, d}$) and the respective yield stress f_{yl}, steel transverse reinforcement ratio ($\rho_v = \frac{A_v}{b_w\, s_v}$) and the respective yield stress (f_{yv}).

The transverse stress factor K for control beams is given by:

$$K = 1.29 - 0.62\,\frac{a}{d} - 1.198\,\rho_v\, f_{yv} - 0.012\,\rho_l\, f_{yl} + 0.003\, f_c' - 0.001\, h \qquad (5\text{-}33)$$

Secondly, this current study revealed that for shear-strengthened beams with DE FRP bars and shear span to depth ratio varying between 1.9 ≤ a/d ≤ 3.0, the transverse stress factor (K) is also influenced by the parameters identified in Equation (5-33) as well as the DE FRP strengthening ratio ($\rho_f = \frac{A_f}{b_w\, s_f}$) and the FRP bar effective stress ($f_{fe} = E_f\, \varepsilon_{fe}$), which is estimated by limiting the effective strain (ε_{fe}) of DE FRP bar to 0.004, as suggested by fib (2007).

The transverse stress intensity factor was also found to be influenced by the FRP bar type. An additional term ($c_4\, \rho_f\, f_{fe}$) was included to take into account the contribution by DE FRP bars similar to the contribution by steel stirrups (see Equation 5-34 and 5-35). The model was calibrated using half of FE DE-strengthened beam models. FE predictions for deep embedded shear-strengthened beams (refer to Chapter 4) show that different FRP bars with different elastic moduli have comparable contributions. As a result, coefficient (c_4) is dependent upon the FRP bar material. Carbon-FRP bars with high elastic modulus values will have low c_4 values and glass-FRP bars with low elastic modulus values will have high c_4 values (see Equations 5-34 and 5-35). The proposed model was validated against the results of the remaining FE DE-strengthened beam models until COV reduced to an acceptable level.

Therefore, the transverse stress intensity factor (K) for strengthened beams with DE FRP bars can be expressed as follows:

- Case 1: using DE carbon-FRP bars

$$K = 1.29 - 0.62\,\frac{a}{d} - 1.198\,\rho_v\,f_{yv} - 0.688\,\rho_f\,f_{fe} - 0.012\,\rho_l\,f_{yl} + 0.003\,f_c' - 0.001\,h \qquad (5\text{-}34)$$

- Case 2: using DE glass-FRP bars

$$K = 1.29 - 0.62\,\frac{a}{d} - 1.198\,\rho_v\,f_{yv} - 1.712\,\rho_f\,f_{fe} - 0.012\,\rho_l\,f_{yl} + 0.003\,f_c' - 0.001\,h \qquad (5\text{-}35)$$

The modified ultimate shear strength (v_n) is given by:

$$v_n = 0.93\,f_c'\,[\,K\,(0.024 + \Delta_l) + \sqrt{K^2\,(0.024 + \Delta_l)^2 + 4\,(0.024 + \Delta_l)(0.049 + \Delta_v)(0.049 + \Delta_f)}\,] \qquad (5\text{-}36)$$

The dimensionless reinforcement indices Δ_l and Δ_v consider the contributions of the longitudinal steel reinforcement and transverse steel reinforcement, and can be determined as follows (refer to section 5.2.2):

$$\Delta_l = \rho_l\,f_{yl}/f_c' \qquad (5\text{-}37)$$

$$\Delta_v = \rho_v\,f_{yv}/f_c' \qquad (5\text{-}38)$$

An additional term (Δ_f) is included to take into account the contribution of the DE FRP bars:

$$\Delta_f = \rho_f\,f_{fe}/f_c' \qquad (5\text{-}39)$$

The shear strength values estimated using Equation (5-36) for each FE model are given in Table 5.3. To check the accuracy of the proposed formula, these results are compared with the non-linear FE predictions. The average of the ratios $V_{\text{Caro 3}}/V_{FE}$ between the predicted shear strength using the proposed formula and the nonlinear FE predictions is equal to 1.033 with a standard deviation of 0.265. The results show that Equation (5-36) successfully predicted the shear capacity of all the FE beam models and yielded safe and relevant predictions for the shear

force gain due to DE FRP bars. The average of the ratios $V_{f,Caro\ 3}/\ V_{f,FE}$ between the predicted shear force gain due to FRP bars using the proposed formula and the non-linear FE predictions is equal to 0.987 with a standard deviation of 0.353. Therefore, this study suggests that design formula 3 is applicable for DE shear-strengthened deep beams. However, since the number of FE models is limited, additional experimental tests and FE models are required in order to further establish the accuracy of the proposed model.

Table 5.3 Design formula 3: - predictions of shear strength capacity and shear force gain due to DE FRP bars

	Shear force capacity, V_n (kN)			**Shear force gain due to DE FRP bars V_{frp} (kN)**		
Beam ID	*FE analysis*	*Caro's formula No.3*	*Ratio* $V_{Caro\ 3}/V_{FE}$	*FE analysis*	*Caro's Formula No.3*	*Ratio* $V_{f,Caro\ 3}/V_{f,FE}$
FE3 (U/1.9)	297.6	277.5	0.93			
FE4 (C/1.9)	412.1	382.7	0.93	114.6	105.2	0.919
FE5 (G/1.9)	392.6	358.0	0.91	95.0	80.5	0.848
FE6	281.8	237.9	0.84			
FE7-GFRP	407.6	358.7	0.88	125.8	120.8	0.960
FE8-CFRP	419.6	395.8	0.94	137.9	157.9	1.145
FE9 (U/2.2)	248.7	312.1	1.25			
FE10 (C/2.2)	322.0	419.8	1.31	73.2	107.6	1.470
FE11 (G/2.2)	300.4	394.5	1.31	51.7	82.4	1.593
FE12 (U/2.5)	216.9	343.6	1.58			
FE13 (C/2.5)	277.7	438.4	1.58	60.8	94.7	1.558
FE14 (G/2.5)	259.5	416.1	1.61	42.5	72.5	1.704
FE15	276.5	203.6	0.74			
FE16-GFRP	369.8	284.1	0.77	93.3	80.5	0.862
FE17-CFRP	390.9	308.8	0.79	114.5	105.2	0.919

FE18	316.2	372.6	1.19			
FE19-GFRP	413.9	453.1	1.09	97.7	80.5	0.824
FE20-CFRP	439.98	477.8	1.11	123.8	105.3	0.851
FE21	276.5	203.6	0.74			
FE22-GFRP	360.8	259.5	0.72	84.3	55.9	0.663
FE23-CFRP	377.1	276.6	0.73	100.6	73.1	0.726
FE24	297.6	277.5	0.93			
FE25-GFRP	379.4	333.4	0.88	81.8	55.9	0.684
FE26-CFRP	392.5	350.6	0.89	94.9	73.1	0.770
FE27	316.2	372.6	1.18			
FE28-GFRP	406.9	428.5	1.05	90.7	55.9	0.617
FE29-CFRP	427.3	445.7	1.04	111.1	73.1	0.658
Average			**1.033**			**0.987**
Standard Deviation			**0.265**			**0.353**

5.4 Concluding Remarks

For the first time, this analytical study presented three shear design equations for predicting the shear strength capacity of deep beams shear-strengthened with DE FRP bars.

- The proposed equations are governed by the key parameters influencing the shear behaviour of deep beams. The equations are validated against FE results and two of them demonstrated accurate predictions, which will contribute to the safe application of the DE technique.
- The mean predicted-to-FE shear strength gain ratios for the design formula 2 and 3 were 1.119 and 0.987, respectively. The standard deviations were 0.531 and

0.353, respectively. However, additional experimental tests are required to verify the FE predictions and the reliability of the developed closed-form equations.

CHAPTER 6

CONCLUSIONS AND RECOMMENDATIONS

6.1 Introduction

In this research study, experimental pull-out tests and nonlinear finite element (FE) modelling were used to investigate the bond performance of DE FRP bars and shear behaviour of RC beams shear-strengthened with DE FRP bars respectively. The main objectives of this research that were accomplished are listed as follows:

1- To carry out a comprehensive review of the main parameters that affect the bond behaviour of epoxy-bonded DE bars in concrete;
2- To carry out a comprehensive review of the main parameters that govern the shear capacity of DE strengthened RC beams;
3- To perform pull-out tests that investigate DE FRP bar-to-concrete bond behaviour;
4- To investigate the effect of the main parameters that influence the bond behaviour of epoxy-bonded DE bars in concrete;
5- To propose a new bond strength mathematical model and validate it against experimental results;
6- To develop and validate a three-dimensional FE beam model capable of simulating the shear behaviour of RC beams shear-strengthened with DE FRP bars;
7- To carry out a parametric study using the developed FE model to examine the impact of the main parameters affecting the shear force capacity and the shear strength contribution due to DE FRP bars in deep beams;
8- To develop a new design formula for calculating the shear gain due to DE FRP bars in deep beams shear-strengthened with DE FRP bars.

6.2 Conclusions

Based on the results of the experimental, numerical and analytical work, the following conclusions can be drawn:

1- The state-of-the-art analysis of the published research studies on the bond behaviour of the DE embedment technique revealed that the impact of variables related to the properties of the FRP such as bar diameter, surface coating and bonded length, was investigated in particular for carbon-FRP bars but not sufficiently for glass-FRP bars. The impact of surface treatment on bond properties was investigated only for smooth and sand-coated FRP bars but not for ribbed FRP bars. The impact of embedment length of FRP bar was not addressed sufficiently for both carbon-FRP and glass-FRP bars. The influence of the concrete strength was very limitedly examined and additional bond tests need to be performed with concrete strength varying between 25 to 60 MPa. The potential procedure for controlling the bonded length during casting, using plastic tubes as an alternative for the post-drilling procedure, should be examined.

2- The published experimental studies examining the shear behaviour of RC beams strengthened in shear with DE bars documented that there is limited experimental data available which addresses the influence of concrete strength, shear span-to-effective depth, longitudinal steel reinforcement ratio, scale effect, depth of RC beam and existing level of pre-cracking of the RC beams on the shear capacity and strains experienced by the transverse shear and DE reinforcement. Most of the tested DE shear-strengthened RC beams had a shear span to effective depth (a/d) ratio greater than 2.5; thus, there is lack of rationale behind the shear behaviour and impact of the aforementioned parameters for deep RC beams with a/d <2.5. The analysis carried out

in this study identified the impact of the a/d ratio, depth of the beam and the potential interaction between the DE bars and the internal longitudinal reinforcement, on the shear gain of DE FRP bars.

3- The experimental programme examined the bond performance of DE FRP bars by conducting pull-out tests on both CFRP and GFRP bars, epoxy-bonded into 200 mm × 200 mm × 200 mm concrete cubes. The impact of embedment length, bar type and diameter, concrete strength and hole diameter on the bond behaviour was examined. The increase in embedded length enhanced the pull-out capacity but reduced both the maximum average bond stress and the initial stiffness of the bond stress-slip curves. The GFRP bars with embedded lengths of $15d_b$ failed by rupture, whereas the GFRP bars with shorter embedded lengths ($5d_b$ and $10d_b$) failed due to bar pull-out. Except for one specimen which failed due to concrete splitting, the CFRP bars failed due to bar pull-out. The specimens with CFRP bars had higher pull-out and bond strengths, as well as higher initial bond-slip stiffness, than the corresponding specimens with GFRP bars. The slip values corresponding to both the peak pull-out forces and the maximum average bond stresses were lower while the average bond stresses were higher for the specimens with CFRP bars, confirming a better bond performance. The increase in bar diameter from 10 to 12 mm led to a 30.4% increase in the pull-out capacity and 9.2% decrease in the maximum average bond stress for the specimens with DE CFRP bars. The behaviour of the corresponding specimens with DE GFRP bars was not affected by the change in bar diameter and these specimens failed due to bar rupture. The increase in concrete compressive strength from 26.1 to 45.6 MPa increased both the pull-out capacity and the maximum average bond stress for the specimens with DE CFRP bars by about 33%. The concrete compressive strength did not have a

significant impact on the initial stiffness, pull-out capacity or failure mode of the specimens with DE GFRP bars. The increase in hole diameter from $1.5d_b$ to $1.8d_b$ reduced the initial stiffness of the specimens with DE GFRP bars, but affected neither the failure mode (bar rupture) nor the failure loads.

4- A new mathematical model was proposed to predict the bond strength of DE FRP bars epoxy-bonded into concrete. The model was validated against experimental results and was demonstrated to produce accurate predictions in comparisons between predicted and measured values. The typical error of the proposed model for the examined data set was ±2% and the standard error was ±18%. The predictions were more accurate for CFRP and GFRP bars compared to AFRP bars, but this could be addressed through a change to the alpha value used in the model.

5- FE modelling proved to accurately simulate the overall behaviour of shear-strengthened RC beams with DE FRP bars, if appropriate element types, constitutive models and robust analysis procedure are adopted that can achieve convergence and result in computational efficiency by achieving less expensive equilibrium iterations. In this research study, a three-dimensional FE model was successfully developed and validated using experimental results of large-scale slender and deep beams shear-strengthened with DE FRP bars. The FE results provided accurate predictions of the shear behaviour and capacity of the DE shear-strengthened beams. The ratio between the FE-predicted and experimental shear strength gain due to DE FRP bars was 0.963 with a standard deviation of 0.036.

6- A comprehensive numerical FE parametric study was performed to investigate the effect of DE FRP bar diameter, shear span-to-effective depth ratio, DE FRP bar shear

reinforcement ratio, FRP bar type and internal steel stirrup-to-DE FRP bar ratio, on the shear strength of deep beams strengthened with DE FRP bars. This study concluded that the predicted shear strength gain depends on most of the investigated parameters. The DE shear-strengthened FE beam models with carbon-FRP bars achieved higher shear strength capacities than the corresponding FE beam models with DE glass-FRP bars. It was demonstrated that the predicted shear strength gain due to DE FRP bars increased with the increase in FRP bar diameter and DE FRP bar shear strengthening ratio. The shear span-to-effective depth ratio and internal steel stirrup-to-DE FRP bar ratio affected negatively the shear strength gain, which reduced in both cases.

7- Existing design guidelines for predicting the shear strength contribution due to DE FRP bars in RC slender beams are not fully developed. To date, there are only three design procedures available for shear strengthening of slender RC beam with DE technique. TR55 design guidance (2012) provides a set of shear design guidelines. The other procedures are proposed by Mofidi et al. (2012) and Qapo et al. (2016) in the form of analytical design models. Secondly, there are no published design models for predicting the shear strength contribution due to embedded FRP bars in concrete deep beams. For the first time, new analytical design equations were formulated for predicting the shear strength capacity of deep beams strengthened in shear with DE FRP bars. The proposed equations are governed by the main parameters influencing the shear capacity of deep beams. The equations are validated against FE results and two of them demonstrated accurate predictions. The mean predicted-to-FE shear strength gain ratios for that design formula 2 and 3 were 1.119 and 0.987, respectively. The standard deviations were 0.531 and 0.353, respectively. It is suggested that additional experimental tests should be carried out in order to confirm the FE predictions and the accuracy of the developed closed-form equations.

6.3 Recommendations for Future Work

This research study presented significant work on the bond behaviour and shear performance of concrete beams shear-strengthened with DE bars. The experimental pull-out test programme, numerical and analytical work covered substantial gaps in the DE technique shear strengthening application in deep RC beams. However, recommendations for future work are required to provide a thorough understanding of the following topics:

1- The proposed bond-slip mathematical model revealed that it can explicitly consider the constituent parameters that affect the bond behaviour in the DE FRP bar-epoxy-concrete interface, thus allowing variations during the design process. However, further experimental work is required to improve the values associated with these parameters in order to then incorporate this mathematical model into the development process of design guidelines for the DE technique.

2- For the first time, this study developed a finite element (FE) model and conducted a parametric study on the shear behaviour of deep beams strengthened with DE FRP bars. However, additional experimental tests are needed to establish the accuracy of FE predictions, extend the knowledge and expand the database of deep beams retrofitted with DE FRP bars.

3- The analytical work addressed the shortcoming with respect to design guidelines for RC deep beams shear-strengthened with DE FRP bars by proposing a couple of new closed-form design models based on the FE parametric study results. However, additional experimental tests are required to examine the accuracy of the proposed formulae.

APPENDIX A: BRE (1997) GUIDELINES-DESIGN MIX CONCRETE

Design mix of concrete

Stage	Item	Values				
1	1.1 Characteristic Strength		Specified	N/mm2	30	at 28days
		Proportion Defective			5	%
	1.2 Standard Deviation	Fig 3	Less than 20 results s=		8	N/mm2
		5% defective	k (Sec 4.4 p12)=		1.64	
	1.3 Margin	CI		M=k*s	13.1	N/mm2
		or specified				N/mm2
	1.4 Target Mean strength	C2		fm=fc+M	43.1	N/mm2
	1.5 Cement Type	Specified	Ordinary Portant Cement			
	1.6 aggregate Type: Coarse : Fine		Crushed(100%) + Uncrushed(0%)			
	1.7 Free-water/Cement ratio	Table2, Fig 4	0.51	Use the lower Value		
	1.8 Maximum Free-Water/Cement ratio	Specified	0.5		0.5	
2	2.1 Slump or Vebe time	Specified	Slump	60~180mm	Vebe time	0-3 s
	2.2 Maximum Aggregate Size	Specified	Crushed(100%) + Uncrushed(0%)		10 mm	mm
	2.3 Free-water Content	Table3	(see pfa sheet) table 9B	Wwater=	230	kg/m³
3	3.1 Cement content C3	C= Free-water contenet/free-water/cement ratio			460	kg/m³
	3.2 Maximum Cement content	Specified				kg/m³
	3.3 Minimum Cement content	Specified				kg/m³
			use3.1 if〉 3.2			
			use3.3 if〉 3.1			kg/m³
4	4.1 Relative Density of aggregate (SSD)		2.7			
	4.2 Concrete Density	Fig 5		D=	2390	kg/m³
	4.3 Total Aggregate content	C4		Aggregate=D-C-W	1700.0	kg/m³
5	5.1 Grading of Fine Aggregate		Percentage Passing 600μm sieve=		75	%(assumed)
	5.2 Proportion of Fine Aggregate	Fig 6			40	%
	5.3 Fine Aggregate content	Fine=Total aggregate*Proportion of fine=			680.0	kg/m³
	5.4 coarse Aggregate content C5	Total aggregate-Fine aggregate=			1020.0	kg/m³

6	Quantities(kg)	Cement	Water	Fine Aggregate	Coarse Aggregate (10mm)	
					Natural 100%	Recycled 0%
	6.1 Per m³ (based on SSD, Moisture content of SSD was compared with that of Oven Dry)	460.0	230.0	680.0	1020.0	0.0
	Absorption of Aggregate (constant) fine; 1.52%, natural coarse; 1.3% @ (SSD)			1.52	1.30	
	6.2 Per m³ (based on Oven dry)	460.0	253.3	669.8	1006.9	
	6.2.1 Per volume of 0.01 required	4.6	2.5	6.7	10.1	
	6.3 per m³(based on Air dry : moisture content of Air Dry was compared with that of Oven dry)					
	Absorption of Aggregate (variable) fine; 7.97%, natural coarse; 2.51 % @ (Air dry)			7.97	2.51	
		460.0	169.3	727.8	1032.8	
	6.3.1 Per volume of 0.01 required	4.6	1.7	7.3	10.3	
	Note * the water vol (1.7 l) was reduced by 470 ml so final H2O conntent = 1230 ml					

Design mix of concrete

Stage	Item	Values				
1	1.1 Characteristic Strength		Specified	N/㎟	**50**	at 28days
		Proportion Defective			**5**	%
	1.2 Standard Deviation	Fig 3	Less than 20 results s=		**8**	N/㎟
		5% defective	k (Sec 4.4 p12)=		**1.64**	
	1.3 Margin	**CI**		M=k*s	**13.1**	N/㎟
		or specified				N/㎟
	1.4 Target Mean strength	**C2**		fm=fc+M	**63.1**	N/㎟
	1.5 Cement Type	Specified	Ordinary Portant Cement			
	1.6 aggregate Type: Coarse : Fine		Crushed(100%)+Uncrushed(0%)			N/㎟
	1.7 Free-water/Cement ratio	Table2, Fig 4	0.34	Use the lower Value		
	1.8 Maximum Free-Water/Cement ratio	Specified	0.5		**0.34**	
2	2.1 Slump or Vebe time	Specified	Slump	**60~180mm**	Vebe time	**0-3 s**
	2.2 Maximum Aggregate Size	Specified	Crushed(100%)+Uncrushed(0%)		**10 mm**	mm
	2.3 Free-water Content	Table3	(see pfa sheet) table 9B	Wwater=	**230**	kg/㎥
3	3.1 Cement content C3	C= Free-water contenet/free-water/cement ratio			**676**	kg/㎥
	3.2 Maximum Cement content	Specified				kg/㎥
	3.3 Minimum Cement content	Specified				kg/㎥
			use3.1 if> 3.2			
			use3.3 if> 3.1			kg/㎥
4	4.1 Relative Density of aggregate (SSD)		**2.7**			
	4.2 Concrete Density	Fig 5		D=	**2390**	kg/㎥
	4.3 Total Aggregate content	C4		Aggregate=D-C-W	**1626.0**	kg/㎥
5	5.1 Grading of Fine Aggregate		Percentage Passing 600㎛ sieve=		**75**	%(assumed)
	5.2 Proportion of Fine Aggregate	Fig 6			**40**	%
	5.3 Fine Aggregate content		Fine=Total aggregate*Proportion of fine=		**650.4**	kg/㎥
	5.4 coarse Aggregate content C5		Total aggregate-Fine aggregate=		**975.6**	kg/㎥

6	**Quantities(kg)**	**Cement**	**Water**	**Fine Aggregate**	**Coarse Aggregate (10mm)**	
					Natural 100%	**Recycled 0%**
	6.1 Per ㎥ (based on SSD, Moisture content of SSD was compared with that of Oven Dry)	**534.0**	**230.0**	**650.4**	**975.6**	**0.0**
	Absorption of Aggregate (constant) fine; 1.52%, natural coarse; 1.3% @ (SSD)			**1.52**	**1.30**	
	6.2 Per ㎥ (based on Oven dry)	**534.0**	**252.3**	**640.7**	**963.1**	
	6.2.1 For 0.07 m3 volume required	**34.7**	**16.4**	**41.6**	**62.6**	
	6.3 Per ㎥ (based on Air dry : moisture content of Air Dry was compared with that of Oven dry)					
	Absorption of Aggregate (variable) fine; 7.97 %, natural coarse; 2.51 % @			**2.12**	**1.37**	
		534.0	**225.0**	**654.5**	**976.5**	
	6.3.1 For 0.065 m3 volume required	**34.7**	**14.6**	**42.5**	**63.5**	

Design mix of concrete

Stage	Item	Values				
1	1.1 Characteristic Strength		Specified	N/㎟	**50**	at 28days
		Proportion Defective			**5**	%
	1.2 Standard Deviation	Fig 3	Less than 20 results s=		**8**	N/㎟
		5% defective	k (Sec 4.4 p12)=		**1.64**	
	1.3 Margin	**CI**		M=k*s	**13.1**	N/㎟
		or specified				N/㎟
	1.4 Target Mean strength	**C2**		fm=fc+M	**63.1**	N/㎟
	1.5 Cement Type	Specified	Ordinary Portant Cement			
	1.6 aggregate Type: Coarse : Fine		Crushed(100%)+Uncrushed(0%)			N/㎟
	1.7 Free-water/Cement ratio	Table2, Fig 4	0.34	Use the lower Value		
	1.8 Maximum Free-Water/Cement ratio	Specified	0.5		**0.34**	
2	2.1 Slump or Vebe time	Specified	Slump	**60~180mm**	Vebe time	**0-3 s**
	2.2 Maximum Aggregate Size	Specified	Crushed(100%)+Uncrushed(0%)		**10 mm**	mm
	2.3 Free-water Content	Table3	(see pfa sheet) table 9B	Wwater=	**230**	kg/㎥
3	3.1 Cement content C3	C= Free-water contenet/free-water/cement ratio			**676**	kg/㎥
	3.2 Maximum Cement content	Specified				kg/㎥
	3.3 Minimum Cement content	Specified				kg/㎥
			use3.1 if> 3.2			
			use3.3 if> 3.1			kg/㎥
4	4.1 Relative Density of aggregate (SSD)		**2.7**			
	4.2 Concrete Density	Fig 5		D=	**2390**	kg/㎥
	4.3 Total Aggregate content	C4		Aggregate=D-C-W	**1483.5**	kg/㎥
5	5.1 Grading of Fine Aggregate		Percentage Passing 600㎛ sieve=		**75**	%(assumed)
	5.2 Proportion of Fine Aggregate	Fig 6			**37**	%
	5.3 Fine Aggregate content		Fine=Total aggregate*Proportion of fine=		**548.9**	kg/㎥
	5.4 coarse Aggregate content C5		Total aggregate-Fine aggregate=		**934.6**	kg/㎥

6	**Quantities(kg)**	**Cement**	**Water**	**Fine Aggregate**	**Coarse Aggregate (10mm)**	
					Natural 100%	**Recycled 0%**
	6.1 Per ㎥ (based on SSD, Moisture content of SSD was compared with that of Oven Dry)	**676.5**	**230.0**	**548.9**	**934.6**	**0.0**
	Absorption of Aggregate (constant) fine; 1.52%, natural coarse; 1.3% @ (SSD)			**1.52**	**1.30**	
	6.2 Per ㎥ (based on Oven dry)	**676.5**	**250.2**	**540.7**	**922.6**	
	6.2.1 For 0.01 m3 volume required	**6.8**	**2.5**	**5.4**	**9.2**	
	6.3 Per ㎥ (based on Air dry : moisture content of Air Dry was compared with that of Oven dry)					
	Absorption of Aggregate (variable) fine; 7.97 %, natural coarse; 2.51 % @ (Air dry)			**7.97**	**2.51**	
		676.5	**179.6**	**587.5**	**946.4**	
	6.3.1 Per volume of 0.01 required	**6.8**	**1.8**	**5.9**	**9.5**	
	Note * the water vol (1.8 l) was increased by 160 ml so final H2O conntent = 1960 ml					

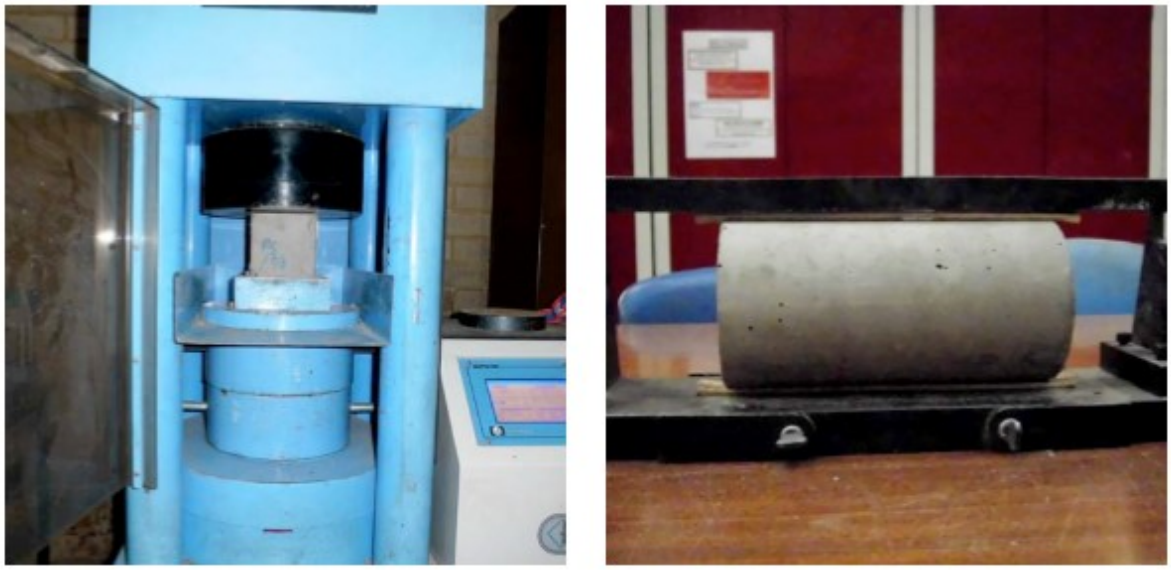

(a) (b)

Figure A.1 Concrete tests: a) Cube compressive test (BS EN 12390-3:2009) and b) Cylinder split test (BS EN 12390-6:2000)

Date of casting – 2.08.2016 **Age: 28 days**			
cube 1	32.7	cylinder 1	26.2
cube 2	33.5	cylinder 2	26.8
cube 3	31.5	cylinder 3	25.2
cube 4	32.5		
average	32.8	**average**	26.1

Date of casting – 2.08.2016 **Age: 28 days**			
cube 1	31.1	cylinder 1	24.9
cube 2	31.3	cylinder 2	25.0
cube 3	30.8	cylinder 3	24.6
cube 4	30.9		
average	31.1	**average**	24.8

Date of casting – 2.08.2016 **Age: 28 days**			
cube 1	58.5	cylinder 1	46.8
cube 2	57	cylinder 2	45.6
cube 3	55.8	cylinder 3	44.6
cube 4	56.9		
average	57.1	**average**	45.6

APPENDIX B: LINEAR REGRESSION ANALYSIS

Input: Data of specimens (pull-out failure only)

FRP type	Study	Specimen	f_c'	E_f	d_b	E_p	l_b	d_b	τ_b	Pull-out force
			MPa	GPa	mm	MPa	mm	mm	Mpa	kN
CFRP		C26-15db-CFRP10-1.8db	26.1	130	10	1493	150	18	11.4	53.9
GFRP		C25-5db-GFRP12-1.5db	24.8	40	12	1493	60	18	10.1	22.8
CFRP		C25-5db-CFRP12-1.5db	24.8	130	12	1493	60	18	13.8	31.3
GFRP		C25-5db-GFRP12-1.5db	24.8	40	12	1493	60	18	11.6	26.5
CFRP		C25-5db-CFRP12-1.5db	24.8	130	12	1493	60	18	13	29.5
GFRP		C25-10db-GFRP12-1.5db	24.8	40	12	1493	120	18	7.8	35.2
CFRP	Caro et al. (2017)	C25-10db-CFRP12-1.5db	24.8	130	12	1493	120	18	10.7	48.3
GFRP		C46-5db-GFRP10-1.5db	45.6	40	10	1493	50	15	13.5	21.2
GFRP		C46-10db-GFRP10-1.5db	45.6	40	10	1493	100	15	12.6	39.7
CFRP		C46-10db-CFRP10-1.5db	45.6	130	10	1493	100	15	13.8	43.5
CFRP		C46-15db-CFRP10-1.5db	45.6	130	10	1493	150	15	15.6	73.4
CFRP (smooth)		C2-1.25d-9.5S-15d	42.7	155	9.52	2830	143	12	18.8	80.4
CFRP (smooth)		C2-1.50d-9.5S-15d	42.7	155	9.52	2830	143	15	22.3	91.2
CFRP (smooth)		C2-2.00d-9.5S-15d	42.7	155	9.52	2830	143	19	18.4	78.5
CFRP (smooth)		C2-1.50d-9.5S-5.0d	42.7	155	9.52	2830	48	15	29.9	42.8
CFRP (smooth)		C2-1.50d-9.5S-7.5d	42.7	155	9.52	2830	71	15	26.9	57.4
CFRP (smooth)	Godat et al.(2012)	C2-1.50d-9.5S-10.0d	42.7	155	9.52	2830	95	15	22.3	63.4
CFRP (smooth)		C2-1.50d-9.5S-12.5d	42.7	155	9.52	2830	119	15	20.1	71
CFRP (smooth)		C2-1.50d-9.5S-17.5d	42.7	155	9.52	2830	166	15	20.3	100.7
CFRP (smooth)		C2-1.50d-9.5S-20.0d	42.7	155	9.52	2830	190	15	18.1	102.4

Input: Log-linear model

FRP type	Study	Specimen	$ln\ (f_c')$ MPa	$ln(E_f)$ GPa	$ln(d_b)$ mm	$ln(E_p)$ MPa	$ln(l_b)$ mm	$ln(d_h)$ mm	$ln(\tau_b)$ Mpa
GFRP	Caro et al. (2017)	C25-5db-GFRP12-1.5db	3.2619	4.8675	2.3026	7.3085	5.0106	2.8904	2.4336
CFRP		C25-5db-CFRP12-1.5db	3.2108	3.6889	2.4849	7.3085	4.0943	2.8904	2.3125
GFRP		C25-5db-GFRP12-1.5db	3.2108	4.8675	2.4849	7.3085	4.0943	2.8904	2.6247
CFRP		C25-5db-CFRP12-1.5db	3.2108	3.6889	2.4849	7.3085	4.0943	2.8904	2.4510
GFRP		C25-10db-GFRP12-1.5db	3.2108	4.8675	2.4849	7.3085	4.0943	2.8904	2.5649
CFRP		C25-10db-CFRP12-1.5db	3.2108	3.6889	2.4849	7.3085	4.7875	2.8904	2.0541
GFRP		C46-5db-GFRP10-1.5db	3.2108	4.8675	2.4849	7.3085	4.7875	2.8904	2.3702
GFRP		C46-10db-GFRP10-1.5db	3.8199	3.6889	2.3026	7.3085	3.9120	2.7081	2.6027
CFRP		C46-10db-CFRP10-1.5db	3.8199	3.6889	2.3026	7.3085	4.6052	2.7081	2.5337
CFRP		C46-15db-CFRP10-1.5db	3.8199	4.8675	2.3026	7.3085	4.6052	2.7081	2.6247
CFRP (smooth)	Godat et al. (2012)	C2-1.25d-9.5S-15d	3.7542	5.0434	2.2534	7.3085	5.0106	2.7081	2.7473
CFRP (smooth)		C2-1.50d-9.5S-15d	3.7542	5.0434	2.2534	7.9480	4.9628	2.4849	2.9339
CFRP (smooth)		C2-2.00d-9.5S-15d	3.7542	5.0434	2.2534	7.9480	4.9628	2.7081	3.1046
CFRP (smooth)		C2-1.50d-9.5S-5.0d	3.7542	5.0434	2.2534	7.9480	4.9628	2.9444	2.9124
CFRP (smooth)		C2-1.50d-9.5S-7.5d	3.7542	5.0434	2.2534	7.9480	3.8712	2.7081	3.3979
CFRP (smooth)		C2-1.50d-9.5S-10.0d	3.7542	5.0434	2.2534	7.9480	4.2627	2.7081	3.2921
CFRP (smooth)		C2-1.50d-9.5S-12.5d	3.7542	5.0434	2.2534	7.9480	4.5539	2.7081	3.1046
CFRP (smooth)		C2-1.50d-9.5S-17.5d	3.7542	5.0434	2.2534	7.9480	4.7791	2.7081	3.0007
CFRP (smooth)		C2-1.50d-9.5S-20.0d	3.7542	5.0434	2.2534	7.9480	5.1120	2.7081	3.0106

Output

Regression Statistics	
Multiple R	0.977959489
R Square	0.956404762
Adjusted R Square	0.940835034
Standard Error	0.085010263
Observations	20

ANOVA

	df	*SS*	*MS*	*F*	*Significance F*
Regression	5	2.219593	0.443919	61.4272	5.03E-09
Residual	14	0.101174	0.007227		
Total	19	2.320768			

	Coefficients	*Standard Error*	*t Stat*	*P-value*	*Lower 95%*	*Upper 95%*	*Lower 95.0%*	*Upper 95.0%*
Intercept	-0.51787	2.434881	-0.21269	0.834637	-5.74017	4.704432	-5.74017	4.704432
ln (f_c')	0.31144	0.180263	1.727677	0.10603	-0.07519	0.698062	-0.07519	0.698062
ln(l_b)	-0.31963	0.051669	-6.18606	2.37E-05	-0.43044	-0.20881	-0.43044	-0.20881
ln(E_f)	0.22549	0.046622	4.836678	0.000264	0.1255	0.325487	0.1255	0.325487
ln(E_p)	0.51969	0.099706	5.212188	0.000132	0.305839	0.733537	0.305839	0.733537
ln(d_b)	-0.59005	0.59281	-0.99534	0.336463	-1.8615	0.681402	-1.8615	0.681402

Residual Output

Observation	*Predicted Ln(stress)*	*Residuals*
1	2.4336	0.0000
2	2.3372	-0.0247
3	2.6030	0.0217
4	2.3372	0.1138
5	2.6030	-0.0380
6	2.1157	-0.0615
7	2.3814	-0.0112
8	2.6928	-0.0901
9	2.4712	0.0625
10	2.7370	-0.1123
11	2.6074	0.1399
12	3.0032	-0.0694
13	3.0032	0.1014
14	3.0032	-0.0909
15	3.3521	0.0457
16	3.2270	0.0651
17	3.1339	-0.0293
18	3.0619	-0.0612
19	2.9555	0.0551
20	2.9124	-0.0165

REFERENCES

Achillides, Z. and Pilakoutas, K. (2004) Bond Behaviour of Fiber Reinforced Polymer Bars Under Direct Pull-out Conditions. **Journal of Composites for Construction**, 8 (2): 173-181

ACI Committee 318 (2005) **Building Code Requirements for Structural Concrete and Commentary**. ACI 318R-05. USA: Farmington Hills, MI

ACI Committee 318 (2008) **Building Code Requirements for Structural Concrete and Commentary**. ACI 318-08. USA: Farmington Hills, MI

ACI Committee 318 (2011) **Building Code Requirements for Structural Concrete and Commentary**. ACI 318-11. USA: Farmington Hills, MI

ACI Committee 440 (2006) **Guide for the Design and Construction of Structural Concrete Reinforced with FRP Bars**. ACI 440.1R-06. USA: Farmington Hills, MI

ACI Committee 440 (2008) **Guide for the Design and Construction of Externally Bonded FRP Systems for Strengthening Concrete Structures**. ACI 440.2R-08. USA: Farmington Hills, MI

ADINA (2009) **Automatic Dynamic Incremental Nonlinear Analysis, Finite Element Software (Version 8.5.4)**. Watertown, MA: ADINA R&D Incorporation

Advisory Council of ASCE (2013) **Report Card for America's Infrastructure**. [online]. Available from: http://dx.doi.org/10.1061/9780784478837 [Accessed 13 July 2016]

Ali, A.H., Mohamed, H. M. and Benmokrane, B. (2016) Shear Behavior of Circular Concrete Members Reinforced with GFRP Bars and Spirals at Shear Span-to-Depth Ratios Between 1.5 and 3.0. **Journal of Composites for Construction**, 20 (6): 04016055

Andermatt, M.F. and Lubell A.S. (2013) Behavior of Concrete Deep Beams Reinforced with Internal Fiber Reinforced Polymer-Experimental Study. **ACI Structural Journal**, 110 (4): 585-594

ASCE-ACI Committee 445 (1998) Recent Approaches to Shear Design of Structural Concrete. **Journal of Structural Engineering**, 124 (12): 1375-1417

Baena, M., Torres, L., Turon, A. et al. (2009) Experimental Study of Bond Behaviour between Concrete and FRP Bars Using a Pull-out Test. **Composites Part B: Engineering**, 40 (8): 784-779

Bank, L. C. (2006) **Composites for Construction: Structural Design with FRP Materials**. New Jersey: John Wiley & Sons

Bank, L.C., Gentry, R.T. and Barkatt, A. (1995) Accelerated Test Methods to Determine the Long-Term Behavior of FRP Composite Structures: Environmental Effects. **Journal of Reinforced Plastics and Composites**, 14 (6): 559-587

Barros, J.A.O. and Dalfre, G.M. (2013) Assessment of the Effectiveness of the Embedded Through-Section Technique for the Shear Strengthening of Reinforced Concrete Beams. **Strain**, 49 (1): 75-93

Baẑant, Z.P. and Oh, B.H. (1983) Crack Band Theory for Fracture of Concrete. **Materials and Structures**, 16 (3): 155-177

Birrcher, D. B., Tuchscherer, R. G., Huizinga, M. et al. (2009) **Strength and Serviceability Design of Reinforced Concrete Deep Beams**. CTR Technical report 0-5253-1, University of Texas, Austin, United States

Birrcher, D.B., Tuchscherer, R.G., Huizinga, M. et al. (2013) Minimum Web Reinforcement in Deep Beams. **ACI Structural Journal**, 110 (2): 297-306

Bousselham, A. and Chaallal, O. (2008) Mechanisms of Shear Resistance of Concrete Beams Strengthened in Shear with Externally Bonded FRP. **ASCE Journal of Composite Construction**, 12 (5): 499-512

Breveglieri, M., Aprile, A. and Barros J.A.O. (2015) Embedded Through-Section Shear Strengthening Technique Using Steel and CFRP Bars in RC Beams of Different Percentage of Existing Stirrups. **Composite Structures**, 126: 101-113

Breveglieri, M., Barros, J.A.O., Aprile, A. et al. (2016) Strategies for Numerical Modelling the Behavior of RC Beams Strengthened in Shear Using the ETS Technique. **Engineering Structures**, 128: 296-315

Brown, M. D. and Bayrak, O. (2007) Investigation of Deep Beams with Various Load Configurations. **ACI Structural Journal**, 104 (5): 611-620

Canadian Standards Association (2004) **Design of Concrete Structures**. CSA-A23.3-04. Canada, Toronto, Ontario

Canadian Standards Association (2007) **Design and Construction of Building Components with Fibre-Reinforced Polymers**. CAN/CSA-S806-02. Canada, Rexdale

Canadian Standards Association (2012) **Design and Construction of Building Components with Fiber-Reinforced Polymers**. CAN/CSA S806-12. Canada, Mississauga, Ontario

Canadian Standards Association (2014) **Design of Concrete Structures**. CSA A23.3-14. Canada, Mississauga, Ontario

Caro, M., Yemaa, Y., Dirar, S. et al. (2017) Bond Performance of Deep Embedment FRP Bars Epoxy-Bonded into Concrete. **Engineering Structures**, 147: 448-457

Chaallal, O., Mofidi, A., Benmokrane, B. et al. (2011) Embedded Through-Section FRP rod Method for Shear Strengthening of RC Beams: Performance and Comparison with Existing Techniques. **ASCE Journal of Composites for Construction**, 15 (3): 374-383

Collins, M. P. and Mitchell, D. (1997) **Prestressed Concrete Structures**. Canada, Toronto: Response Publications

Comptroller and Auditor General, National Audit Office (NAO), Department for Transport and Highways Agency (2014) **Maintaining strategic infrastructure: roads**. [online] Available from: https://www.nao.org.uk/wp-content/uploads/2015/06/Maintaining-Strategic-Infrastructure-Roads.pdf [Accessed 12 February 2018]

Concrete Society (2012) **Design Guidance for Strengthening Concrete Structures Using Fibre Composite Materials**. Technical Report TR55. Crowthorne: The Concrete Society

Cosenza, E., Manfredi, G., and Realfonzo, R. (1997) Behaviour and Modelling of Bond of FRP Rebars to Concrete. **ASCE Journal of Composites for Construction**, 1 (2): 40-51

De Lorenzis, L. and Nanni, A. (2001) Shear Strengthening of Reinforced Concrete Beams with Near-Surface Mounted Fibre-Reinforced Polymer Rods. **ACI Structural Journal**, 98 (1): 60-68

De Paiva, H. A. R. and Siess, C. P. (1965) Strength and Behaviour of Deep Beams in Shear. **Proceedings of American Society of Civil Engineers**. 91: 19-41

Dirar, S. and Theofanous, M. (2017) "Large-Scale Reinforced Concrete T-beams Strengthened in Shear with Embedded GFRP bars." In **Advanced Composites in Construction**. University of Sheffield. pp 114-119

Dirar, S., Lees, J.M. and Morley, C. (2013a) Phased Nonlinear Finite-Element Analysis of Pre-Cracked RC T-Beams Repaired in Shear with CFRP sheets. **ASCE Journal of Composites Construction**, 17 (4): 476-487

Dirar, S., Lees, J.M. and Morley, C.T. (2013b) Precracked Reinforced Concrete T-Beams Repaired in Shear with Prestressed Carbon Fiber-Reinforced Polymer Straps. **ACI Structural Journal**, 110 (5): 855-866

Eligehausen, R., Popov, E.P., and Bertero, V. (1983) **Local Bond Stress-Slip Relationships of Deformed Bars Under Generalized Excitations**. Report No. 83/23, University of California, Berkeley: Earthquake Engineering Research

El-Sayed, A. K., El-Salakawy, E. F. and Benmokrane, B. (2006) Shear Strength of FRP-Reinforced Concrete Beams without Transverse Reinforcement. **ACI Structural Journal**, 103 (2): 235-243

Farghaly, A.S. and Benmokrane B. (2013) Shear Behavior of FRP-Reinforced Concrete Deep Beams Without Web Reinforcement. **ASCE Journal of Composite Construction**, 17 (6): 04013015

fib (2007) **FRP reinforcement in RC structures**. Technical Report Volume 40 of Bulletin. Switzerland: Fédération Internationale du Béton

fib (2011) **Design Examples for Strut-and-Tie Models**. Technical Report Volume 61 of Bulletin. Switzerland: Fédération Internationale du Béton

fib (2012) **Model Code 2010 - Final draft: Volume 1**. Technical Report Volume 65 of Bulletin. Switzerland: Fédération Internationale du Béton

GangaRao, H.V.S., Taly, N. and Vijay, P.V. (2007) **Reinforced Concrete Design with FRP Composites**. Boca Raton: CRC Press

Godat, A., Chaallal, O. and Neale, K.W. (2013) Nonlinear Finite Element Models for the Embedded Through-Section FRP Shear Strengthening Method. **Computers and Structures**, 119: 12-22

Godat, A., L'Hady, A. and Chaallal, O. et al. (2012) Bond Behavior of the ETS FRP Bar Shear-Strengthening Method. **ASCE Journal of Composites for Construction**, 16 (5): 529-539

Guadagnini, M., Pilakoutas, K. and Waldron, P. (2003) Shear Performance of FRP Reinforced Concrete Beams. **Journal of Reinforced Plastics and Composites**, 22 (15): 1389-1407

Hee, S.C. and Jefferson, A.D. (2008) A New Model for Simulating Cracks in Cementitious Composites. **Engineering and Computational Mechanics**, 161 (1): 3-16

Holicky, M., Markova, J. and Sykora, M. (2010) "Assessment of Deteriorating Reinforced Concrete Road Bridges." In Bris, R., Soares, C.G. and Martorell, S. (eds) **Reliability, Risk, and Safety: Theory and Applications**. London: Taylor and Francis. pp 1377-1383

Hwang, S.J., Lu, W.Y. and Lee, H. J. (2000) Shear Strength Prediction for Deep Beams. **ACI Structural Journa**l, 97 (3)

Jemaa, Y., Jones, C. and Dirar, S. (2015) "Deep Embedment Strengthening of Full-Scale Shear Deficient Concrete Beams." In Wu, Z., Wu, G. and Wang, X. (eds) **Proceedings of the 12th International Symposium on Fiber Reinforced Polymers for Reinforced Concrete Structures (FRPRCS-12) and the 5th Asia-Pacific Conference on Fiber Reinforced Polymers in Structures (APFIS-2015) Joint Conference**. Nanjing, China: International Institute for FRP in Construction (IIFC). pp 1-6

Kanakubo, T., Yonemaru, K., Fukuyama, H. et al. (1993) "Bond Performance of Concrete Members Reinforced with FRP bars" In Nanni, A. and Dolan, C. W. (eds) **Proceedings of**

the International Symposium on Fiber Reinforced Plastic Reinforcement for Concrete Structures. ACI Special Publication, SP-138. pp 767-788

Kani, G. N. J. (1964) The Riddle of Shear Failure and Its Solution. **ACI Journal Proceedings**, 61 (4): 441-468

Kani, M.W., Huggins, M.W., Kani, G.et al. (1979) **Kani on Shear in Reinforced Concrete**. Toronto: University of Toronto.

Kassem, W. (2015) **Shear Strength of Deep Beams: A Mathematical Model and Design Formula**. Ernst & SohnVerlag für Architektur und technische Wissenschaften GmbH & Co. KG. Berlin: Structural Concrete, No. 2, 184-194

Kong, F.K., Robins P.J., Kirby, D.P. et al. (1972) Deep Beams with Inclined Web Reinforcement. **ACI Structural Journal**, 69: 172-176

Lubell, A., Sherwood, T., Bentz, E. et al. (2004). Safe Shear Design of Large, Wide Beams. **Concrete International**, 26 (1): 66-78

Marti, P. (1985) Basic Tools of Reinforced Concrete Beam Design. **ACI Structural Journal**, 82 (1): 46-56

Mau, S. and Thomas, S. T. C. (1989) Formula for the Shear Strength of Deep Beams. **ACI Structural Journal**, 86 (5)

Mau, S. T. and Hsu, T. T. C. (1987) Shear Strength Prediction for Deep Beams with Web Reinforcement. **ACI Structural Journal**, 84 (6): 513-523

Meyer, R.W. (1985) **Pultrusion technology handbook**. New York: Chapman and Hall.

Mihaylov, B. I., Bentz, E. C. and Collins, M. P. (2010) Behavior of Large Deep Beams Subjected to Monotonic and Reversed Cyclic Shear. **ACI Structural Journal**, 107 (6): 726-734

Mihaylov, B. I., Bentz, E. C. and Collins, M. P. (2013) Two-Parameter Kinematic Theory for Shear Behavior of Deep Beams. **ACI Structural Journal**, 110 (3)

Mofidi, A., Chaallal, O., Benmokrane B. et al. (2012) Experimental Tests and Design Model for RC Beams Strengthened in Shear Using the Embedded Through-Section FRP method. **ASCE Journal of Composites for Construction**, 16 (5): 540-550

Mohamed K., Farghaly A.S., Benmokrane B. (2017) Effect of Vertical and Horizontal Web Reinforcement on the Strength and Deformation of Concrete Deep Beams Reinforced with GFRP Bars. **Journal of Structural Engineering**, 143 (8): 04017079

Mohamed, K., Farghaly, A. S., Benmokrane, B. et al. (2016) Strut Efficiency-Based Design for Concrete Deep Beams Reinforced with Fiber-Reinforced Polymer Bars. **ACI Structural Journal**, 113 (4), 791-800

Mohamed, K., Farghaly, A.S., Benmokrane B. et al. (2013) Nonlinear Finite-Element Analysis for the Behavior Prediction and Strut Efficiency Factor of GFRP-Reinforced Concrete Deep Beams. **Engineering Structures**, 137 (7): 145-161:0141-0296

Mohammed, A. K. and Gomaa, S. T. (1993) Finite Element Modelling of Deep Beams. **Computers and Structures**, 48 (1): 63-71

Nagasaka, T., Fukuyama, H. and Tanigaki, M. (1993) **Shear Performance of Concrete Beams Reinforced with FRP Stirrups. Fiber Reinforced Plastic Reinforcement for Concrete Structures**, ACI 138: 789-811, USA: Farmington Hills, MI

Nanni, A., AI-Zaharani, M. M., AI-Dulaijan. S. U. et al. (1995) "Bond of FRP reinforcement to Concrete Experimental Results". In Taerwe, L. (ed) **Proceedings of the Second International RILEM Symposium**. FRPRCS-2J. Belgium, Ghent: E& FN Spon. pp 135-145

Oh, J. K. and Shin, S. W. (2001) Shear Strength of Reinforced High Strength Concrete Deep Beams. **ACI Structural Journal**, 98 (2): 164-173

Qapo, M. (2016a) **Nonlinear Finite Element Modelling of FRP Shear-Strengthened Prestressed and Reinforced Concrete Beams**. PhD thesis, University of Birmingham

Qapo, M., Dirar, S. and Jemaa Y. (2016b) Finite Element Parametric Study of Reinforced Concrete Beams Shear-Strengthened with Embedded FRP bars. **Composite Structures**, 149: 93-105

Qapo, M., Dirar, S., Yang, J. et al. (2015) Nonlinear Finite Element Modelling and Parametric study of CFRP Shear-Strengthened Prestressed Concrete Girders. **Construction of Building Materials**, 76: 245-255

Qin, S., Dirar, S., Yang J. et al. (2014) CFRP Shear Strengthening of Reinforced-Concrete T-Beams with Corroded Shear Links. **ASCE Journal of Composites for Construction**, 19 (5): 04014081

Quintero-Febres, C. G., Parra-Montesinos, G. and Wight, J. K. (2006) Strength of Struts in Deep Concrete Members Designed Using Strut-and-Tie Method. **ACI Structural Journal**, 103 (4): 577-586

Rahal, K.N. and Rumaih, H.A. (2011) Tests on Reinforced Concrete Beams Strengthened in Shear Using Near Surface Mounted CFRP and Steel Bars. **Engineering Structures**, 33: 53-62

Razaqpur, A. G., Isgor, O. B., Cheung, M. S. et al. (2001) "Background to Shear Design Provisions of the Proposed Canadian Standard for FRP Reinforced Concrete Structures" **Proceedings of the International Conference, Composites in Construction-CCC**. Porto/Portugal. pp. 403-408

Remmel, G (1994) **Zum Zug-und Schubtragverhalten von Bauteilen aus hochfestem Beton.**: Report No. 444. Berlin: Deutscher Ausschuss für Stahlbeton (In German)

Rizzo, A. and De Lorenzis, L. (2009) Behavior and Capacity of RC Beams Strengthened in Shear with NSM FRP Reinforcement. **Construction and Building Materials**, 23 (4): 1555-1567

Russo, G., Venir, R. and Pauletta, M. (2005) Reinforced Concrete Deep Beams-Shear Strength Model and Design Formula. **ACI Structural Journal**, 102 (3)

Schlaich, J., Schäfer, K. and Jennewein, M. (1987) Toward a Consistent Design of Structural Concrete. **PCI Journal**, 32 (3): 74-150

Siao, W. B. (1994) Shear Strength of Short Reinforced Concrete Walls, Corbels, and Deep Beams. **ACI Structural Journal**, 91 (2): 123-132

Smith, K.N. and Vantsiotis, A.S. (1982) Shear Strength of Deep Beams. **ACI Structural Journal**, 79 (3): 201-213

Tan, K. H., Kong, F. K., Teng, S. et al. (1997) Effect of Web Reinforcement on High-Strength Concrete Deep Beams. **ACI Structural Journal**, 94 (5): 572-582

Tan, K. H., Tong, K. and Tang C.Y. (2001) A Direct Strut-and-Tie Model for Prestressed Deep Beams. **ASCE Journal of Structural Engineering**, 127: 1076-1084

Tan, K.H., Tang, C.Y. and Tong, K. (2003) A direct method for deep beams with web reinforcement. **Magazine of Concrete Research**, 55 (1): 53-63

Taylor, H.P.J. (1974) The Fundamental Behavior of Reinforced Concrete Beams in Bending and Shear. **ACI Special Publication**, 42: 43-78

Tepfers, R. and De Lorenzis, L. (2003) Bond of FRP Reinforcement in Concrete – a Challenge. **Mechanics of Composite Materials**, 39 (4): 315-332

Teychenné, D.C, Franklin, R.E. and Erntroy, H.C. (1997) **Design of Normal Concrete Mixes**. United Kingdom, Watford: Building Research Establishment Ltd

Thorenfeldt, E., Tomaszewicz, A. and Jensen, J.J. (1987). "Mechanical Properties of High Strength Concrete and Applications in Design." In **Utilization of High-Strength Concrete**, **Stavanger, 15-18 June, 149-159**

Tighiouart, B., Benmokrane, B., and Gao, D. (1998) Investigation of Bond in Concrete Member with Fibre Reinforced Polymer (FRP) bars. **Construction and Building Materials**, 12 (8): 453-462

TNO DIANA BV (2012) **DIANA User's Manual (Release 9.4.4)**. Delft, The Netherlands: TNO DIANA BV

TNO DIANA BV (2016) **DIANA User's Manual (release 9.4.6)**. Delft, The Netherlands: TNO DIANA BV

Triantafillou, T.C. (1998) Shear Strengthening of Reinforced Concrete Beams Using Epoxy-Bonded FRP Composites. **ACI Structural Journal**, 95 (2): 107-115

Tuchscherer, RG., Birrcher D., Huizinga, M. et al. (2011) Distribution of Stirrups Across Web of Deep Beams. **ACI Structural Journal**, 108 (1): 108-115

Valerio, P. and Ibell, T.J. (2003) Shear Strengthening of Existing Concrete Bridges. **Structures and Buildings**, 156 (1): 75-84

Valerio, P., Ibell, T.J and Darby A.P. (2009) Deep Embedment of FRP for Concrete Shear Strengthening. **Structures and Buildings**, 162 (5): 311-321

Vecchio, F.J and Collins, M.P. (1993) Compression Response of Cracked Reinforced Concrete. **ASCE Journal of Structural Engineering**, 119 (12): 3590-3610

Wight, J.K. and MacGregor, J. (2009) **Reinforced Concrete: Mechanics and Design (5th edition**. New Jersey: Pearson Prentice Hall, Upper Saddle River

Yun, Y. M. and Ramirez, J. A. (1996) Strength of Struts and Nodes in Strut-and-Tie Model. Journal of Structural Engineering, 122 (1): 20-29

Zhang, L., X. B. and Hsu, T. T. C. (1998) Behavior and Analysis of 100 MPa Concrete Membrane Elements. **Journal of Structural Engineering**, 124 (1): 24-34

Zhao, W., Maruyama, K. and Suzuki, K. (1995) "Shear Behavior of Concrete Beams Reinforced by FRP Rods as Longitudinal and Shear Reinforcement" In Taerwe, L.(eds) **Proceedings of the Second International RILEM Symposium on Non-Metallic (FRP) Reinforcement for Concrete Structures (FRPRCS-2)**. London: E&FN Spon. pp 352-359

Zsutty, T. (1968) Beam Shear Strength Prediction by Analysis of Existing Data. **ACI Structural Journal**, 65 (11): 943-951